Morphodynamic modelling of a wave-dominated tidal inlet : the Albufeira lagoon

Guillaume Dodet

THÈSE

Présentée à

L'UNIVERSITÉ DE LA ROCHELLE

ÉCOLE DOCTORALE SCIENCES POUR L'ENVIRONNEMENT
GAY-LUSSAC

Par Guillaume DODET

Pour obtenir le grade de

DOCTEUR

Spécialité: Terre, enveloppes fluides

Morphodynamic modelling of a wave-dominated tidal inlet: the Albufeira Lagoon

---

Soutenue le 19 décembre 2013:

Devant la commission d'examen formée de:

Huib de Swart	Professeur, Utrecht University (Pays-Bas)	Rapporteur
Giovanni Coco	Chercheur, IH Cantabria (Espagne)	Rapporteur
Edward Anthony	Professeur, Université d'Aix en Provence	Examinateur
Bruno Castelle	Chargé de recherche au CNRS HDR, UMR EPOC	Examinateur
Guy Woppelmann	Professeur, Université de La Rochelle	Examinateur
Eric Chaumillon	Maitre de Conférences HDR, Université de La Rochelle	Examinateur
André Fortunato	Directeur de Recherche, LNEC (Portugal)	Co-Directeur
Xavier Bertin	Chargé de recherche au CNRS, UMR 7266 LIENSs	Directeur

- 2013 -

A mon père, Antoine

Financial support for this investigation (PTDC/ECM/103801/2008, FCT) was provided by the *Fundação para a Ciência e a Tecnologia* of the Portuguese *Ministério da Ciência, Tecnologia e Ensino Superior*.

Remerciements, Acknowledgements, Agradecimentos

We shall not cease our exploration
And the end of all our exploring
Will be to arrive where we started
And know the place for the first time

T.S. Eliot, *Four Quartets*, 1942

Finalement... l'aboutissement de ce travail de thèse. Une page se tourne, le voyage touche à sa fin. Ou plutôt une simple escale avant de repartir. Le chemin était long et sinueux pour atteindre les rivages de l'Atlantique depuis les contreforts du Vercors; mais parsemé de rencontres inoubliables.

Tout d'abord, merci à vous Alphonse (Nahon), Florent (Birrien) et François (Batifoulier) de m'avoir transmis votre passion pour l'Océan alors que nous voguions ensemble entre les amphis bordelais et les plages landaises durant nos années d'école d'ingénieurs.

Namasté Shankar (Doraiswamy)! Thank you for having supervised my second-year internship at the National Institute of Oceanography, Dona Paula, India. This three-month stay at NIO definitely aroused my interest for physical oceanography and I will never forget your charisma and kindness. Living in India has been a fascinating experience and the roads I travelled along have influenced my life more than I could imagine.

Kia Ora Andrew (Moores), Cyprien (Bosserelle), Dougal (Greer), James (Frazerhurst), Jose (Borrero), Kerry (Black), Laurent (Lebreton), Moira (Healey), Shaw (Mead) and Shawn (Harrison). Doing my final-year internship at ASR Limited, in the idyllic town of Raglan, New-Zealand was a dream come true. I learned a lot by your side thanks to your great availability, your awesome individual skills and your contagious passion for coastal sciences, and waves in particular. Et merci à toi, Pierre (Lubin) pour m'avoir encouragé du début à la fin de ce projet de fin d'étude, depuis le campus de Bordeaux I.

Hier ergreife ich die Gelegenheit, um meiner liebsten Freundin Ruth (Brune) von ganzem Herzen zu danken. Herzlichen Dank Ruth, für deine nachdrückliche Unterstützung vor, während, und nach diesen PhD-Jahren. Unsere gemeinsame Reise und die Freuden, die sie begleitet haben, waren mir zweifellos eine riesige Hilfe, um die Herausforderungen erfolgreich zu überstehen und

nie aufzugeben. Vielen Dank für das alles, Ruth!

Chris (Blenkinsopp), I still remember this after-work-talk at Raglan's pub when you mentioned a giant field trip in the South-West of France, in which you would take part soon. A few months and emails later, I was driving from Germany to Cap-Ferret in order to volunteer in the UK-Australia team led by Gerd (Masselink) and Ian (Turner) for the ECORS project: a one-month field survey at the Truc-Vert Beach. Many thanks to you Chris, Gerd and Ian for making this spontaneous request possible. This amazing field work, and the one that followed in Slapton, UK, have for sure triggered my wish to become a researcher in coastal sciences. It was also a great opportunity to meet many inspiring scientists among whom I particularly thank André (Pacheco), Daniel (Buscombe), Paul (Russell), Saul (Reynolds) and Tim (Scott), for their amazing kindness and hospitality.

C'est à Lisbonne, quelques mois après le projet ECORS, que je fais la rencontre de Xavier (Bertin), co-encadrant avec Rui (Taborda) d'un projet de recherche en collaboration entre le Laboratoire National d'Ingénierie Civile et l'Université de Lisbonne, et futur directeur de thèse. Merci à toi Xavier pour ton encadrement irréprochable, ta grande disponibilité et ton immense sympathie. Ton enthousiasme, ton efficacité et la justesse de tes analyses m'épateront toujours; je mesure pleinement la chance que ce fût d'apprendre à tes côtés. Merci de m'avoir fait confiance! Também agradeço profundamento ao André (Fortunato), o meu segundo mentor e co-director desta tese de doutoramento. André, ter um director de tese excelente já é uma grande sorte, mas ter dois em simultâneo é mesmo um milagre! O teu profissionalismo, rigor no trabalho e eficácia estão ao mesmo nível da tua gentileza e simpatia. Tive imenso prazer em poder trabalhar e aprender contigo.

Agradeço também a todos os colegas portugueses do LNEC com quem tive oportunidade de trabalhar, discutir e aprender; em particular: Alberto (Azevedo), Alda (Silveira), Ana (Mendes), Anabela (Oliveira), Filipa (Oliveira), Francisco (Sancho), Gonçalo (de Jesus), Lourenço (Mendes), Martha (Guerreiro), Marta (Rodrigues), Paula (Freire) e Sérgio (Den Boer). Tenho a agradecer à Diretora do Departamento de Hidráulica e Ambiente, Rafaela Matos, por me ter acolhido no LNEC. Um agradecimento especial ao Rui (FCUL) por ter sido um supervisor motivante, disponível e sempre simpatico. Muito obrigado também a Conceição (Freitas) e César (Andrade), grandes especialistas da Lagoa de Albufeira, pelas discussões sobre a morfodinâmica da Lagoa. O capitulo 3.2 desta tese é, em grande parte, baseado no trabalho deles.

Ces années passées au LNEC m'ont aussi donné la chance de partager mon bureau avec Nicolas (Bruneau), puis Florian (Ganthy), deux chercheurs talentueux et infatigables avec qui j'ai eu un immense plaisir à travailler, deux très bons amis avec qui j'ai pu savourer le bonheur de vivre à Lisbonne.

I take the opportunity to thank Joseph (Zang) and Aron (Roland) for their precious help during the developing stage of the numerical model. It has been a real pleasure to work with you and I am sure we will have further opportunities to collaborate (wave-current modelling still has a long life ahead). Thank you Joseph for double-checking the chapter about the modelling

system. Aron, thanks a lot for providing access to your personal cluster, on which I had to run simulations until the very last night.

I also would like to warmly thank the thesis jury: Bruno (Castelle), Edward (Anthony), Eric (Chaumillon), Giovanni (Coco), Guy (Wöppelmann) and Huib (de Swart), for their very constructive remarks. It was a real honour to defend my work in front of such a panel of experts and I really enjoyed the discussion that followed my presentation. I am particularly grateful to Giovanni and Huib for reviewing this thesis; your final reports were of great help to prepare the defence.

Un grand merci à tous mes collègues et amis du LIENSs, à La Rochelle, pour m'avoir soutenu et supporté pendant les périodes les plus difficiles de ma thèse. Ne pouvant citer tout le monde, je chargerai une équipe de luxe, à savoir: Antoine, Caio, Camille, Gaël, Kai, Luc, Paula, Pascal, Thibault, Thomas, Thomas et Virginia, de faire passer le mot. Une mention toute particulière, évidemment, à mes deux grands potes Jeff et Médéric, pour m'avoir si bien accueilli dans ce labo (et chez eux!), pour tous ces fou-rires "made in bureau 127", et ces immanquables pauses sur la passerelle. Bref un grand merci à vous deux pour tous ces excellents moments passés ensemble. Merci à Guy, Isabelle et Micha, pour vos conseils et votre soutien pendant les longs mois de rédaction/ATER. Merci à Aziz Hamdouni et Paco Bustamante de m'avoir permis de réaliser cette thèse au LIENSs dans d'excellentes conditions, merci à Nicolas Alligner et Lucia Picard d'avoir réussi à jongler avec mes ordres de mission improbables et merci à Jennifer de La Corte Gomez et Isabelle Hirsch d'avoir rendu les contraintes administratives aussi simples et limpides que possible.

A tous ces collègues de travail qui sont pour beaucoup devenus d'excellents amis, s'ajoute la longue liste des bons vieux (et plus récents) potes que je tiens à remercier ici. Ceux du 26: Alex, Geoff, Marl, Mat, Marine, Phil, Ro, Vio, Xav, Yo; ceux de Lyon: Flo, Héb, Jérem, Juan, Koutch, Mathias, Moana, Rémi, Reynatou, Rooks, Salomé; ceux d'Allemagne: Aurélie, Denis, Edith, Hanna, Jacques, Jakob, Jeannette, Malte, Martin, Mathieu, Timo; ceux de Lisbonne: Alex, Coco, Elisabete, Maria João, Mat, Oliv, Thib, Xavière; et ceux que j'aurais oublié et auprès de qui je m'excuse.

L'aboutissement de cette thèse n'aurait pu être possible sans le soutien infaillible de ma merveilleuse famille: mes trois frères, François, Pierre et Benjamin, mes trois belles-sœurs, Marie, Cécile et Elodie, tous mes adorables neveux et nièces, mes grands-parents Cécile et André, mes oncles, tantes, cousins et cousines, qui ont toujours manifesté leur intérêt et leurs encouragements pendant mon parcours (peu) académique. Merci infiniment à ma mère, Véronique, qui m'a transmis son intarissable soif de lire, d'apprendre et de comprendre, son optimisme débordant, et qui m'a aidé tout au long de la vie à surmonter les épreuves et réaliser mes rêves.

Merci à toi Lara pour avoir donné à ces deux dernières années de thèse un sens infiniment plus fort que celui du simple travail de recherche. Et pour tout le reste...

Un grand merci à Alex, Maria et Martin pour avoir relu et corrigé les paragraphes précédents.

Abstract

Wave-dominated tidal inlets are very dynamic coastal systems, whose morphology is continuously shaped by the combined action of the waves and the tides. The rapid morphological changes they experience impact directly their ecological and socio-economic environments. In order to implement adequate regulations for the sustainable management of tidal inlets, systematic environmental studies are necessary. The main objective of this PhD research work is to gain a better understanding of the physical processes that control the morphological evolutions of an ephemeral tidal inlet in Portugal - the Albufeira Lagoon inlet - based on the analysis of hydrodynamic and topographic data and on the results of a newly developed morphodynamic modelling system. The processes that impact the dynamics of the inlet at short time-scales, particularly those related to wave-current interactions, are investigated through the application of the modelling system to the inlet. The seasonal modulations of the wave climate and mean sea level strongly affect the sediment dynamics of the inlet and contribute to the natural closure of the inlet during the winter period. Long-term processes are also investigated based on a 65-year hindcast of mean wave parameters at regional and local scales. The large inter-annual variability of the wave climate and the associated longshore sediment transport – both correlated to the North-Atlantic Oscillation – are proposed to explain the differences in the morphological behaviour of the inlet-lagoon system at pluri-annual time-scales.

Résumé

Les embouchures tidales dominées par la houle sont des systèmes côtiers particulièrement dynamiques dont la morphologie est continuellement remodelée par l'action des vagues et de la marée. Les rapides évolutions morphologiques auxquelles elles sont sujettes impactent directement leurs environnements écologiques et socio-économiques. Afin de mettre en œuvre des réglementations adaptées à la gestion durable des embouchures tidales, des études environnementales systématiques sont nécessaires. L'objectif principal de cette thèse est de mieux comprendre les processus physiques qui contrôlent les évolutions morphologiques d'une embouchure tidale éphémère au Portugal - l'embouchure de la lagune d'Albufeira – à partir de l'analyse de mesures hydrodynamiques et topographiques et de résultats d'un système de modélisation morphodynamique récemment développé. Les processus qui influent sur la dynamique de l'embouchure tidale à court terme, notamment ceux liés aux interactions vague-courant, ont été étudiés à travers l'application du système de modélisation à l'embouchure. Les modulations saisonnières du climat de vagues et du niveau moyen de la mer affectent fortement la dynamique sédimentaire de l'embouchure et contribuent au comblement naturel de l'embouchure pendant l'hiver. Les processus à long terme ont également été étudiés à partir de simulations rétrospective de paramètres moyens de vagues pour des échelles régionales et locales sur une période 65 ans. Les fortes variabilités interannuelles du climat de vagues et de la dérive littorale qui lui est associée pourraient expliquer les différences d'évolutions morphologiques du système embouchure-lagune sur des échelles de temps pluri–annuels.

Contents

List of Figures

List of Tables

Chapter 1

Introduction

According to the United Nations, 44% of the world's population (more people than inhabited the entire globe in 1950) lived within 150 kilometres of the coast in 2010 [*United Nations*, 2013a]. With a global population estimated at 7.11 billions by the *United States Census Bureau* [2011], it stands out that more than 3 billions people interact, directly or indirectly, with the coastal zone. Moreover, 13 of the 20 largest megalopolis of the world are coastal cities. The rising demography, projected to reach 9.6 billion by 2050 [*United Nations*, 2013b], the natural erosion of many coasts around the world accelerated by anthropogenic processes [*Eurosion*, 2004; *Komar*, 2011], the accelerating sea-level rise[1] and the booming of seaside tourism and real-estate markets, are causing together an extreme pressure on coastal environments that is no longer sustainable (Fig.1.1). This alarming situation has provoked a surge of interest for coastal sciences during the last twenty years.

Figure 1.1: Left: Satellite image of western Europe at night, showing the concentration of population on the littoral (credits: NASA); middle: aerial photograph of the city of Malé, Maldives islands, a stunning example of intense urbanization of low-lying lands (credits: National Geographic); right: storm-induced erosion on the Outer Banks of North Carolina (credits: USGS)

Coastal lagoons occupy around 13% of the world's coastlines and occur on every continent, principally on the coastal plains of passive continental margins [*Stutz and Pilkey*, 2011]. In Europe, they represent only 5% of the littoral, while in the United-States more than 17% of the shoreline corresponds to coastal lagoons, often separated from the ocean by barrier-island systems [*Cromwell*, 1971]. Regarding the favouring hydrodynamic conditions, *Hayes* [1979a] found that lagoon systems mainly occur in micro- and meso-tidal environments (mean tidal

[1] *Meyssignac and Cazenave* [2012] computed a global sea-level rise of 1.7 mm.year^{-1} for the 20^{th} century and 3.2 mm.year^{-1} for the period 1993-2010, based on tide gauge data and satellite altimetry.

range lower than 4 m) with low-to-moderate wave regime (mean wave height lower than 1.5 m). Thanks to their privileged location at the land-ocean interface, coastal lagoons are among the most productive environments of the biosphere. Their connections with the open sea allow fish and larvae migrations and nutrient exchanges, while their shallow back-barrier waters provide a means of protection for the ichthyological fauna and represent a choice location for the reproduction of a large number of fish species. Coastal lagoons are also used as strategic sites along the migratory route of many populations of aquatic birds, and their surrounding lands often comprise a tremendous diversity of plants. In temperate zones, coastal lagoons also support large fisheries, aquaculture, tourism and recreation activities, as well as intense agriculture on their watersheds. The considerable ecological and socio-economic values of coastal lagoons combined with the growing anthropogenic pressure and associated environmental concerns have fostered systematic scientific studies to support the implementation of new regulations for the sustainable management of these fragile coastal systems.

In the wide range of coastal environments, barrier-lagoon systems and their associated tidal inlets appear as some of the most dynamic coastal features [*FitzGerald*, 1996]. Indeed, the combined actions of tides and waves continuously shape the morphology of these environments through the mobilization of sediments. In particular, the tidal inlets that connect the back-barrier bay to the open sea are subjected, on the one hand, to the periodically reversing tidal currents that can carry sediments landwards or seawards, and on the other hand, to the stochastic action of the waves that induce long-shore and cross-shore currents - and associated sediment fluxes - and facilitate sediment lifting by increasing the turbulent kinetic energy in the water column. All these processes impact the different morphological units of the tidal inlet and can result in the erosion or accretion of the ebb- and flood-tidal deltas, or the scouring, infilling, migration or even closure of the main channel. Given that such morphological changes may occur on very short time-scales (*e.g.* the breaching of a barrier island during a storm surge may take a couple of hours) and are hardly predictable with sufficient accuracy, the integrated coastal management of the littoral adjacent to tidal inlets is particularly challenging (Fig.1.2).

This dissertation focuses on the inlet morphodynamics of the Albufeira Lagoon located on the west coast of Portugal. Like many coastal lagoons [*De Swart and Zimmerman*, 2009], the Albufeira Lagoon and its barrier beach have formed in the incised valley of a paleo-river as a result of sea-level rise during the Holocene transgression [*Freitas et al.*, 2002]. This lagoon-barrier system located in the central region of the Portuguese west coast is characterized by a small, deep, elongated lagoon connected to the ocean by a shallow and narrow inlet that undergoes considerable morphological changes at infra-annual time scales, leading to its systematic closure. Every year the barrier is artificially breached to allow the renewal of the lagoon waters. The newborn tidal inlet follows a new morphological cycle, whose duration may vary from a fortnight to several months. The dual state of this lagoon has considerable impacts on the biodiversity and water quality of the lagoon, hence the related economic activities, such as aquaculture and fisheries, have always struggled to adapt to these constant changes. The local authorities in charge of the yearly opening of the inlet have always sought for a sustainable management of the lagoon in order to mitigate the problems of pollutions and anoxia of the bay waters, particularly virulent when the lagoon is separated from the ocean. Different strategies for the opening of

inlet were tested, in the hope that the lagoon remains open for a longer period. However, the lack of knowledge on the morphodynamic behaviour of the Albufeira Lagoon inlet in particular, and on wave-dominated tidal inlets in general, has often resulted in unpredicted evolutions of the inlet, and the use of "hard" solutions such as artificial jetties is often considered.

Figure 1.2: Top left: aerial photograph of Plettenberg Bay inlet, South Africa, a very mobile wave-dominated tidal inlet (credits: Ian D. Samson); Top right: new inlet in Pea Island, North Carolina, as a result of Hurricane Irene (credits: Tom Mackenzie); bottom left: aerial photograph of Ocean beach, Maryland, showing extreme urbanization on a barrier island (credits: USGS); bottom right: aerial photograph of the Ria Formosa Natural Park, Portugal, an important stop-over point for aquatic birds migrating between the European and African continents (credits: relpro.co.uk).

Nowadays, the science of coastal morphodynamics provides a robust means of investigating the causes and consequences of morphological changes, in terms of hydrodynamic circulation and sediment budget, and is therefore frequently invoked when coastal environments do not comply with humans needs, and coastal engineers are contracted to elaborate adequate solutions[2]. During the last decades, the emergence of increasingly sophisticated numerical tools has stimulated the scientific investigations on morphodynamics. Indeed, morphodynamic modelling systems that integrate various modules for wave propagation, hydrodynamic circulation and sediment transport, appear as a promising avenue for the study of complex coastal systems such as tidal inlets.

Nevertheless, the accuracy and reliability of the complex morphodynamic modelling platforms

[2]While coastal engineering has for long been associated to the unsightly "hard" structures that spoil numerous coastal landscapes, it is worth mentioning the large efforts of the coastal engineer community to develop innovative soft solutions that preserve the nature more than it damages it. The principle "Building with Nature" supported by the European consortium EcoShape is, in this respect, a good example.

are still relatively poor, compared to the predictive skills of meteorological and oceanic circulation models, and this for several reasons: 1) the science of coastal morphodynamics emerged a few decades ago [a review of the pioneering works is given in *de Vriend et al.*, 1993] and its community is restricted, hence the overall advances take time; 2) the difficulty of measuring sediment transport in energetic environments and the complexity and wide range of scales involved in the underlying mechanisms have favoured the use of empirical formulae, elaborated against limited testbed conditions, to simulate the transport of sediment [3]; 3) despite the easier access to computer resources, the computational costs of morphodynamic models are still prohibitive and an excessive amount of processors is often necessary to simulate fine-scale or long-term morphodynamic evolutions; 4) the prediction of sediment fluxes strongly depends on the accuracy of the simulated current field, but the highly non-linear physics of wave propagation and wave-current interactions in shallow waters impede the performance of hydrodynamic and wave models; 5) the bathymetric and topographic data necessary to investigate morphological changes at adequate space and time resolutions, and to validate the results of morphodynamic models are very sparse and often incomplete. In addition, the collection of these data requires a sufficiently long time that does not always comply with the constraints of research projects. The silver lining of all these clouds is the room left for improvements in the field of coastal morphodynamics, and research studies based on numerical tools appear as highly valuable to improve our understanding of the morphological behaviours of coastal environments such as coastal inlets.

In this context, the research project *3D-MOrphodynamic modelling of WAve-Dominated tidal Inlets* (3D-MOWADI) funded by the Portuguese Foundation for Research and Technology (PTDC/ECM/103801/2008) was undertaken at the National Civil Engineering Laboratory (LNEC) of Lisbon, from 2010 to 2013. This project involved the collection of *in-situ* hydrodynamic and topographic data at two very dynamic tidal inlets located on the Portuguese west coast: the Albfueira Lagoon inlet and the Óbidos Lagoon inlet. The analysis of this data set combined with the development and application of a morphodynamic modelling system was undertaken to gain a better understanding of the dynamics of wave-dominated tidal inlets. The research work presented in this dissertation was carried out within the framework of the 3D-MOWADI project and shared several objectives with it, listed as follows:

1. collecting hydrodynamic and bathymetric data at the Albufeira Lagoon inlet during energetic conditions with a particular focus on the characterization of the wave conditions from the entrance of the inlet to the inner part of the main channel;

2. implementing, calibrating and validating a regional wave model for the North-Atlantic Ocean and the Iberian margin in order to characterize the wave conditions near the study site and to provide local circulation models with spectral forcing at their open boundaries;

3. developing a morphodynamic modelling system, based on a new 2DH sediment-transport-bottom-update model and existent wave and circulation models, to simulate the morphological changes of tidal inlets induced by the combined effect of tides and waves;

[3] *According to legend, a conversation that took place more than 70 years ago between Albert Einstein and his eldest son, Hans Albert Einstein, gives rise to the favourite anecdote of every scientist or engineer working in the field of sediment transport. During this conversation, Hans told his father of his intent to carry out research on the mechanics of sediment transport. Albert had done some work in this area, notably on hindered settling in sediment suspensions, and he advised his son not to pursue study in this field, as he felt sediment transport was so difficult that it was intractable* [*Nelson*, 1999]

4. implementing, calibrating and validating the new 2DH morphodynamic modelling system in order to reproduce the tidal currents, the propagation of the waves, and the wave-current interactions in the vicinity of the inlet, as well as the associated sediment transport and its impact on the evolution of the morphology of the inlet;

5. investigating the dominant processes that control the morphological changes of the Albufeira Lagoon inlet, in particular, and wave-dominated tidal inlets, in general, based on model applications and data analyses.

Outline of the dissertation

The dissertation is organized in nine chapters:

Following the overall introduction given in this first chapter, Chapter 2 provides a bibliographic review of the topics tackled in this dissertation. In particular: the geomorphological concepts related to coastal lagoons and tidal inlets are defined based on the existing scientific literature, the most advanced morphodynamic modelling systems are presented, and the principal studies on the morphodynamics of wave-dominated tidal inlets are summarized.

Chapter 3 presents the study area in both a regional and a local perspective. On the one hand, the geomorphological setting of the Western Iberia Margin, the regional circulation and the wave climate off the Portuguese coast, and the coastal lagoons in Portugal are described. On the other hand, the local wave climate and the circulation of the coastal region of the Albufeira Lagoon are presented and the geomorphology and hydro-sedimentary characteristics of this lagoon-barrier-inlet system are described.

Chapter 4 presents the field work that took place in September 2010 at the Albufeira Lagoon. The deployment of the sensors, the collection of *in-situ* and remote data, and the processing methods are detailed.

Chapter 5 is a detailed presentation of the modelling system developed collaboratively during the project. The wave, circulation, sediment transport and bottom update models that compose the modelling platform are described.

Chapter 6 presents an application of the wave model at regional scale (the North Atlantic Ocean) and local scale (the coastal region of the Albufeira Lagoon), which produced a 62-year (1948-2012) hindcast of mean wave parameters. The spatial and temporal analysis of the model results provide a detailed characterization of the wave climate variability at regional and local scales.

Chapter 7 is an application of the coupled wave-current modelling system to the Albufeira Lagoon inlet. This application provides a means for validating the boundary forcing and the performance of the wave-current model by comparing the model results against observations. The impacts of the wave-current interactions on the overall inlet circulation are analysed and

the potential effect on the equilibrium of the inlet is discussed.

Chapter 8 investigates the morphodynamic processes that control the evolution of the Albufeira Lagoon inlet. First, the morphological changes of the inlet observed in 2010 and the associated hydrodynamic conditions are described. Then, the fully coupled wave-current-sediment modelling system is applied to the study area and the skills of the model are assessed qualitatively and quantitatively. The modelling system is then used to investigate the sediment dynamics for various forcing conditions. In addition, the inter-annual variability of the wave-induced longshore transport is analysed from the results of the 62-year wave hindcast.

Finally, Chapter 9 summarizes the main findings of the dissertation and addresses a number of issues that require further investigations.

Chapter 2

State of the art

Coastal lagoons are of great ecological and socio-economic importance given their privileged location at the land-ocean interface. In particular, their associated tidal inlets that connect the open ocean with a back-barrier lagoon constitute navigation routes and enable fish and larvae migrations, nutrient exchanges, and maintenance of water quality and salinity levels in the lagoon water. Tidal inlets are very dynamic and since their morphology is partly controlled by stochastic processes of meteorological and oceanic nature, dramatic morphological responses may occur very rapidly. Numerous authors have investigated the physiographic and hydro-sedimentary characteristics of tidal inlets around the world, from which they built up empirical rules, analytical theories and conceptual models that laid the foundations for understanding the dynamics of these coastal features. More recently, process-based numerical models have been developed and applied to idealised and natural inlets, with the objective to verify the validity of existing theories, predict the evolution of specific inlets, and assess engineering solutions. This chapter provides the definitions of the main concepts manipulated within this dissertation and summarizes the findings of some of the major studies related to the morphodynamics of tidal inlets.

2.1 Coastal lagoons

2.1.1 Definitions

Defining precisely the various types of coastal environments is an arduous task given the diversity of parameters controlling these complex environments at the land-sea interface, and the definitions encountered in the literature rarely meet an overall agreement within the community of specialists. The concept of coastal lagoons being intimately related to the one of estuaries, the distinction between them has always been a controversial issue.

The first definitions for coastal lagoons referred to a shallow water body oriented parallel to the coastline, connected to the open sea through one or more inlets and separated from it by a littoral barrier [*e.g.*, *Reineck and Singh*, 1973]. For estuaries, a common definition is the one of *Cameron and Pritchard* [1963]: *a semi-enclosed coastal body of water which has free connection to the open sea and within which sea water is measurably diluted with fresh water derived from land drainage*. *Pritchard* [1952] divided estuaries in three categories, based on their topographic characteristics: fjords, coastal-plain estuaries (or drowned-river valleys estuaries) and bar-built

estuaries. Fjords are river valleys deepened by glaciers during former ice ages and where the scouring of the valley floor resulted in very deep estuaries, while coastal plain and bar-built estuaries are shallow systems formed by the flooding of river valleys during the sea level rise of the Holocene transgression. The distinction between drowned-river valley estuaries and bar-built estuaries is attributed to the sedimentation rates, which are much higher in the case of bar-built estuaries and resulted in the formation of a depositional barrier. *Kjerfve* [1986] defined the coastal lagoons as one of the three major type of estuaries and proposed to replace the term *bar-built estuaries* of *Pritchard* [1952] by *coastal lagoons*, which required to extend the definition for estuaries of *Cameron and Pritchard* [1963] to include freshwater and hypersaline systems. However, coastal lagoons may present morphologies very different from those of estuaries and this definition is not always adequate [*Freitas*, 1995]. Furthermore, some tidal inlets are totally disconnected from continental drainage systems and thereby cannot be considered as estuaries.

For *Lankford* [1977], coastal lagoons are characterized by a depression in the coastal topography, lower than the height of Mean High Water Springs, and with a permanent or ephemeral communication to the ocean through a littoral barrier of any kind. For this author, the orientation of the lagoon relative to the coastline is no longer a determinant factor. Indeed, although most of the coastal lagoons are oriented parallel to the coast, some of them are oblique or normal to the coast. Later, *Boyd et al.* [1992] proposed a classification of coastal environments based on their morphologies and characteristics of evolution. This classification is illustrated in a ternary diagram, whose horizontal axe represents the relative importance of the waves and tides, and the vertical axe, the importance of the fluvial discharge (Fig.2.1). These authors defined the estuaries as the lower segment (closest to the sea) of drowned-river valleys that receives sediment from oceanic and fluvial sources and that are influenced by tides, waves and fluvial processes. In this classification, the coastal lagoons are seen as an extreme case of estuaries where the fluvial influence is negligible. Later, *Kjerfve* [1994] included coastal lagoons as one of the six

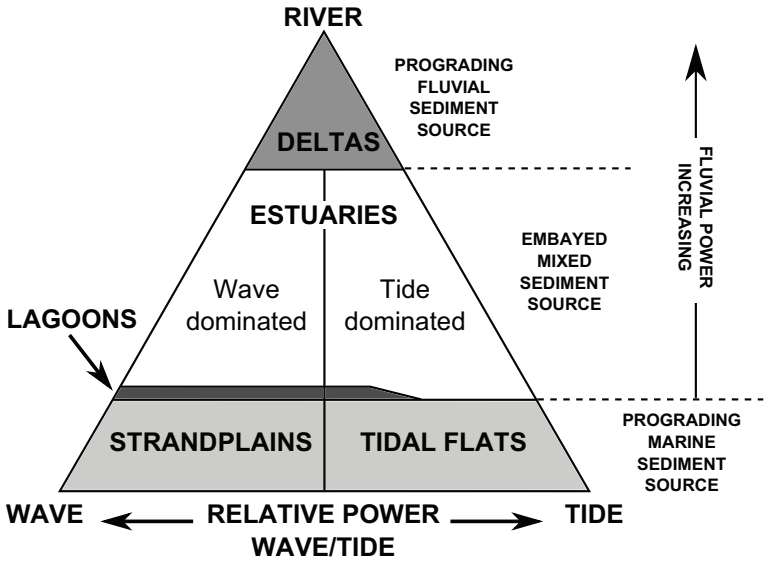

Figure 2.1: Classification of coastal environment, according to Boyd et al. [1992]

major types of inland coastal ocean-connected systems and formulated the following definition: *a coastal lagoon is a shallow coastal water body separated from the ocean by a barrier, connected*

at least intermittently to the ocean by one or more restricted inlets, and usually oriented shore-parallel. Freitas [1995] adopted a general definition that includes most of the considerations described here-above: *coastal lagoons are coastal environments characterized by a depression in the coastal topography, separated from the ocean by a barrier allowing ephemeral or permanent communication with the open sea, and where the fluvial discharge is weak or null.* In the present dissertation, the term *coastal lagoon* will always refer to this definition.

2.1.2 Classification of coastal lagoon systems

Despite some commune characteristics, each lagoon differs from all others either from a morphologic or a functional viewpoint. These differences involve the dimensions and the shape of the lagoon, the range of the tide and its interaction with the inlet topography, the contribution of the lagoon tributaries, the local climatology, the number and dimensions of the inlets, the nature and the quantity of available sediments, the nature and origin of the topographic depression and the modality of construction and evolution of the barrier system [*Freitas*, 1995]. Variations of these basic factors result in differences in the inlet hydrodynamics, in the chemical composition of the lagoon waters and in many other geological and ecological aspects which impede some generalization applicable to the majority of the lagoons [*Phleger*, 1981].

Several classifications of coastal lagoon system have been proposed with the goal to systematize the distinction of coastal lagoon types. *Lankford* [1977] proposed a classification of the Mexican coastal lagoons in five different types, essentially based on the geological origin of the inundated depression and the processes which governed the barrier formation, as following (Fig.2.2): **Type I** - originated from differential erosion - the depressions formed when the sea level

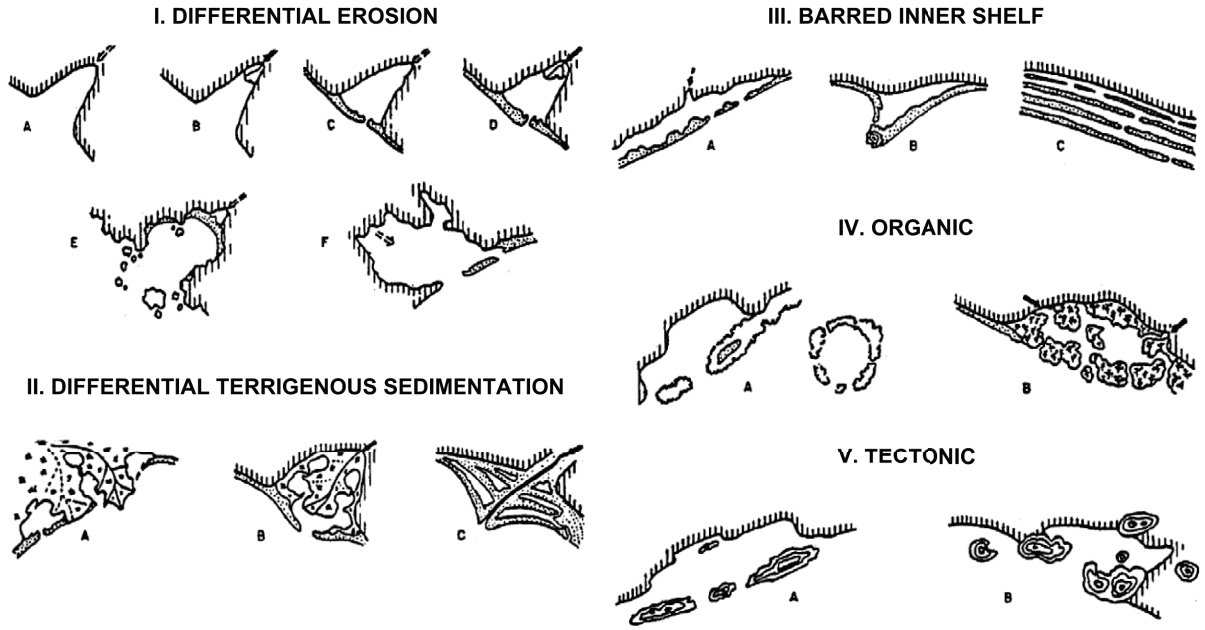

Figure 2.2: Classification of coastal lagoons based on their geomorphic type, according to Lankford [1977]

was lower than the present one and was inundated during the Holocene transgression; since the stabilization of the sea level, approximately 5000 years ago, they suffered some modifications; the barrier built up with coastal sediment through littoral drift mechanism; **Type II** - originated from differential terrigenous sedimentation - these lagoons are associated with deltaic/fluvial

systems, produced by irregular sedimentation and/or subsidence due to compaction effect; they generally formed and suffered various evolution during the last 5000 years, but some of them are geologically younger (hundreds of years); the barrier is constructed by the river flow or by littoral retention of the sediments it transports; **Type III** - originated by barrier formation on the continental shelf - the depressions are protected from the sea by sand barriers formed by waves and currents and limited internally by the continent; the formation of these barriers dates from the stabilization of the sea level during the last 5000 years; the main axis of these lagoons is parallel to the coast; **Type IV** - originated from organic deposits - the depressions are produced by the growing organic barrier (generally coral reefs) on the continental shelf since the stabilization of the sea level during the last 5000 years; their shapes are variable (*e.g.* parallel to the coast, elliptic, strongly irregular); **Type V** - originated from tectonic mechanism - the depressions and/or barriers are produced by faulting, folding or volcanism in coastal zones, independently from the sea level; their shape varies from elongated to elliptic or strongly irregular.

Nichols and Allen [1981] proposed a classification of coastal lagoons in four main types, based on the dominant processes: tides and river discharge on the one hand and wave action on the other hand, the former promoting the open state of the lagoon, and the latter promoting its closure (Fig. 2.3). *The estuarine lagoons* are characterized by large tidal prism and river discharge;

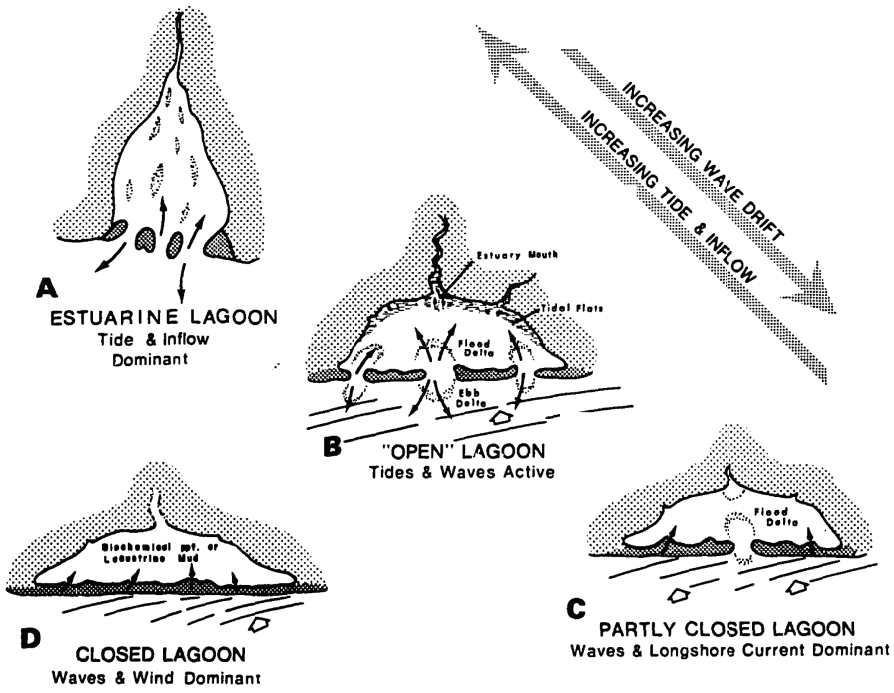

Figure 2.3: Classification of coastal lagoons based on the dominant processes controlling the open/close state of the lagoon, according to Nichols and Allen [1981]

the wave energy and the littoral drift are relatively small compared to the effect of the tide, which maintains the inlet open and promotes large exchange between fresh and saline waters. *The open lagoons* result from the action of the waves combined with the moderated actions of the tide and river discharge; the waves build-up the barrier through littoral drift mechanism while the tidal currents are sufficient to maintain the inlets open and promote the development of flood and ebb deltas. *The lagoons partially closed*, in which the strong action of the waves and littoral drift build up extensive barriers, while the tidal currents play a secondary role; these lagoons present

a well-developed flood delta but an under-developed ebb delta. *The closed lagoons* (designated as *percolation lagoons* by *Barnes* [1994] when there is water exchange between the lagoon and the ocean by permeability through the barrier) are produced by a large wave-induced littoral drift; the effects of wind and wave-overtopping are dominant in these lagoons.

Kjerfve [1986] analysed relevant geographic, hydrological and oceanographic characteristics of ten coastal lagoons in the world in an attempt to formulate some generalizations. He classified these lagoons in three geomorphic types based on the degree of water exchange with the adjacent coastal ocean (Fig. 2.4): *Choked lagoons* are connected to the sea by a single narrow entrance channel and occurred on coasts with high wave energy and significant littoral drift; they are characterized by strongly attenuated tide ($\leq$ 5% of the oceanic tide), long flushing times, dominant wind forcing and intermittent stratification events due to intense solar radiation or run-off; these lagoons may be either fresh water systems in areas of high rainfall and run-off or hypersaline in arid regions where they can be closed off from the sea for prolonged time periods; choked lagoons are mostly oriented shore-parallel but are sometimes found associated with river deltas and then occasionally oriented shore-normal. *Restricted lagoons* usually exhibit two

Figure 2.4: Classification of coastal lagoons based on the degree of water exchange with the adjacent coastal ocean [Kjerfve, 1986].

or more entrance channels; they have a well-defined tidal circulation, are influenced by winds and are mostly vertically well-mixed; flushing times are usually considerably shorter than for choked lagoons; restricted lagoons are usually oriented shore-parallel. *Leaky lagoons* are elongated shore-parallel water bodies with many ocean entrance channels along coasts where tidal currents are sufficiently strong to overcome the tendencies by wave action and littoral drift to close the channel entrances.

2.2 Geomorphology and variability of tidal inlets

2.2.1 Morphological units of a tidal inlet

Coastal lagoons are connected to the ocean through a channel that may be permanent or ephemeral. When the channel is maintained opened by tidal flows, it is referred to as a tidal inlet. Tidal inlets are dynamic morphological features often subjected to drastic changes in response to the hydrodynamic forcing. *Hayes et al.* [1972] distinguished three main morphological units that compose a tidal inlet: 1) the ebb-tide delta; 2) the inlet gorge; and 3) the flood-tide delta. The development of the tidal deltas is explained by the divergence of the sediment fluxes on either side of the inlet, which promotes the deposition of sediments. The flood-tidal delta, on the lagoon-side, is mainly controlled by the tidal flow while the ebb-tidal delta, on the seaward side, is where the tidal and wave processes interact.

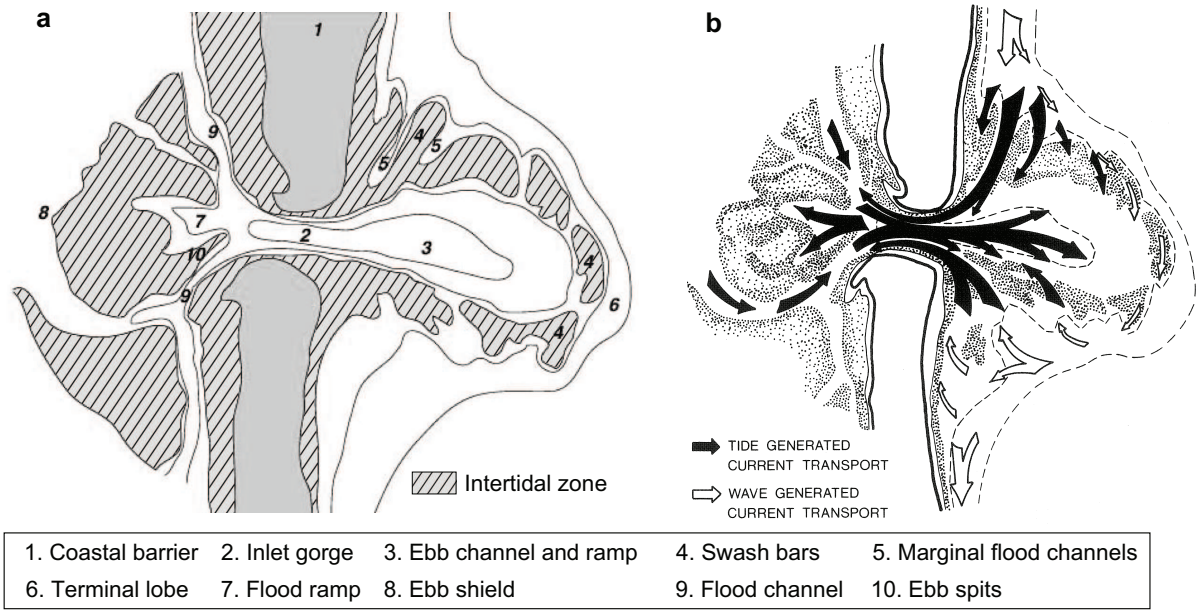

Figure 2.5: a) Schematic illustration of the morphological units that compose a tidal inlet; b) Wave and tide generated current transport pathway around and over the flood and ebb deltas. [adapted from Smith, 1987].

A widely-accepted terminology for the different morphological units of a tidal inlets was given by *Hayes* [1975] and was further detailed by *Smith* [1975] (Fig.2.5a):
- the flood-tidal delta is delimited by several flood channels that bifurcate around it. On the seaward outer face of the flood-tidal delta, the gently-sloping flood ramp focuses the flood currents (mega-ripples are often encountered on the flood ramp). On either sides of the flood-delta, the ebb-spits are elongated sandbanks pointing towards the ocean, shaped by the ebb-tidal currents (Fig.2.5b).
- the inlet gorge corresponds to the narrowest and deepest part of the inlet. With the minimal inlet section, the gorge is subjected to the largest tidal currents (Fig.2.5b).
- the ebb-tidal delta is shaped on the seaward side of the inlet by the combined action of tides and waves. It results from the deposition of sediments taken from the main channel and the adjacent beaches, and transported by the tidal currents and the wave-induced longshore drift. The main ebb-tidal channel is dominated by ebb-tidal currents and splits the delta into several swash platforms, over which swash bars are formed and pushed shoreward by the action of the waves. Nearshore, the delta is bounded by marginal flood channels that are dominated by flood-tidal currents. The terminal lobe corresponds to the seaward extent of the ebb-jet and results from the deposition of sediments transported by the ebb-tidal currents (Fig.2.5b).

2.2.2 Classifications of tidal inlets

Inlet types are recognized primarily by the morphology of their main geomorphic units. Early classifications of tidal inlets were thus based on morphological considerations, such as the one of *Hubbard et al.* [1979], who investigated the morphological variability of tidal inlets along the southeastern coast of the United States. These authors defined three major types of tidal inlets: 1) *tide-dominated inlets*, characterized by a deep, ebb-dominant main channel flanked

by long, linear channel-margin bars and poorly developed or non-existent flood-tidal deltas; 2) *wave-dominated inlets*, characterized by shallow tidal channels, large flood-tidal deltas and small ebb-tidal deltas extending only a short distance from the beach; 3) *transitional inlets*, characterized by major sand bodies typically concentrated in the inlet throat. The data of *Hubbard et al.* [1979] also indicated that the morphologic variability in the selected inlets was largely explained as a response to waves and tides.

Hayes [1979a] compiled the hydrodynamic characteristics of a large number of tidal inlets in the United-States and classified them according to the local tidal range (R) and mean wave height (H_s). He distinguished five types of tidal regime: micro-tidal ($R < 1$ m), moderate meso-tidal ($1 < R < 2$ m), high meso-tidal ($2 < R < 3.5$ m), moderate macro-tidal ($3.5 < R < 5.5$ m) and high macro-tidal ($R > 5.5$ m). Similarly, he divided the wave regime into low energy ($H_s < 0.6$ m), moderate energy ($0.6 < H_s < 1.5$ m) and high energy ($H_s > 1.5$ m) wave regimes. Based on the relative contribution of these two hydrodynamic parameters, four categories of tidal inlets were defined: the wave-dominated tidal inlets, the mixed-energy wave-dominated inlets, the mixed-energy tide-dominated inlets and the tide-dominated inlets (Fig.2.6).

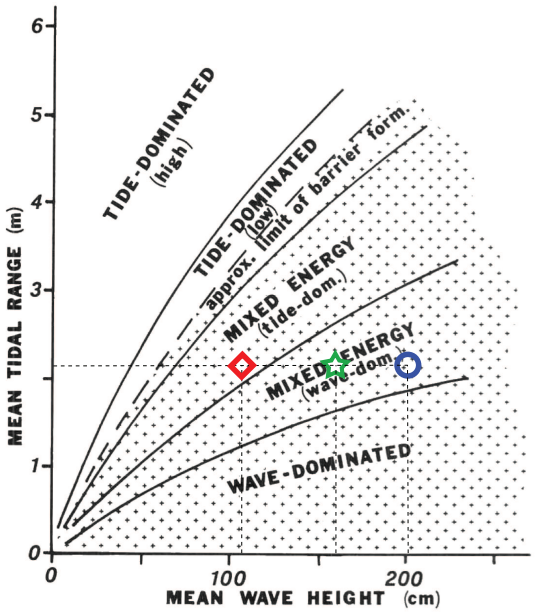

Figure 2.6: Classification of tidal inlets based on hydrodynamic parameters [adapted from Davis and Gibeaut, 1990]. The coloured symbols indicate the mean tidal range and annual (green star), summer (red diamond) and winter (blue circle) mean wave heights at the Albufeira Lagoon.

The classification of *Hayes* [1979a] provides a good overview of the type of inlets occurring along the world's coastlines according to their energetic regime, and is therefore very useful to understand the presence of large scale morphological features and their long-term changes. Nevertheless, the restriction of this classification to the mean tidal range and the mean wave height limits its scope of application. Indeed, the dynamics of tidal inlets is essentially controlled by the tidal prism (involving the tidal range and the morphological characteristics of the lagoon-inlet system), and the littoral drift (involving the sediment type, the wave height but also the direction and period of the waves). Shallow tidal inlets subjected to energetic waves, such as the Albufeira Lagoon inlet considered in this dissertation, often present a seasonal morphological

behaviour with a significant inter-annual variability, which reflects the variability of the hydrodynamic forcing and the associated morphological state of the inlet [1]. The hydro-sedimentary dynamics of these inlets may alternatively be dominated by tidal and wave processes and the resulting morphological characteristics for a given mean tidal range and wave height are not always in agreement with the classification of Hayes.

2.2.3 Stability of tidal inlets

Tidal inlets are dynamic coastal features that constantly adapt their morphology to the oceanic forcing, the sediment supply and the characteristics of the back-barrier bay. The question of the stability of tidal inlets, *i.e.* their ability to preserve their shape and position over a defined time period, has been the subject of numerous studies during the last century, particularly for its implications in the field of coastal engineering.

A relation between the cross-sectional area of tidal inlets (A) and the tidal prism (P) was first proposed by *Leconte* [1905] who analysed these parameters for several inlets along the Pacific coast of the United-States. The pioneering works of *Leconte* [1905] were then followed by *O'Brien* [1931, 1969], who derived the general form of this empirical relationship, known as the A-P relationship:

$$A = C.P^n \tag{2.1}$$

where
A = equilibrium cross-sectional area relative to the mean sea level (in m^2)
P = spring tidal prism (in m^3)
C and n = empirical coefficients computed from the observations by linear regression

This formula has been validated by several authors and the empirical coefficients have been determined for a wide range of tidal inlets around the world [*O'Brien*, 1969; *Jarrett*, 1976; *Hume and Herdendorf*, 1992; *Townend*, 2005]. In particular *Jarrett* [1976] analysed more than one hundred inlets on the Atlantic and Pacific coasts of the United States and in the Gulf of Mexico. He obtained values comprised between 7.76 10^{-6} and 5.02 10^{-4} for C and between 0.84 and 1.1 for n (with A in m^2 and P in m^3), which indicates that a universal form of the relationship does not exist and that local conditions (*e.g.,* incident wave forcing, inlet stabilization by jetties) also need to be taken into account [*Gao and Collins*, 1994].

In 1960, *Bruun and Gerritsen* [1960] introduced the concept of overall stability for tidal inlets. They provided a mean to quantify the morphologic stability of an inlet through the ratio of the tidal prism volume during spring tides (P in m^3) to the gross annual littoral drift (M_{tot} in $m^3.year^{-1}$). According to *Bruun* [1978], the stability of an inlet is rated as good, fair or poor depending on the ratio P/M_{tot}, as follows:

[1] In tropical and sub-tropical regions presenting a high seasonal hydrometric variability (*e.g.* monsoon), tidal inlets also present a well-defined seasonal behaviour [*Thanh Tung*, 2011; *Bond et al.*, 2013]

when $P/M_{tot} > 150$	the stability is good
when $100 < P/M_{tot} < 150$	the stability is fair
when $50 < P/M_{tot} < 100$	the stability is fair to poor
when $P/M_{tot} < 50$	the stability is poor

The gross annual littoral drift used by *Bruun* [1978] corresponds to a long-term averaged value. However, several authors have shown that the strong inter-annual variability of the littoral drift may result in changes larger than 100% of the mean value [*Silva et al.*, 2012; *Idier et al.*, 2013]. Hence, the Bruun's rule for inlet stability seems inadequate to predict the evolution of an inlet at infra-annual and annual time-scales.

The stability of a tidal inlet is controlled by the relative strength of opposing forces that promote either the accretion or the erosion of sediments in the inlet. This concept was developed analytically by *Escoffier* [1940, 1977] and is illustrated by the Escoffier's stability diagram (Fig. 2.7) in which the maximum velocity (V_m) in the gorge of the inlet and the equilibrium velocity (V_e) are plotted against the cross-sectional area of the inlet (A).

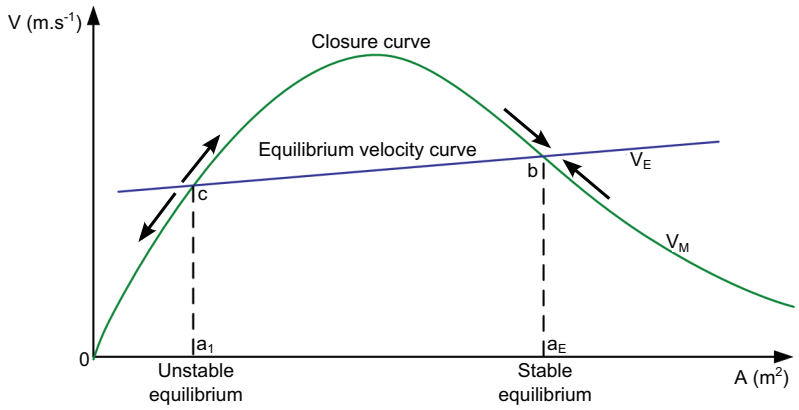

Figure 2.7: Escoffier diagram for tidal inlet stability [adapted from Escoffier, 1940].

The parabolic shape of the maximum velocity indicates that as the cross-sectional area approaches zero, the current velocity also approaches zero due to increasing frictional forces, which are inversely proportional to the channel area. For large values of the cross-sectional area the tidal prism attains a maximum and an increase of the cross-sectional area results in a decrease of the current velocities to satisfy the principle of mass conservation. The values of V_m can be computed with analytical methods [*e.g.*, *Brown*, 1928; *Keulegan*, 1967] or through numerical simulations. The second curve of the stability diagram corresponds to the equilibrium velocity that was assumed to be constant and close to 1 m.s^{-1} by *Escoffier* [1940], although it can be estimated more accurately using the A-P relationship of *O'Brien* [1969]. The equilibrium curve can intersect the closure curve at two locations, one location (tangent case) or not at all. In the first case (shown on Fig. 2.7), point b is a stable root in that any deviation in the cross-sectional area from its equilibrium position produces a negative feedback that brings it back to its initial position. If the channel area increases (moving to the right on the curve from point b) velocity will fall and sediment deposition will fill in the channel until it recovers its equilibrium state. If the channel area decreases, the velocity will increase scouring back to the equilibrium point. On the contrary, point c is an unstable root, where a decrease of the channel area (moving to the left of point c) produces a positive feedback: the current velocities will decrease until the

inlet closes. Moving to the right of point c, as velocity increases, area increases until the velocity starts falling and the stable root at point b is reached. If the stability curve is tangent to or below the stability criterion curve, the inlet will close.

2.3 Morphodynamic models for tidal inlets

2.3.1 Conceptual models

Inlet sediment bypassing is the process by which sediment moves from the updrift to the downdrift side of the inlet, involving the inlet channel and ebb-tidal delta. Several authors investigated this research field [*Bruun*, 1966; *FitzGerald*, 1982, 1988] after the pioneering work of *Bruun and Gerritsen* [1959]. *FitzGerald et al.* [2000] proposed a synthesis of the conceptual models for sediment bypassing and associated morphological changes at tidal inlets.

Model 1. Inlet Migration and Spit Breaching

Sand transported along the beach and deposited in a tidal inlet constricts the inlet throat decreasing the flow area. As Escoffier's stability concept states, the constriction causes an increase in current velocity which leads to greater scouring of the inlet channel and re-establishment of the equilibrium channel cross-sectional area [*Escoffier*, 1940]. Because longshore transport along most coasts adds sand predominantly to one side of the inlet, the opposite side erodes preferentially causing the inlet to migrate [*Johnson*, 1919]. The rate of migration is dependent on sediment supply, wave energy, tidal current strength, and composition of the channel banks. If a migrating inlet becomes entrenched into resistant sediments, further migration will be impeded. Shallow inlets tend to migrate and deeper inlets tend to be more stable because there is a greater likelihood that their channels have scoured into semi-indurated sediments. As an inlet migrates, it leaves behind a series of curved beach ridges that define the updrift spit. Inlet migration commonly lengthens the inlet channel, which connects the open ocean to the back-barrier bay, lagoon, or marsh and tidal creek system. Elongation of the inlet channel increases frictional resistance of tidal flow thereby reducing tidal range in the bay. Differences in tidal phase and tidal range between the ocean and back-barrier bay can augment the breaching of the spit and formation of a new (relocated) tidal inlet (Fig.2.8). Spits are usually breached during storms when waves erode the beach and dune system, reducing the width of the barrier. Storm surges produce washovers (precursors of inlets) and increase tidal flow. The new inlet is commonly located along the updrift spit at a position where the barrier is narrow and the back-barrier tidal prism is easily accessed. The hydraulically favourable position of the new inlet promotes the capture of the old inlet's tidal prism and its eventual closure. The end product of the spit breaching process is that a large quantity of sand is transferred from the updrift to the downdrift inlet shoreline.

Model 2. Stable Inlet Processes

A stable inlet is one that has a stable inlet throat (non-migrating) and a stable main ebb channel position through the ebb-tidal delta. The stability of the inlet is usually related to

the channel being anchored in a substrate resistant to erosion. Bypassing at these inlets occurs through the formation, landward migration, and attachment of large bar complexes to the downdrift shoreline (Fig.2.8). The development of bar complexes results from the stacking and coalescence of swash bars on the delta platform. Wave-built swash bars move onshore due to the dominance of landward flow created by wave swash. Their stacking results from a decrease in the rate of onshore migration. As the bars migrate up the shoreface, they gain a greater and greater intertidal exposure. Consequently, wave swash, which causes their onshore movement, operates over an increasingly shorter period of the tidal cycle. The size of bars and the volume of sand moved onshore generally increases with increasing inlet size.

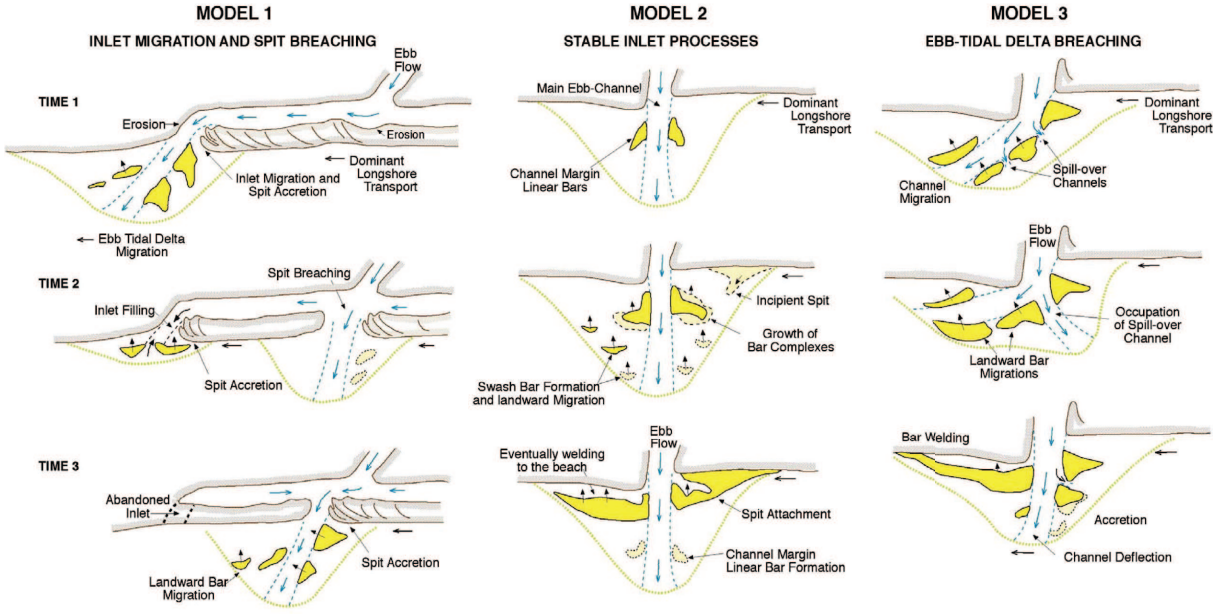

Figure 2.8: Conceptual models (1-3) for tidal inlets evolution [FitzGerald et al., 2000].

Model 3. Ebb-Tidal Delta Breaching

Ebb-tidal delta breaching occurs at tidal inlets that have stable throat positions, but whose main ebb channels cyclically migrate downdrift (Fig.2.8). The dominant direction of longshore transport at these sites produces a preferential accumulation of sediment on the updrift side of the ebb-tidal delta. The sediment accumulation causes a downdrift deflection of the main ebb channel, which at some inlets may ultimately impinge against the downdrift inlet shoreline. This pattern of channel migration commonly induces erosion along the adjacent beach. A severe deflection of the main channel produces flow at the inlet that is hydraulically inefficient. Eventually, this condition results in the ebb discharge being diverted to a more direct seaward pathway through the ebb-tidal delta. The breaching process can occur gradually over a period of 6 to 12 months or catastrophically during a single storm when discharge of flood-waters increases the scouring of the ebb currents. Once formation of the new channel is completed, it will convey most of the inlet tidal prism. Thus, the abandoned channel gradually fills with sediment deposited by both tidal and wave-generated currents. The breaching process commonly results in the bypassing of a large portion of the ebb delta sand. Some of this sand fills the old channel, while the rest forms a subtidal or intertidal bar complex that migrates onshore ultimately attaching to the landward beach. These bars are identical to the ones previously described for the stable

inlet processes and contain equal or greater volumes of sand.

Model 4. Outer Channel Shifting

This mechanism of inlet sediment bypassing is similar to ebb-tidal delta breaching, but is limited to the seaward end of the main ebb channel and involves smaller volumes of sand (Fig.2.9). In this process, the inner portion of the main channel remains in a fixed position while the outer channel is deflected downdrift because of preferential accumulation of sand on the seaward, updrift side of the swash platform. As the outer portion of the channel becomes more deflected, which at some inlets can produce a right angle end, flow through the outer portion of the channel becomes increasingly less efficient. Eventually, a new channel is cut through the distal portion of the ebb delta that shortens the pathway of flow. Cutting of a new channel is commonly initiated during high spring tides when peak flows occur in the channel. The sand that had been located on the updrift side of the outer channel and is now on the downdrift side has bypassed the inlet. As the bypassed sand moves onshore by flood-tidal and wave-generated currents, it is commonly moulded into a large swash bar that migrates landward and attaches to the downdrift beach.

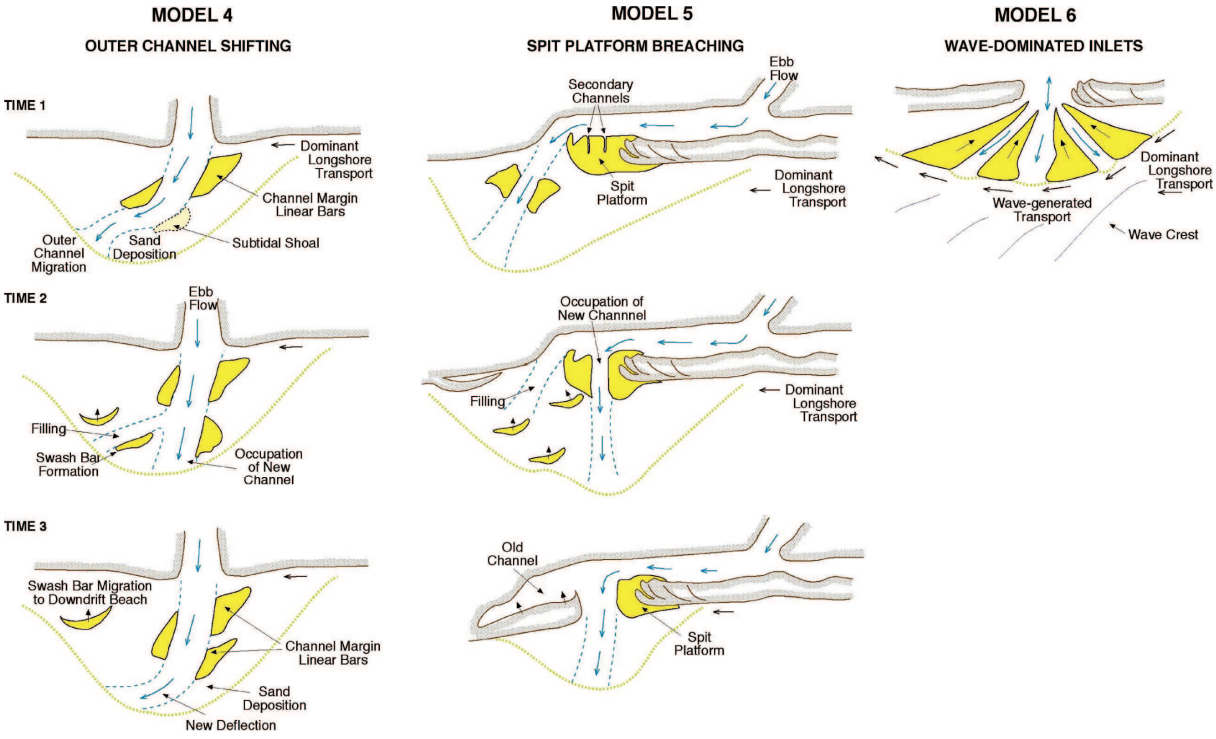

Figure 2.9: Conceptual models (4-6) for tidal inlets evolution [from FitzGerald et al., 2000].

Model 5. Spit Platform Breaching

At most migrating inlets, the updrift barrier spit is fronted by a large intertidal spit platform. The platform may extend from 100 to more than 1000 m into the inlet producing a highly asymmetric channel configuration. In Model 5, large quantities of sand are bypassed when a new channel is breached through the spit platform (Fig.2.9). The major channel in the back-barrier usually runs parallel to the rear of the spit as it nears the inlet and then turns to flow around the spit platform. Spit platforms usually exhibit considerable relief having many small shallow channels and numerous bars and bed forms. Spit accretion and downdrift extension of the spit

platform increase the length of the inlet channel, thereby decreasing flow efficiency between the ocean and bay. Inlets of this type are susceptible to inlet channel shortening particularly during storms when surges elevate water levels. At these times, early ebb discharge from the back-barrier flows out the main channel as well as in a short cut route across the spit platform. At some inlets, seaward flow across the spit platform may become channelized in one of the secondary shallow channels. Deepening of this channel may avulsively form a new, shorter channel for water to exit the inlet. At other inlets the spit platform breaching process occurs gradually over a period of 1 to 2 years. Depending upon the size of the inlet, this can result in very large volumes of sand bypassing the inlet. Not only is a portion of the spit platform transferred to the downdrift side of the inlet as the old channel fills, but also most of the former ebb-tidal delta sediment is transported onshore to the downdrift beach as flow is diverted to the new updrift inlet channel.

Model 6. Wave-Dominated Inlets

Wave-dominated inlets are defined as those in which the distribution of sand bodies and general morphology of the ebb-tidal delta indicate the dominance of wave-generated rather than tide-induced sediment transport. These inlets are usually small (widths < 200 m) with shallow main ebb channels (depths < 6 m). They have sand shoals that are pushed close to the mouth of the inlet, producing a slightly arcuate ebb delta shape. The overall shallow nature of the distal portion of the ebb delta, much of which may be exposed at low tide, coupled with its gently arcuate shape, allows waves to transport sand along the periphery of the delta, especially at high tide (Fig.2.9). The transport of sand along the outer delta takes place in the same manner as that in the surf and breaker zones. Sediment bypassing at these inlets occurs continuously, unlike the episodic landward bar migration dominant in the other models. This mechanism of bypassing is similar to Bruun and Gerritsen's "bar-bypassing model" [*Bruun and Gerritsen*, 1959] and has been mathematically modelled by *Kraus* [2000].

2.3.2 Numerical models

Process-based morphodynamic modelling systems have been intensely developed during the past 30 years. Comprehensive morphodynamic modelling systems like Mike-21 [*Warren and Bach*, 1992], Delft3D [*Lesser et al.*, 2004], ROMS [*Warner et al.*, 2008], Morsys2D [*Fortunato and Oliveira*, 2004; *Bertin et al.*, 2009b], Telemac [*Villaret et al.*, 2013] or SHYFEM [*Ferrarin et al.*, 2008] generally include a circulation model, a wave propagation model, a sand transport model for bed-load and suspended load and a bottom update model that computes bed changes through the sediment continuity equation. Most of these models have been used to simulate the morphological changes at tidal inlets and investigate the underlying physical processes.

The morphodynamic modelling of tide-dominated coastal environments has seen considerable progress during the last decades. In slowly varying environments, the time-scale of the bed evolution is generally much larger than the time-scale of the modulations of the hydrodynamic forcing and some simplifications can be performed to speed up the computational time. Based on the pioneering works of *de Vriend et al.* [1993] and *Latteux* [1995], several methods were implemented and tested, such as the tide-averaging method, the continuity correction and the morphological factor approach [a review of these methods is given in *Roelvink*, 2006]. Thanks to these improvements, the first millenial-time scale simulations were realized by Roelvink and

co-workers [*Dastgheib et al.*, 2008; *van der Wegen and Roelvink*, 2008; *Dissanayake et al.*, 2009] and the comprehension of the long-term dynamics of tidal basins took a huge leap forward.

Meanwhile, the morphodynamic modelling of wave-dominated tidal inlets has been facing a number of constraints due to the stochastic nature of the wave forcing and the fast changes of wave-dominated coastal systems, which still limits the feasibility of long-term predictions. However, significant progress were realized in the last decades and several medium-term studies (from a few months to several years) on wave-dominated tidal inlets brought to light some of the complex mechanisms that control these environments.

Ranasinghe and Pattiaratchi [1999] applied a morphodynamic model to Wilson Inlet, an ephemeral tidal inlet in Western Australia, to gain insight into the processes governing seasonal inlet closure. Their model results showed that the seasonal closure of this inlet was due to onshore sediment transport under typical summer conditions. The application of the same morphodynamic model by *Ranasinghe et al.* [1999] to a synthetic inlet under idealised scenarios also revealed that cross-shore processes governed inlet behaviour when longshore transport rates were low. However, these authors could not consider the impact of the wave-current interactions on the inlet dynamics due to the loose-coupling between the different modules of their modelling system.

Cayocca [2001] realized pluri-decadal simulations with a morphodynamic model to investigate the respective roles of tides and waves in driving the long-term morphological changes of the Arcachon Lagoon inlet, France. To overcome the large computational cost of long-term simulations, representative mean annual wave and tide conditions with respect to sediment transport were defined. The model results showed that the tide was responsible for the opening of a new channel at the extremity of the sand spit, where tidal currents were the strongest, while the waves induced a littoral transport responsible for the longshore drift of sand bodies across the inlet.

Bertin et al. [2009a] performed a modelling-based analysis of the physical processes driving the morphological changes of wave-dominated inlets. They applied a morphodynamic modelling system to the Óbidos Lagoon inlet, Portugal, in order to investigate the physical processes responsible for channel development during fair weather conditions and shoaling during periods of larger waves. The inlet development during fair weather conditions was attributed to the strong ebb-dominance of the main channel due to very distorted tides, enhanced by the combination of shallow channels and a meso-tidal range. The inlet infilling during the maritime winter was attributed to three main wave-induced mechanisms: 1) a "bulldozer effect" caused by the onshore component of wave forces, only partly balanced by a barotropic pressure gradient; 2) the acceleration and convergence of longshore transport toward the inlet, due to the presence of a strong lateral gradient in free surface elevation on both sides of the inlet, and, to a smaller extent, to wave refraction around the ebb-delta; 3) the increase in mean water level inside the lagoon, which reduces tidal asymmetry and subsequent ebb-dominance.

Tung et al. [2009] investigated the migration and closure of an idealized tidal inlet system due to wave-driven longshore sediment transport through numerical experiments with a mor-

phodynamic modelling system. They simulated the morphological evolution of the inlet for a wide range of tidal and wave conditions and they computed the changes in the cross-sectional area, the mean tidal velocities and the tidal prism for each scenario. Their results showed a good agreement with the Bruun's empirical criterion and Escoffier's closure curve. The model was also able to reproduce the migration of the inlet and its closure due to wave-induced longshore transport. However, the 500 m progradation of the shoreline throughout the simulation questions their parametrization of wave asymmetry/cross-shore transport.

Nahon et al. [2012a] applied a 2DH morphodynamic modelling system to an idealized tidal inlet-lagoon system with different combinations of significant wave height, tidal range and tidal prism. The model results were compared to the empirical models of Hayes, Bruun, O'Brien and FitzGerald and to morphologies observed at natural tidal inlets. The results presented good accordance with observations. The predicted morphologies satisfied the relation of O'Brien between the tidal prism and the cross-sectional area, the model reproduced the conceptual model of sand by-passing by ebb-tidal delta breaching of FitzGerald and the classifications of Hayes and Bruun were generally respected. However, some inconsistencies between model results and Hayes classification highlighted the limitations of applying this classification to a single tidal inlet case.

Summary

In this chapter, several concepts that pepper the present dissertation were defined. Among the numerous and sometimes contradictory definitions for coastal lagoons, *Freitas* [1995] proposed one that encapsulates the major concepts underlined by pioneer authors. For this author, coastal lagoons are *coastal environments characterized by a depression in the coastal topography, separated from the ocean by a barrier allowing ephemeral or permanent communication with the open sea, and where the fluvial discharge is weak or null.*

Despite these intrinsic properties, coastal lagoons present a wide range of physiographic and hydro-sedimentary characteristics that require means of classification to distinguish them. Three common classifications of the literature were presented: the classification of *Lankford* [1977], based on geomorphic parameters and formation processes; the classification of *Nichols and Allen* [1981], based on the dominant processes controlling the open/close state of the lagoon; and the classification of *Kjerfve* [1986] based on the degree of water exchange with the adjacent coastal ocean.

Coastal lagoons are connected to the ocean through one or more tidal inlets that may be permanent or ephemeral. A tidal inlet is generally characterized by an ebb-tidal delta, an inlet gorge and a flood-tidal delta. The principal morphological units that compose a tidal inlet were described with reference to the terminology of *Hayes* [1975].

Three categories of tidal inlets are considered in the literature: *tide-dominated inlets*, *wave-dominated inlets*, and *transitional tidal inlets* (or *mixed-energy tidal inlets*). The morphological characteristics of each type of tidal inlets were described based on the work of *Hubbard et al.* [1979]. The classification of *Hayes* [1979a], based on two hydrodynamic parameters - the mean tidal range and the mean wave height - was recalled together with the limitations associated to its simplicity.

General theories on the stability of tidal inlets were elaborated during the last century, based on empirical considerations and analytical developments. Among these theories, the *P-A* relationship of *O'Brien* [1969], the overall stability concept of *Bruun and Gerritsen* [1960] and the closure diagram of *Escoffier* [1940] laid the foundations for a better understanding of the complex morphodynamic behaviours of tidal inlets and are still widely used nowadays.

Eventually, the conceptual models of *FitzGerald et al.* [2000] for sand bypassing at tidal inlets and the associated morphological changes were presented, and the results of some recent numerical applications of process-based morphodynamic modelling systems to tidal inlets were summarized.

Chapter 3

Study area

3.1 The Western Iberia Margin

3.1.1 Geomorphological settings

The rifting history of the Newfoundland-Iberia conjugate Margin started in the Late Triassic. The continental breakup between Iberia and the Grand Banks of Newfoundland occurred in the Early Cretaceous between 134 Ma and possibly 112 Ma [*Crosby et al.*, 2008; *Srivastava et al.*, 2000]. During its post-rifting history the tectonic settings of the Iberian Peninsula changed significantly, acting either as an independent plate or as an accreted terrain of the Eurasian or the African Plate. Since the early Oligocene (30 Ma), Iberia has been part of the Eurasian plate, north of the Eurasian-African plate boundary located along the Azores-Gibraltar Fracture Zone (AGFZ) [*Pinheiro et al.*, 1996] (Fig. 3.1).

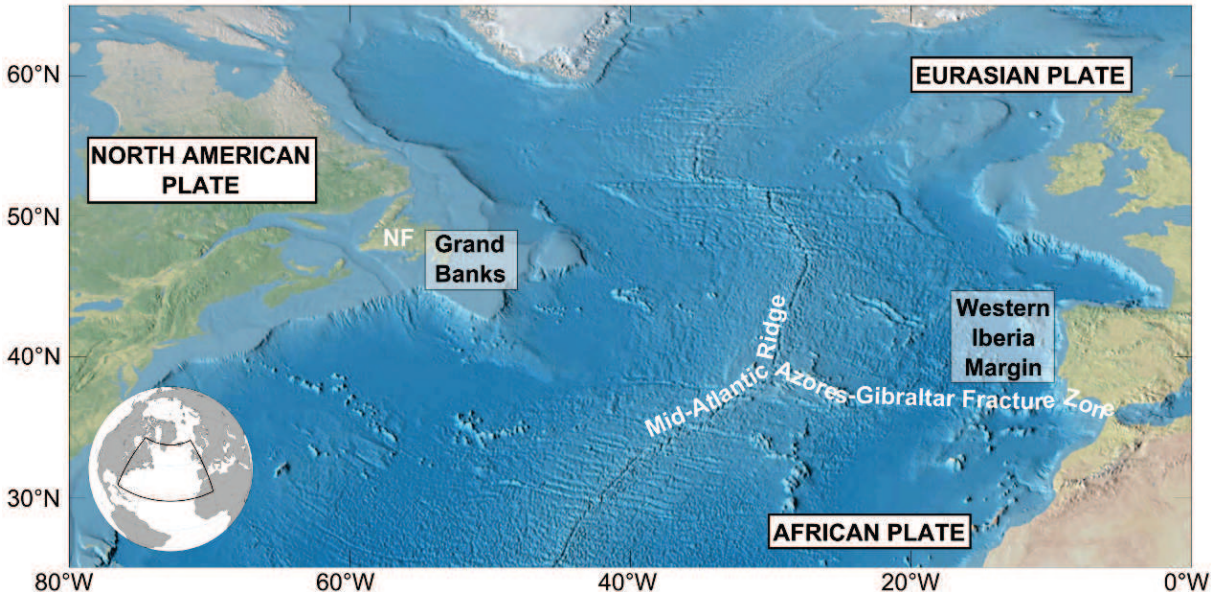

Figure 3.1: Present topography of the North-Atlantic basin showing the locations of the Western Iberia Margin, the Grand Banks of Newfoundland (NF), the Mid-Atlantic Ridge and the Azores-Gibraltar Fracture Zone.

Presently located between the latitudes 36°N and 44°N, the Western Iberia Margin (Fig. 3.2) is a non-volcanic passive margin characterized by a narrow continental shelf intersected by

several canyons, steep continental slopes and two distinct abyssal plains (the Iberian abyssal plain and the Tagus abyssal plain), where average depths are between 5000-5500 m [*Vanney and Mougenot*, 1981] . With a shelf break at around 160-200 m, the width of the continental shelf varies between 10 and 65 km along its approximate 700 km length (Fig. 3.2). The continental shelf of the Western Iberia margin can be divided into three distinct segments, separated by the major canyons: 1) north of the Nazaré canyon, 2) between the Nazaré and the Setúbal canyons, and 3) between the Setúbal and the St.Vincent canyons. In the northern segment, between Oporto and Cape Finisterre, the continental shelf is only about 30 km wide and is oriented roughly north-south. To the south of Oporto, the continental shelf widens a little to about 40 km, and south of Aveiro its width further increases to 50-55 km. The segment between the Nazaré and the Setúbal canyons is characterized by a relatively wide continental shelf, except for the region south-west of Lisbon where the Lisbon and Cascais canyons dissect the margin. Also along this segment, small islands (Farilhões and Berlengas) occur close to the coast (10-15 km) to the north-west of Peniche. The segment between the Setúbal and the Saint Vincent canyons is characterized, in general, by a fairly narrow (10-20 km) continental shelf [*Pinheiro et al.*, 1996; *Vanney and Mougenot*, 1981]. Regarding the shelf slope, the northern sector of the western continental shelf has a lower gradient (2-6‰) than the southern sector (8-11‰) [*Mil-Homens et al.*, 2007].

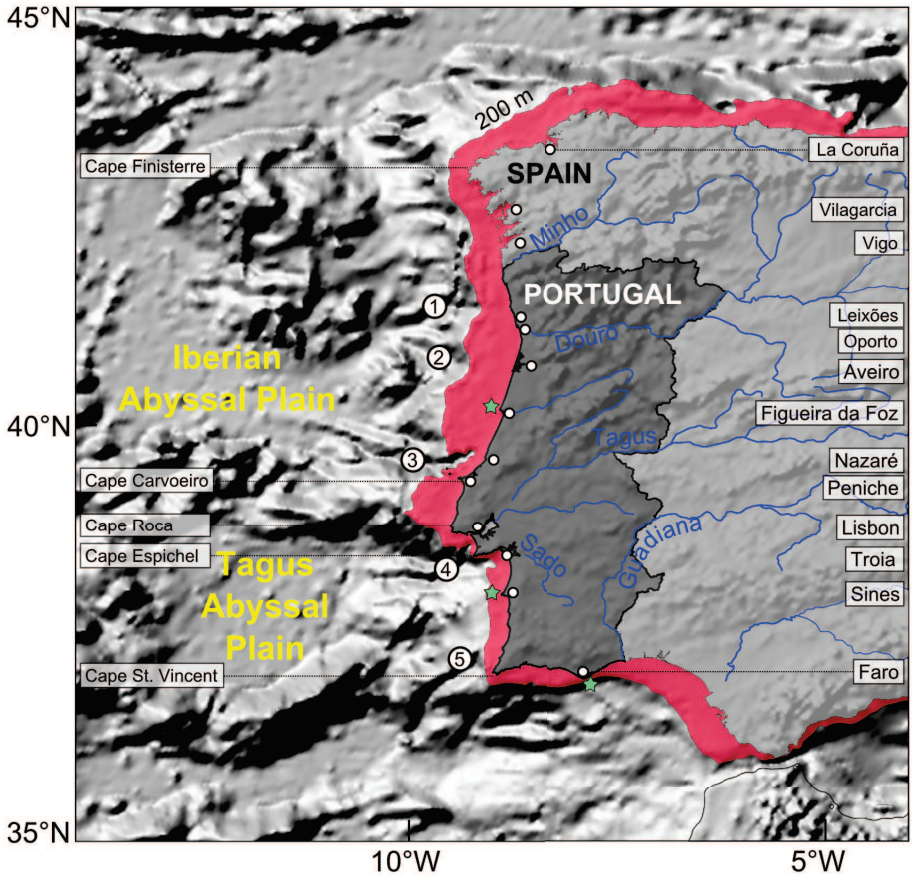

Figure 3.2: Topography of the Iberian continental margin. The red area represents the continental shelf (depth between 0-200 m). The numbers indicate the locations of the canyons: 1) Oporto Canyon, 2) Aveiro Canyon, 3) Nazaré Canyon, 4) Cascais-Lisbon-Setúbal Canyons, and 5) St. Vincent Canyon. The blue lines represent the main rivers. The green stars indicate the locations of the wave buoys of Figueira da Foz, Sines and Faro, from North to South.

Recent grain-size and geochemical analyses of sediment samples over the continental shelf (from 13 to 180 m) revealed the sedimentary and geochemical distribution and provenance of the Portuguese continental shelf soft-bottom sediments [*Martins et al.*, 2012]. The coarser deposits (ranging from gravel to coarse sand) occur mainly in the inner and mid-shelf of the north-western sector, at depths between 20 and 80 m and immediately south of the Nazaré and Setúbal canyons. Fine and very fine sands are found along a continuous band in the nearshore shelf and in the outer shelf of the north-western sector and constitute the dominant sediment type in the central and south-western sectors and in the western part of the southern shelf. Mud deposits are generally restricted to the shelf areas off the mouths of the Minho, Douro, Tagus and Guadiana Rivers, at water depths of nearly 100 m, 64–97 m, 87–137 m and 44–174 m, respectively. The geochemical signature of the Portuguese shelf sediments supports a major riverine input and shows that the terrigenous component is mainly derived from weathering of igneous and metamorphic source rocks. In the northern part of the shelf, the Douro River is the main supplier of the shelf sediment. Between the Nazaré and the Setúbal Canyons, the shelf is mostly fed by the suspended load delivered by the Tagus River. In the south-western continental shelf, the Sado River is the major sediment carrier of terrigenous sediments, although a significant fraction of the water-borne material is trapped in the estuary before reaching the continental shelf. Wave-induced coastal erosion, as a result of mechanical breakdown, is another non-negligible source of non-biogenic sediments along the Portuguese coastline where severe coastline retreat occurs and was reported to locally reach up to 200 m between 1958 and 1998 [*Taveira-Pinto et al.*, 2009]. Finally, a fraction of the shelf sediments is transported down to the abyssal plains by turbidity currents taking place in the submarine canyons that intersect the continental shelf, particularly in the Nazaré Canyon, which cuts the entire shelf and extends until a few hundreds of meters of Nazaré beach [*Oliveira et al.*, 2007].

3.1.2 Wave climate

Westernmost shores of the European continent, the Portuguese coastlines have to face the North-Atlantic swells with no other barrier than the rocky cliffs and the sand beaches. The straight and narrow continental shelf and the quasi-absence of islands close to the coast make the littoral even more exposed to the ocean waves generated by the extra-tropical storms. Nevertheless, these storms usually reach the European shores at latitudes comprised between 40°N and 65°N (Fig. 3.3) and the Portuguese littoral - especially in the south - is relatively spared by the severe wind seas that regularly hit the shores of the North of France, Ireland and Great-Britain. As a result, energetic long period swells from the WNW-NNW quadrant prevail all year long, sporadically disturbed by severe wind seas when an extra-tropical storm shifts south and passes over the Iberian Peninsula.

In order to characterize the Portuguese wave climate, *Costa et al.* [2001] analysed the entire data set of offshore wave measurements available along the Portuguese coast: 3-hourly time-series of mean wave parameters recorded between 1986 and 2000 at three representative deep-water locations ($\sim$ 100-m depth): the buoys of Figueira da Foz, Sines and Faro (locations on Fig.3.2). They found yearly-averaged significant wave heights ($\overline{H_s}$) of 2.2 m for the Figueira da Foz buoy, 1.7 m for the Sines buoy, and 1.0 m for the Faro buoy with standard deviations (σ_{H_s}) of 1.1 m, 0.9 m and 0.6 m respectively. During the winter period, H_s larger than 5 m occurred on the west

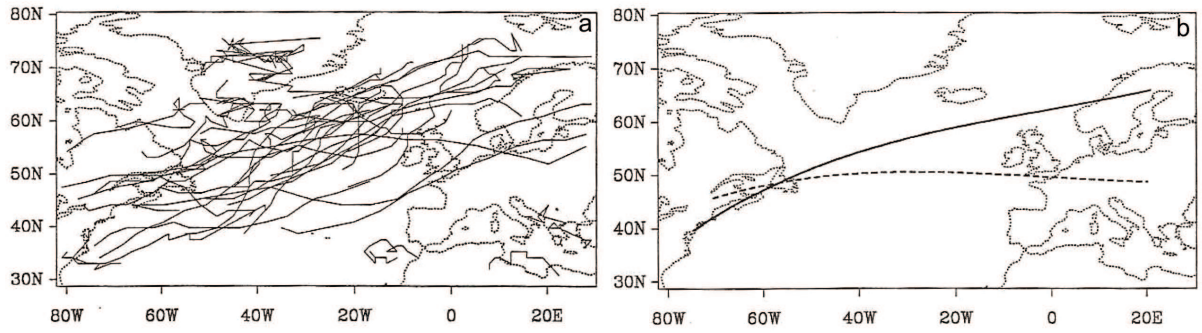

Figure 3.3: a) Path of cyclones with a minimum lifetime of 3 days (November 1990 to March 1991) [Blender et al., 1997]; b) Principal traces of the cyclone positions in the north-eastward (solid) and the zonal (dashed) clusters obtained from cluster analysis of cyclone tracks based on a high-resolution ECMWF data-set of the 1000 hPa height-field [Blender et al., 1997].

coast with a maximum of 7% of occurrence in January at Figueira da Foz (and maximum H_s up to 8 m). The mean values and standard deviations computed for the mean period ($\overline{T_m}$, σ_{T_m}) and the peak period ($\overline{T_p}$, σ_{T_p}) are summarized in Table 3.1. Regarding the direction associated to the peak wave period, 90% of the observations at Figueira da Foz came from the W-NW sector and 97% at Sines, while waves coming from the SW sector corresponded to less than 3 % of the observations. For the south coast, the distribution of the direction was bimodal with 71 % of the observations coming from the SW and 23% from the SE. Although these statistical values of H_s, T_m, T_p and directions are representative of the average wave regime off the Portuguese coast, the authors mentioned that significant gaps were present in data, particularly during the winter period, which might have biased the overall results. In addition the rather short period covered by the instruments did not allow a detailed analysis of extreme conditions nor the detection of significant trends in the wave climate, as evidenced by *Bacon and Carter* [1991] at northern latitudes.

Table 3.1: Mean wave parameters at Figueira da Foz and Sines [Costa et al., 2001].

Station	$\overline{H_s}^*$(m)	${\sigma_{H_s}}^*$(m)	$\overline{T_m}$ (s)	σ_{T_m} (s)	$\overline{T_p}$ (s)	σ_{T_p} (s)
Figueira da Foz	2.2	1.1	7.2	1.7	11.4	2.5
Sines	1.7	0.9	6.6	1.8	10.8	2.7
Faro	1.0	0.6	4.7	1.1	8.2	3.3

* ($^-$) = Annual mean. σ = Standard deviation.

Costa et al. [2001] also quantified the seasonal variability of the wave climate by computing monthly means of H_s, T_m and T_p (Fig. 3.4). They found similar behaviours for the west and the south coasts with the largest values of wave heights and periods occurring during the winter months and the lowest values occurring during the summer season.

With the view to assess projected changes in the Portuguese wave climate by the end of the 21^{st} century, *Andrade et al.* [2007] compared a 30-year (1961-1990) reference wave regime hindcast with an equivalent IPCC-based future scenario for 2070-2099. The distribution of Hs for the reference simulation (1961-1990) showed a southward decrease along the western Iberian façade (Fig. 3.5a), in agreement with the observation-based study of *Costa et al.* [2001]. The

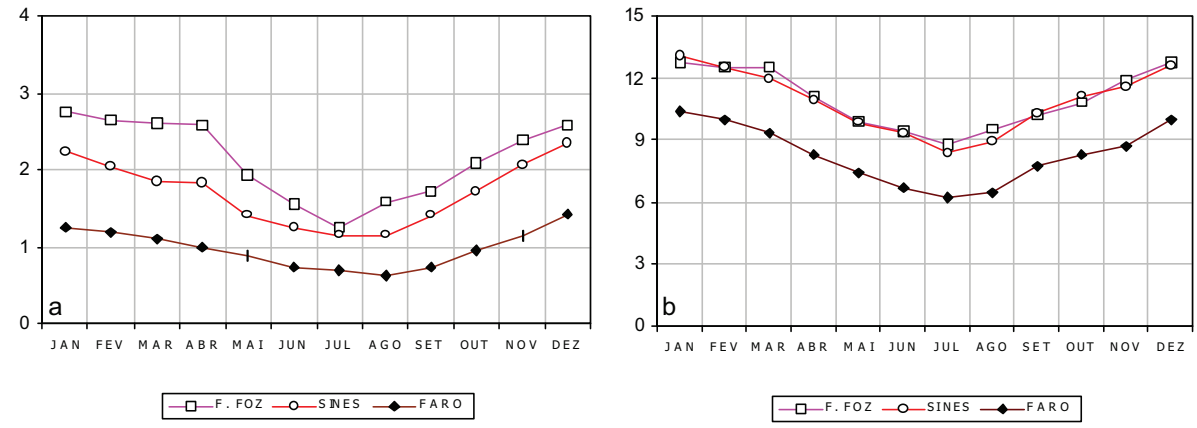

Figure 3.4: Monthly mean evolution along the year of the significant wave height (in m) (a) and the peak period (in s) (b) at Figuera da Foz, Sines and Faro [Costa et al., 2001].

Hs computed in Portugal for the end of the 21^{st} century did not show any significant changes yet the mean wave direction showed a 5° to 7° clockwise rotation indicating that waves would reach the Portuguese shoreline with a higher positive angle of incidence in the future (Fig. 3.5b). These results are in agreement with the results of *Woolf* [2002] and *Kushnir et al.* [1997] who obtained negligible trends for the significant wave height at latitudes lower than 40° based on long-term time-series of satellite observations and model hindcast results in the North-Atlantic, for the periods 1991-2000 and 1960-1990, respectively.

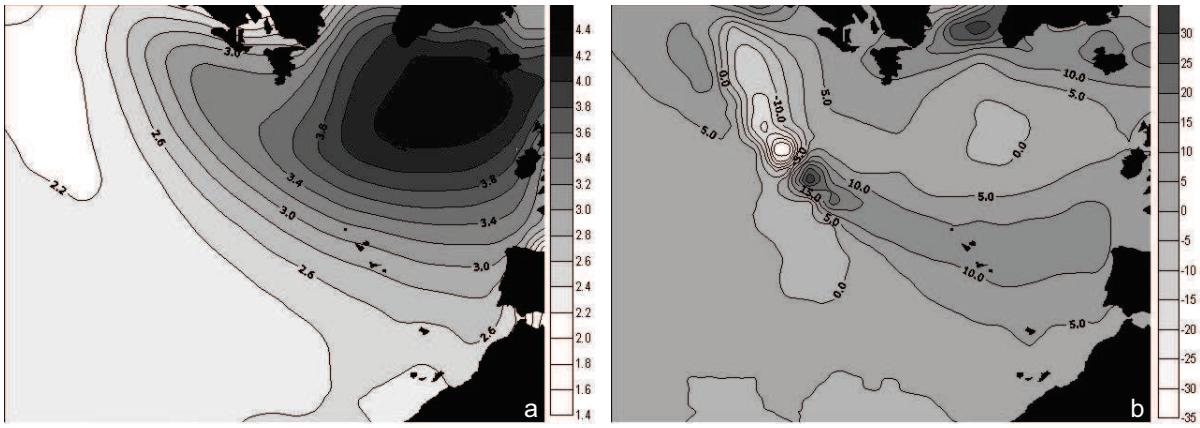

Figure 3.5: a) Wave height (m) distribution in the north Atlantic for the reference simulation corresponding to the period 1961-1990 [Andrade et al., 2007]. b) Rotation of the mean wave direction in the future scenario in relation to the control simulation [Andrade et al., 2007].

3.1.3 Regional circulation

The Portugal Current System

The dominant regional circulation pattern over the Western Iberia Margin is known as the Portugal Current (PC) and is generally considered - together with the Canary Current - as the eastern limb of the North-Atlantic subtropical gyre [*Martins*, 2002]. Typically depicted in marine atlases as a strictly southerly flow regime, the Portugal Current system actually presents a large seasonal variability and is still poorly defined spatially because of the intricate interactions between coastal and offshore currents, bottom topography, and water masses [*Bischof et al.*, 2003].

The Portugal Current system extends from about 36°N to about 46°N and from the Iberian shores to about 24°W and is supplied mainly by the intergyre zone in the Atlantic, a region of weak circulation bounded to the north by the North Atlantic Current and to the south by the Azores Current. It is also influenced by the more dominant neighbouring Canary and Azores Currents [*Pérez et al.*, 2001]. The Portugal Current system is comprised of the following main currents (Fig. 3.6):

1. the Portugal Current, a slow and variable southward large-scale surface circulation between continental Portugal and the Azores;

2. the Portugal Coastal Countercurrent (PCCC), a poleward warm and salty surface current, observed north of 41°N along the coasts of the Iberian Peninsula during the fall, winter, and early spring [*Haynes and Barton*, 1990; *Frouin et al.*, 1990]. According to *Haynes and Barton* [1990] the PCCC is generated by thermohaline forcing when the southward trade winds, characteristics of the summer months, weaken or reverse;

3. the southward Portugal Coastal Current (PCC), an equatorward current along the west coast of Portugal south of 41°N [*Martins*, 2002].

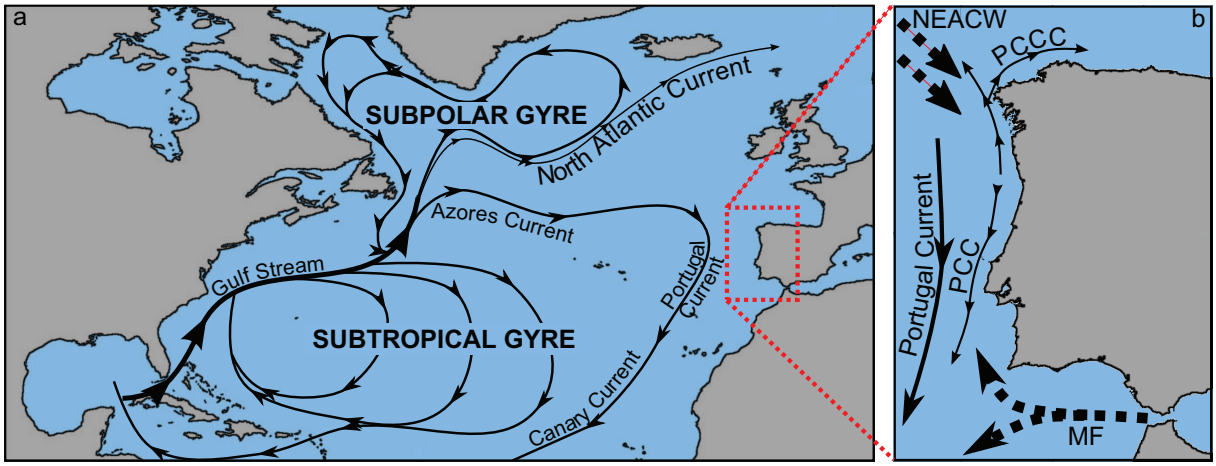

Figure 3.6: a) Schematic representation of the surface currents of the North-Atlantic Ocean [adapted from Tomczak and Godfrey, 1994] . b) Schematic representation of the surface (plain arrows) and subsurface (dashed arrows) currents influencing the Portugal Current system [based on Ambar et al., 2002; Martins, 2002].

Underlying water masses also affect the seasonal surface variability and the mean flow of the Portugal Current [*Pérez et al.*, 2001]. CTD (Conductivity, Temperature, Density) measurements off the west coast of the Iberian Peninsula during May 1993 revealed the intrusion of Eastern North Atlantic Central Waters (ENACW) below the seasonal thermocline at a few tens of km offshore the shelf break. This warm and saline ENACW of subtropical origin was transported by the poleward Portugal Coastal Countercurrent that was identified to reach down 250 m depth [*Fiúza et al.*, 1998]. The presence of thermohaline maxima, centred at levels of 800 and 1100 m, also indicated the presence of Mediterranean Water (MW) in the southern sector of the Western Iberia Margin.

Coastal upwelling

The local meteorological conditions play a significant role in the overall circulation of the PC and its seasonal variability. In summer predominant north winds cause wind-driven and persistent upwelling along the coast of the Iberian Peninsula. *Fiúza et al.* [1982] analysed 30 years of monthly-averaged winds measured at Portuguese coastal stations and of sea surface temperature (SST) taken from an atlas of the North-Atlantic in order to investigate the space and time variation of the Portuguese coastal upwelling. They found that the monthly wind regime is strongly dependent on the evolution of the atmospheric circulation on regional scales, being related with the latitudinal migration of the subtropical front and with the dynamics of the Azores anticyclonic cell. In particular, the meridional component of the wind is generally southwards, except in winter when it is frequently northwards, with considerable higher maxima in summer. Also, the standard deviation of the meridional wind presented minima in summer and maxima in

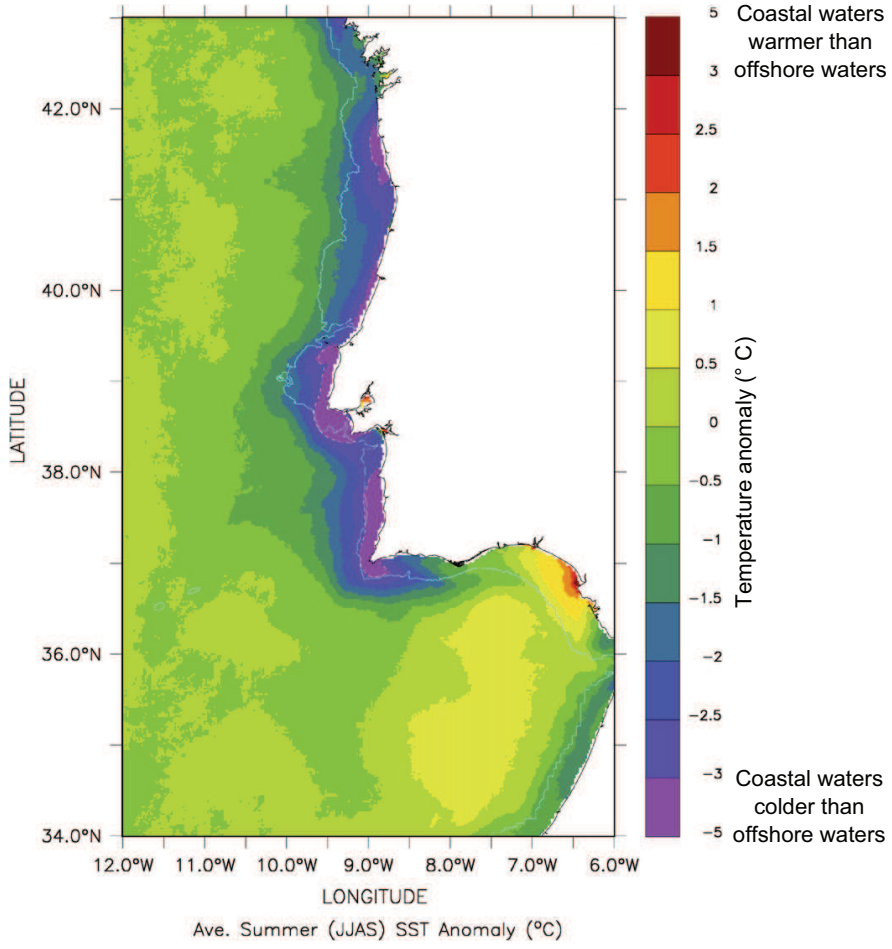

Figure 3.7: Average summer SST anomaly (June–September 2001–2005). Blue line represents the 200 m bathymetric contour [Relvas et al., 2007].

winter, in agreement with the evolution of the meteorological systems prevailing in these seasons over Portugal: westerly perturbed currents in winter and northerly semi-permanent circulation associated with the eastern margin of the Azores anticyclone, in summer. By analysing the SST anomalies between coastal and offshore waters along the Portuguese coast and by comparing them with wind observations, *Fiúza et al.* [1982] showed that the average Portuguese coastal upwelling occurs from July to September (one-month phase lagged with maximum northerly wind intensities), with sporadic appearance of smaller intensity upwelling in December-January

also induced by favourable northerly wind and explained by the wind-induced coastal Ekman divergence theory. The SST anomalies also revealed that average upwelling conditions are more pronounced south of Cape Carvoeiro (39.3°) with intensity maxima in the coastal region of Sines (38°N). To illustrate the average effect of the upwelling structures, *Relvas et al.* [2007] realized maps of average SST anomaly using satellite observations, for June to September of the years 2001–2005 (Fig. 3.7). The SST anomaly was defined here as the temperature difference relative to the zonal mean values for the range 11–12°W.

Tidal propagation

Over the Western Iberian Margin, the tides are dominated by the M_2 semi-diurnal constituent and mainly modulated over one moon cycle by the S_2 semi-diurnal constituent [*Sauvaget et al.*, 2000]. Revolving around an amphidromic point located in the North-West Atlantic Ocean (Fig. 3.8), the tidal wave associated to M_2 propagates over the Western Iberia Margin from South to North with an amplitude close to 1 m and a 1 hour phase lag between latitudes 36°N and 44°N. *Fortunato et al.* [2002] computed the amplitude and phases of the constituents M_2, S_2, N_2,

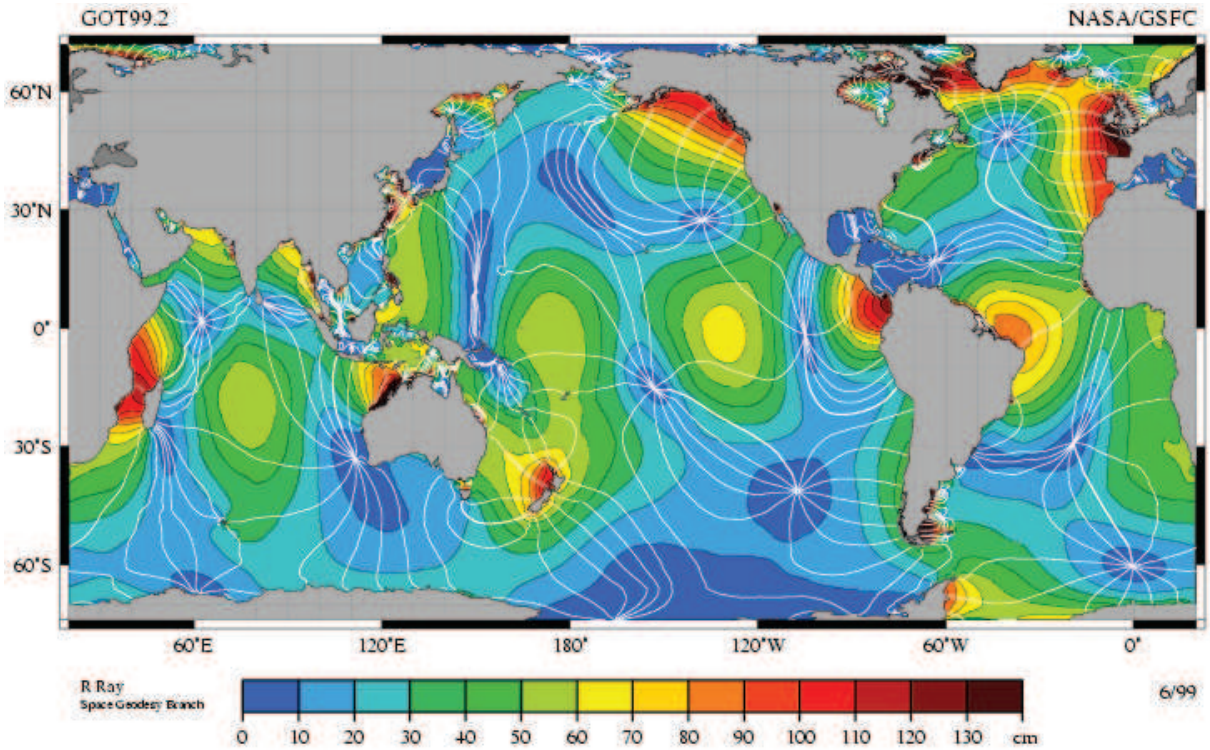

Figure 3.8: The global distribution of M2 amplitude (colour scale) and phases (white lines are cotidal lines spaced every 30°) computed from satellite observations (credits: R. Ray, TOPEX/Poseidon: Revealing Hidden Tidal Energy GSFC, NASA: http://svs.gsfc.nasa.gov/stories/topex/).

K_1 and O_1 along the Portuguese coastline through the harmonic analysis of tide gauge records covering more than one year (Table 3.2). The increase of the amplitudes of the semi-diurnal constituents from south to north induces a difference in the tidal elevation of the order of 20% between Sines and La Coruña. *Sauvaget et al.* [2000] realized a harmonic analysis with a 1-year tide gauge record at Leixões and found that the constituents with amplitude higher than 0.03 m were the semi-diurnal constituents M_2, S_2, N_2, K_2, ν_2, μ_2, $2N_2$ and the diurnal constituents K_1 and O_1. Based on the results of a calibrated circulation model they found that M_2 currents on the continental shelf were mainly alternating (ellipcity $< 25\%$), oriented south-north and lower than

0.25 m.s^{-1} (between 0.04 and 0.06 m.s^{-1} in deep areas). They also computed the amplitude of the highest astronomical tide, which did not exceed 2 m, and its associated currents, rarely above 0.2 m.s^{-1}, except near the Tagus Plateau where locally amplified currents were up to 0.5 m.s^{-1}. The study of *Sauvaget et al.* [2000] finally revealed the existence of diurnal shelf waves along the Portuguese continental shelf. *Fortunato et al.* [2002] used a high resolution finite element model for barotropic tides to investigate the mechanisms responsible for the generation of these diurnal shelf waves. The results of synthetic test cases with various bathymetric configurations showed that shelf waves are generated as the diurnal tidal waves are intercepted by a shallow plateau and propagate northward, inducing eddies and strong currents. The generation of the observed shelf waves along the Portuguese shelf was attributed to the presence of the Tagus Plateau, which can explain the local current amplification in this area observed by *Sauvaget et al.* [2000].

Table 3.2: Amplitudes in cm and (phases) in degrees of M_2, S_2, N_2, K_1 and O_1 [Fortunato et al., 2002].

Station	O_1	K_1	N_2	M_2	S_2
La Coruña	6.6 (325.4)	7.5 (72.3)	24.4 (68.4)	119.8 (87.3)	42.1 (118.7)
Villagarcia	6.9 (319.5)	7.7 (65.4)	24.3 (61.5)	114.5 (79.7)	40.1 (110.0)
Vigo	6.4 (318.5)	7.1 (64.2)	23.1 (58.9)	108.6 (77.8)	38.0 (106.2)
Leixões	6.2 (313.9)	6.8 (60.3)	21.7 (51.9)	103.2 (72.9)	36.9 (102.8)
Cascais	6.1 (313.4)	7.0 (53.4)	21.9 (46.9)	101.8 (64.5)	36.1 (91.3)
Sines	6.2 (313.3)	7.0 (57.0)	21.1 (46.8)	98.3 (64.1)	34.7 (90.9)

3.1.4 The fate of sediments along the Portuguese coast

The majority of terrigenous sediments along the western Portuguese shoreline come from riverine inputs: the Douro, the Tagus and the Sado rivers being the main sediment carriers. These sediments are redistributed along the coastline by wave-induced longshore transport with, for the exposed beaches of northern Portugal, an average rate of 1 million m^3.year^{-1} most of the time southward-directed [*Andrade et al.*, 2007; *Silva et al.*, 2012]. *Silva et al.* [2012] computed monthly and yearly means of longshore sand transport at the north-west coast of Portugal based on a 58-year wave model hindcast, and put in evidence the large variability of longshore transport both at seasonal and decadal scales. They obtained annual minimum rates one order of magnitude lower than the mean value computed over the 58 years and maximum annual rate exceeding the mean value by more than 100%, with every annual means being southward-directed. This variability was mainly explained by the relative importance of episodes of northward transport that occurred when the wave direction was farther south-than-average and the waves broke with a larger angle of incidence.

During the last decades, intensive anthropogenic activities have significantly affected the fate of sediments along their course from the rivers to the shore of Portugal. These activities include coastal urbanization and associated sand extraction, constructions of dams and coastal defence structures (breakwater, groins), dredging works for channel navigation, and artificial nourishments. The consequence of these anthropic activities is a disruption of the natural equilibrium between sedimentation processes and the resulting morphologies of riverine, estuarine and coastal landforms that have formed over millennial time-scales. When the rates of sediment supply change abruptly, rapid morphological evolutions are likely to occur and erosive hotspots

appear. A well-known example is the 3-km sand spit retreat observed at Cova do Vapor, south of Lisbon, between 1870 and 1970, and the associated loss of beach width at Costa do Caparica [*Veloso-Gomes et al.*, 2009] which might be related to human interferences with the sediment supply capacity of the Tagus River and the rapid urban expansion along the Tagus River's margins [*Veloso-Gomes and Taveira-Pinto*, 2004].

Finally, climate change is expected to have three major effects on the sediment fate along the Portuguese littoral: 1) the increasing sea level rise, estimated as 2.5 mm.year^{-1} at the Cascais tide gauge for the period 1990-2000 [*Antunes and Taborda*, 2009], will cause a shifting of the coastline; 2) the 5 °C increase of mean annual temperature and 20% decrease of annual precipitation computed for the end of the 21^{st} century through ensemble climate modelling [*van der Linden and Mitchell*, 2009] might cause a significant weakening of fluvial discharge and river-sediment supplies; 3) the potential clockwise rotation of the incident wave regime in Portugal expected for the next decades is likely to impact the longshore drift in the north of Portugal [*Andrade et al.*, 2007; *Bruneau et al.*, 2011b].

3.1.5 Coastal lagoons along the Portuguese coast

The Portuguese littoral present a large diversity of coastal environments: rocky cliffs, sand beaches, tombolos, dune barriers, estuaries and lagoons. From north to south, the following coastal lagoons, as defined in Chapter 2, have been identified: Barrinha de Esmoriz, Ria de Aveiro, Lagoa de Óbidos, Lagoa de Albufeira, Lagoa de Melides, Lagoa de Santo André, Ria de Alvor, Lagoa dos Salgados and Ria Formosa (Fig. 3.8). Table 3.3 summarizes the physiographic characteristics of these lagoons, based on the work of *Freitas* [1995]. Other coastal systems could be considered as coastal lagoons, such as the Concha de São Martinho do Porto, the Sado estuary or even the Tagus estuary, but the morpholodynamics of their inlet is strongly controlled by rocky cliffs, which do not fall within the scope of this dissertation. Hence, they will not be discussed herein.

Table 3.3: Physiographic characteristics of coastal lagoons in Portugal [adapted from Freitas, 1995].

Name	River basin area (km^2)	Lagoon area (km^2)	Maximum depth (m)
Barrinha de Esmoriz	74	0.9	2
Ria de Aveiro	3109	115	10-12
Lagoa de Óbidos	440	6	4.5
Lagoa de Albufeira	106	1.6	>15
Lagoa de Melides	56	0.4	2
Lagoa de Santo André	140	2.3	2.5
Ria de Alvor	250	4	
Lagoa dos Salgados			
Ria Formosa	740	84	5 - 7

The Ria de Aveiro is with no doubt the largest lagoon system in Portugal and presents a very intense evolution, according to *Teixeira* [1994]. The 100-km sand barrier has been migrating southward until the tidal inlet was artificially stabilized for the first time in 1808. According

Figure 3.9: Locations and aerial photographs of the coastal lagoons along the Portuguese coastline. Credits: Duarte Fernandes Pinto (http://portugalfotografiaaerea.blogspot.fr), João Ferrand (http://www.jferrand.com/eng/portfolio/aerial/), IGP/EPRL and SulInformação

to the classification of *Lankford* [1977] this lagoon corresponds to an intermediate type between type I and type II. The next largest lagoon system is the barrier island system of the Ria Formosa, which can be considered as a lagoon of type III in the Lankford's classification. The sand barrier is composed of two peninsula and five islands. Among the six inlets that separate the barrier islands, two of them were artificially stabilized while the others are natural and present a tendency to migrate eastward [*Balouin*, 2001; *Bertin et al.*, 2009b]. The remaining systems are less extended and their natural sand barrier episodically isolates them from the ocean (except for the Ria do Alvor that was artificially stabilized with jetties). The tidal inlets of these lagoons are regularly dredged and the lagoons remain open during a variable period, ranging from a few days to several years. These lagoon systems are of type I in Lankford's classification and of type III and IV migrate according to *Nichols and Allen* [1981]. The lagoons of the Portuguese littoral are generally shallow coastal systems, with maximum depths localized in the main channels, sometimes at the cost of repeated dredging. Hence, the Albufeira lagoon is an exception, with maximum depths (> 10 m) much larger than average values.

Despite their diversity, all these lagoons have in common important environmental problems, among which pollution and sedimentation appear as the most important ones. Given the ecological and economic roles of these systems, it is primordial to gain a better knowledge of their complex behaviours in order to promote their sustainable management. This research work was obviously motivated by this context.

3.2 The Albufeira lagoon

The Albufeira Lagoon is a beautiful coastal lagoon of great ecological and socio-economic values. Privileged location for fish and mussel farming, this Wetland of International Importance recognized within the Ramsar Convention is a choice residence during the autumnal migration of aquatic birds and passeriforms. The tidal inlet that connects the lagoon to the ocean is continuously shaped by the combined action of winds, waves and tides and closes naturally every year. Human intervention is then needed to dig a new channel and allow the lagoon water to renew. The fragility of this coastal system makes it particularly vulnerable to the anthropic pressure associated to growing urbanization and tourism, and an adequate regulation, based on ecological and morphological research efforts, is therefore necessary to ensure its sustainable management. Several authors conducted intensive researches on the morphological evolutions of the Albufeira Lagoon from geological to seasonal scales, resulting in a comprehensive interdisciplinary characterization of the lagoon system and its associated tidal inlet [*Freitas and Andrade*, 1994; *Freitas*, 1995; *Freitas et al.*, 2002; *Nahon et al.*, 2012b]. This section is mostly based on their results and discusses some of their conclusions.

3.2.1 Geomorphological settings

The Albufeira lagoon is located on the west coast of Portugal, on the western edge of the Setúbal Peninsula, around 20 km south of Lisbon. The width of the continental shelf along the Caparica-Espichel littoral arc ranges from 40 km, at the mouth of the Tagus estuary, to 5 km, in front of the lagoon where the Lisbon Canyon crosscuts the shelf (Fig. 3.10a).

The formation of the Albufeira lagoon occurred during the late Holocene (∼ from 6000 BP to present), after the rapid sea level rise characterizing the Holocene transgression (∼ from 12000 BP to 6000 BP) resulted in the inundation of a formerly excavated river valley [*Freitas*, 1995]. During the following millennia, the sea level was still rising but at a lower rate, which enabled depositional barriers to develop and to migrate onshore. Around 2000 BP, the morphology of the lagoon was already very similar to the present one and most of its subsequent changes were attributed to anthropological activities such as the expansion of agriculture and the associated land reclamation [*Freitas and Ferreira*, 2004]. Considering this sedimentation process, the Albufeira lagoon corresponds to a lagoon of type I as defined by *Lankford* [1977].

Nowadays, the lagoon covers an approximate surface area of 1.3 km^2, which can be considered as relatively small compared to the lagoon systems usually depicted in the scientific literature [*e.g., Nichols and Allen*, 1981; *Kjerfve*, 1986]. It presents an elongated shape almost normal to the coast, with the major axis slightly oblique, following a SW-NE direction (Fig. 3.10). Its

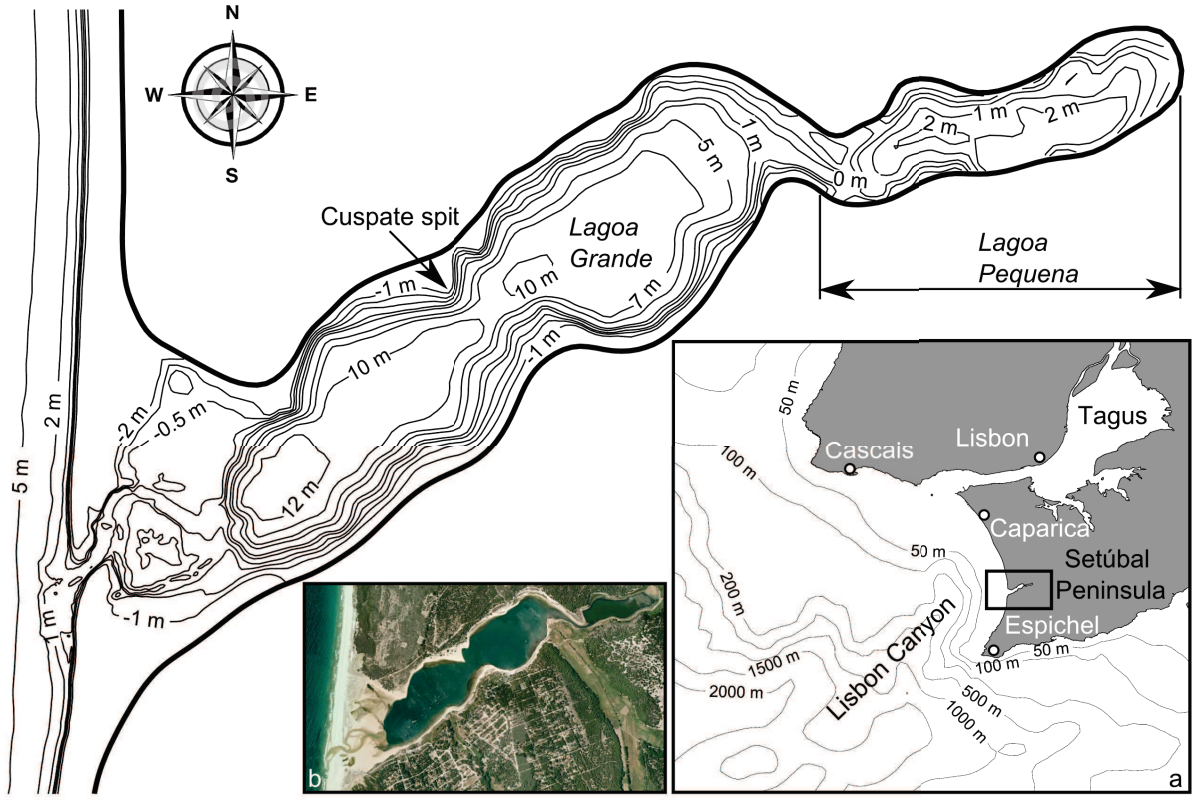

Figure 3.10: Bathymetry of the continental shelf in front of the Caparica-Espichel littoral arc (box a), aerial photograph of the Albufeira lagoon (Google Earth) (box b), and bathymetry of the Lagoon (relative to MSL) realized in March 2010 by the Research Centre of Coastal and Marin Environments of the University of Algarve (CIMA/UALg).

.

maximum length is 3.5 km and its maximum width is 625 m. The lagoon is composed of two semi-enclosed bodies connected by a narrow, shallow and sinuous channel: the upstream part of the lagoon, called the *Lagoa Pequena*[1] in the local toponymy, is a shallow basin of around 350 m by 900 m; the downstream basin, the *Lagoa Grande*[2] is roughly three times as large as the "small lagoon" and is much deeper (the maximum depth exceeds 12 m). This large lagoon

[1]Small lagoon
[2]Large lagoon

is composed of two elliptical bodies, delimited by two sandy cuspate spits, one on each margin. Cuspate spits are often encountered in elongated lagoons [*Zenkovitch*, 1959] and their formation may be attributed to the differential longshore transport induced by the locally generated wind waves that promote the development of coastal instabilities when breaking at high incident angle (Fig. 3.11). This "high-wave angle instability" mechanism, first described by *Zenkovitch* [1959] was then demonstrated analytically and numerically by *Ashton et al.* [2001].

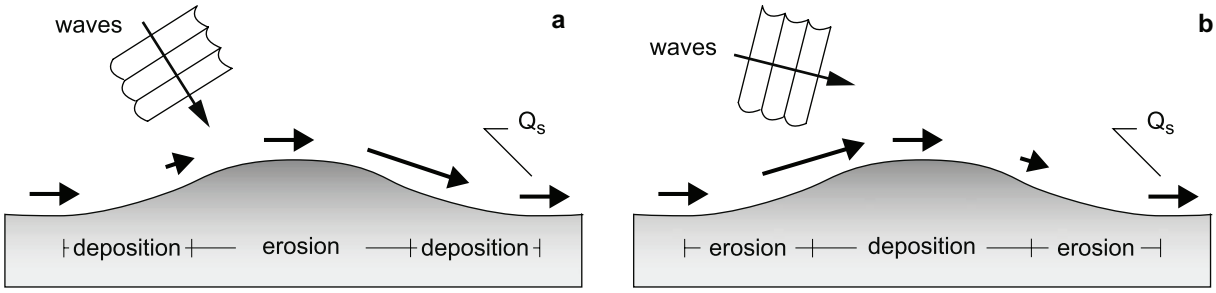

Figure 3.11: Illustrations depicting the high wave angle instability in shoreline shape [from Ashton and Murray, 2006]. (a) Response of a perturbation to a plan view shoreline subjected to low-angle waves. Sediment flux Q_s increases downdrift along the flanks and increases along the crest, resulting in flattening of the shape. (b) Opposite response for high-angle waves, with erosion along the flanks (Qs diverging) and accretion along the crest (Q_s converging).

.

The lagoon is separated from the ocean by a littoral barrier that is artificially opened every year to renew the lagoonal water. The morphology of the littoral barrier can be sub-divided into three distinct regions (Fig. 3.12): (1) the subaerial beach, including the beach face with one or several berms on the upper beach face and a low-tide terrace on the lower beach face; (2) a shallow region forming a complex system of channels and sandbanks corresponding to relict deposits (flood delta fragments, washovers) and the present tidal inlet system. This region is hardly, partly or fully immersed depending on the stage of the tide, the state of the lagoon (closed/open) and the quantity of freshwater inputs; (3) a region of vegetated sand dunes overtopping the berms and the channel-sandbank system at an approximate 8 m height (relative to the mean sea level) and occurring only on the northern part of the barrier. This barrier system, approximately 1200 m long and 600 m wide, is anchored at its north and south extremities to a cliff composed of detritic deposits dating from the mio-pliocene epoch (between 11 Ma and 2 Ma) [*Freitas and Ferreira*, 2004].

The barrier beach is characterized by coarse sediments and steep faces. A set of topographic transects across the beach realized in 1975, 1986 and 1992 exhibited very large topographic gradients, ranging from 6.6° to 14.3° for the upper beach and from 2.2° to 5.3° for the low-tide terrace [*Freitas*, 1995]. Similar values were measured during the 3D-MOWADI field campaign in September 2010. Given these values, the barrier beaches of the Albufeira lagoon can be considered as reflective beaches, according to the classification of *Wright and Short* [1984]. The fact that the beach face slope can locally exceed the 14° maximum threshold of inclination for sandy beaches estimated by *Bascom* [1951] [in *Freitas*, 1995] can be explained by the coarse sediment that composed the beach of this coastal region. *Reis and Gama* [2010] investigated the relationship between beachface slope and grain size based on sediment samples and topographic measurements along the south littoral of Portugal. Their study showed that several beaches

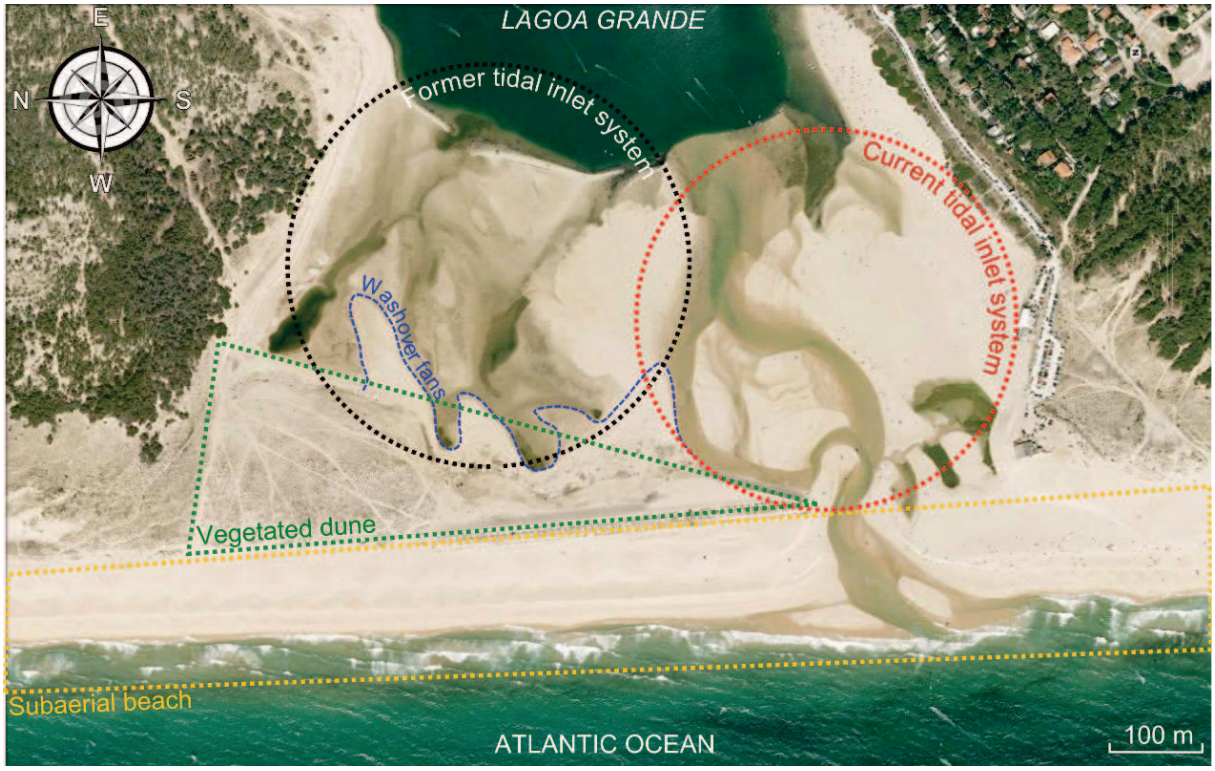

Figure 3.12: Satellite image of the Albfueira littoral barrier taken on 8 June 2004 (Google Earth) and schematic localization of the morphological units.

.

between Tróia and Sines also exhibited strong gradients with values ranging between 10° and 14° and these values were well correlated to the grain size when the offshore wave height and sediment porosity and permeability were taken into account.

The sand dunes overtopping the littoral barrier were confined to the northern extremity of the barrier until the mid-90's. This region was later extended to the south by accumulation of dredged material resulting from the recurrent openings of the inlet. While the dune increased in height, wood fences were installed in order to trap aeolian sand and strengthen the barrier [*Freitas and Ferreira*, 2004]. Afterwards, vegetation colonized this region, but only temporarily at first, since winter storms overflooded regularly the barrier and destroyed the vegetation. It is only from the early 90's that the vegetation has maintained and developed, as the equilibrium state reached by the northern part of the barrier was sufficiently high to resist the overwashes.

The inner part of the littoral barrier, comprised between the sub-aerial beach on the west side and the *Lagoa Grande* on the east side, is composed of a complex system of shallow channels and sand banks. This shallow region of approximately 300 m width has been subjected to large morphological changes that reflect the past and current evolutions of the tidal inlet system. The morphological patterns observed on the northern part are former deposits of washover fans and flood delta that occurred at a time when the overtopping dunes were lower and the channel between the lagoon and the ocean was systematically trenched at the northern extremity of the barrier, a place called *Velha Boca*[3] in the local toponymy. This very shallow region is now relatively stable. In the south, at the actual location of the inlet, highly mobile sand banks and

[3]Literally, "Old Mouth"

channels are constantly reshaped by the tidal currents and the waves, when the lagoon is open, and by episodic wave washovers when the lagoon is closed. When the lagoon is connected to the ocean, a tidal inlet system develops in this region, with several tidal channels, and flood and ebb shoals.

3.2.2 Climatology and hydrodynamics

The climate of the Setúbal Peninsula is temperate, oceanic with two dominant seasons: a cold and rainy season and a dry and warm season. According to the classification of Köppen, the climate is mesothermal humid with dry summers of moderate heat (Csb type). The annual mean temperature is around 16 °C, with minimum monthly means around 9 °C in January and maximum monthly means around 20 °C in August. The mean annual precipitation is around 650 mm with maximum monthly mean values occurring generally in December and January, and minimum values in July and August [*Freitas*, 1995]. Since these values were computed based on time-series from 1941 to 1970 and from 1953 to 1982, the mean temperature (resp. precipitation) of the current decade is likely to be larger (resp. lower). Indeed, the variation of temperatures in Portugal between 1931 and 2000 showed an increasing trend, with the six hottest years occurring between 1988 and 2000, while the variation of precipitations showed a weak decreasing trend [*Santos et al.*, 2001]. In addition, ensemble climate modelling studies predict for Portugal a 5 °C increase of the mean temperature (up to 6 °C for the summer temperatures) and a 20% decrease of the annual precipitation by the end of the 21^{st} century, with increased precipitation rates during the winter months and decreased rates for the rest of the year [*van der Linden and Mitchell*, 2009; *Fischer and Schär*, 2010].

The wave regime along the Caparica-Espichel littoral arc is dominated by long-period oceanic swells, occasionally disturbed by short-lived (but violent) W or SW storms. The observations of the wave buoys installed at Figueira da Foz and Sines give a bulk estimate of the wave conditions at intermediate latitudes. However, the presence of the Cape Roca significantly affects the propagation of the waves in the region south of it through sheltering, refraction and diffraction effects. As a consequence the beaches of this coastal stretch are sheltered from the waves coming from NW-N directions and the distribution of the wave heights is strongly modulated along the Caparica-Espichel Cape [*Teixeira*, 1990]. *Pires and Pessanha* [1986] analysed the measurements of a wave buoy located at the Cape Roca during the period 1976-1980. They found annual means of significant wave heights of 2 m and mean periods of 8 s, which is comprised within the results of *Costa et al.* [2001] for the wave buoys of Figueira da Foz and Sines. *Teixeira* [1990] applied a numerical wave model and computed the angle of refractions at the breaking point along the Caparica-Espichel littoral arc. He found that offshore wave directions coming from SW to NW directions presented a minimum angle of refraction always located near the centre of the littoral arc, a dozen of kilometres north of the Albufeira Lagoon. These incident waves induced favourable conditions for a diverging longshore transport, with northward transport along the northern part of the coast and southward transport along the southern part, with increasing intensity towards the extremity. The net littoral drift was thus assumed to be negligible in the central part of this coastal stretch and oriented southward near the Albufeira Lagoon, except for SW waves that induced northward transport along the whole littoral arc. This author computed annual longshore drifts ranging from 2500 to 3000 m^3 for a location north of the lagoon and 4700

m^3 south of the lagoon. *Nahon et al.* [2012b] computed the littoral drift in front of the Albufeira Lagoon from April to December 2010 based on the CERC empirical formula [*USACE*, 1984] and mean wave parameters at the breaking point computed with a nested wave modelling system. They found a net littoral drift of 21000 m^3 oriented towards the north and a gross littoral drift of 316400 m^3. These values are very different from the much lower values computed by *Teixeira* [1990] for the same region. These contrasting results highlight the need to investigate more intensely the amplitude and variability of the littoral transport in this area in order to estimate its impact on the sediment dynamics of the Albufeira Lagoon.

When tides propagate into the lagoon, the semidiurnal tidal constituents are damped, whereas higher harmonic constituents develop [*Friedrichs and Aubrey*, 1988]. As a consequence, the durations of the flood- and ebb-tides in the lagoon are asymmetric and dominance of the flood or ebb currents occurs, affecting the stability of the tidal inlet. The main sources of tidal distortion are the non-linear processes of advection and bottom friction and the interactions between the tide and the geometry of the bay and the channel [*Mota Oliveira*, 1970]. *Lincoln and Fitzgerald* [1988] identified an additional process influencing the tidal propagation through very shallow inlets: when the channel depth relative to mean sea level is lower than the average tidal amplitude, an elongated ebb duration in the lagoon is necessary to prevent the truncation of the lower portion of the oceanic tide. This situation is typical at the Albufeira Lagoon, where the minimum water level in the lagoon is higher than the minimum water level in the ocean. *Freitas* [1995] carried out four field surveys between April 1990 and April 1991 in order to characterize the tidal propagation in the Albufeira Lagoon in contrasting settings: spring tide and high efficiency of the inlet (17 April 1991), neap tide and similar efficiency level (8 April 1991), spring tide and intermediate efficiency stage (24 April 1990) and low efficiency of the inlet (19 July 1990) (Fig. 3.13). They found ratio of lagoon/oceanic tidal ranges varying between 43% and 8% and time

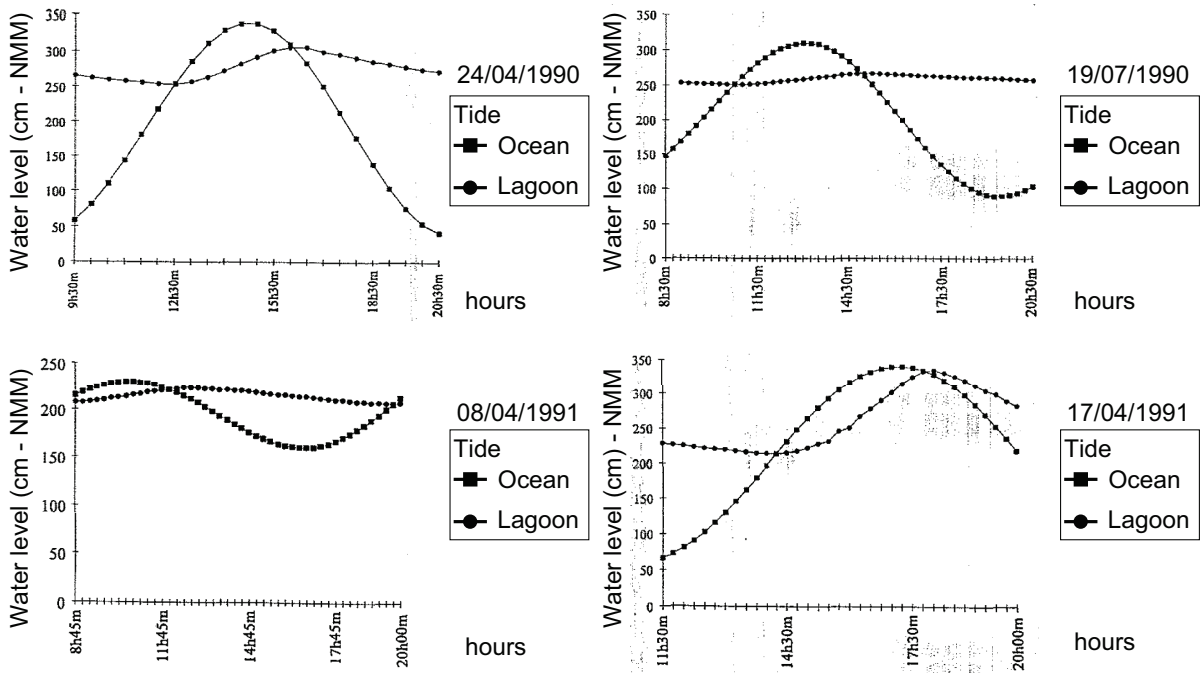

Figure 3.13: Comparisons of oceanic and lagoon tides [adapted from Freitas, 1995].

lags between low tide (resp. high tide) slack-waters ranging from 3h to 4.5h (resp. from 0.8h to

2.7h) with the maximum tidal attenuation and phase lag corresponding to the lower efficiency of the inlet (on 19 July 1990, one month before the inlet closure). The attenuation of the tidal range in the lagoon led to one order of magnitude differences in the tidal prism volumes (10^5 m^3 to 10^6 m^3) [*Freitas and Andrade*, 1994]. Assuming that the Bruun's approach [*Bruun*, 1978] is valid for this tidal inlet, they computed the averaged flood (resp. ebb) currents V as:

$$V = \frac{\Omega}{AT_{1/2}} \tag{3.1}$$

where Ω is the tidal prism, A is the minimum cross-sectional area computed with the Jarret's tidal prism - inlet area relationship [*Jarrett*, 1976], and $T_{1/2}$ is the flood (resp. ebb) duration. They found average currents of 1.2 m.s^{-1} during flood and 0.64 m.s^{-1} during ebb, with flood velocities always exceeding ebb velocities regardless of the tidal amplitude, and concluded about the flood dominance (shorter flood with stronger velocities than during ebb) of the Albufeira Lagoon system. Yet, *Bertin et al.* [2009a] applied a hydrodynamic model to a very similar lagoon-inlet system and obtained longer ebb-currents of higher magnitudes than the shorter flood currents. They proposed that for tidal inlets where the ratio between the average water depth and tidal range is below unity the average tidal elevation in the lagoon is lower on ebb than on flood, which leads to higher velocities on ebb. Since *Freitas and Andrade* [1994] used a constant cross-sectional area in the Bruun's formula, and thus did not take into account the difference in the average water level during the flood- and ebb-tidal stage, their estimation of the magnitudes of the tidal currents may be biased. Moreover, these authors mentioned measurements of tidal current obtained by timing floating object along the main channel with faster currents during the ebb tide than during flood tide. *Fortunato et al.* [2014] showed that the tidal signal in the lagoon presented a strong fortnight modulation in phase with the spring-neap cycle, based on model results. During spring tides, the large tidal range favoured the inflow during flood but attenuated the outflow during ebb and the water level in the lagoon was always higher during spring tides than during neap tides. Finally, *Freitas and Andrade* [1994] measured low fluctuations of the sea level O(1 cm) when the lagoon was closed that were attributed to water exchange between the ocean and the lagoon through percolation.

3.2.3 River inputs and sediments distribution

The drainage basin of the Albufeira Lagoon covers an approximate area of 106 km^2 within a perimeter of 53 km (Fig. 3.14). It is composed of several sub-basins, among which the largest one is formed by the confluence of the Apostiça stream (called Pateira stream further upstream), the Brava stream, the Vale da Vinha stream and the Ferraria stream. All these streams flow into the eastern extremity of the Albufeira Lagoon, the *Lagoa Pequena*. Minors sub-basins also occur along the left margin of the lagoon, such as the Aiana stream, whose deposits are responsible for the constriction between the *Lagoa Grande* and the *Lagoa Pequena*, and the Sachola stream [*Freitas*, 1995]. The average drainage density is 34 km.km^{-2} which corresponds to a well-drained basin, and the maximum height of the basin is 322 m, with 80% of the basin area lower than 100 m. All the streams that flow into the lagoon are ephemeral and even the larger ones only have a significant water flow during years of exceptional precipitation [*Freitas and Ferreira*, 2004]. *Freitas* [1995] reported that the discharge of the two main rivers that flow into the lagoon is zero

during the summer months and maximal between December and April after periods of intense precipitations. But even then, the discharge is still very low: *e.g.*, monthly means of river dis-

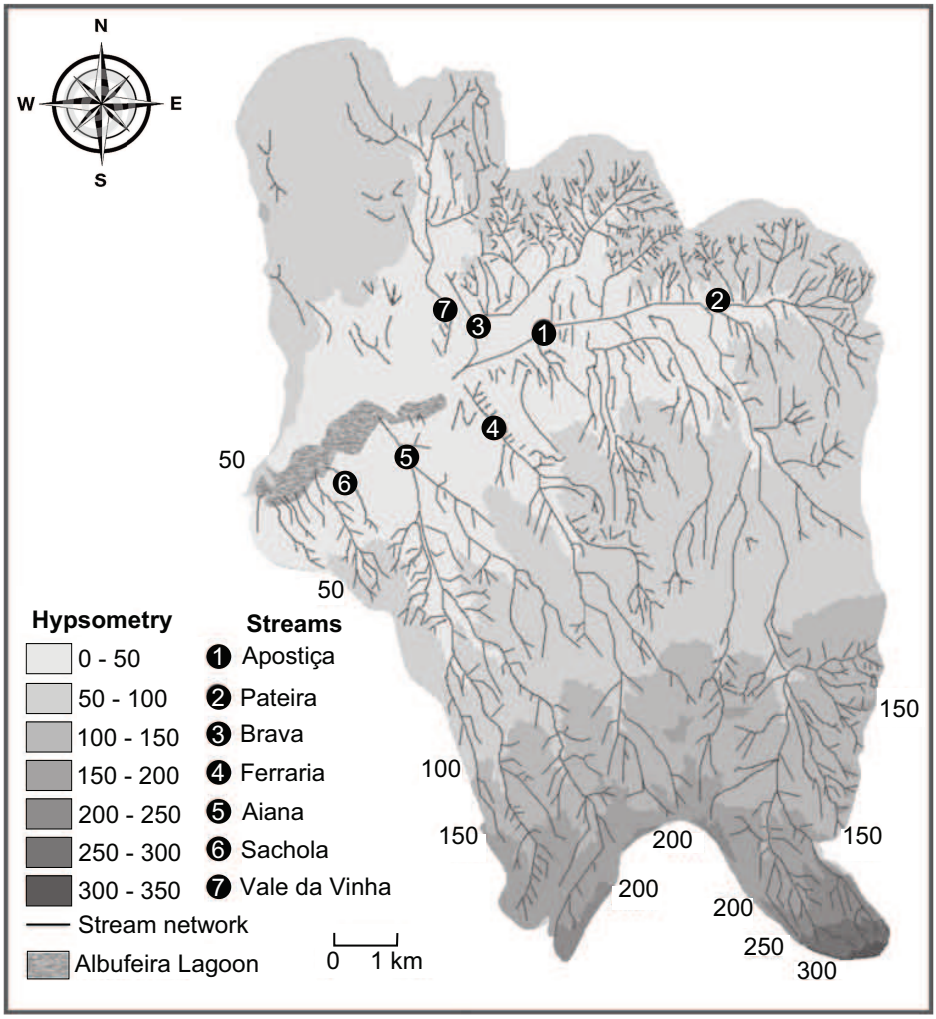

Figure 3.14: The drainage basin of the Albufeira Lagoon and its associated stream network [adapted from Freitas and Ferreira, 2004].

.

charge between 1986 and 1989 never exceeded 0.25 $m^3.s^{-1}$ and during the months of September and October, these values were always lower than 0.1 $m^3.s^{-1}$. The contribution of the freshwater discharge on the overall hydrodynamics of the lagoon is thus relatively weak compared to the contribution of the tidal flow. In addition, the lagoon is generally closed during winter, when the freshwater discharge reaches its maximum. Nevertheless, the riverine input is still responsible of the major part of the sediments found in the lower lagoon.

The sediments eroded and carried along the stream channels differ significantly from one stream to another: the Aiana stream carries very heterogeneous sediments, ranging from weakly-calibrated very coarse sands (1 - 2 mm) to well-calibrated fine sands (125 - 250 µm); the Ferraria stream carries moderately calibrated medium sands (0.25 - 0.5 mm) and fine sands; the Apostiça streams carries moderately calibrated medium sands and the Sachola stream carries moderately calibrated fine sands. The total sediment discharge is estimated between 110 and 480 $ton.km^{-2}.year^{-1}$, corresponding to erosion rates of the drainage basin between 12000 and 51000 $ton.year^{-1}$. Such values should normally lead to sedimentation rates in the lagoon between 1 and

4 cm.year^{-1}. However, most of the sands transported by the streams are deposited in alluvial fans at their mouths (Fig. 3.15) and only the suspended sediments reach the bottom of the lagoon. Thus the actual sedimentation rate is likely to be around 1 cm.year^{-1} or lower [*Freitas and Ferreira*, 2004].

Figure 3.15: Aerial photograph of the alluvial deposits of the Aiana stream taken on 15 December 2010 (credits: IGP / EPRL).

.

The sediments deposited on the bottom of the lagoon system originate from three different sources: (1) the ocean, through wave action, tidal currents and overwashes; (2) the continent, through the erosion of the lagoon banks induced by alluvial or aeolian transport; and (3) the bio-chemical activity in the lagoon itself. The two first (external) sources carry detritic and bioclastic material, while the third (internal) source leads to the formation of sediments through chemical precipitation, carbonation and evaporation and produces the major part of organic material, essentially from phytoplankton and microphytobenthos. Once they reach the lagoon, the sediment are deposited according to its hydrodynamic regime, depending essentially on the waves, the tide, the wind and the freshwater discharge. In the Albufeira Lagoon, the sediments organization is concentric, with the sands (from medium to very coarse) covering the region near the tidal inlet, the river mouths and the lagoon banks; the finer sediments (from coarse to fine silts) are principally located in the central region of the *Lagoa Grande* and over the whole bottom of the *Lagoa Pequena* (Fig. 3.16).

3.2.4 Physico-chemical characterization

The physico-chemical properties of the Albufeira lagoon are fundamentally influenced by the dual state of the tidal inlet (open versus closed) and the meteorological factors, essentially the temperature and precipitations, which present a significant seasonal variability. When the lagoon is isolated from the ocean, its salinity is strongly related to the precipitations and the associated freshwater discharge, with the lowest superficial values observed during the period

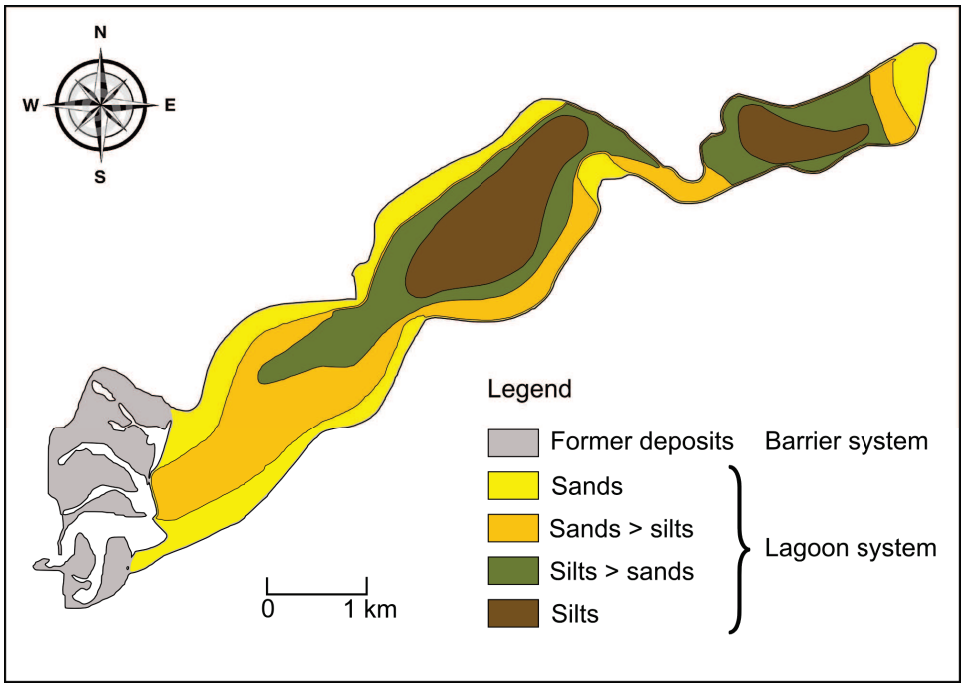

Figure 3.16: Sediment distribution over the bottom of the lagoon system [adapted from Freitas and Ferreira, 2004].

.

of most intense precipitations. A strong stratification of the water column then occurs with a layer of fresh-to-brackish water flowing over a denser layer of brackish-to-saline water. The halocline occurs generally between 2-3 m and 5-6 m water depth. When the lagoon is connected to the ocean, the salinity becomes much more homogeneous along the water column, with values similar to the ocean water (35‰) (Fig. 3.17). The water temperature is directly related to the

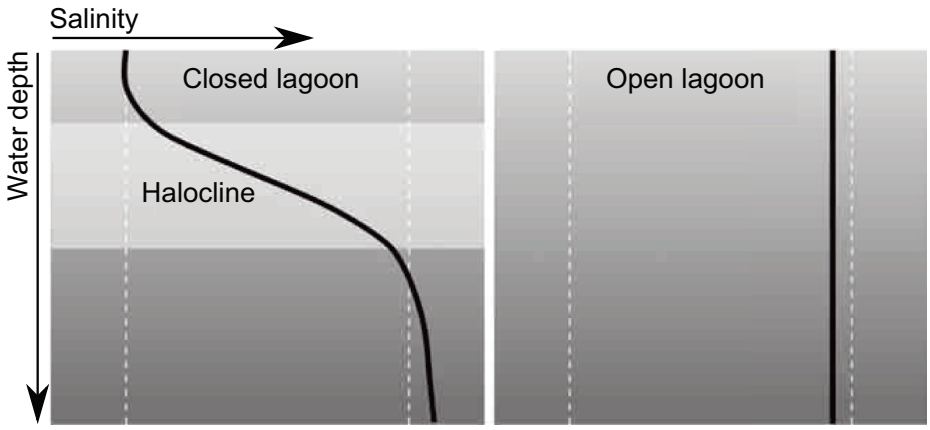

Figure 3.17: Vertical profiles of the salinity in the water when the lagoon is open (left panel) or closed (right panel) [adapted from Freitas and Ferreira, 2004].

.

atmospheric temperature and thus its variability is mainly seasonal. The thermocline, occurring between 2-4 m and 6 m water depth, is characterized by a decrease of temperature with depth during the summer when superficial water temperature is warmer and an opposite variation during the winter, when the superficial temperature is colder than in deeper water depth. When the lagoon is closed an accentuated stratification of the temperature along the water column is observed, related to the salinity stratification, while in the other state (open lagoon) the

temperature is more homogeneous (Fig. 3.18). The oxygen dissolved in the water (of atmospheric

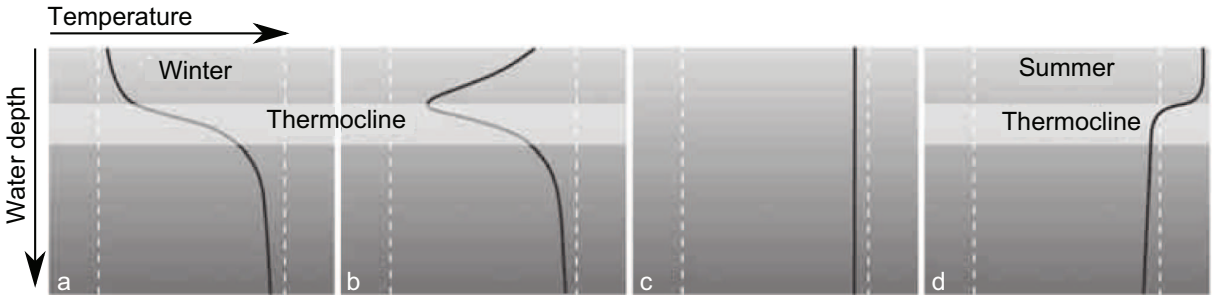

Figure 3.18: Variation of the vertical profiles of water temperatures along the year (from a to d). (c) also represents a situation with the lagoon opened [adapted from Freitas and Ferreira, 2004].

.

or photosynthetic origins) is essential for all aquatic aerobic organisms and is thus a fundamental parameter for the biota of lagoon environments. The solubility of the oxygen in water is influenced in a non-linear way by the temperature (a warmer temperature promotes a higher solubility) and the salinity (the solubility decreases exponentially with the increase of salinity). In the case of the Albufeira Lagoon, the oxygen solubility is mostly affected by the existence or not of a tidal inlet. When the lagoon is closed, the values of dissolved oxygen are higher at the surface (8-13 $mg.l^{-1}$) and uniform until around 2 m water depth, due to the mixing with atmospheric oxygen and the existing biomass in the photosensitive layer of the water column. The oxycline occurs between 2 and 4-8 m water depth, with homogeneous values close to zero (anoxic conditions) further down until the bottom. Values of dissolved oxygen lower than 4 $mg.l^{-1}$ that may occur in shallow depths in the Albufeira Lagoon are of concern from an ecological point of view. However, when the lagoon is connected to the ocean, the dissolved oxygen presents a more homogeneous distribution along the water column and anoxic conditions only occur near the bottom when the renewal of water is insufficient [*Freitas and Ferreira*, 2004] (Fig. 3.19).

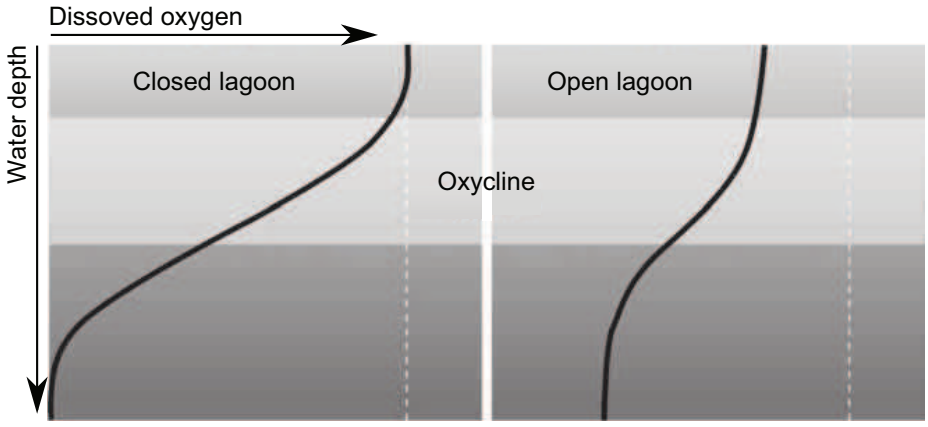

Figure 3.19: Vertical profiles of the oxygen dissolved in the water when the lagoon is open (left panel) or closed (right panel) [adapted from Freitas and Ferreira, 2004].

.

3.2.5 Morphological evolution of the Albufeira lagoon

The Albufeira Lagoon has existed as a coastal lagoon system for more than 500 years and human interventions were already necessary to dig a trench through the littoral barrier and allow the renewal of the lagoon water. Indeed, *Freitas* [1995] analysed historical archives, maps

of Portugal realized between the 15^{th} and the 20^{th} centuries and aerial photographs of the lagoon taken by the Royal Air Force and the United States Air Force between 1947 and 1990 in order to investigate the hyperscale [as defined by *Metha*, 1996] morphological evolutions of the Albufeira Lagoon. Based on this historical data set, their main conclusions were: the lagoon was often represented connected to the ocean until the beginning of the 18^{st} century, while the representations of an isolated lagoon predominated from the second half of the 18^{st} century; the main differences along the external rim of the lagoon occurred at the mouth of the main streams, while the rest of the lagoon morphology did not change significantly during the last 150 years; the lagoon bathymetry showed small differences between 1849 and 1990, indicating sedimentation rates of the order of 1 cm.year^{-1}; between 1947 and 1990, an increase of the surface area covered by the relic deposits over the littoral barrier was observed.

The artificial opening of the lagoon has thus been carried out for several centuries, probably for similar reasons as today: the drainage of the water lagoon is crucial for controlling the water quality and hindering the eutrophication of the water mass dammed in the lagoon. After its opening, the tidal inlet is shaped by the waves and the tidal currents, and to a lesser extent, by the wind, until its eventual closure. Once the tidal inlet has closed, the water level in the lagoon increases with the precipitations and the river inputs and the surface area of the lagoon enlarges (Fig. 3.20). The lagoon may naturally breach during periods of exceptional storms

Figure 3.20: Aerial photograph of the Albufeira Lagoon on 22 December 2012, approximately two months after is natural closure (credits: IGP / EPRL).

.

and/or precipitations but this phenomenon is extremely rare and was only episodically observed during the last two centuries [*Freitas and Ferreira*, 2004]. Traditionally, the lagoon is opened during Easter (between March and April) and the local population still attends this ritual every year (Fig. 3.21). Back in the 14^{th} century the channel was dug by hands but the spades were later replaced by mechanical means. A narrow channel is dug from the inner side of the sand barrier to the beach so that the final opening occurs when the oceanic conditions are optimal: namely, the lowest possible water level, which requires the opening date to coincide with spring tides, and relatively small waves. The strong water discharge induced by the large gradient between the water level in the ocean and in the lagoon rapidly erodes the bed and the banks of

Figure 3.21: Opening of the Albufeira Lagoon inlet on 28 March 2013. a) Discharge of the lagoon water into the ocean; b) The local population attending the traditional "abertura da barra"; c) panoramic view of the channel before opening.

the channel that enlarges and deepens during several days after the opening.

The selected location for the opening of the inlet has often changed in the past and the relict flood delta fragments located on the north of the barrier system attest of former positions of the inlet while the active channels in the south correspond to its actual location. The efficiency and longevity of the inlet strongly depends on several parameters, the most important being the height of the water level in the lagoon before the opening and the wave regime and the tidal range during and after the opening of the inlet. Since optimal conditions involving a large tidal range and small waves are not always met it appears valuable to estimate the impact of the wave conditions on the success of the operations. In particular the wave-induced setup can significantly increase the water level and the largest gradient between the ocean and the lagoon will not necessarily occur during the largest astronomical tide.

Once opened, the tidal inlet is subjected to large morphological changes involving the development of a flood delta and the meanderization of its associated channels, the sporadic inputs of foreshore sediment through overwashes, the formation of sand bars seawards, and the migration of the inlet itself, which eventually leads to its natural closure. The inlet's life span varies between a fortnight and 5-6 months, although in the last years the inlet often persisted until the end of the year ($\sim$ 8 months). This intense dynamics, illustrated by satellite images taken between 2004 and 2009 at different morphological stages of the inlet (Fig. 3.22), is still poorly understood and the predictability of these morphologic evolutions is far from being achieved, despite its necessity for a sustainable management [*Fortunato et al.*, 2014].

Freitas [1995] proposed a conceptual model to describe the evolution of the tidal inlet. This model is divided in six stages of variable durations, with some of them that do not necessarily occur (Fig. 3.23): (stage 1) after the artificial opening: the channel is roughly straight and symmetric, the water discharge erodes a large volume of sediments that are first deposited in the nearshore and then reworked to form subtidal bars and swash platforms migrating towards the beach. The channel section enlarges, with a "V-shape" due to the escarpment of its margins; (stage 2) the main channel migrates southward (in the dominant direction of the littoral transport) in response to the accumulation of sediments updrift and the erosion of the downdrift margin. As a consequence, the channel section becomes strongly asymmetric with the thalweg closely following the south margin of the channel (2A). The subtidal bars migrate shoreward and weld to the northern margin that keeps on migrating southwards while the downdrift margin starves. Hence the extension and meanderization of the channel accentuates and the hydraulic efficiency of the inlet decreases (2B); (stage 3) the ebb jet shifts towards the north to maximize its efficiency, breaking through the swash platforms and releasing sediments on the south margin; (stage 4) depending on the channel depth, the sediment availability and the direction and energy of the incident waves, the northern margin may rapidly extend towards the south, leading to a shallow and strongly asymmetric channel section; (stage 5) the loss of hydraulic efficiency induced by stage 3 usually leads to the breaching of the barrier and the updrift relocation of the tidal channel. Two channels may coexist during this stage (5A) although the less efficient south channel is rapidly abandoned in favour of the new north channel (5B); (stage 6) the rapid shoreward migration of the swash platforms can obstruct the channel (6A) and the vertical accretion

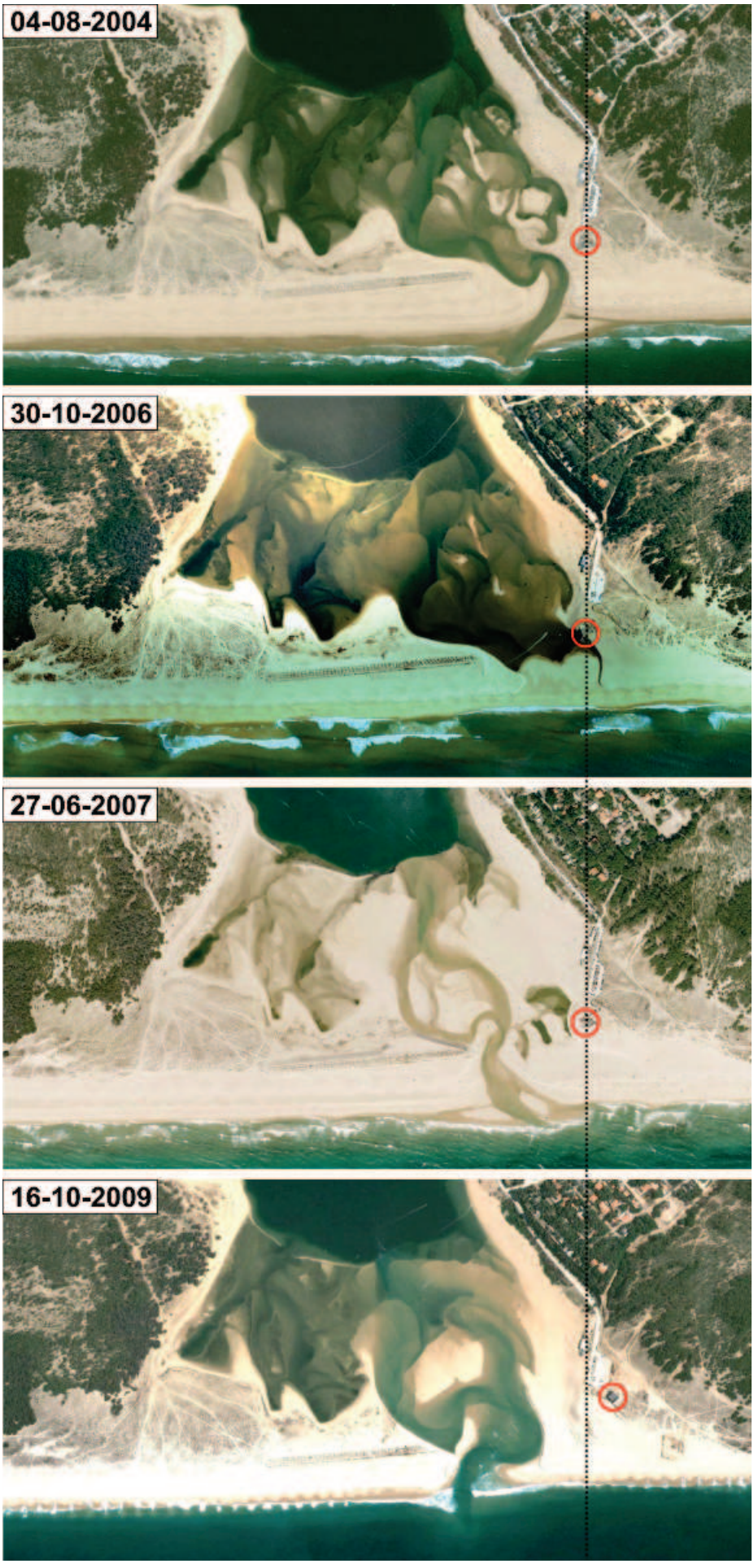

Figure 3.22: Satellite photographs of the Albufeira Lagoon littoral barrier showing the different morphologies of the tidal inlet (the restaurant indicated by the red circle was reconstructed further inland after severe erosion occurred in front of it).

and shoreward migration of this new sand bank during the spring-neap tidal cycles result in the full recovery of the littoral barrier. In this conceptual model, several scenarios are possible and some of the stages described above may occur several times or not at all until the inlet closed (see Fig. 3.23).

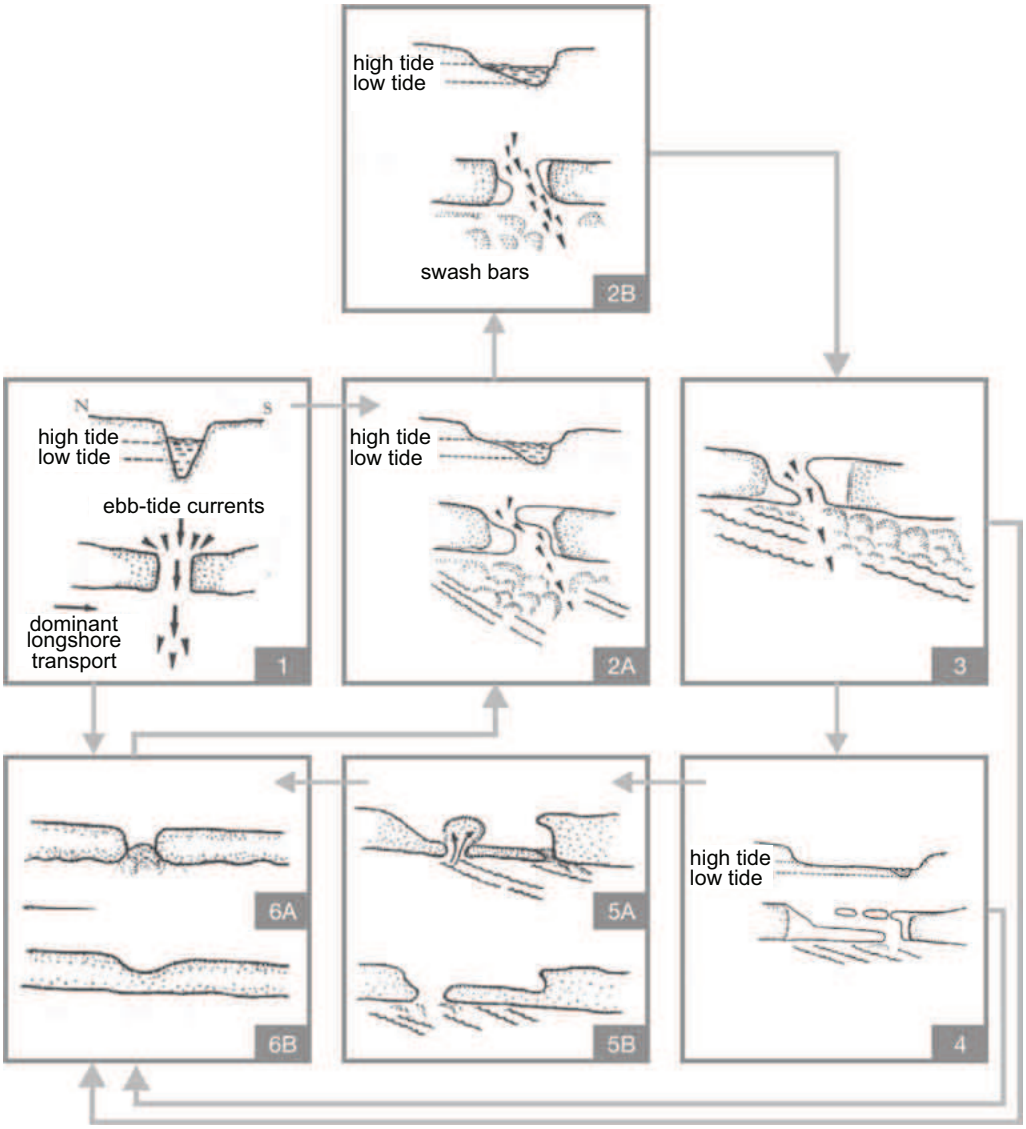

Figure 3.23: Conceptual model depicting the morphodynamic stages after artificial opening of the tidal inlet [adapted from Freitas and Ferreira, 2004].

Nahon et al. [2012b] analysed the 8-month evolution of the Albufeira Lagoon inlet from its opening to its closure, based on topographic surveys, and showed that the inlet was migrating northward before its closure, and that occasional overwash events radically modified the morphology of the inlet. These recent observations highlighted new mechanisms that were not accounted for in the conceptual model of *Freitas* [1995]. *Fortunato et al.* [2014] combined a data nudging method with a morphodynamic model in order to improve model results and gain a better insight in the morphodynamics of the Albufeira Lagoon inlet. Yet, the strong dependence of their results on the feeding observations did not allow a detailed analysis of the physical processes that controlled the closure of the inlet. And further research is needed to better understand the hydrodynamics and morphodynamics of the Albufeira Lagoon inlet.

Summary

The Western Iberia Margin is characterized by a narrow continental shelf intersected by several canyons. The continental shelf is approximately 700 km long and its width is comprised between 10 and 65 km, with a shelf break at around 160-200 m. Most of the sediments covering the shelf originate from the Douro River, the Tagus River.

The wave climate along the west coast of Portugal is characterized by long period swells coming mostly from the W-NW sector, with average wave height and peak period of 2 m and 10 s, respectively. Severe wind seas occur regularly during winter and maximum wave heights can reach up to 8 m.

The regional circulation is characterized by the interaction of superficial and sub-surface currents, among which the southward Portugal Current represents the dominant feature. Coastal upwelling occur frequently from July to September as it is induced by the northerly winds that prevail during the summer season. The tidal regime is semi-diurnal meso-tidal with a mean tidal range around 2 m. The tidal wave associated to M_2 propagates from South to North with an amplitude close to 1 m and a 1 hour phase lag between latitudes 36°N and 44°N.

A large variety of coastal lagoons systems occur along the Portuguese coastline, ranging from small lagoons intermittently connected to the ocean through a shallow ephemeral inlet to vast barrier island - tidal network systems.

The Albufeira Lagoon is located on the middle part of the west coast of Portugal, on the western edge of the Setúbal Peninsula around 20 km south of the Tagus estuary. The lagoon is separated from the ocean by a barrier beach and a tidal inlet is open artificially every year during Spring to allow the renewal of the lagoon water. The combined effect of the waves and the tide strongly impact the morphology of the inlet that systematically closes after a period ranging from a few weeks to several months.

Several studies have investigated some of the complex mechanisms that affect the hydrodynamics and the morphodynamics of this tidal inlet. In particular, a strong tidal distortion was evidenced with large attenuation of the tidal amplitude in the lagoon and ebb-currents lasting always longer than the flood currents. Although a conceptual model of the morphological stages undergone by the Albufeira Lagoon inlet was formerly developed, recent observations of the inlet evolutions have revealed complex morphodynamic mechanisms that were not fully explained by the conceptual model, stressing the need for further research on this topic.

Chapter 4

Data acquisition and processing

A 2-day field experiment was conducted in September 2010 at the Albufeira Lagoon in order to collect hydrodynamic data along the tidal inlet and survey the inlet system morphology through topographic measurements. Although a limited number of instruments was deployed, with some of them providing partial or corrupted information due to battery limitation, accretion events or inadequate environments, the atmospheric and hydrodynamic conditions were ideal and the final data set was rich enough for the purpose of the project. After the campaign, robust methods were developed to process accurately the field observations and extract the desired information. The field data were complemented with bathymetric measurements, tide gauge and wave buoy observations and atmospheric reanalysis products in order to provide the numerical model with initial or boundary conditions and to extend the validation of the models. The first section of this chapter presents the field experiment and the deployment of the instruments. Then the data and the methods to process them are described. The additional sources of data used for this dissertation are listed in the last section.

4.1 Field experiment

4.1.1 Overview

The field experiment took place on September 23 and 24, 2010. The Albufeira Lagoon inlet was one of the two tidal inlets selected within the framework of the project 3D-MOWADI. The main objective of this project was to gain a better understanding of the dynamics of wave-dominated tidal inlets, based on data analysis and numerical modelling applications. Meanwhile, two other FCT-funded collaborative projects carried out within the LNEC, the Faculty of Sciences of the University of Lisbon (FCUL), the University of Algarve (UAlg) and the Portuguese Hydrographic Institute (IH) required hydrodynamic and topographic measurements at the Albufeira Lagoon: the projects DETI (Dynamic of Ephemeral Tidal Inlets, PTDC/MAR/65585/2006) and Beach Sand Code (Sand beach textural and compositional variability as indicator of sedimentary dynamics). The field team was thus a combined LNEC-FCUL-IH team of 18 students and researchers (Table 4.1).

The main objectives of the field experiment were: 1) the characterization of the hydrodynamic conditions (waves and currents) at various locations of the tidal inlet for the calibration and validation of numerical modelling systems; 2) the characterization of the textural and compo-

sitional variability of the sediments; and 3) the characterization of the short-term morphological evolution of the tidal inlet system;

Table 4.1: List of participants in the 3D-MOWADI field experiment.

Persons	Institution	Responsibility
Alphonse Nahon	LNEC	
André Fortunato	LNEC	
Francisco Sancho	LNEC	
Guillaume Dodet	LNEC	
Nicolas Bruneau	LNEC	
Paula Freire	LNEC	
Xavier Bertin	LNEC	Hydrodynamic data
Bárbara Proença	FCUL	
César Andrade	FCUL	
Conceição Freitas	FCUL	
Frederico Ribeiro	FCUL	
Ivana Bosnic	FCUL	
João Cascalho	FCUL	
Marco Alves	FCUL	
Rita Pires	FCUL	Topographic survey
Rui Taborda	FCUL	Field work
Tiago Silva	FCUL	
Mónica Ribeiro	IH	Sediment sampling

4.1.2 Atmospheric conditions

During the campaign, anticyclonic conditions prevailed, with relatively high atmospheric pressures and light-to-moderate breeze. The stable atmospheric situation was only disturbed by the passage of a cold front over the Iberian peninsula during the night of September 23, as shown by the Met Office surface pressure charts (Fig. 4.1). The local wind measured by an anemometer deployed on the beach during the experiment exhibited the direction shift associated to the passage of the front, from southerly directions to northerly directions (see Fig. 4.2). Yet the wind magnitude never exceeded 6 m.s^{-1} while the instruments were recording data and the hydrodynamic circulation was not significantly affected by this light breeze. The surface

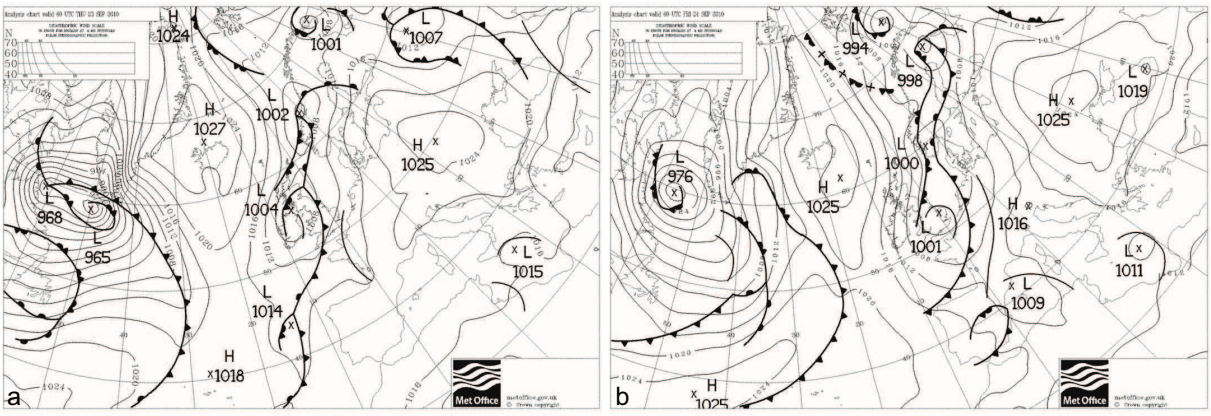

Figure 4.1: Pressure charts over the North-East Atlantic Ocean on September 23 2010 at 00:00 (a) and September 24 2010 at 00:00 (b) provided by the UK Met Office.

atmospheric pressure is continuously measured at the Cascais meteorological station (the location of Cascais is indicated on Fig.3.10) and averaged every 10 minutes. During the experiment, the atmospheric pressure was relatively stable with values comprised between 1018 hPa and 1022 hPa (Fig.4.2).

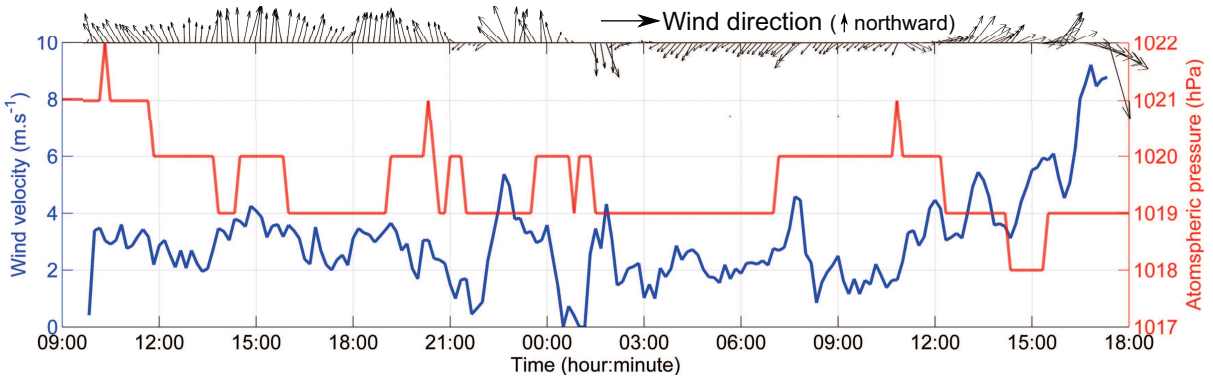

Figure 4.2: Magnitude (blue line) and direction (black vectors) of the wind velocity measured at the Albufeira lagoon and atmospheric pressure (red line) measured at the Cascais meteorological station between 23 September 09:00 and 24 September 18:00.

4.1.3 Hydrodynamic conditions

The field experiment period coincided with spring tides. The tidal ranges measured at the Cascais tide gauge for the three tidal cycles were respectively 2.55 m, 2.51 m, and 2.61 m (Fig. 4.3, top panel). The wave conditions were recorded by a wave buoy located 5 km off the Sines

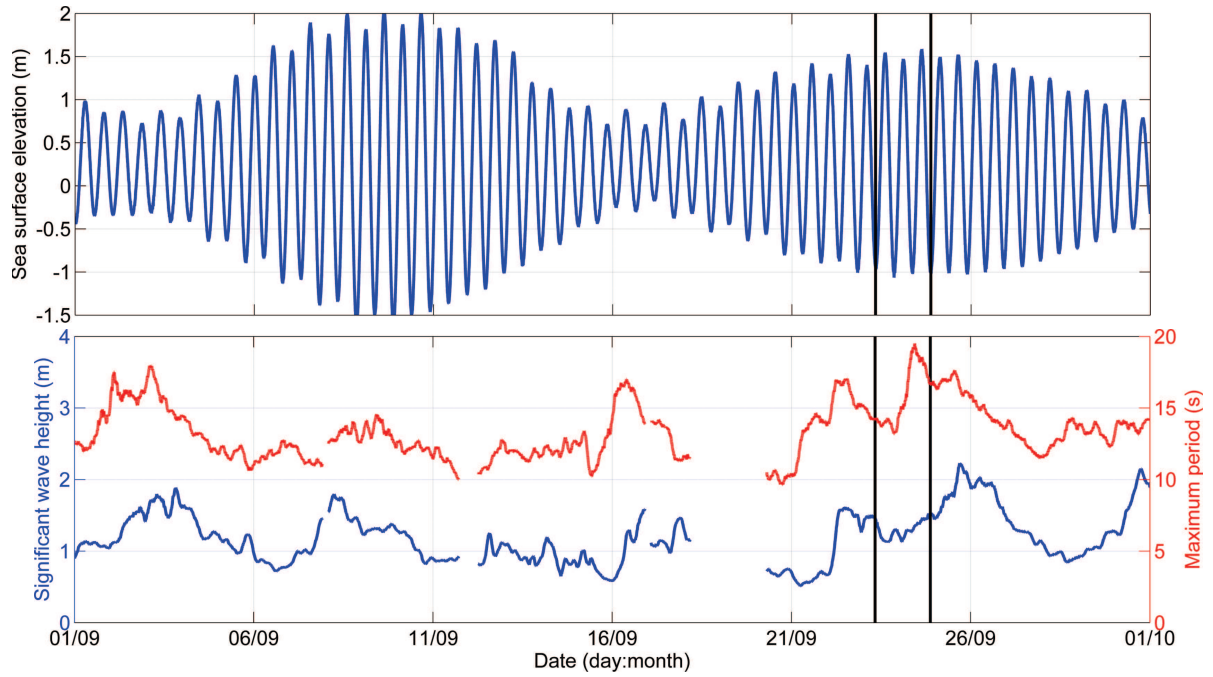

Figure 4.3: Sea surface elevation measured at Cascais tide gauge (top panel) and mean wave parameters measured at Sines wave buoy during September 2013(bottom panel; the significant wave height is represented with the blue line and the maximum period is represented with the red line). The vertical black lines delimit the field experiment period.

Cape, in 97 m water depth (the location of this buoy is indicated on Fig.3.2). Although the Sines cape is located approximatively 70 km south of the Albufeira lagoon, the mean wave parameters

measured by the Sines buoy provide a good estimation of the wave conditions near the study site, except when the incident waves are coming from the North and the *Cabo da Roca* shelters the shorelines of Caparica. The bottom panel of Fig.4.3 shows the time-series of the significant wave heights and maximum periods during September 2013. During the field experiment the wave heights were moderate, with values comprised between 1 m and 1.5 m. However, the maximum period exhibited a strong increase from 15 s to 20 s during the night of September 23, indicating that a new swell just arrived. Such high wave periods rarely occur along the Portuguese coastline and additional investigation was necessary to understand that this very long swell started developing a week before when hurricane Igor reached the Bermuda Islands.

4.1.4 Hurricane Igor

Hurricane Igor originated from a broad area of low pressure that moved off the west coast of Africa on September 6, 2010 (the storm track is shown in Fig. 4.4). Tracking slowly westward, it developed into a tropical depression on September 8 and strengthened into tropical storm shortly thereafter. On September 12, explosive intensification took place and Igor reached Category 4 status on the Saffir–Simpson Hurricane Wind Scale. By this time, Igor had already begun a prolonged turn around the western periphery of the subtropical ridge. Peaking with winds of 250 km.h^{-1}, the cyclone began to enter an area unfavourable for continued strengthening, and Igor gradually weakened before brushing Bermuda as a minimal hurricane on September 20. After turning northeastward, the system began an extra-tropical transition, which it completed shortly after striking southern Newfoundland. The remnants of Igor were later absorbed by another large extra-tropical cyclone over the Labrador Sea on September 23. According to the National Hurricane Centre of the United States, Igor was the strongest tropical cyclone of the 2010 Atlantic season and was the most damaging hurricane in recent history for the Bermuda islands [*Pasch and Kimberlain*, 2011].

The wave model WAVEWATCH-III [*Tolman*, 2009] was used to backtrack the 20 s swell observed along the Portuguese coastline on September 24 and to verify that hurricane Igor was the source of this swell. Fig. 4.4 shows the significant wave height and the peak period simulated with the wave model from September 21 to September 24 over the North-Atlantic Ocean. The observed hurricane track is represented on the colour maps with a black line and the variance density spectra simulated at a location near the Albufeira lagoon (9.55° ; 38.5°: this location is indicated by the green star on Fig.4.4) are also provided. The simulated hurricane position, estimated from the maximum wave height matches very well the observed track (on September 21 for instance). The very long swell that crosses over the Atlantic basin and reaches the Iberian peninsula on September 24 appears to originate near the hurricane path around September 21. The assumption that the swell occurring during the field campaign originated from a tropical cyclone was thus confirmed. The implications for data processing are discussed in Section 4.2.

4.1.5 Deployment

The field experiment aimed to characterize the hydrodynamic circulation at the Albufeira lagoon inlet and its short-term morphological changes. The instruments, listed on Table 4.2, were

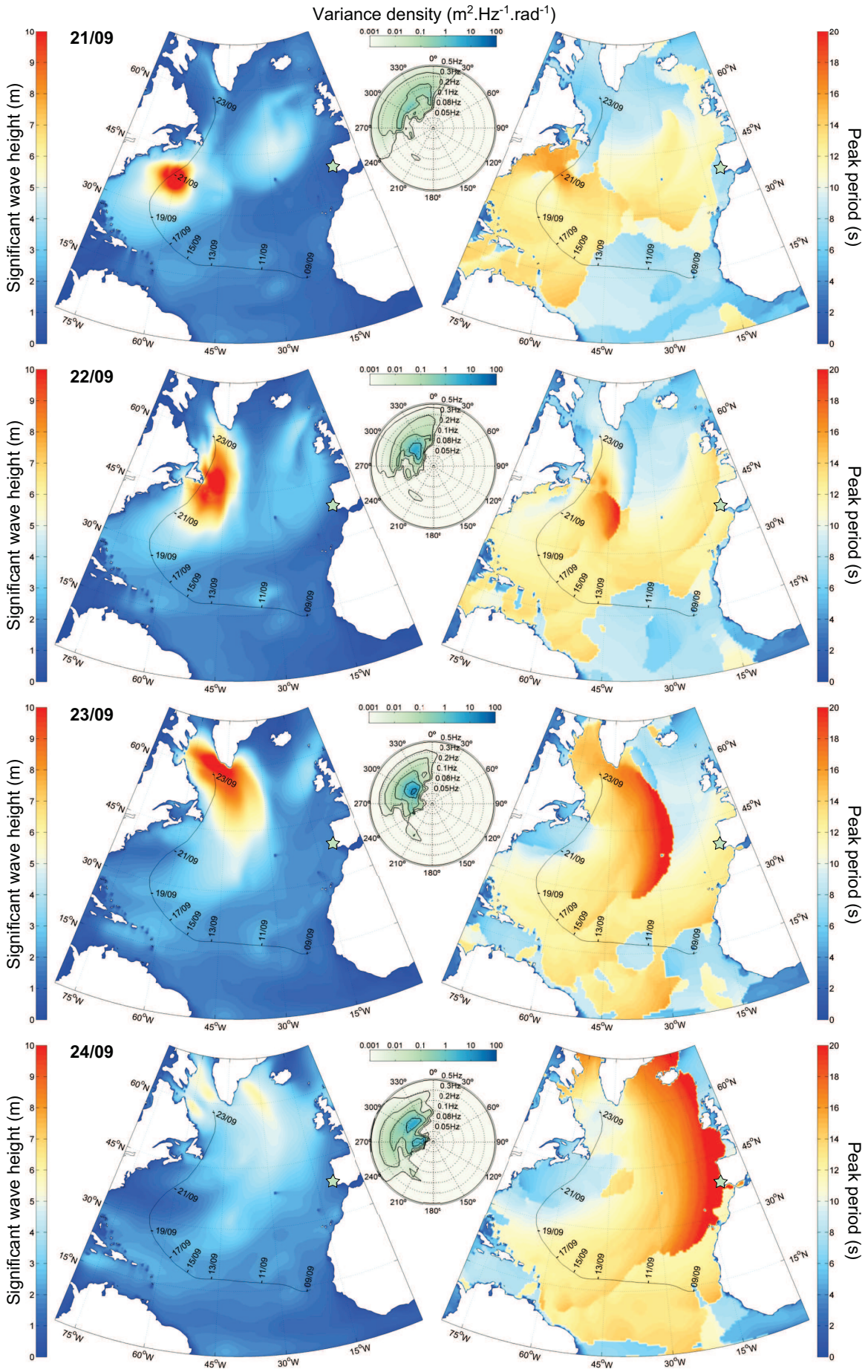

Figure 4.4: Significant wave height (left panels) and peak period (right panels) over the North-Atlantic Ocean on September 21, 22, 23 and 24 at 00:00 (from top to bottom panel respectively). Track of hurricane Igor (black line) and variance density spectra computed at location (9.55° W;38.5° N), off the Albufeira lagoon (green star).

synchronized and deployed during the morning low tide of September 23 ($\sim$ 10:00 UTC[1]), at strategical locations defined prior to the experiment (see Table 4.3 and Fig.4.5 for the position and the identification name of each instrument). Two scaffold frames, each composed of one

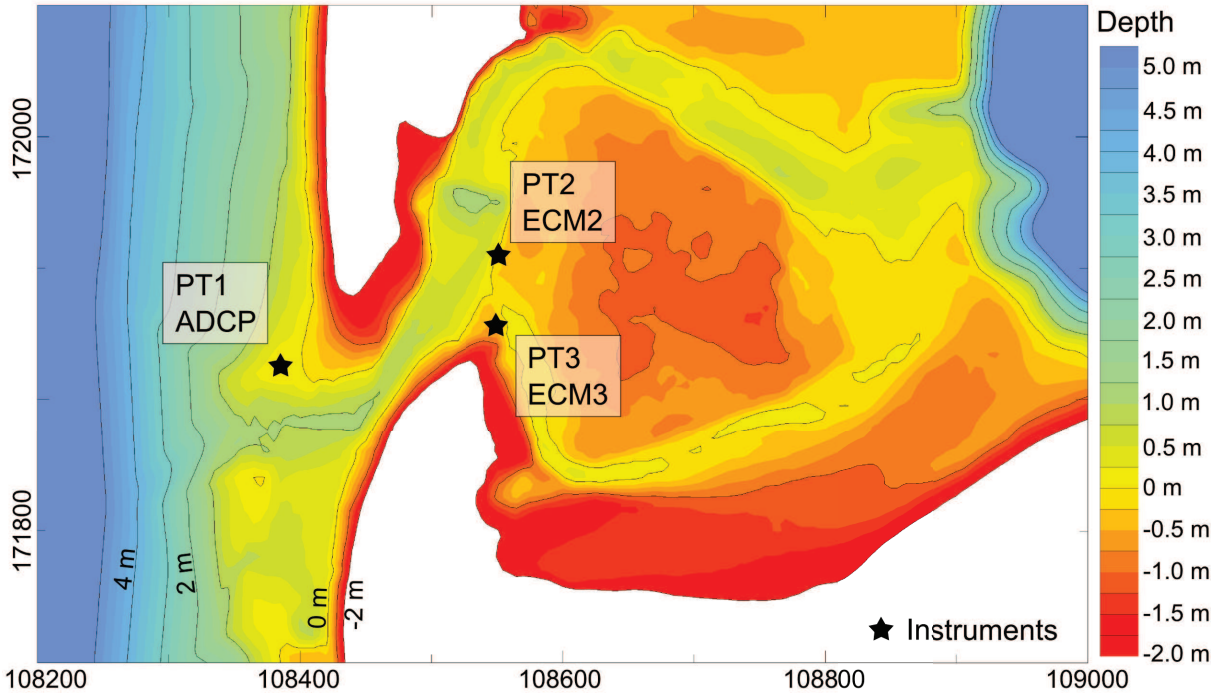

Figure 4.5: Topography (relative to MSL) of the inlet on 23-24 September 2010 and positions of the instruments.

pressure transducer and one current meter, were installed along the main channel: one on the flooding ramp of the flood-delta, the other one on a small sand spit along the main channel bypassed by a secondary channel. Both arrays recorded pressure variations and local currents at a 2 Hz frequency of acquisition. The current profiler was fixed on top of a robust steel stake ending with a large screw, which was buried on the flat part of an ebb-shoal connected to the northern barrier beach. Pressure and current profiles were sampled continuously at 1 Hz. The

Table 4.2: Equipment deployed during the field experiment.

Application	Quantity	Name	Manufacturer
Topography	2	GPS RTK *	Leica
Topography	1	DGPS Hiper pro *	Topcon
Hydrodynamics	1	ADCP Aquadopp Profiler 2MHz *	Nortek AS
Hydrodynamics	1	Integrated pressure sensor	Nortek AS
Hydrodynamics	1	Pressure sensor Level TROLL 500	In-Situ Inc.
Hydrodynamics	2	ECM Infinity-EM *	JFE Advantech Co., Ltd.
Sediments	2	OBS *	Campbell Scientific
Wind	1	Anemometer NRG40	NRG Systems

* GPS RTK = Global Positioning System Real Time Kinematic; DGPS = Differential Global Positioning System ; ADCP = Acoustic Doppler Current Profiler; ECM = Electromagnetic Current Meter; OBS = Optical Backscatter Sensor

sand spit at the intersection of the main channel and the secondary channel, where the current

[1]Time information will always be given in Coordinated Universal Time (UTC) from hereon.

meter ECM3 was installed, accreted by 25 cm during the first tidal cycle and the sensor got buried around 12:30. At 16:30, the sensor was dug out and the vertical bar on which it was mounted was rotated by 180° around the horizontal axle that held the bar, so that it looked upwards (the reference frame of the sensor was thus inverted). During the following low tide, the horizontal axle was shifted up so that the sensors remained over the bottom. Next morning at 04:30, during the second tidal cycle, the battery of ECM3 was flat and was changed at low tide. During the last tide flood, a new accretion event occurred and ECM3 got buried from 15:30 to 18:00. On the evening of September 24 ($\sim$ 21:00), after the collection of hydrodynamic measurement for three tidal cycles, the equipment was recovered.

Table 4.3: Additional information on the instruments.

Instrument type	Identifier	Acquisition rate (Hz)	x / y coordinates in Datum Lisboa (m)	Vertical position relative to MSL (m)
Ppressure transducer	PT1	1	108388.5 / 171825.9	0.16
Current profiler	ADCP	1	108388.5 / 171825.9	0.16
Pressure transducer	PT2	2	108549.5 / 171911.9	0.26
Current meter	ECM2	2	108549.5 / 171911.9	0.26
Pressure transducer	PT3	2	108549.9 / 171854.4	0.38
Current meter	ECM3	2	108549.9 / 171854.4	

The topographic measurements were conducted during the two days of the experiment. On September 23, the northern and southern ebb shoals, the main canal and the south margin of the inlet were surveyed. On September 24, the secondary channels, the flood delta and the north margin of the inlet were surveyed. The topography of the inlet is represented on Fig.4.5.

4.2 Data processing

4.2.1 Water levels

The pressure records were converted into time-series of sea surface elevation, assuming hydrostaticity. First, the atmospheric pressure measured at the Cascais meteorological station was subtracted from the pressure records so that only the pressure of the water column remained in the data. Then, the pressure time-series was shifted so that the minimum pressure corresponds to zero. The pressure time-series was converted into water depth based on the hydrostatic pressure formula:

$$h = \frac{\rho g}{P_0 - P_a} \tag{4.1}$$

where h is the water depth over the head of the pressure transducer, ρ is the water density, g is the gravity acceleration, P_0 is the pressure of the water column measured by the sensor (in Pa) and P_a is the atmospheric pressure (in Pa). Then, the water depth was converted into sea surface elevation by adding the distance between the pressure sensor's head and the *Nível Médio do Mar* (NMM) de Cascais (1938), which is the local reference for mean water level. The periods when the sensor was not fully immersed were selected manually and the corresponding elevations were discarded. Eventually, the high-frequency "noise" associated to the waves was removed by applying a 10-min moving-average to the signal.

Figure 4.6: Photographs of the instruments' deployment: a)Panorama of the Albufeira lagoon as seen from the south margin, b)Anemometer, c)PT2 an ECM2, d) PT3 and ECM3, e) Overview of the inlet as seen from the north margin, f) PT1 and ADCP, g) Ebb shoal where PT1 and ADCP are located. The red letters indicate where the instruments are located.

Additional processing was necessary for the pressure transducer integrated in the ADCP. Indeed, the signal measured by PT1 presented an unexpected linear trend, with the pressure increasing with time for the whole record. The manufacturer confirmed that this artefact was a construction problem already detected for similar products and they replaced the defective product. Yet, no method existed to correct the biased observations. The signal was thus corrected manually: a dry level was computed for each low tide, when the sensor was out of the water, and the pressure measured when the sensor was wet was shifted down by the average value of the two adjacent "dry levels". Besides the undesired trend, a strong pressure increase was recorded by PT1 during the morning low tide of September 24, which has not been explained yet. The raw PT1 pressure time-series is shown in Fig. 4.7 where the linear trend, the levels used in the correction method and the correction offsets are represented schematically. These water level corrections had a negligible impact on the computation of the wave parameters since the correction factor for pressure attenuation with depth was always close to one (see next Section).

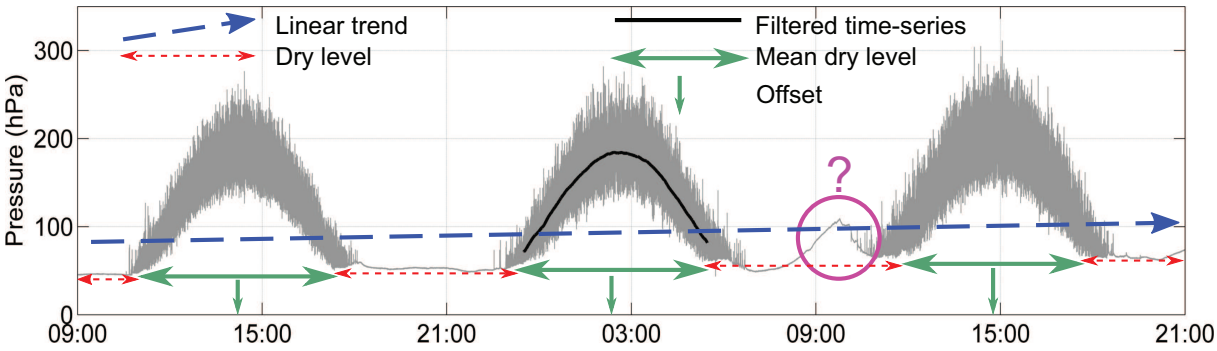

Figure 4.7: Raw pressure time-series measured by PT1 on September 23/24, showing the linear trend (blue arrow) observed in the data and the mean levels used for the correction procedure (dashed red double-arrows and green double-arrows). The black curve represents the 10-min sliding-window averaged time-series. The pink circle shows the unexplained pressure peak.

Finally, the processing of the data recorded by PT3 was carefully adjusted so that the reference level remained constant over the whole experiment duration. The vertical adjustment mentioned in the previous paragraph was taken into account and each tidal cycle was processed separately and referred to the same MSL before being concatenated.

4.2.2 Wave parameters

The mean wave parameters were computed from the time-series of water depths derived from the previously corrected time-series of sea surface elevations. Based on the matlab package *wavesp.m* provided by Dr.Urs Neumeier (ISMER, CA), the wave parameters were computed from spectral analysis and the attenuation of pressure variation with depth was taken into account. The step-by-step procedure is described hereafter:

1. a 10-min burst of water depths is selected and linearly detrended;

2. a Fourier transform is applied to the detrended data burst to compute the spectral energy density E;

3. a correction factor K is computed for each frequency within the range $[fcorr_{min} : fcorr_{max}]$[2], following the formula given in *Tucker and Pitt* [2001]:

$$K(f) = \frac{\cosh(k(f)h)}{\cosh(k(f)z_0)} \tag{4.2}$$

where k is the wavenumber computed for each frequency f from the linear dispersion relation and z_0 is the height of the sensor above the bed. The spectral energy density is then multiplied by K to correct the attenuation of pressure variation with depth;

4. the significant wave height H_{m0} and the mean period T_{m02} are then computed from the n^{th} moment of the energy density spectrum following:

$$H_{m0} = 4\sqrt{m_0} \tag{4.3}$$

$$T_{m02} = \sqrt{\frac{m_0}{m_2}} \tag{4.4}$$

with m_n defined as:

$$m_n = \int_0^{2\pi} \int_{f_{min}}^{f_{max}} f^n E(f,\theta) df d\theta \tag{4.5}$$

where f_{min} and f_{max} are the cut-off frequencies;

5. the peak period Tp is taken as the frequency bin with the highest energy density within the cut-off frequencies f_{min} and f_{max};

6. the steps 1-5 are applied to the next 10-min consecutive burst and so on until the end of the record.

This procedure is illustrated in Fig. 4.8.

Several considerations were necessary to ensure a consistent computation of the energy density spectra and the integral parameters H_{m0} and T_{m02}. First the selection of the low cut-off frequency f_{min} required a particular attention, since the computed spectra contained a significant part of energy density in the infra-gravity band ($\sim$ 0.004 Hz - 0.04 Hz) that did not correspond to gravity wave energy (see Chapter 7). Yet, this cut-off frequency had to be set to a sufficiently low value $f_{min} = 0.36$ Hz to capture most of the low-frequency energy of the very long incident swell described in Section 4.1. The choice of the high cut-off frequency f_{max} was constrained by the instruments' minimum acquisition rate (1 Hz) and its corresponding Nyquist frequency (0.5 Hz) and was thus set to 0.5 Hz. The pressure correction factor was accounted only for frequencies up to $fcorr_{max} = 0.33$ Hz to avoid over-amplifying high frequency variations that do not correspond to surface waves but to noise. The lower bound $fcorr_{min}$ was set equal to f_{min} without extra considerations since the attenuation of low frequency pressure variation is almost null in shallow water.

[2]For lower frequencies, no correction is applied and for larger frequencies, a linear decreasing function is applied.

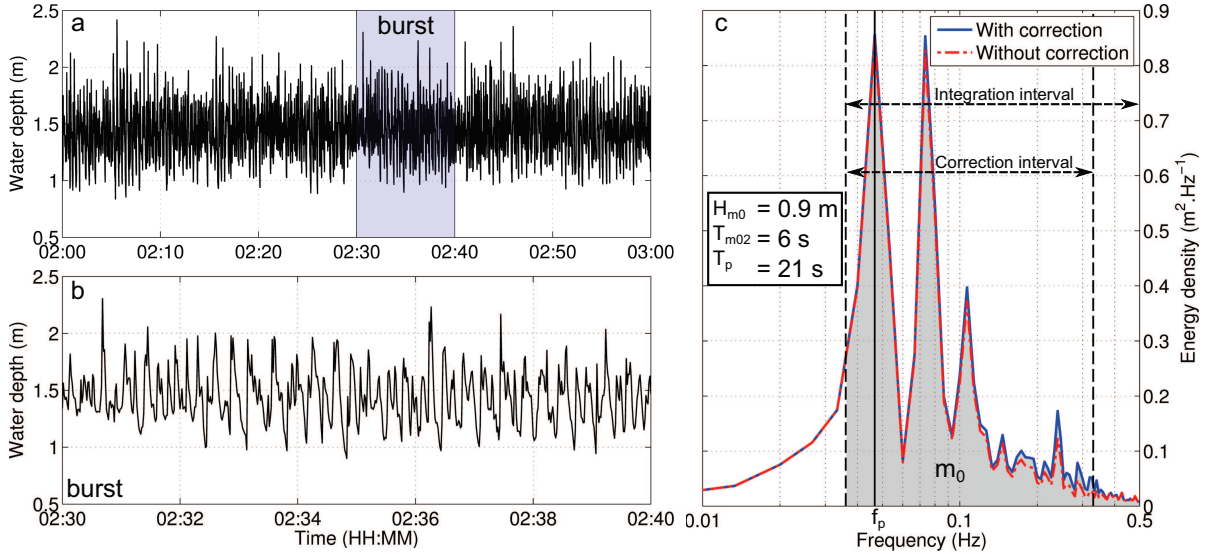

Figure 4.8: The wave processing procedure: a) 10-min burst extraction from the water depth time-series; b) detrended 10-min burst; c) energy density spectrum computed from the 10-min burst after (resp. before) correction for the pressure attenuation with depth (blue curve, resp. red curve), cut-off frequencies for correction and spectral integration (vertical dashed black lines), peak frequency (vertical black line) and mean wave parameters deduced from m_0 (represented by the grey surface area).

4.2.3 Velocities

The processing of the data from the two current meters ECM2 and ECM3 was done in a similar way. First the abnormal velocities measured when the sensor was either off the water, partly submersed or buried were discarded. A 10-min moving-average was then applied to the raw data in order to remove the contribution of the wave orbital velocities and retain only the mean current. The x and y components of the currents were projected in a East-North-Up (ENU) coordinate system by considering the magnetic direction of the instrument measured with a compass during the experiment, corrected by the local magnetic declination. It should be noted that the consecutive accretion events that were responsible of the burying of ECM3 as well as the battery limitations of this sensor made its effective measurements very sparse and these data were hardly usable for analysis and model validation.

Regarding the current profiler, it was situated in the surf zone most of the time, where intense wave breaking occurred and the current measurements were spoiled by the presence of bubbles in the upper layer of the water column. Little confidence was given to this data set. Thus, the procedure used to compute the current profiles from this instrument will not be described.

4.2.4 Topography

The topography of the inlet area was surveyed during the two days of the field work (September 23 and 24), using two Real Time Kinematic GPS and one Differential GPS. The survey covered the inlet principal and secondary channels, the flood-tidal delta and ebb-tidal shoals, and the barrier and the intertidal area of the adjacent beaches.

4.3 Additional sources of data

4.3.1 Bathymetry

Reliable bathymetric data are extremely important if one wants to simulate wave propagation and hydrodynamic circulation in coastal waters with great accuracy. Several data sources were used to generate the bathymetric map used in the modelling system. First, the 2-min global seafloor topography derived from satellite altimetry and ship depth soundings by *Smith and Sandwell* [1997] provided bathymetric information over the North-Atlantic basin. The coastal waters along Portugal have been extensively sounded by the Portuguese Hydrographic Institute and bathymetric charts of the Iberian Peninsula margin with isolines every 10 m were used to softly transition from the seafloor bathymetry with the local bathymetry off the Albufeira Lagoon. Finally, the bathymetry of the beach shore face near the study site was realized in March 2010 with an onboard echo sounder by the Research Centre of Coastal and Marine Environments of the University of Algarve (CIMA/UALg).

4.3.2 Topography

Within the framework of the research project 3D-MOWADI, the topography of the Albufeira Lagoon inlet was surveyed from the artificial opening of the inlet on April 2010 to its closure on December 2010, on a monthly-basis. Ten topographic surveys were realized with RTK-DGPS during the spring low tides of the 8-month period, on: April 24, May 28, June 29, July 27, August 26, September 23, September 28, November 5, November 24 and December 27. The topographic measurement were then processed into ten digital elevation models, as described in *Nahon et al.* [2012b].

4.3.3 Tide gauge data

The Cascais tide gauge has been recording sea-level variations since 1882. This time series is more than 80% complete and thus represents one of the longest tide gauge time series in the world [*Antunes and Taborda*, 2009]. The gauge is located at an open coast (9.415384°W ; 38.693158°N), at a site of low tectonic activity, low-impacted by vertical land movements due to the Glacial isostatic Adjustment [*Peltier*, 2004]. Sea level estimations at this site has been improved in order to meet the standards of international sea level change monitoring such as the Global Sea Level Observing System [GLOSS *Merrifield et al.*, 2010]. Thus, the Portuguese Geographic Institute (IGP) installed in 1997 a permanent GNSS station at the tide gauge site to measure the local vertical displacement. According to the ULR5 GNSS solution [*Santamaría-Gómez et al.*, 2012] provided by the GLOSS GNSS data assembly center SONEL (www.sonel.org), the vertical velocity at Cascais is 0.37 +/- 0.29 mm.yr^{-1} over the 2000-2007 period. This observed stability is proper to passive margins such as the Western Iberia Margin.

4.3.4 Wave data

Two Waveriders (Datawell) located near Sines and Leixões respectively are maintained by the Portuguese Hydrographic Institute. They provide time-series of significant wave height, mean

and maximum periods and mean wave direction derived from zero-crossing analysis of 10-minute observations. In addition, mean wave parameters from a Triaxys buoy located at the entrance of the Tagus estuary and maintained by the Lisbon Harbour were retrieved to extend the offshore wave parameters dataset. The mean wave direction of each wave buoy was corrected to take into account the magnetic declination for the corresponding location and time period. The coordinates of the wave buoys are given in table

Table 4.4: Coordinates and depths of the wave buoys along the west coast of Portugal.

Wave buoy	Latitude (°N)	Longitude (°W)	Depth (m)	Instrument type
Leixões	41.316667	8.983333	83	Wavec (Datawell)
Lisboa	38.623611	9.385833		Triaxys (Axys Technologies Inc.)
Sines	37.921111	8.928889	97	Wavec (Datawell)

4.3.5 Atmospheric reanalysis

Two atmospheric reanalysis products were used to provide the wave models with wind fields:

1. the 6-hour wind fields from the NCEP/NCAR Reanalysis project [*Kalnay et al.*, 1996], available from 1948 to present on a 1.875° (longitude) by 1.905∘ (latitude) Gaussian grid (T62), where longitudes are equally spaced but latitudes are unequally spaced according to Gaussian quadrature;

2. the 3-hour wind fields from the ERA-Interim atmospheric reanalysis [*Dee et al.*, 2011] provided by the European Centre for Medium-Range Weather Forecast (ECMWF) available from 1979 to present on a reduced Gaussian grid (N255) with an approximate resolution of 0.75°.

Summary

A field experiment was conducted at the Albufeira Lagoon inlet on September 23 and 24, 2010. The main objectives of this campaign were: 1) the collection of hydrodynamic data along the main channel of the inlet during three tidal cycles; 2) the characterization of the textural and compositional variability of the sediments in the vicinity of the tidal inlet; and 3) the topographic survey of the tidal inlet system;

During the campaign, the atmospheric pressure was relatively stable with values comprised between 1018 hPa and 1022 hPa and the wind magnitude never exceeded 6 $m.s^{-1}$ while the instruments were recording data. The spring tide tidal range reached 2.55 m, 2.51 m and 2.61 m at the Cascais tide gauge. The wave heights measured at Sines were moderate, with values comprised between 1 m and 1.5 m. The maximum period increased from 15 s to 20 s after the swell generated a week earlier by Hurricane Igor reached Portugal.

Three pressure sensors, two current-meters and one Acoustic Doppler Current Profiler were deployed along the main channel. They measured the sea surface elevation and the current velocities with sampling rates comprised between 1 and 2 Hz. Several methods were applied to process the data measured by the instruments in order to correct some discrepancies inherent to the sensor. A particular care was given to the computation of the mean wave parameters from the elevation time-series. The cut-off frequencies were selected to capture the most of the low-frequency energy of the long-period swell.

Complementary data were retrieved from various sources: bathymetry, atmospheric reanalysis, tide gauge and wave observations. These data were used as initial or boundary conditions for the numerical modelling system, described in Chapter 5 or to validate the model results.

Chapter 5

The numerical modelling system

This dissertation has been carried out in the context of a research project whose main objectives were the development of a morphodynamic modelling system and its application to two tidal inlets in Portugal, the overall goal being a better understanding of the physical processes that govern the dynamics of wave-dominated tidal inlets. The modelling platform has been in continuous development over the last six years in an international and collaborative framework, involving researchers from the Oregon Health & Science University, the Virginia Institute of Marine Science, the Portuguese National Civil Engineering Laboratory, the Technical University of Darmstadt and the UMR7266 - LIENSs of La Rochelle. During the last three years, considerable efforts have been dedicated to the coupling between the wave and circulation models and the development of a morphodynamic module compatible with the 2DH version of the wave-current modelling system. These tasks rapidly appeared as important requirements for the success of the research project and the implementation of the spectral boundary forcing in the wave model and the development of the sediment transport and bottom update modules became integral parts of this dissertation. This chapter gives a general presentation of the numerical platform and a detailed description of the different models that compose it.

5.1 Overview

The modelling system that is being developed aims to simulate the hydrodynamics and non-cohesive sediment dynamics in estuaries and coastal zones under the combined effect of tides and waves. This modelling system couples a set of modules to simulate the hydrodynamic circulation, wave propagation, sediment transport and bottom evolution. An overview of the modelling system is represented in Fig. 5.1. The core model of the system is the Semi Eulerian-Lagrangian Finite Element hydrodynamic model [SELFE, *Zhang and Baptista*, 2008a]. This unstructured-grid model is computationally very efficient, thanks to the Eulerian-Lagrangian Method (ELM) to treat the advection in the momentum equations and the parallelization through Message Passing Interface (MPI). The ELM method and the semi-implicit schemes relax the numerical stability constraints of the model (*e.g.,*CFL) and allow the use of larger time step than allowed by explicit methods. This key advantage motivated the choice for this model as the core of the morphodynamic platform instead of other existent morphodynamic modelling systems. Hence, SELFE provides an ideal framework for modelling coastal processes along complex coastlines typical of estuaries and coastal inlets. A description of SELFE is given in Section 5.2.

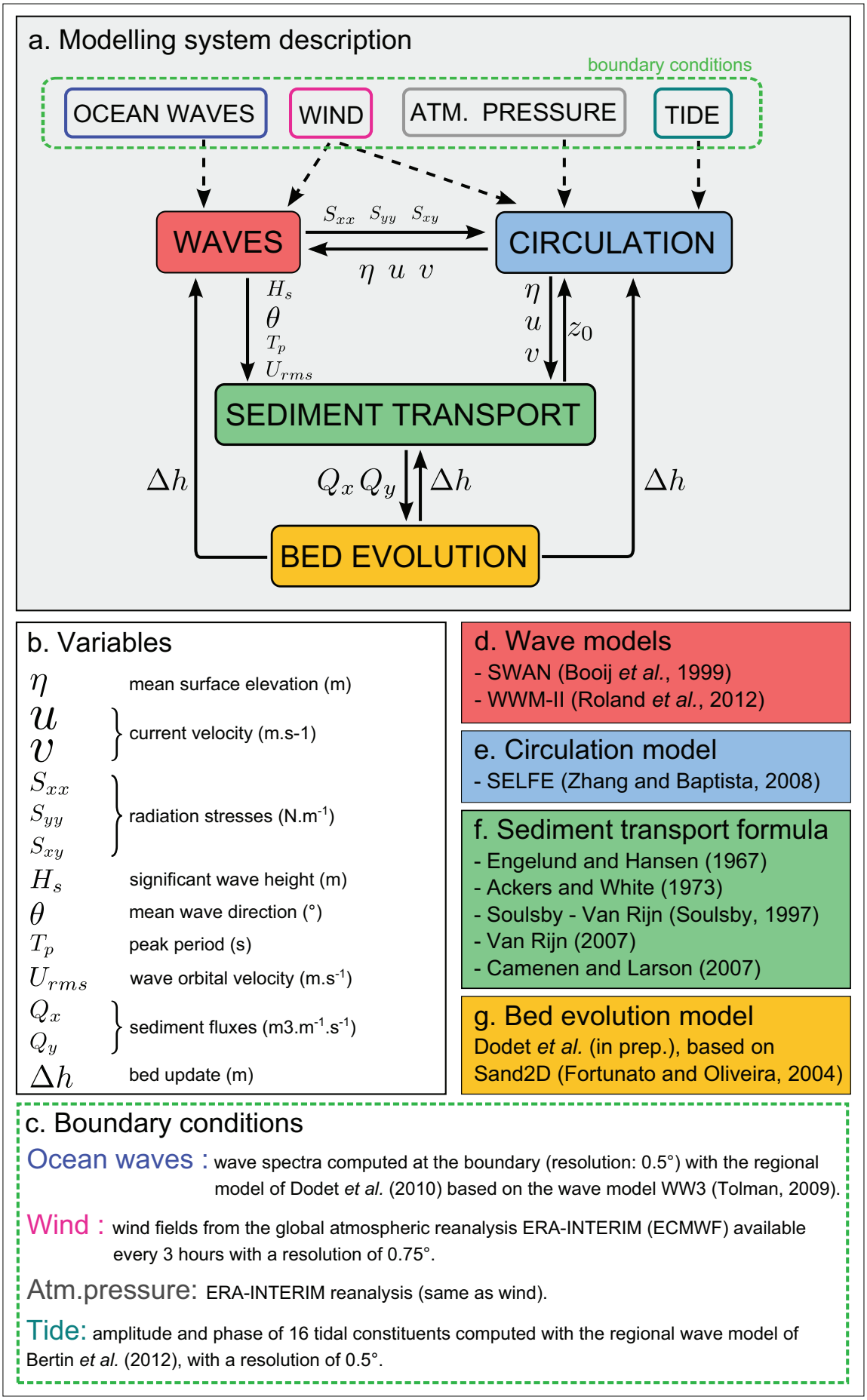

Figure 5.1: The numerical modelling system: schematic description (a), exchanged variables (b), boundary conditions (c), model details (d, e, f, g).

The wave module plays a key role in the modelling system. The impact of the waves on the dynamics is indeed preponderant in wave-dominated environments such as ephemeral tidal inlets and accurate wave model results are necessary to reproduce the hydrodynamic circulation, subsequent sediment transport and morphological changes of these systems. In addition, the small scales (in time, geographical space and spectral space) that need to be resolved to simulate the evolution of the wave field in shallow water amplify the numerical constraints. Therefore, without efficient numerical methods, most computational time is dedicated to wave modelling. The wave modelling strategy and the different existing wave models that are involved in the modelling system are described in Section 5.3.

Sediment transport rates are calculated with classical semi-empirical formulations based on the depth-averaged velocity, the water depth, the bottom roughness, the sediment properties and in some cases the wave field properties. The various sediment transport formulae implemented in the modelling system are described in Section 5.4.

Finally, the bottom evolution that results from the divergence of the sediment fluxes is computed within the bed update module by solving the Exner equation. The inherent instability of a morphodynamic model due to the non-linear coupling between the bed update module and the other modules requires adequate numerical methods and several filters to prevent the development of instabilities. The numerical method and the filters implemented are described in Section 5.5.

5.2 The hydrodynamic model

Since the original paper by *Zhang and Baptista* [2008a], SELFE has evolved into a comprehensive modelling system that can be configured in many different ways; e.g., hydrostatic or non-hydrostatic modes; 3D bottom deformation as occurred during a seismically or landslide generated tsunamis; in 2D or 3D configuration; in Cartesian or spherical coordinates; with several tracer transport modules (sediment, oil, ecology etc.). In its default configuration, however, SELFE solves the free surface elevation η and the 3D velocities (u, v, w) based on the shallow water equations. In a barotropic configuration, the governing equations in Cartesian coordinates are:

$$\nabla \cdot \boldsymbol{u} + \frac{\partial w}{\partial z} = 0 \tag{5.1}$$

$$\frac{\partial \eta}{\partial t} + \nabla \cdot \int_{-d}^{\eta} \boldsymbol{u} dz = 0 \tag{5.2}$$

$$\frac{D\boldsymbol{u}}{Dt} = -g\nabla\eta + \frac{\partial}{\partial z}\left(\nu \frac{\partial \boldsymbol{u}}{\partial z}\right) + \boldsymbol{f} \tag{5.3}$$

where D denotes the material derivative, d is the bathymetric depth, $\boldsymbol{u} = (u, v)$ is the horizontal velocity and w the vertical velocity, ν is the vertical eddy viscosity, $\nabla = (\partial/\partial x, \partial/\partial y)$ is the horizontal gradient operator, (x,y) are the Cartesian coordinates, z is the vertical coordinate

positive upward, t is the time, and $\boldsymbol{f}$ combines the explicit terms:

$$\boldsymbol{f} = \nabla \cdot (\mu \nabla \boldsymbol{u}) - f\boldsymbol{k} \times \boldsymbol{u} - \frac{1}{\rho_0}\nabla p_A + \boldsymbol{R_s} \tag{5.4}$$

where μ is the horizontal eddy viscosity, f is the Coriolis factor, $\boldsymbol{k}$ is a unit vector of the z-axis, ρ_0 is a reference water density, p_A is the atmospheric pressure, and $\boldsymbol{R_s}$ is the wave-induced radiation stress term.

SELFE runs on unstructured horizontal grids with hybrid vertical coordinates: partly terrain-following S coordinates and partly Z coordinates (Fig. 5.2a). In 3D a basic computational unit is a triangular prism with uneven top and bottom surfaces, while in depth-averaged mode (2DH) only one vertical layer is considered and the computational unit is a triangular element. The elevation is computed at the vertices, the horizontal components of the velocity are computed at the sides, and the vertical velocity (in 3D) is computed at the element centre (Fig. 5.2b).

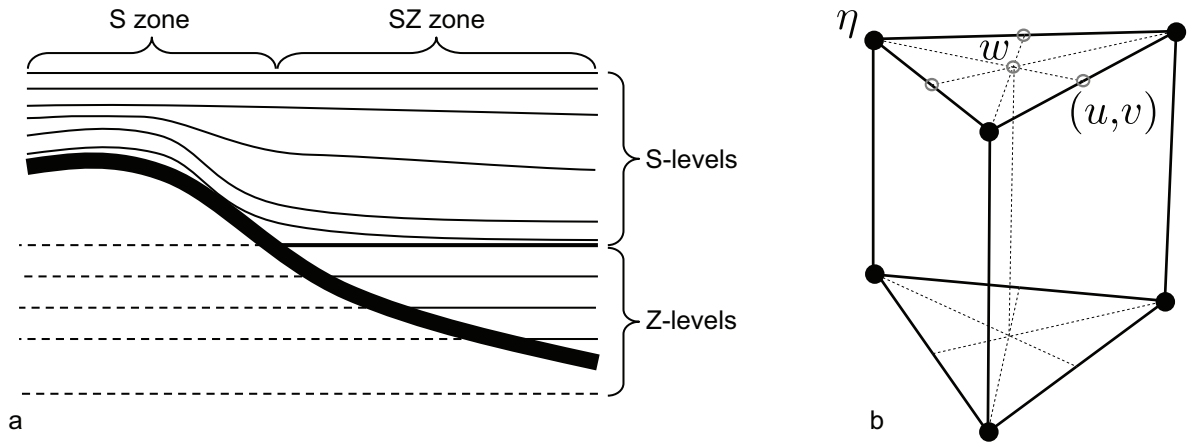

Figure 5.2: Schematic description of the vertical hybrid S-Z coordinates used in SELFE (a) and location on computational unit of the computed elevations and velocities (b). Adapted from Zhang and Baptista [2008a].

SELFE uses the bottom boundary condition to decouple the continuity equation 5.2 (in its depth-averaged form) from the momentum equation 5.3. At the bottom, SELFE enforces the balance between the internal Reynolds stress and the applied bottom frictional stress as follows:

$$\nu \frac{\partial \boldsymbol{u}}{\partial z} = \boldsymbol{\tau}_b \text{ at } z = -d \tag{5.5}$$

The bottom stress is computed with a quadratic law:

$$\boldsymbol{\tau}_b = C_D |\boldsymbol{u}_b| \boldsymbol{u}_b \tag{5.6}$$

where $\boldsymbol{u}_b$ is the velocity at the top of the bottom computational cell and C_D is the drag coefficient computed as:

$$C_D = \left(\frac{\kappa}{\log(z_b/z_0)} \right)^2 \tag{5.7}$$

where $\kappa = 0.4$ is the von Karman's constant and z_b is the height from the bottom to the top of the bottom computational cell. The bottom roughness z_0 depends on the sediment grain size

and the dimensions of bedforms when the bed is not flat. Although z_0 can be estimated locally from current measurements, a map of the roughness distribution over the whole model domain is rarely available and z_0 is often used as a tuning parameter to calibrate the model. An alternative method is to use a bedform predictor that computes bedforms' dimensions from the simulated hydrodynamic conditions based on semi-empirical formulae. In shallow waters, the presence of waves significantly affects the bottom stress in the wave bottom boundary layer and an apparent bottom roughness z_{0app} can be used to represent the enhanced bottom stress by replacing z_0 with z_{0app} in Eq. 5.7. In the theory of *Grant and Madsen* [1979], implemented in SELFE by *Roland et al.* [2012], the maximum wave bottom stress is defined as:

$$\tau_w = 0.5\rho_0 f_w U_w^2 \tag{5.8}$$

where U_w is the wave orbital velocity amplitude:

$$U_w^2 = 2\int_0^{\infty}\int_0^{2\pi} \frac{N\sigma^3}{\sinh^2(kh)} d\theta d\sigma \tag{5.9}$$

where N is the wave action, σ is the intrinsic frequency and θ is the wave direction. The combined wave-current friction factor f_w is a function of both the current and waves [*Zhang et al.*, 2004]:

$$\begin{cases} \gamma = \frac{|\boldsymbol{\tau}_b|}{\tau_w} \\ C_\gamma = (1 + 2\gamma|\cos\theta_w| + \gamma^2)^{1/2} \\ f_w = C_\gamma \exp\left[5.61\left(\frac{C_\gamma U_w}{30 z_0 \omega}\right)^{-0.109} - 7.3\right] \end{cases} \tag{5.10}$$

where ω is the absolute wave frequency. Eqs. 5.8 and 5.10 are solved iteratively for (γ,C_γ,τ_w) by first assuming $\gamma = 0$, $C_\gamma = 1$. After these quantities are found, the apparent roughness is given by:

$$z_{0app} = \delta_{wc}\left(\frac{\delta_{wc}}{z_0}\right)^{-\sqrt{|\boldsymbol{\tau}_b|/(C_\gamma \tau_w)}} \tag{5.11}$$

where the wave boundary layer thickness is given by:

$$\delta_{wc} = \frac{\sqrt{\frac{C_\gamma \tau_w}{\rho_0}}}{\omega} \exp\left[2.96\left(\frac{C_\gamma U_w}{30 z_0 \omega}\right)^{-0.071} - 1.45\right] \tag{5.12}$$

At the sea surface, SELFE enforces the balance between the internal Reynolds stress and the applied wind shear stress as follows:

$$\nu\frac{\partial \boldsymbol{u}}{\partial z} = \tau_b \text{ at } z = -d \tag{5.13}$$

where the wind stress τ_w is parametrized using the approach of *Pond and Pickard* [1983] or with a wave-dependent formula as described in *Bertin et al.* [2012b]. The vertical eddy viscosities are solved with the Generic Length Scale (GLS) turbulence closure model of *Umlauf and Burchard* [2003].

In 2DH (depth-averaged mode), the coupling is readily done using the assumption that the velocity profile is uniform and only one vertical layer is necessary. Eq. 5.3 becomes:

$$\frac{D\boldsymbol{u}}{Dt} = -g\nabla\eta + \frac{\partial}{\partial z}\left(\nu\frac{\partial \boldsymbol{u}}{\partial z}\right) + \nabla\cdot(\mu\nabla\boldsymbol{u}) - f\boldsymbol{k}\times\boldsymbol{u} - \frac{1}{\rho_0}\nabla p_A + \boldsymbol{R_s} + \frac{\boldsymbol{\tau}_w - \boldsymbol{\tau}_b}{\rho_0 h} \tag{5.14}$$

where h is the total water depth ($h = \eta + d$) and the quadratic law used to compute τ_b uses the depth-averaged velocity $\boldsymbol{u}$, while the drag coefficient C_D is computed from a Manning formulation. The wave-induced radiation stress term $\boldsymbol{R_s}(R_{sx}, R_{sy})$ is computed with the formulation of *Longuet-Higgins and Stewart* [1964] [1]:

$$R_{sx} = -\frac{1}{\rho_0 h}\left(\frac{\partial S_{xx}}{\partial x} + \frac{\partial S_{xy}}{\partial y}\right) \tag{5.15}$$

$$R_{sy} = -\frac{1}{\rho_0 h}\left(\frac{\partial S_{xy}}{\partial x} + \frac{\partial S_{yy}}{\partial y}\right) \tag{5.16}$$

where S_{xx}, S_{xy} and S_{xy} are the components of the radiation stress tensor, defined for an irregular wave spectrum according to *Battjes* [1974] as:

$$S_{xx} = \int_0^\infty \int_0^{2\pi} N(\sigma,\theta)\sigma\left[\frac{c_g(\sigma)}{c_p(\sigma)}(\cos^2\theta + 1) - \frac{1}{2}\right] d\theta d\sigma \tag{5.17}$$

$$S_{yy} = \int_0^\infty \int_0^{2\pi} N(\sigma,\theta)\sigma\left[\frac{c_g(\sigma)}{c_p(\sigma)}(\sin^2\theta + 1) - \frac{1}{2}\right] d\theta d\sigma \tag{5.18}$$

$$S_{xy} = \int_0^\infty \int_0^{2\pi} N(\sigma,\theta)\sigma\frac{c_g(\sigma)}{c_p(\sigma)}\sin\theta\cos\theta d\theta d\sigma \tag{5.19}$$

where c_g is the wave group velocity and c_p is the wave phase velocity.

SELFE solves Eqs. 5.2 and 5.3 simultaneously using a semi-implicit scheme, with an Eulerian-Lagrangian Method (ELM) for the advection in Eq. 5.3. A continuous Galerkin finite-element scheme is applied to Eqs. 5.2 and 5.3 resulting in a positive-definite, symmetric and sparse matrix that can be solved with an efficient iterative solver like the Jacobian Conjugate Gradient Method [*Zhang and Baptista*, 2008b]. Due to the hydrostatic assumption used in the shallow-water equations, w is solved from Eq. 5.1 with a finite-volume method after Eqs. 5.2 and 5.3 are solved. Other details can be found in *Zhang and Baptista* [2008a] and *Zhang et al.* [2011].

5.3 The wave models

With the purpose to investigate the dynamics of environments subjected to very energetic wave climate, a particular care was given to the choice and implementation of the wave module as well as the generation of the offshore wave boundary conditions. In this regard, a regional application to the North-East Atlantic Ocean of the wave model WAVEWATCH III [WW3,

[1] Other formulations with depth-dependant radiations stresses are available in 3D mode [eg. *Bennis et al.*, 2011; *Mellor*, 2013].

Tolman, 2009] was first implemented in order to generate spectral boundary conditions at desired spectral and spatial resolutions. This regional model is described by *Dodet et al.* [2010] and further validated by *Bertin and Dodet* [2010]. Then, a wave-current coupling was realized between SELFE and the Simulating WAves Nearshore wave model [SWAN, *Booij et al.*, 1999] in its structured version (Version 40.81). This preliminary release of the modelling system [*Bruneau et al.*, 2011a] was used to investigate the complex wave-current interactions at the Albufeira inlet system, described in Chapter 7 and by *Dodet et al.* [2013]. Meanwhile, *Roland et al.* [2012] integrated the Wind Wave Model II (WWM-II) into SELFE and eventually WWM-II replaced the SWAN model in the modelling system. Indeed SWAN revealed some limitations when simulating wave breaking on very steep slopes (as the ones that occurred at the Albufeira lagoon) and a fully coupled wave-current model using the same unstructured grid appeared as an important step forward. The three spectral wave models WW3, SWAN and WWM-II solve the wave action equation, which is described in the following paragraph. A description of the source terms and the numerical approaches is then given, with a particular attention to the difference between the three models and the recent improvements that they benefited from.

5.3.1 The wave action equation

The wave action equation can be written as follows [eg. *Komen et al.*, 1994]:

$$\frac{\partial}{\partial t}N + \nabla(\dot{\boldsymbol{X}}\ N) + \frac{\partial}{\partial \sigma}(\dot{\theta}\ N) + \frac{\partial}{\partial \theta}(\dot{\sigma}\ N) = S_{tot} \tag{5.20}$$

where the wave action, which is invariant in slowly varying media [*Bretherton and Garrett*, 1967], is defined as:

$$N(t, \boldsymbol{X}, \sigma, \theta) = \frac{E(t, \boldsymbol{X}, \sigma, \theta)}{\sigma} \tag{5.21}$$

where E is the variance density of the sea level elevations. The advection velocities in the different spaces are obtained following the geometrical optics approximation [eg. *Keller*, 1958]:

$$\dot{\boldsymbol{X}} = \boldsymbol{c_X} = \frac{d\boldsymbol{X}}{dt} = \frac{d\omega}{dk} = \boldsymbol{c_g} + \boldsymbol{U}_{A(\boldsymbol{k})} \tag{5.22}$$

$$\dot{\theta} = c_\theta = \frac{1}{k}\frac{\partial \sigma}{\partial h}\frac{\partial h}{\partial m} + \boldsymbol{k} \cdot \frac{\partial \boldsymbol{U}_{A(\boldsymbol{k})}}{\partial s} \tag{5.23}$$

$$\dot{\sigma} = c_\sigma = \frac{\partial \sigma}{\partial h}\left(\frac{\partial h}{\partial t} + \boldsymbol{U}_A \cdot \nabla_{\boldsymbol{X}} h\right) - c_g \boldsymbol{k}\frac{\partial \boldsymbol{U}_{A(\boldsymbol{k})}}{\partial s} \tag{5.24}$$

Here s represents the coordinate along the wave propagation direction and m is perpendicular to it. $\boldsymbol{X}$ is the Cartesian coordinate vector (x,y) in the geographical space, and $\boldsymbol{k}$ is the wave number vector (with $k = |\boldsymbol{k}|$). The effective advection velocity $\boldsymbol{U}_A$ depends in general on the wave number vector of each wave component [*Andrews and McIntyre*, 1978], but in the present formulation this is approximated by the depth-averaged current. Since scales of variation of depths and currents are assumed to be much larger than those of an individual wave, the quasi-uniform (linear) wave theory can be applied locally, giving the following dispersion relation and Doppler type equation to interrelate the phase parameters:

$$\sigma^2 = gk \tanh kh \tag{5.25}$$

$$\omega = \sigma + \boldsymbol{k}\boldsymbol{U_A} \tag{5.26}$$

S_{tot} is the sum of the source terms including the non-linear interactions in deep and shallow water (S_{nl4} and S_{nl3}, respectively), the energy input due to wind (S_{in}), the energy dissipation in deep and shallow water due to whitecapping and wave breaking (S_{ds} and S_{br}, respectively) and the energy dissipation due to bottom friction (S_{bf}). S_{tot} is defined as follows:

$$\frac{DN}{Dt} = S_{tot} = S_{nl4} + S_{nl3} + S_{in} + S_{ds} + S_{br} + S_{bf} \tag{5.27}$$

5.3.2 Non-linear interactions S_{nl4} and S_{nl3}

The treatment of the non-linear interactions in third generation wave models corresponds to the major improvement compared to the first and second generations of wave models. In deep and intermediate water depths resonant weakly non-linear interactions between sets of four waves play an important role in the evolution of the energy spectrum. *Hasselmann* [1962] found that a set of four waves, called a quadruplet, could exchange energy when the following resonance conditions were satisfied:

$$\begin{cases} \boldsymbol{k_1} + \boldsymbol{k_2} = \boldsymbol{k_3} + \boldsymbol{k_4} \\ \omega_1 + \omega_2 = \omega_3 + \omega_4 \end{cases} \tag{5.28}$$

The basic equation describing these interactions is known as the Boltzmann integral, which can be solved using exact methods such as the Webb-Resio-Tracy method [WRT, *Webb*, 1978; *Tracy and Resio*, 1982]. Although these methods solve the Boltzmann integral with great accuracy, they are computationally very demanding and cannot be used in operational applications. To overcome this hurdle, various approximations have been developed, of which the Discrete Interactions Approximations [DIA, *Hasselmann et al.*, 1985] is most commonly used. The DIA suffers from many shortcomings, yet it preserves a few but important characteristics of the full solution, such as the slow down-shifting of the peak frequency and shape stabilization during wave growth. This method is much faster than the WRT method and was selected for the three wave models.

The lower order triad interactions are non-resonant in deep and intermediate water depths, forcing second-order bound components that can be important locally but do not contribute to the wave evolution over large distances. However, as ocean surface waves propagate from deep to shallow water, triad interactions approach resonance and assume a significant role in the wave energy balance. This transition from quadruplet to triad interactions is the result of the change in the dispersion relation from a dispersive deep water regime that does not support resonant triad interactions [*Phillips*, 1960] to a non-dispersive shallow water regime where all wave components travel with the same speed. In general triad interactions transfer energy from the incident wave components to higher- (e.g., harmonic) and lower- (e.g., infra-gravity) frequency components. SWAN and WWM-II use the Lumped Triad Approximation (LTA) of *Eldeberky et al.* [1996] to compute S_{nl3}, while the actual release (V3.14) of WW3 does not include triad interactions.

5.3.3 Wave growth S_{in}

The source term S_{in} is composed of a linear growth term and an exponential growth term. The linear term, which allows for the consistent spin-up of the model from quiescent conditions

and improves initial wave growth behaviour, is included in the three wave models following the theory of *Cavaleri and Rizzoli* [1981], with a filter to eliminate wave growth at low-frequency as introduced by *Tolman* [1992]. Regarding the exponential growth, the widely used WAM-Cycle4 parametrization [*Günther et al.*, 1992] is available in WW3, SWAN and WWM-II. It is based on the wave growth theory of *Miles* [1957], modified by *Janssen* [1982]. The pressure slope correlations that give rise to part of the wave generation are parametrized following *Janssen* [1991].

In addition, several improvements are included in WW3 and WWM-II: first, the WAM-Cycle4 parametrization was further extended by *Bidlot* [2007] to take air density into account and increased wind gustiness in unstable atmospheric conditions. *Ardhuin et al.* [2010] also included a sink term to S_{in} to reproduce swell decay observations [*Ardhuin et al.*, 2009] due to shear stresses variations in phase with the orbital velocity. The resulting wave growth term S_{in}^{*} is expressed as $S_{in}^{*} = S_{in} + S_{out}$ and S_{out} is related to a laminar-to-turbulent transition of the oscillatory boundary layers over swell through the boundary Reynolds number defined as $Re = 4u_{orb}a_{orb}/\nu_a$, where u_{orb} and a_{orb} are the significant surface orbital velocity and displacement amplitudes, and ν_a the air viscosity. S_{out} is defined as:

$$S_{out}(k,\theta) = \begin{cases} -C_{dsv}\frac{\rho_a}{\rho_w}\left(2k\sqrt{2\nu\sigma}\right)F(k,\theta) & for Re < Re_c \\ -\frac{\rho_a}{\rho_w}\left(16 f_e \sigma^2 u_{orb}/g\right)F(k,\theta) & for Re \geq Re_c \end{cases} \tag{5.29}$$

where F is the variance density spectrum defined as a function of k and θ and that can be inferred from $E(\sigma,\theta)$ using straightforward Jacobian transformation. Re_c is a threshold value set to $2 \cdot 10^5$ and $C_{dsv} = 1.2$.

5.3.4 Wave dissipation S_{ds}, S_{br} and S_{bf}

Spectral wave energy dissipation represents the least understood part of the physics relevant to wave modelling. There is a general consensus that the major part of this dissipation is due to the wave breaking, but physics of this breaking process, particularly for the spectral waves, is poorly understood. In deep water, the dissipation of spectral energy S_{ds} is mainly attributed to the whitecapping dissipation process. This process has been represented by the pulse-based model of *Hasselman et al.* [1973] where S_{ds} depends on the mean spectral steepness. However, this model was shown to underestimate the dissipation of the spectral tail in the presence of swell, due to its dependence on the mean spectral wavenumber and steepness [*van Vledder and Hurdle*, 2002]. In addition *Ardhuin et al.* [2010] demonstrated that an increase in swell steepness would result in a decrease in swell dissipation, while the opposite effect is expected. To counteract these limitations, *van der Westhuysen et al.* [2007] implemented in SWAN an adapted form of the saturation-based model of *Alves and Banner* [2003]. The local treatment of whitecapping dissipation in the frequency space improved the model results in fetch and depth-limited conditions, yet the steepness-induced breaking dissipation was still underestimated in the presence of strong counter currents [*Ris and Holthuijsen*, 1996]. To overcome this limitation, *van der Westhuysen* [2012] used an enhanced-dissipation term with an additional term in S_{ds} proportional to the current gradient in the wave propagation direction, defined as:

$$S_{ds,curr}(\sigma,\theta) = -C_{ds} max\left(\frac{c_\sigma(\sigma,\theta)}{\sigma}, 0\right)\left(\frac{B(k)}{B_r}\right)^{\frac{p}{2}} E(\sigma,\theta) \tag{5.30}$$

where $B(k)$ represents the spectral saturation, p is a function of the inverse wave age, based on scaling arguments involving a spectral balance between the wind input, whitecapping and nonlinear interaction terms [see *van der Westhuysen et al.*, 2007, for details], and B_r is a threshold saturation level, as in *Alves and Banner* [2003], and C_{ds} is a calibration parameter. Although this parametrization improved model results in several cases [*van der Westhuysen*, 2012; *Dodet et al.*, 2013], the underlying physics is still questionable, particularly in blocking conditions. In WW3, the whitecapping dissipation term S_{ds} combines the parametrization of *Bidlot* [2007] with an additional saturation term. The effect of wave-turbulence interactions is also included in this source term following the expression of *Teixeira and Belcher* [2002]. The calibration settings used in the North-Atlantic regional model were provided by Dr. Fabrice Ardhuin and corresponded to TEST405 as described in *Ardhuin et al.* [2010].

To model the energy dissipation due to depth-induced breaking, the bore-based model of *Battjes and Janssen* [1978] is used in the three wave models. This model is based on the assumption that all waves in a random field exceeding a threshold height, defined as a function of bottom topography parameters, will break. For a random wave field, the fraction of waves satisfying this criterion is determined by a statistical description of surf-zone wave heights (a Rayleigh-type distribution, truncated at a depth-dependent wave-height maximum is generally used). The bulk rate δ of spectral energy density dissipation of the fraction of breaking waves is estimated using an analogy with dissipation in turbulent bores as:

$$\delta = 0.25 Q_b f_m H_{max}^2 \tag{5.31}$$

where Q_b is the fraction of breaking waves in the random field, f_m is the mean frequency and H_{max} is the maximum individual height that a component in the random wave field can reach without breaking (conversely, above which all waves would break). In the model of *Battjes and Janssen* [1978] the maximum wave height H_{max} is defined using a Miche-type criterion [*Miche*, 1944],

$$\overline{k} H_{max} = \gamma_M \tanh(\overline{k} h) \tag{5.32}$$

where γ_M is a constant factor. This approach also removes energy in deepwater waves exceeding a limiting steepness and can potentially result in double counting of dissipation in deep-water waves. Alternatively, H_{max} can be defined using a McCowan-type criterion, which consists of a simple constant ratio:

$$H_{max} = \gamma h \tag{5.33}$$

where γ is a constant derived from field and laboratory observations of breaking waves (default value is 0.73). This approach represents exclusively depth-induced breaking and is the default option in the three models. The fraction of breaking waves Q_b is determined in terms of a Rayleigh-type distribution truncated at H_{max} (i.e., all broken waves have a height equal to H_{max}), which results in the following expression:

$$\frac{1 - Q_b}{-\ln Q_b} = \left(\frac{H_{rms}}{H_{max}} \right) \tag{5.34}$$

where H_{rms} is the root-mean-square wave height. With the assumption that the total spectral energy dissipation δ is distributed over the entire spectrum so that it does not change the

spectral shape [*Eldeberky and Battjes*, 1996] the following depth-induced breaking dissipation source function is obtained:

$$S_{br}(k,\theta) = -\alpha \frac{\delta}{E_{tot}} F(k,\theta) = -0.25 \alpha Q_b f_m \frac{H_{max}^2}{E_{tot}} F(k,\theta) \tag{5.35}$$

where E_{tot} is the total energy (computed as the zero moment of the variance density spectrum, see Eq. 4.5) and $\alpha = 1.0$ is a tunable parameter.

Eventually, the interactions of the wave orbital motion with the sea floor in shallow water will dissipate spectral energy through bottom friction. In the three wave models, the default parametrization of the dissipation term S_{bf} is based on the empirical, linear JONSWAP parametrization [*Hasselman et al.*, 1973], that can be expressed in the following form:

$$S_{bf} = -C_b \frac{\sigma^2}{g^2 \sinh^2 kh} E(\sigma,\theta) \tag{5.36}$$

where the empirical coefficient C_b is suggested to be $C_b = 0.038$ m^{2}s^{-3} for swell [*Hasselman et al.*, 1973] and $C_b = 0.067$ m^{2}s^{-3} for wind sea [*Bouws and Komen*, 1983]. Alternatively, in SWAN and WWM-II, the coefficient C_b can be computed as a function of the bottom roughness height and the actual wave conditions, following the formulation of *Madsen et al.* [2011]:

$$C_b = f_w \frac{g}{\sqrt{2}} U_{rms} \tag{5.37}$$

where U_{rms} is the wave bottom orbital motion:

$$U_{rms}^2 = 2 \int_0^{\infty} \int_0^{2\pi} \frac{\sigma^2}{g^2 \sinh^2 kh} E d\theta d\sigma \tag{5.38}$$

and f_w is a non-dimensional friction factor estimated as:

$$\frac{1}{4\sqrt{f_w}} + \log -10 \left(\frac{1}{4\sqrt{f_w}} \right) = m_f + \log_{10} \left(\frac{U_w}{K_n} \right) \tag{5.39}$$

in which $m_f = -0.08$, U_w is the wave orbital velocity amplitude (Eq. 5.9) and K_n is the bottom roughness length scale.

5.3.5 Numerical approaches

The different numerical approaches implemented in the three wave models discussed herein emerged from the original applications of these models (basin-scale, nearshore or multi-scale). Although, WW3, SWAN and WWM-II share the same discretization of the spectral grid with equally-spaced directional bins and logarithmically-spaced frequency bins, they present important difference in their other numerical aspects.

WW3 is particularly adequate for hindcasting and forecasting wave conditions at ocean scales. It solves the wave action equation on structured grids based on the Fraction Step Method (FSM): an Operator Splitting Method developed by *Yanenko* [1971]. The propagation part of the wave

action equation is split in four one-dimensional parts which are solved with the third-order Ultimate Quickest (UQ) scheme of *Leonard* [1991]. The UQ-scheme solves very accurately the advection problem with very little numerical diffusion and is computationally effective in comparison to other schemes [*Roland*, 2009]. Afterwards the source terms are integrated with an adaptive time integration method using a semi-implicit integration scheme. Other important features such as the treatment of unresolved islands [*Chawla and Tolman*, 2008] or the multi-grid nesting strategy [*Tolman*, 2008] have been implemented in the last decade. Thanks to these improvements and the inclusion of the accurate source terms formulations of *Ardhuin et al.* [2010], WW3 represents one of the most effective approach for deep-water wave modelling.

SWAN runs on structured (regular or curvi-linear) grids and treats the propagation part fully implicitly with an upwind Euler method [*Booij et al.*, 1999]. Two finite-difference schemes are implemented for solving the geographical advection part in the wave action equation: the Backward Time and Backward Space (BSBT), a first-order scheme and the higher-order SORDUP scheme [*Rogers et al.*, 2002]. The discretization of the spectral space is based on an hybrid central-upwind scheme, in which the degree to which the scheme is upwind or central can be controlled by adjusting some coefficients. The fully implicit treatment of the advection part and the semi-implicit integration of the source terms within the advection part lead to a robust scheme that converges to a unique solution, independently of the chosen integration time step. Although this unconditional stability is a major advantage of SWAN, the inflexibility of the structured mesh makes the model applications cumbersome in complicated coastal environments [*Roland*, 2009].

WWM-II runs on unstructured (triangular) meshes and solves the wave action equation using the FSM method described by *Yanenko* [1971], similarly to WW3. The geographical part is solved using a Residual Distribution Scheme (e.g., *Abgrall* [2006]), which borrows ideas from the Finite Element (FE) and the Finite Volume framework [*Roland et al.*, 2012]. Then the spectral advection is treated with the UQ scheme following the WW3 approach. Finally the source terms are integrated in three separate fractional steps according to their time scales or nonlinearity, using a TVD Runge-Kutta third-order scheme for the wave breaking and the bottom friction, a dynamic method for the triad interactions and a semi-implicit approach for the deep-water source terms. The flexibility of the unstructured mesh combined with the robust and accurate method of WWM-II makes this model particularly adequate for simulating wave-current interactions in complicated coastal zones such as tidal inlets.

5.4 The sediment transport model

Sediment transport rates are usually calculated with classical semi-empirical formulations based on the assumption that the bed load or the total load (both bed and suspended loads) are instantaneously in equilibrium with the local hydrodynamic conditions [with some exceptions, e.g., *Wu*, 2004]. These formulae often use the depth-averaged velocity to compute the total load directly [e.g., *Engelund and Hansen*, 1967] or the bed load and the suspended load separately [e.g., *van Rijn*, 2007b,a]. Such formulae have been implemented in several morphodynamics models, such as DELFT3D [*Lesser et al.*, 2004] or MORSYS2D [*Bertin et al.*, 2009a]. Alternatively,

the vertical profile of the suspended sediment concentration can be treated as a passive scalar and is determined by solving an advection/diffusion equation, as for instance in the morphodynamic modelling systems TELEMAC [*Villaret et al.*, 2013], ROMS [*Warner et al.*, 2008], DELFT3D [*Lesser et al.*, 2004] and MORSELFE [*Pinto et al.*, 2012]. Although the latter method is more physical, it is also computationally much more expensive and only too few comparisons between both methods have been realized to this day to conclude about their relative accuracy. The choice is even more subtle when depth-averaged hydrodynamic models are used to compute the velocities, since additional parametrizations are needed to emulate the vertical distributions of currents and sediment concentrations. As the computational cost of a morphodynamic modelling system is usually a key factor for its applicability, a depth-averaged approach with semi-empirical formulae to compute the sediment transport rates was selected. Among the wide range of semi-empirical formulations available in the literature, each of them being developed for particular conditions (steady-state, with or without waves etc...) or validated against a specific test bed, five formulations have been implemented so far in the modelling system presented herein. These formulations are presented in the following paragraph.

5.4.1 Sediment transport formulae

Engelund and Hansen (1967)

Engelund and Hansen [1967] proposed a formula to compute the total sediment transport rate in rivers. This formula is less appropriate for use in the sea than in rivers, because of the assumption of quasy-steady flow and that the sandwaves/dunes are in equilibrium with the instantaneous flow velocity, which is not true in tidal flows. However this formula is still widely used in coastal environments in the absence of waves due to its simplicity and reasonable accuracy. The total sediment transport is computed as:

$$q_t = \frac{0.04 C_d^{3/2} \boldsymbol{u}^5}{g(s-1)^2 d_{50}} \tag{5.40}$$

where $\boldsymbol{u}$ is the mean flow velocity, $s = \rho_s/\rho_0$ is the specific sediment density, d_{50} is the mean particle diameter and C_d is the drag coefficient.

Ackers and White (1973)

Ackers and White [1973] derived a formula for total transport in rivers by considering the form of the transport relations for bedload (coarse sediments) and suspended sediment load (fine sediments) separately, and uniting them with a transition in the range $1 < D_* \leq 60$ through empirical coefficients that were fitted to a large data set. The total transport is computed as:

$$q_t = C_{AW} \boldsymbol{u} h \left(\frac{\boldsymbol{u}}{u_*}\right)^n \left(\frac{F_{AW} - A_{AW}}{A_{AW}}\right)^m \tag{5.41}$$

where

$$F_{AW} = \frac{u_*^n}{\sqrt{g(s-1)d_{35}}} \left[\frac{\boldsymbol{u}}{2.46 \log(10h/d_{35})}\right]^{1-n} \tag{5.42}$$

The dimensionless grain size D_* is defined as $D_* = d_{35}\left[g(s-1)/\nu^2\right]^{1/3}$ with ν the kinematic viscosity of the fluid. For $1 < D_* \leq 60$

$$n = 1 - 0.243 \log D_* \tag{5.43}$$

$$A_{AW} = \frac{0.23}{\sqrt{D_*}} + 0.14 \tag{5.44}$$

$$m = \frac{6.83}{D_*} + 1.67 \tag{5.45}$$

$$C_{AW} = \exp\left[2.79 \log D_* - 0.426(\log D_*)^2 - 7.97\right] \tag{5.46}$$

and for $D_* > 60$: $n = 0$; $A_{AW} = 0.17$; $m = 1.78$; $C_{AW} = 0.025$ [2]. Given the threshold $D_* > 1$, this formula only applies for grain sizes larger than 0.1 mm.

Soulsby - Van Rijn (1997)

The Soulsby - Van Rijn formula [*Soulsby*, 1997] is used to compute total sediment transport in the presence of waves and tidal currents. The formula is:

$$q_t = (A_{sb} + A_{ss})\boldsymbol{u}\left[\left(\boldsymbol{u}^2 + \frac{0.018}{C_D}U_{rms}^2\right)^{1/2} - U_{cr}\right]^{2.4}(1 - 1.6\tanh\beta) \tag{5.47}$$

where C_D is the drag coefficient due to current alone , U_{rms} is the root-mean-square wave orbital velocity, U_{cr} is the threshold depth-averaged current speed, β is the slope of the bed in the streamwise direction (positive if flow runs uphill), and A_{sb} and A_{ss} represent the contribution of the bedload and the suspended load respectively and are computed as follows:

$$A_{sb} = \frac{0.005h(d_{50}/h)^{1.2}}{\left[g(s-1)d_{50}\right]^{1.2}} \tag{5.48}$$

$$A_{ss} = \frac{0.012d_{50}D_*^{-0.6}}{\left[g(s-1)d_{50}\right]^{1.2}} \tag{5.49}$$

where D_* is the dimensionless particle size defined as $D_* = d_{50}\left[g(s-1)/\nu^2\right]^{1/3}$.

Van Rijn (2007)

van Rijn [2007a,b] proposed a unified transport formula for bedload and suspended load in the presence of waves and currents, that apply over a large range of particle sizes (0.05 mm to 2 mm). The beload and suspended transport rates are computed as:

$$q_b = 0.015\boldsymbol{u}h(d50/h)^{1.2}M_e^{1.5} \tag{5.50}$$

$$q_s = 0.012\boldsymbol{u}d_{50}M_e^{2.4}D_*^{-0.6} \tag{5.51}$$

where $M_e = (u_e - u_{cr})/\left[(s-1)gd_{50}\right]^{0.5}$ is the mobility parameter (if $u_e \leq u_{cr}$ $M_e = 0$), $u_e = u + \gamma U_w$ is the effective velocity with $\gamma = 0.4$ for irregular waves (and 0.8 for regular waves), u is the depth-averaged flow velocity, $U_w = \pi H_s/\left[T_p \sinh(kh)\right]$ is the peak orbital velocity (based on linear wave theory), H_s is the significant wave height, T_p is the peak wave period, $u_{cr} =$

[2]The coefficients m and C_{AW}, given in *Soulsby* [1997], are taken from a revised set of values based on more recent data.

$\beta u_{cr,c} + (1-\beta)u_{cr,w}$ with $\beta = u/(u+U_w)$, $u_{cr,c}$ is the critical velocity for currents based on Shields (initiation of motion), and $u_{cr,w}$ is the critical velocity for waves based on *Komar and Miller* [1975]:

$$u_{cr,c} = \begin{cases} 0.19(d_{50})^{0.1}\log(4h/d_{90}) & \text{for } 0.00005 < d_{50} < 0.0005m \\ 8.5(d_{50})^{0.6}\log(4h/d_{90}) & \text{for } 0.0005 < d_{50} < 0.002m \end{cases} \tag{5.52}$$

$$u_{cr,w} = \begin{cases} 0.24\left((s-1)g\right)^{0.66} d_{50}^{0.33}(T_p)^{0.33} & \text{for } 0.00005 < d_{50} < 0.0005m \\ 0.95\left[(s-1)g\right]^{0.57} d_{50}^{0.43}(T_p)^{0.14} & \text{for } 0.0005 < d_{50} < 0.002m \end{cases} \tag{5.53}$$

Camenen and Larson (2005, 2008)

Camenen and Larson developed a formula for bed load transport [*Camenen and Larson*, 2005] and for suspended transport [*Camenen and Larson*, 2008], taking into account the following mechanisms: presence of waves and currents, breaking and non-breaking waves, asymmetric wave velocity, angle between waves and current, phase-lag effects between water and sediment motions, and bed features in bed roughness estimate.

The bed load transport rate is computed as:

$$\frac{q_{bw}}{\sqrt{(s-1)gd_{50}^3}} = a_w\sqrt{\theta_{net}}\theta_{cw,m}\exp\left(-b\frac{\theta_{cr}}{\theta_{cw}}\right) \tag{5.54}$$

$$\frac{q_{bn}}{\sqrt{(s-1)gd_{50}^3}} = a_n\sqrt{\theta_{cn}}\theta_{cw,m}\exp\left(-b\frac{\theta_{cr}}{\theta_{cw}}\right) \tag{5.55}$$

where the subscripts w and n correspond respectively to the wave direction and the direction normal to the waves, θ_{cr} is the critical Shields number, θ_{net} the net sediment transporting Shields number (taking into account phase-lag effect), a_w, a_n, and b are empirical coefficients. θ_{cw}, $\theta_{cw,m}$, and θ_{cn} are defined as follows:

$$\begin{aligned} \theta_{cw} &= (\theta_c^2 + \theta_w^2 + 2\theta_w\theta_c\cos\phi)^{1/2} \\ \theta_{cw,m} &= (\theta_c^2 + \theta_{w,m}^2 + 2\theta_{w,m}\theta_c\cos\phi)^{1/2} \\ \theta_{cn} &= \frac{\frac{1}{2}f_c(U\sin\phi)^2}{(s-1)gd_{50}} \end{aligned} \tag{5.56}$$

where fc is the current-related friction factor, ϕ the angle between wave and current directions, θ_c, $\theta_{w,m}$, and θ_w are respectively the current, mean wave, and maximum wave Shields number, and $\theta_{w,m} = \theta_w/2$ for a sinusoidal wave profile.

The suspended load transport rate is computed as :

$$q_{sw} = U_{c,net}c_R\frac{\epsilon}{W_s}\left[1-\exp\left(-\frac{W_s h}{\epsilon}\right)\right] \tag{5.57}$$

$$q_{sn} = U\sin\phi c_R\frac{\epsilon}{W_s}\left[1-\exp\left(-\frac{W_s h}{\epsilon}\right)\right] \tag{5.58}$$

where $U_{c,net}$ is the net mean current after a wave period (taking into account phase-lag effect), c_R the dimensionless reference concentration at the bottom, W_s the sediment fall speed, and ϵ the sediment diffusivity. A description of the swash zone transport formula can be found in *Larson et al.* [2011].

5.4.2 Bed-slope effect

Most of the transport formula described in the previous paragraphs were derived for flat bed conditions. However, bathymetric gradients play an important role in sediment transport. They increase (resp. decrease) the critical shear stress when sediments are moving up-slope (resp. down-slope), acting as a diffusion-like term that stabilizes the numerical simulations. Physically, this effect is considered by modifying the critical shear stress according to the bottom slope along the flow direction [*Carmo*, 1995] or by applying empirical factors to the sediment transport rates in the flow direction and in the transverse direction. This second method has been adopted in this morphodynamic modelling system.

Lesser et al. [2004] proposed a method based on the work of *Bagnold* [1966] and *Ikeda* [1982]. The influence of the bed-slope is included in two parts. In the first part, a longitudinal slope in the direction of the bed-load transport modifies the magnitude of the bed-load vector. This adjustment is computed following a modified form of the expression suggested by *Bagnold* [1966]:

$$(q^*_{b,x}, q^*_{b,y}) = \alpha_s (q_{b,x}, q_{b,y}) \tag{5.59}$$

where

$$\alpha_s = 1 + \alpha_{bs} \left[\frac{\tan\phi}{\cos\beta_s(\tan\phi - \tan\beta_s)} - 1 \right] \tag{5.60}$$

α_{bs} is a user-specified tuning parameter (default = 1), ϕ is the angle of repose of sediments, and β_s is the bed slope angle in the direction of bedload transport vector. In the second part of the method, the direction of bedload transport is adjusted if a bed slope exists in the direction normal to the bedload transport vector. This modification is based on the work of *Ikeda* [1982] and is computed as follows:

$$q^{**}_{b,x} = q^*_{b,x} - \alpha_n q^*_{b,y} \tag{5.61}$$

$$q^{**}_{b,y} = q^*_{b,y} - \alpha_n q^*_{b,x} \tag{5.62}$$

where

$$\alpha_n = \alpha_{bn} \left(\frac{\tau_{cr}}{\tau_b} \right)^{0.5} \tan\beta_n \tag{5.63}$$

in which α_{bn} is a user-specified coefficient (default = 1.5), τ_{cr} is the threshold bed shear-stress for motion of sediments, τ_b is the bed shear-stress due to currents and waves, and β_n is the bed slope angle normal to the bedload transport vector. This method was implemented and tested in several morphodynamic models, such as DELFT-3D [*Lesser et al.*, 2004] and MORSELFE [*Pinto et al.*, 2012].

5.5 The bottom evolution module

The bottom evolution model solves the sediment continuity equation (or Exner equation) to compute the bed changes resulting from the divergence of the sediment fluxes. The Exner equation is:

$$\frac{\partial d}{\partial t} - \frac{1}{1-\lambda}\nabla \boldsymbol{q} = 0 \tag{5.64}$$

where $\boldsymbol{q}$ represents the depth-integrated volumetric sediment flux (expressed in $m^3.s^{-1}.m^{-1}$), λ is the porosity and d is the depth relative to the mean water level. After integration in time, Eq. 5.64 becomes[3]:

$$\Delta d^i = \frac{1}{1-\lambda}\nabla \cdot \boldsymbol{Q}^i \tag{5.65}$$

where $\boldsymbol{Q}^i$ is the sediment transport rate integrated over the morphological time step i. Then, Eq. 5.65 is integrated over a defined control volume, following:

$$\int_\Omega \Delta d \ \mathrm{d}\Omega = \frac{1}{1-\lambda}\int_\Gamma \boldsymbol{Q}.\boldsymbol{n} \ \mathrm{d}\Gamma \tag{5.66}$$

where Ω indicates the control volume with boundary Γ and $\boldsymbol{n}$ is the outward unit normal on Γ [4]. Eq. 5.66 is solved with a node-centred control volume (Fig. 5.3.a) or an element-centred control volume (Fig. 5.3.b).

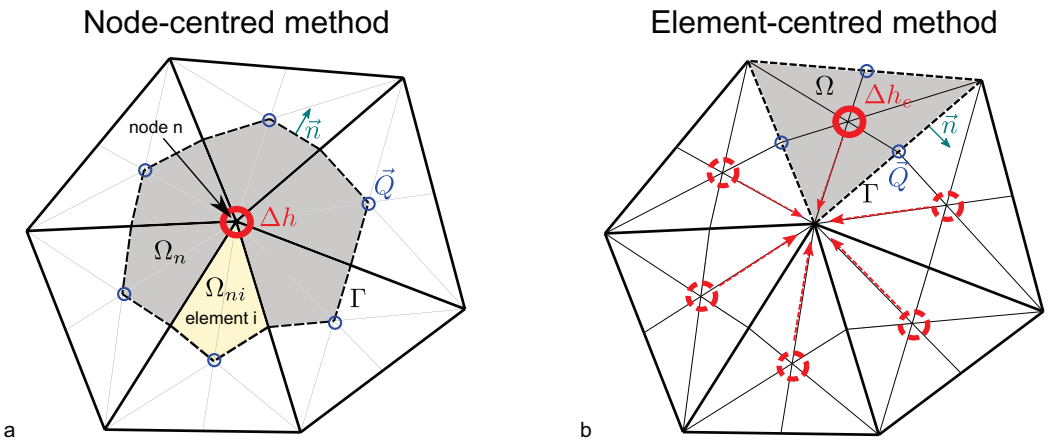

Figure 5.3: Schematic representation of the control volume and associated variable for the node-centred method (a) and the element-centred method (b). The sediment fluxes $\boldsymbol{Q}$ and the bed changes Δh are computed at the points marked with blue and red circles, respectively.

The former method was initially implemented by *Fortunato and Oliveira* [2004] in the morphodynamic model SAND2D and later in MORSYS2D [*Bertin et al.*, 2009a] and MORSELFE [*Pinto et al.*, 2012]. The sediment fluxes are computed at the element centres and are assumed to be constant inside the element while the depth varies linearly within the element. After discretization, the left-hand side term of Eq. 5.66 becomes:

$$\int_\Omega \Delta h \ \mathrm{d}\Omega = \sum_{i=1}^{nel}\left(\sum_{j=1}^{3}\Delta h_{ij}\int_\Omega \phi_j d\Omega_{ni}\right) \tag{5.67}$$

[3]Since the integrated variable is space-independent, the Leibniz rule is invoked to switch the integral and the divergence operators.

[4]Gauss' theorem is used to cast the divergence term into a boundary integral.

where nel is the number of elements surrounding node n, ϕ_j is the element linear shape function that equals 1 at node j and 0 at the two other nodes of the element (Fig. 5.4). The integration of ϕ over the local control volume Ω_{ni} can be expressed as:

$$\int_{\Omega} \phi_j d\Omega_{ni} = C_i A_{ni} \tag{5.68}$$

where A_{ni} is the area of element i and

$$C_i = \begin{cases} 22/108 & \text{if } j = n \\ 7/108 & \text{if } j \neq n \end{cases} \tag{5.69}$$

The right-hand side term of Eq. 5.66 becomes:

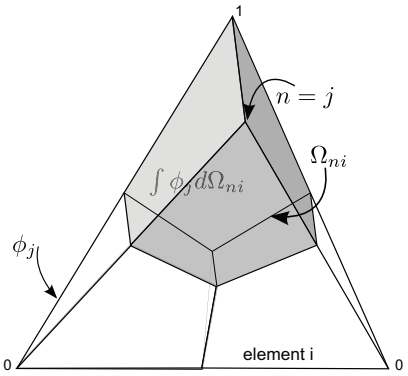

Figure 5.4: Schematic representation of an element i, its associated shape function ϕ_j and the integration volume of ϕ_j over the local control volume Ω_{ni} (shaded volume) used to solve Eq. 5.67

$$\frac{1}{1-\lambda} \int_{\Gamma} \boldsymbol{Q}.\boldsymbol{n} d\Gamma = \frac{1}{1-\lambda} \sum_{i=1}^{nel} \left(\sum_{j=1}^{2} Q_{ix}(y_{ij} - y_{0i}) - Q_{iy}(x_{ij} - x_{0i}) \right) \tag{5.70}$$

where (Q_{ix}, Q_{iy}) are the x and y components of the sediment flux integrated in time at element i, (x_{0i}, y_{0i}) are the coordinates of the centre of element i and (x_{ij}, y_{ij}) are the coordinates of the centre of side j that belongs to element i and includes node n. The system of equations $Ax = b$ where the right-hand side term of Eq. 5.67 represents Ax and Eq. 5.70 represents b is eventually solved with a Jacobi conjugate gradient method to obtain the bed changes at every node.

In the element-centred method, the sediment fluxes are computed and integrated in time at the sides of the elements (Fig. 5.5) and since h is assumed to vary linearly within the element, the left-hand side term of Eq. 5.66 can be reduced to $\Delta h_e A_e$ where A_e is the area of the element. Hence the bed changes at the centre of the elements h_e are obtained through:

$$\Delta h_e = \frac{1}{A_e(1-\lambda)} \int_{\Gamma} \boldsymbol{Q}.\boldsymbol{n} d\Gamma \tag{5.71}$$

Considering the fluxes constant along each side of the element, Eq. 5.71 can finally be expressed as:

$$\Delta h_e = \frac{1}{A_e(1-\lambda)} \sum_{i=1}^{3} \left(Q_{ix}(y_{i+1} - y_i) - Q_{iy}(x_{i+1} - x_i) \right) \text{ with } x_4 = x_1 \text{ and } y_4 = y_1 \tag{5.72}$$

where (Q_{ix}, Q_{iy}) are the x and y components of the sediment flux integrated in time at side i, (x_i, y_i) are the coordinates of node i (Fig. 5.5). The bed changes at the nodes (Δh) are computed

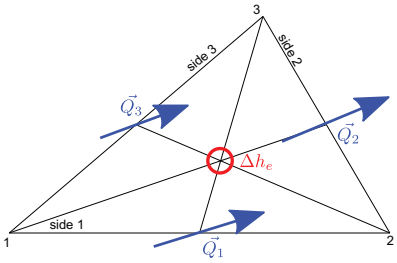

Figure 5.5: Schematic representation of an element with the relative position and names of the nodes, the sides and the associated sediment fluxes.

as the element-area-weighted-averages of the bed changes previously computed for the surrounding elements (Δh_e). While the second method estimates bed changes with a higher resolution [5], the interpolation of bathymetric changes at the nodes (necessary for the next hydrodynamic computation) is not mass-conservative and may lead to some inaccuracies.

The default morphodynamic time step is equal to the hydrodynamic time step, but it can optionally be set to a multiple of the hydrodynamic time step, in order to speed up the computational time. The time integration of Q is realized with a trapezoidal rule. The Courant-Friedrich-Levy (CFL) condition imposed by the explicit method can be estimated as $Cu \approx \frac{bQ}{h\Delta x}$, where C_u is the Courant number, b is the velocity power in the transport formulae (typically between 3 and 5, depending on the specific formulation), according to *Roelvink* [2006]. Numerical experiments realized with the bottom update model SAND2D, from which the numerical methods presented herein were adapted [*Fortunato and Oliveira*, 2004], indicated that the morphodynamic model was stable for maximum Courant numbers of up to 10 [*Fortunato and Oliveira*, 2007b].

Very often, the results of morphodynamic models are spoiled by undesired spatial oscillations, independently of the numerical methods implemented. These oscillations result from the inherent unstable nature of the non-linear coupling between the sediment transport module and the bed evolution module (de Vriend et al 1987). *Johnson and Zyserman* [2002] showed that the dependence of the bed celerity with the bed levels, due to the non-linear relationship between sediment transport and bed levels, is responsible for high wave number spatial oscillations. They applied a diffusion-like filter to the sediment fluxes in order to mimic some natural smoothing effect (bed slope, random waves) and limit these oscillations. *Callaghan et al.* [2006] provided analytical evidence that an inadequate numerical solver for the Exner equation will lead to dispersion and diffusion in the solution and will result in spatial oscillations. *Kubatko et al.* [2006] implemented a discontinuous Galerkin method to solve the Exner equation on unstructured grids which is combined with a slope limiter to dampen spatial oscillations.

In the bottom update module, several approaches were implemented to prevent the development of spatial oscillations. First, a modified expression [*Fortunato and Oliveira*, 2007b] of the diffusion-like term given by *Horikawa* [1988] was included in the Exner equation:

[5] In unstructured triangular grids the number of element is roughly twice the number of nodes.

$$Q^* = Q + \epsilon(1-\lambda)\left(|Qx|\frac{\partial h}{\partial x}, |Qy|\frac{\partial h}{\partial y}\right) \tag{5.73}$$

where ϵ is a dimensionless diffusion coefficient, and Q^* replaces Q in Eq. 5.64. Also, a non-linear filter was implemented to eliminate local extrema in the bathymetry after each morphodynamic time step. This filter, implemented by *Fortunato and Oliveira* [2000] is an extension of the one-dimensional filter of *Shyy et al.* [1992] to two-dimensional unstructured and proceeds as follows: a minimum (maximum) occurs for $h_i < h_{min}$ ($h_i > h_{max}$), where $h_{min} = min(h_j : j = 1, nei)$ ($h_{max} = max(h_j : j = 1, nei)$), and nei is the number of nodes surrounding node i. For each minimum (maximum), h_i and h_{min} (hmax) are made equal while preserving the volume by setting:

$$h_i^f = h_{min}^f = \frac{h_i A_i + h_{imax} A_{imax}}{A_i + A_{imax}} \tag{5.74}$$

$$h_i^f = h_{max}^f = \frac{h_i A_i + h_{imin} A_{imin}}{A_i + A_{imin}} \tag{5.75}$$

where the superscript f indicates a filtered value, and A_i and $A_{imin(imax)}$ are the sum of the areas of the elements surrounding node i and the node where depth is minimum (maximum), respectively. The procedure is repeated until convergence, i.e. until all local extrema have been removed. This filter damps $2\Delta x$ oscillations with minimal introduction of numerical diffusion [*Oliveira and Fortunato*, 2002] (as long as a minimum height threshold under which no extrema can be detected is introduced).

Finally an avalanching method was implemented to reproduce gravity effects on steep bottom surfaces. After each morphodynamic time step, an iterative procedure modifies the bathymetry in a mass-conservative manner to decrease local slopes higher than a certain threshold. Following *Roelvink et al.* [2009] the threshold values of the tangent of the bottom slope for wet and dry sands are set to 0.3 and 1 respectively.

Summary

This chapter presents the morphodynamic modelling system that has been implemented in the Albufeira Lagoon to investigate the physical processes controlling its morphological changes is presented. This numerical platform is being developed in a collaborative framework with the overall goal to simulate accurately the complex estuarine and coastal circulations and the associated morphodynamic processes. For this dissertation, wave, circulation, sediment transport and bottom updates modules in their 2DH version were coupled and applied to the study case. The implementation of the regional wave model, the development of the sediment transport and bottom updates modules and the coupling of these modules to the wave-current model were carried out by the author and formed an integral part of his research work.

The following models were involved in the numerical modelling system:

1) The wave model WW3 was used as a regional wave model to simulate the wind-induced wave-growth and wave propagation over the North-Atlantic Ocean. This model provided spectral boundary forcing for the local wave models. In addition, WW3 was used to produce a 65-year wave hindcast in the North-East Atlantic Ocean, whose results enabled the analysis of the wave climate variability at regional and local scales (Chapter 6);

2) The wave model SWAN was coupled to the circulation model SELFE in the early stage of the project. This modelling system was used to investigate the wave-current interactions at the Albufeira Lagoon (Chapter 7). The loose coupling strategy, involving several computational grids and interpolation methods, and the wave model itself eventually revealed some limitations for the morphodynamic investigations;

3) The wave model WWM-II was coupled to the circulation model SELFE in the course of the project. This fully coupled wave-current modelling system benefits from the most advanced physical formulations and numerical methods and provided the ideal framework for the development of the morphodynamic module;

4) A sediment transport module was developed to compute the sediment fluxes from the depth-averaged currents, the water depth, the nature of the bed and the wave parameters. This module integrates five recognized formulations developed for a wide range of hydrodynamic conditions (rivers, tide-dominated or wave-dominated environments);

5) A bottom update module was developed to reproduce the bathymetric changes induced by the divergence of the sediment fluxes. This module solves the Exner equation explicitly based on finite-volume methods. Several filters were also implemented to attenuate the numerical oscillations inherent to the non-linear interactions between bottom changes and hydrodynamic circulation. The wave-current-sediment-bottom-udpate modelling system was used to investigate the morphodynamics of the Albufeira Lagoon (Chapter 8).

Chapter 6

Characterization of the wave climate

The morphodynamics of wave-dominated tidal inlets is strongly controlled by the local wave climate and its variability. When the freshwater input in the back-barrier lagoon is negligible, the hydraulic efficiency of the inlet is low and the wave climate is energetic, the wave-related processes control the sediment dynamics to a large extent and significantly impact the equilibrium of the inlet. Since the wave climate varies at different time-scales, it is natural to assume that the morpho-sedimentary dynamics of tidal inlets will be affected by these changes in the incident wave forcing. In Portugal, several inlets enlarge during the summer season when the waves are small while they infill, migrate and sometimes close in winter when the wave climate becomes more energetic. Investigating the seasonality of the wave climate is thus primordial to understand the morphological changes of wave-dominated tidal inlets at annual time scales. Superimposed on this seasonal variability, the inter-annual variability of the wave climate is also assumed to have a significant impact, poorly understood though, on the long-term dynamics of wave-dominated tidal inlets. At the Albufeira Lagoon, the time during which the lagoon remains open varies from a fortnight to several months but the reasons of such differences from one year to another have not been elucidated yet. It appears thus necessary to investigate the different modes of variability of the wave climate in the North-East Atlantic (NEA) basin and off the Albufeira Lagoon in order to determinate their impact on the morphodynamics of this tidal inlet. For this study, a wave modelling system was implemented and a 65-year wave hindcast (1948-2012) was carried out at both regional and local scales. The first section of this chapter summarizes some of the main results on the wave-climate variability in the NEA published during the last decades. The implementation and validation of the wave models are then presented (Section 6.2), followed by a description of the wave climate variability in the NEA based on the analysis of the regional model results (Section 6.3). The origin of the inter-annual wave climate variability is discussed in Section 6.4. Finally the results of the local wave model are analysed and the implication of the wave climate variability for the Albufeira Lagoon are discussed in Section6.5. A significant part of this chapter is based on the results of *Dodet et al.* [2010] who analysed the wave-climate variability in the NEA based on a 57-year wave model hindcast. However the longer time period investigated herein, the deeper analysis of the results and the confrontation to other results recently published have significantly enriched the conclusions of this former study.

6.1 State of the art

During the last four decades, several studies have been undertaken to analyse wave climate changes in the North Atlantic Ocean. *Walden et al.* [1970] examined the mean values of visually estimated wave heights from nine Ocean Weather Stations in the North Atlantic from 1950 to 1967 and revealed a high variability in wave statistics from year to year. Later, based on shipborne wave recorder data, *Bacon and Carter* [1991] showed an increase in significant wave height (Hs) of 2.4 cm.yr^{-1} for the period 1962–1986. In 1995, the Waves and Storms in the North Atlantic (WASA) project was setup to verify the hypothesis of a worsening storm and wave climate in the North-East Atlantic and concluded that the wave climate had roughened in the last decades but seemed yet to be comparable with the one from the beginning of this century [*WASA*, 1998]. Using a 40-year wave hindcast, *Wang and Swail* [2002] detected an upward trend in seasonal extremes of Hs (from 1958 to 1997) with higher rates in winter off the north-west coast of Ireland. However, based on a 20-year time-series of wave buoy data in the Bay of Biscay, *Dupuis et al.* [2006] found no particular tendency for Hs over the period 1980–1998. *Kushnir et al.* [1997], by combining a 10-year numerical wave hindcast and an empirical extrapolation backward in time, even suggested a decrease in wave height south of 40°N during the period 1962–1986. Based on a 23-year (1985-2008) database of calibrated and validated satellite altimeter measurements, *Young et al.* [2011] analysed wind and wave height at global scale and found no significant trends in the North-East Atlantic for the mean Hs but a significant increase (up to 1 cm.year^{-1}) for the Hs 99^{th} percentile. Recently, *Bertin et al.* [2013] used the 20CR atmospheric reanalysis [*Compo et al.*, 2011] to realize a 109-year wave hindcast (1900-2008) for the North Atlantic Ocean. They found an increase in the mean wave height up to 1 cm.year^{-1} at latitudes higher than 55°N and attributed this increase to a rise in wind speed for the same period. However, *Krueger et al.* [2013] reported some inconsistencies between wind observations and the 20CR Reanalysis, and the National Center for Atmospheric Research (NCAR-NOAA) that supplies this data recommends special care in interpreting long-term trends derived from this data product. The combination of all these results suggest a likely increase in wave height for the North Atlantic. However this result seems to be valid only locally and reveals a strong dependence on the studied period and the chosen parameter, which still needs some clarification.

In the early 1990s, a link to the North Atlantic Oscillation (NAO) was suggested by *Bacon and Carter* [1993] who noticed a relationship between visual estimates and instrumental records of wave heights and the atmospheric pressure gradient measured between the Iceland low and the Azores high, represented by the NAO index [*Hurrell*, 1995]. However, these results were obtained from a few isolated weather ships and buoys located northward of 50°N, and were not sufficient to describe the spatial distribution of the wave climate. More recently, several studies used either satellite altimetry or numerical models to investigate the wave climate in the North Atlantic Ocean. Thus, *Woolf* [2002] analysed data sets from the ERS-1, ERS-2 and TOPEX satellites and showed decreasing correlations between Hs and the NAO index from northern to southern latitudes over the period 1991 – 2000. *Bauer* [2001] analysed a high-resolution wave hindcast from 1981 to 1993 using the WAM model [*WAMDI*, 1988] and obtained low correlations between the monthly values of the NAO index and Hs, but high correlations when using winter-mean values. These authors also found higher correlations at northern latitudes. *Dupuis et al.* [2006] locally corroborated this spatial distribution, finding no correlation between Hs and

the NAO index in the Bay of Biscay (43°). However, they found a weak positive correlation (r = 0.38) between the NAO index and the annual-mean 1/3 highest wave periods. This result suggests that comparisons between other wave parameters and the NAO index could be relevant. *Dodet et al.* [2010] re-examined and extended the conclusions of the above-mentioned studies with a 57-year (1953-2009) numerical wave hindcast for the NEA and obtained: 1) for Hs 90^{th} percentile, a strong positive correlation with the NAO index at northern latitudes and a significant negative correlation at southern latitudes; 2)for the winter-mean directions, a positive correlation at latitudes lower than 40°N; and 3) for the winter-mean peak periods, a positive correlation increasing from south to north. Based on their 109-year wave hindcast, *Bertin et al.* [2013] also obtained significant positive correlation coefficients between the mean wave height and the NAO index at latitudes higher than 45°.

The local studies on the wave climate variability off the coast of Portugal are much scarcer. Nevertheless, *Andrade et al.* [1996] analysed newspaper records on storminess for the north-west coast of Portugal and reported an increase in frequency and duration of the storms throughout the late 19^{th} and 20^{th} centuries. These results were refuted by *Quadrio and Taborda* [2010] who computed statistics on storminess based on a 44-year wave hindcast and did not find any significant trends. Finally, *Almeida et al.* [2011] investigated the variability and trends in wave storminess for the south coast of Portugal, using observation data and a 48-year wave hindcast. They found a strong variability in the statistical parameters representative of the storminess but no statistically significant trends. They also obtained low correlation coefficients between the NAO index and the computed storminess parameters, suggesting that local factors are more likely to explain the storminess variability in this region.

6.2 Implementation and validation of the regional and local wave models

6.2.1 Modelling strategy

The wave models WavewatchIII (WW3) and SWAN were used to realize a 65-year hindcast of mean wave parameters over the NEA Ocean (regional scale) and near the Albufeira Lagoon (local scale). To simulate the wave climate at these two scales, a one-way nesting strategy was adopted involving three computational grids: 1) a regional grid covering the North Atlantic Ocean, from 80.0°W to 0.0°W in longitude and 0.0°N to 70.0°N in latitude, with a 0.5° resolution; 2) an intermediate grid extending from 10.0°W to 8.5°W in longitude and from 37.5°N to 40.0°N in latitude, with a 0.05° resolution; and 3) a local grid extending from the Cape Roca at the North-West to the Cape Espichel at the South-East, covering an area of 39 km by 33 km with a 1-km resolution (Fig.6.1). The NEA regional hindcast was performed with WW3 and provided the intermediate grid with wave spectra along its open boundaries. Similarly, the intermediate run, also performed with WW3, generated the spectral forcing for the local grid that was used with SWAN afterwards. This intermediate run was necessary to allow a smooth nesting between the 0.5° resolution grid ($\sim$ 50 km) and the 1-km resolution grid. The same spectral grid was used for each model and consisted of 24 regularly spaced directions over 360° and 25 logarithmically spaced frequencies ranging from 0.041 Hz to 0.41 Hz.

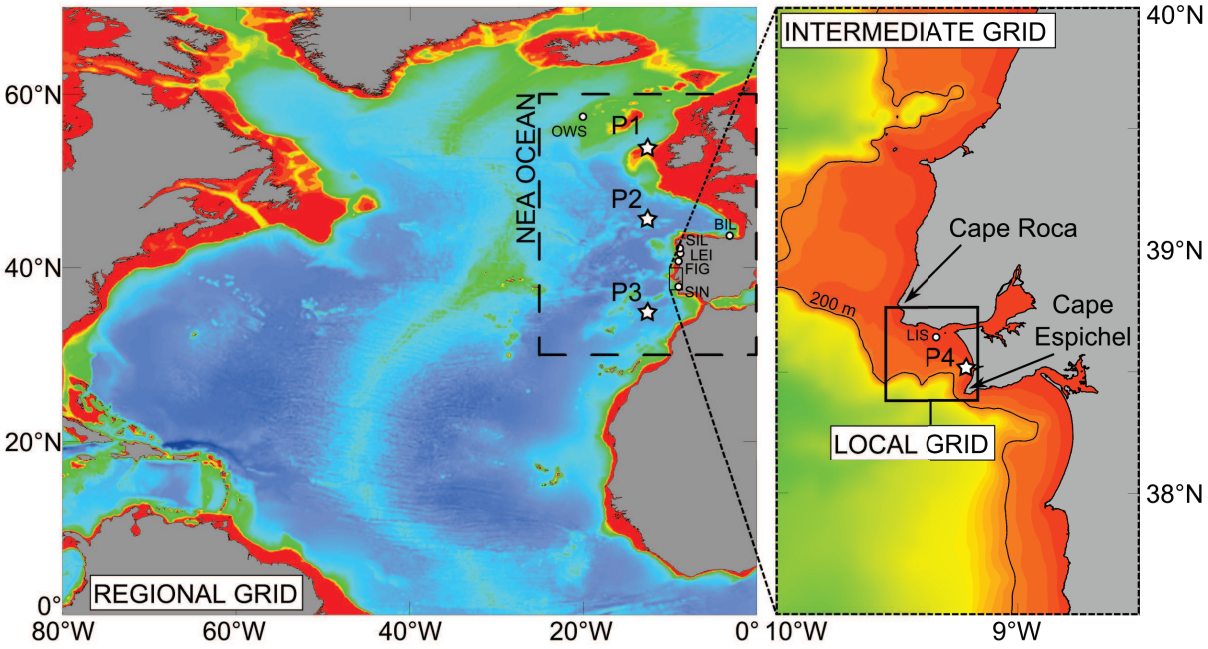

Figure 6.1: Bathymetric map of the North Atlantic Ocean showing the extensions of the regional, intermediate and local computational grids and the study area referred to as North-East Atlantic Ocean. The white circles indicate the locations of the wave buoys: Bilbao-Vizcaya (BIL), Cabo Silleiro (SIL), Leixões (LEI), Figueira da Foz (FIG), Sines (SIN) and Ocean Weather Station "Juliett" (OWS). The white stars indicate the location of the regional and local model outputs P1, P2, P3 and P4.

The regional and local grids were forced with 6-h wind fields from the NCEP/NCAR Reanalysis project [*Kalnay et al.*, 1996], available from 1948 to present. For the SWAN run on the local grid, wind direction and intensity were retrieved from the NCEP-NCAR Reanalysis wind field at the nearest node of the study area and were used to feed the model with homogeneous wind forcing. The wave-current interactions were not considered as they were assumed to have a minor impact on the results at the temporal and geographical scales considered herein. Ice coverage was neither taken into account in the regional implementation since the required data were not available when this study was conducted. Moreover, the assumption was made that ice coverage had only a weak impact on wave climate in the area considered in this study. This assumption is corroborated by *Tolman* [2003], who showed only minor improvements for wave predictions in this specific area when considering ice coverage. The water level was constant in the WW3 simulations while the SWAN local run was fed with time-series of water elevations synthesized from the amplitude and phases of 13 harmonic constituents computed with the regional model of *Fortunato et al.* [2002] at a node closed to the model boundary. The parametrization of the source terms in WW3 corresponds to the package "WAM-4 and Variants" described in *Tolman* [2009], with the additional improvements for the wind input and dissipation source terms detailed in *Ardhuin et al.* [2010]. The physical processes taken into account in SWAN were the whitecapping dissipation, according to the formulation of *van der Westhuysen et al.* [2007], the bottom friction with the default Madsen coefficient ($C_b = 0.05$) and the quadruplet wave-wave interactions.

The 65-year regional and local simulations (January 1^{st}, 1948 to January 1^{st}, 2012) provided time-series of significant wave heights (Hs), mean wave directions (Mwd), peak periods (Tp)

and directional spreading (Spr) over a region extending from 25.0°W to 0°W and from 30.0°N to 60.0°N hereafter referred to as the NEA region and over the whole extension of the local domain, respectively. The outputs of the WW3 run were retrieved every 6 hours, following the constraints of the temporal resolution of the wind forcing, and every 3 hours for the SWAN run in order to resolve adequately the tidal cycles. For each output of the regional simulation, annual, winter- (from 1^{st} December to 1^{st} April) and summer-means (from 1^{st} June to 1^{st} October) were computed in order to investigate the spatial and temporal variability of the wave climate in the NEA. The results of the SWAN local run were converted into monthly-means in order to analyse the seasonal variability with a higher resolution.

6.2.2 Validation of the model results

The regional model was validated against observations at three buoys off the Portuguese coast – Sines (SIN), Leixões (LEI) and Figueira da Foz (FIG) – and two buoys off the Spanish coast – Cabo Silleiro (SIL) and Bilbao-Vizcaya (BIL). An additional comparison was realized with data from the Ocean Weather Station (OWS) "Juliett" (20.0°W; 52.5°N) to cover the period 1952–1975. Before being compared against model results, the data of each buoy was processed following a common methodology: (1) Mwd was corrected to take into account the magnetic declination occurring at the specific location and time-period; (2) Hs, Mwd and Tp were averaged using (2a) 6-h and (2b) 1-month sliding windows; and (3) these values were finally interpolated on (3a) 6-h and (3b) 1-month regularly spaced time vectors. For consistent comparisons between model and data, steps (2b) and (3b) were also applied to model outputs. The 6-hour time-window was chosen to consistently compare data against 6-hour model outputs. The 1-month time-window was chosen to evaluate the model precision when investigating long-term trends and correlation with the NAO index. Scatter diagrams of measured versus modelled Hs for the entire dataset show an overall good agreement between measured and predicted Hs (Fig.6.2). It can be seen qualitatively that the model reproduces both weak and energetic waves with a similar accuracy, although a linear regression reveals a negative bias of the order of 0.20 m. A comparison between Fig. 6.2a and 6.2b shows how predictions are improved by averaging the dataset over 1 month (Fig. 6.2b) instead of 6 h (Fig. 6.2a).

Bias and Root Mean Square Error (RMSE) were computed for all parameters. For Hs and Tp, the RMSE was normalized by the mean of the observed values (NRMSE). In order to quantify the accuracy of model predictions for winter-means (4 months), this statistical analysis was also applied to monthly averaged data. 4-month means were also considered and resulted in smaller errors tending towards the bias. It is thus assumed that errors for 4-month means predictions are significantly smaller than those derived from the 1-month average analysis. Comparisons between model and data revealed NRMSE of the order of 20% and 16% with 6-h average and 10% and 7% with monthly average, for Hs and Tp, respectively. The RMSE between measured and modelled mean wave directions were around 20° for 6-h average and 5° for the monthly averages. A systematic negative bias in Hs of the order of 0.10 to 0.30 m was observed at every station. Slightly better predictions for Hs were obtained by tuning parameters for the source terms, but this parametrization resulted in less accurate predictions for Mwd and Tp. Also, using the ERA-INTERIM reanalysis wind fields [*Dee et al.*, 2011] to force the model improved significantly the comparisons, but the time extent of this reanalysis being much shorter (from

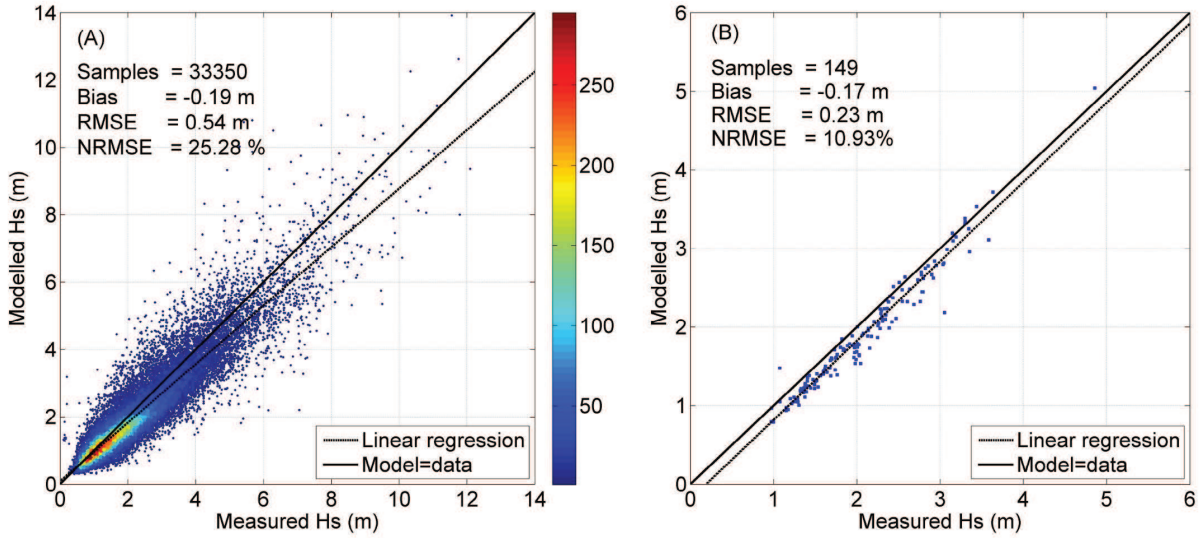

Figure 6.2: Scatter diagrams of 6-h (a) and 1-month (b) modelled Hs versus measured Hs for the entire data set [Dodet et al., 2010]. The colour bar on the left panel corresponds to sample density and is arbitrarily expressed in number of point per 0.10 m^2 squares. The solid line corresponds to $y = x$, the dashed line to a linear regression and the difference between both lines illustrates the slight negative bias of modelled Hs.

1979 onwards), the NCEP wind fields were retained for this study. A detailed description of the validation of the regional model is given in *Dodet et al.* [2010].

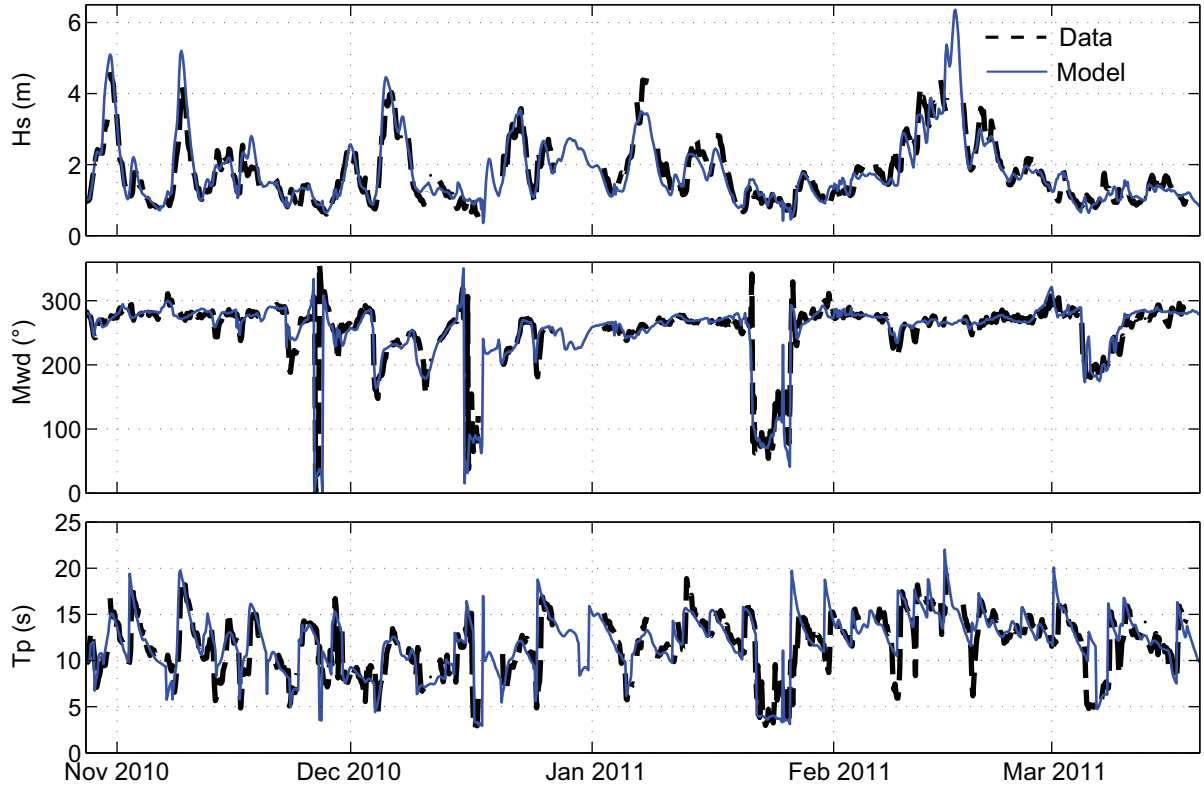

Figure 6.3: Comparisons between modeled (blue dashed line) and measured (black line and circles) mean wave parameters (HS, MWD, and TP) at the Lisbon buoy from October 2010 to March 2011.

The results of the local SWAN simulation were validated against mean wave parameters recorded by a Triaxys buoy located at the entrance of the Tagus estuary (buoy LIS on Fig.6.1)

during the period October 2010 - March 2011, in order to assess the quality of the modelling strategy. Fig.6.3 shows the comparisons between observed Hs, Mwd and Tp and model outputs. The RMSE were computed for each parameter as well as the NRMSE for Hs and Tp (Table6.1). In addition, the RMSE and NRMSE were also computed for the monthly means to provide an estimation of the model skills for these parameters. For the 5-month period considered herein, the 3-hourly model outputs match the observed Hs and Tp with NRMSE of the order of 20% while the 1-month means match Hs and Tp with NRMSE of the order of 5%. For Mwd the respective RMSE are of the order of 18° and 5°.

Table 6.1: Statistical errors between model results and observed data at the Tagus entrance.

	RMSE		NRMSE (%)	
Parameter	3-hourly values	monthly means	3-hourly values	monthly means
Hs (m)	0.34	0.08	19.9	4.8
Mwd (°)	17.23	5.46		
Tp (s)	2.39	0.48	20.6	4.1

6.3 Wave climate variability in the North-East Atlantic Ocean

The analysis of the temporal and spatial variabilities of the wave climate in the NEA is based on two means of representation: 1) 65-year time-series of Hs, Mwd, Tp and Spr at three deep water (> 1000 m) locations along the meridian 12.5°W (P1: 55°N, P2: 45°N and P3: 35°N) and 2) maps of annual and seasonal averages computed for the period 1948-2012. The time-series of 3-month filtered data and summer- and winter-means demonstrate the seasonal and inter-annual variability of each parameter, while the maps give a clear overview of the spatial distribution of the mean values. In addition, averages and standard deviations of the summer and winter time-series were computed and linear regression analyses were carried out to estimate the relative importance of seasonal, inter-annual and pluri-decadal variabilities.

6.3.1 Significant wave height

The spatial distribution of Hs is characterized by a meridional decrease of the mean values from North to South, with yearly means up to 3.5 m at northern latitudes and down to 2 m at southern latitudes (first column on Fig.6.4). The winter means are systematically larger than the summer means and reach up to 5 m in the upper part of the domain. The seasonal variability is well illustrated on the 3-month filtered time-series of Hs (Fig.6.5) with the cyclic rise and fall of Hs in spring and autumn respectively, associated to the seasonal cyclonic activity in the North Atlantic. Moreover a strong inter-annual variability of Hs is observed from P1 to P3, with standard deviations of the winter-means time-series higher than 10% of the 65-year average (σ and mean values are given in Fig.6.5). The Hs summer-means display a weaker inter-annual variability with standard deviations around 7% of the average of all summer-means.

Long-term trends for Hs winter- and summer-means were evaluated by means of linear regressions over the NEA domain. For the winter-means, the only trends statistically significant with 95% confidence are found at latitudes higher than 52°N (such as for P1) where they can

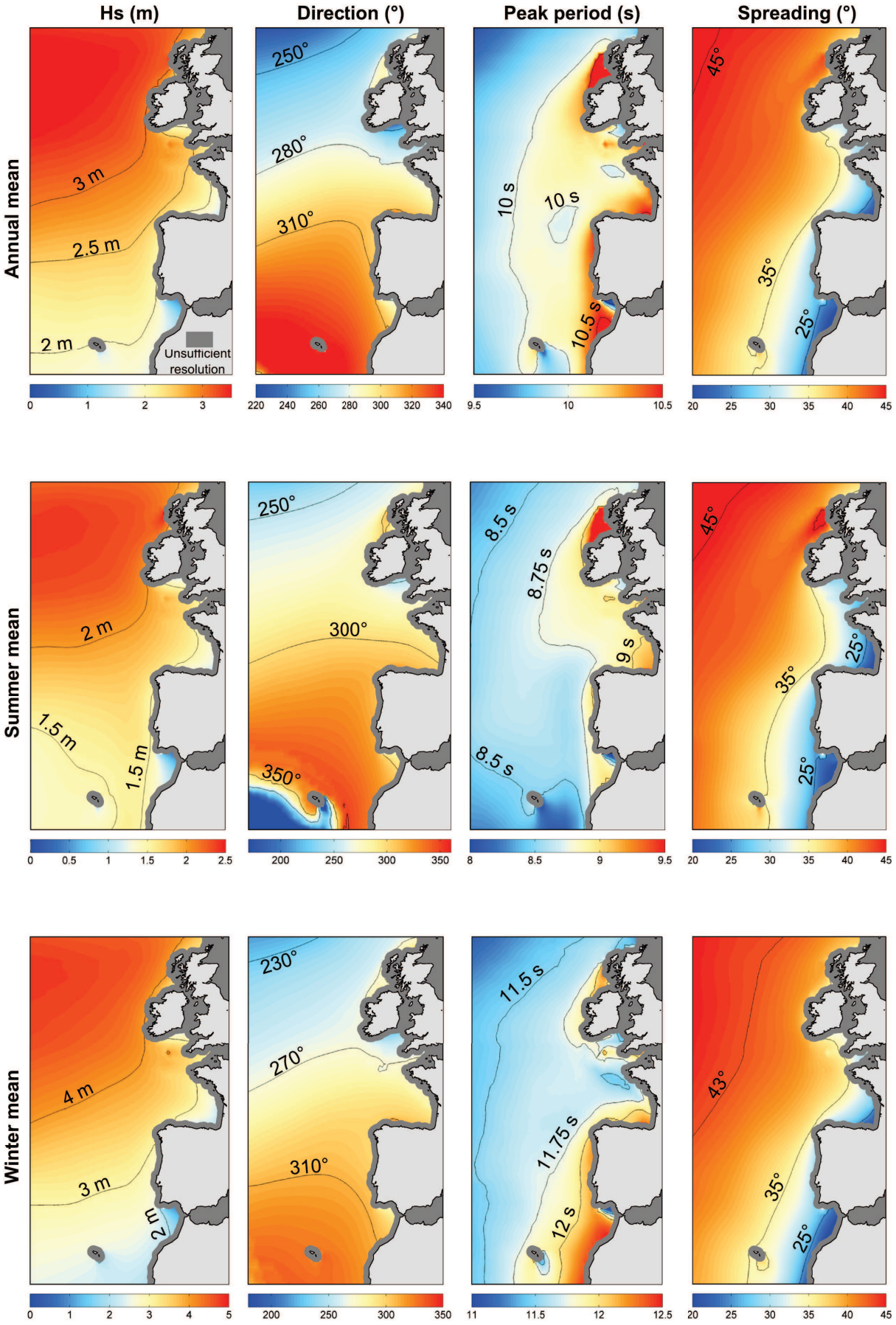

Figure 6.4: Maps of yearly means (top row), summer means (middle row) and winter means (bottom row) of mean wave parameters computed for the period 1948-2013: significant wave height (first colum), mean wave direction (second column), peak period (third column) and directional spreading (fourth column).

reach up to 1 cm.year^{-1}, *i.e.* an increase of around 15% of the average value for the period 1948-2012. The spatial distribution of the trends of Hs winter-means (not shown) is very similar to the one obtained by *Dodet et al.* [2010] for the Hs 90%-ile over the period 1953-2009. However the significance testing performed herein suggests that there is no evidence of trends in

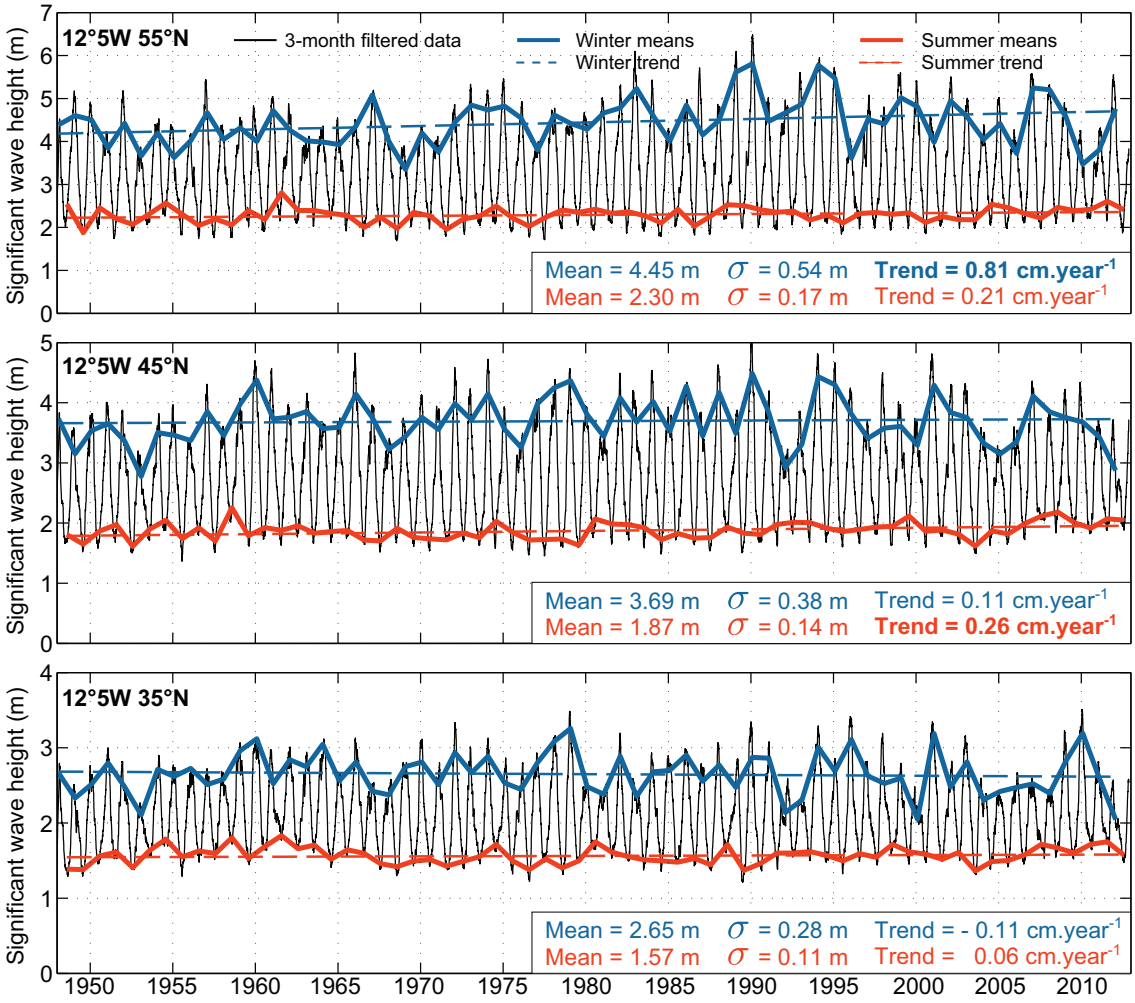

Figure 6.5: Time-series of significant wave heights at P1 (top panel), P2(middle panel) and P3 (bottom panel) from 1948 to 2013: 3-month filtered data(black line), winter averages (blue solid line) and summer averages (red solid line). The dashed lines correspond to linear regressions fitted through the winter (blue) and summer averages (red). The mean values, the standard deviations (σ) and the coefficients of the trends are given for each season (bold font type means that the trend is significant with 95% confidence).

Hs winter-means south of 50°N. The positive trends found for the summer-means are statistically significant between latitudes 35°N and 50°N and also at latitudes higher than 55°, although their values never exceed 0.5 cm.year^{-1}.

6.3.2 Mean wave direction

A similar analysis carried out for Mwd shows that the distribution of the mean values presents a meridional increase from North to South with yearly means ranging from 240°[1] in the North to 330° in the South (second column on Fig.6.4). As for Hs, Mwd exhibit strong seasonal variabilities at the three selected locations, with the summer period characterized by higher

[1]All the directional values given in this chapter follow the nautical convention, *i.e.* measured clockwise from geographic North.

directions than during the winter period. This clockwise (resp. counter-clockwise) shift of the mean wave directions during spring (resp. autumn) is explained by the meridional shift of the storm tracks that pass at higher latitudes during summer than during winter. Nevertheless, the seasonal cycle is less pronounced at northern latitudes than at southern latitudes and even opposite behaviours can be observed at latitudes higher than 40°N (such as for P1 and P2) with winter means higher than summer means. A strong inter-annual variability of the Mwd winter-means is illustrated on Fig.6.6 at the three selected locations, decreasing from northern to southern latitudes (σ = 12.1°, σ = 10.4° and σ = 8.5°, for P1, P2 and P3, respectively). Compared to winter-means, Mwd summer-means are characterized by a smaller variability (σ = 8.1°, σ = 8.6° and σ = 3.7°, for P1, P2 and P3, respectively). The analysis of the long-term trends of Mwd winter-means reveals similar results to the ones obtained by *Dodet et al.* [2010] for the period 1953-2009, with positive trends at latitudes lower than 40°N increasing southward up to 0.15°.$year^{-1}$ and negative trends at latitudes higher than 40°N increasing northward up to -0.15°.$year^{-1}$. However, none of these trends are statistically significant with 95% confidence. For the summer-means, statistically significant trends are only found at latitudes lower than 35°N (such as for P3) with values lower than 0.1°.$year^{-1}$.

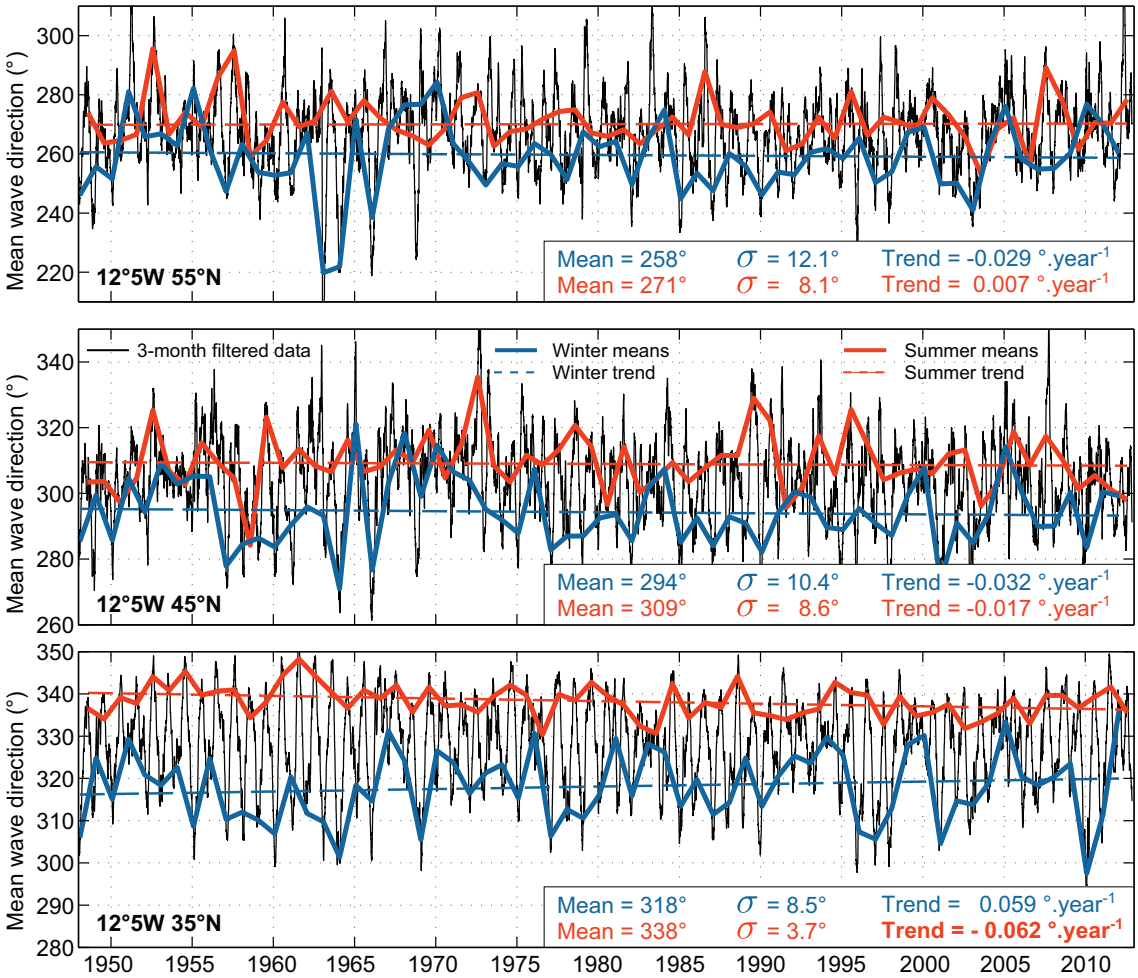

Figure 6.6: Time-series of mean wave directions at P1 (top panel), P2(middle panel) and P3 (bottom panel) from 1948 to 2013: 3-month filtered data(black line), winter averages (blue solid line) and summer averages (red solid line). The dashed lines correspond to linear regressions fitted through the winter (blue) and summer averages (red). The mean values, the standard deviations (σ) and the coefficients of the trends are given for each season (bold font type means that the trend is significant with 95% confidence).

6.3.3 Peak period

The maps of annual, summer and winter means of Tp (Fig.6.4, third column) reveal a zonal gradient with values increasing from West to East. The 3-month filtered time-series at P1, P2 and P3 shown on Fig.6.7 present a very clear seasonality with summer values around 8–9 s and winter values around 11–13 s. The seasonal changes in the atmospheric circulation over the North Atlantic Ocean is characterized by a much stronger storminess in winter than in summer, which explains the higher occurrence of long-period swells in winter. The long distances that the swells travel from northern latitudes to southern latitudes also explains the slightly larger mean values found at P3 compared to P1. At the three locations, the winter-means present significant inter-annual variabilities with standard deviations of the order of 3% of the mean values. The Tp summer-means present a low inter-annual variability, with standard deviations 40% lower than their winter counterparts. Statistically significant positive trends were found at latitudes higher than 50°N (such as for P1) for the winter-means, with values reaching up to 6 ms.year^{-1}. Similar values and spatial distributions of trends of Tp winter-means were found by *Dodet et al.* [2010] for the period 1953-2009. For the summer-means, statistically significant trends are found over most of the domain with maximum values up to 6 ms.year^{-1}.

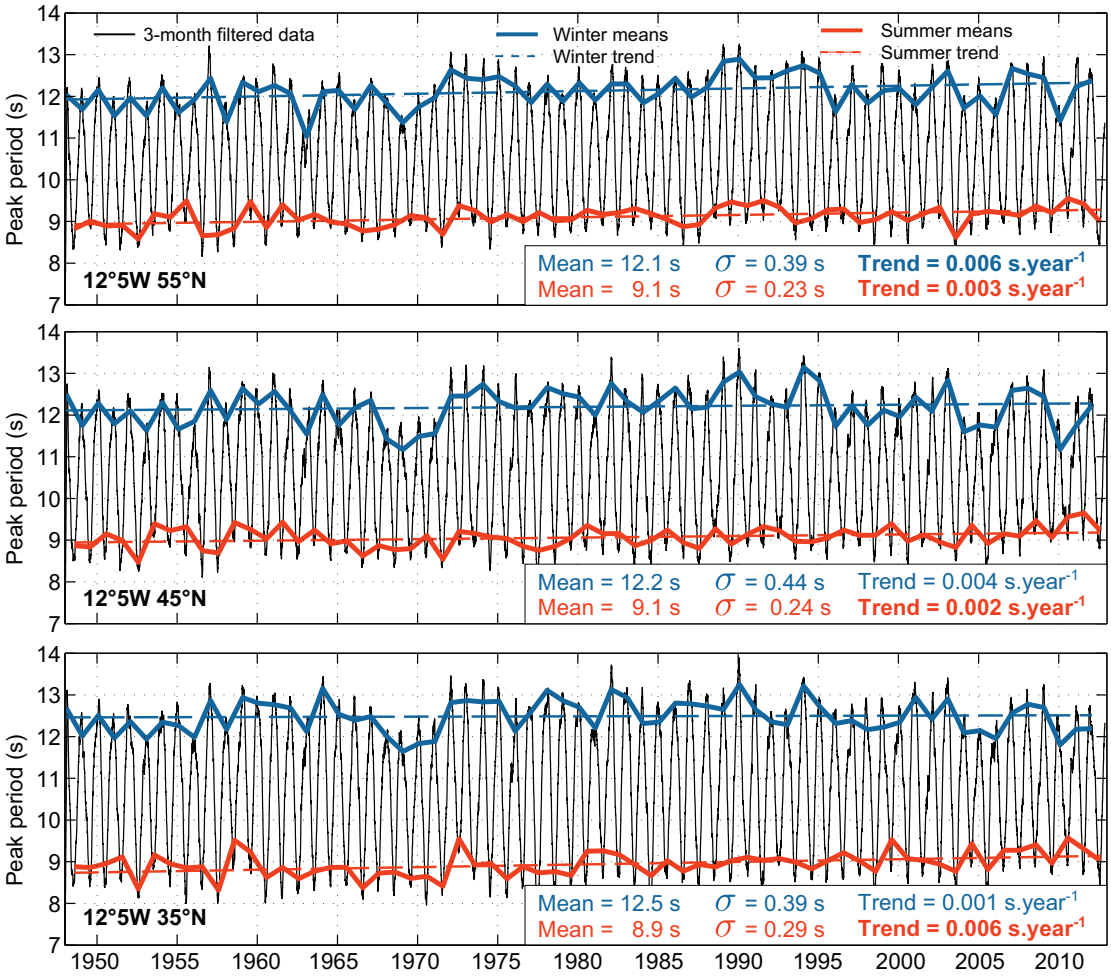

Figure 6.7: Time-series of peak periods at P1 (top panel), P2(middle panel) and P3 (bottom panel) from 1948 to 2013: 3-month filtered data(black line), winter averages (blue solid line) and summer averages (red solid line). The dashed lines correspond to linear regressions fitted through the winter (blue) and summer averages (red). The mean values, the standard deviations (σ) and the coefficients of the trends are given for each season (bold font type means that the trend is significant with 95% confidence).

6.3.4 Directional spreading

The mean values of the directional spreading are comprised between 25° and 50° and decrease from the North-West to the South-East (Fig.6.4, fourth column). The 3-month filtered signals at the three selected locations are noisy and do not present a clear seasonal cycle (Fig.6.8). On the other hand the inter-annual variability, characterized by standard deviations of the order of 2.5° in winter and 1.5° in summer, is relatively large compared to the difference between the overall average of the winter-means and summer means (around 0.8°) and hides the seasonal variability. Finally, the regression analysis performed through the winter- and summer-means did not reveal any statistically significant trends.

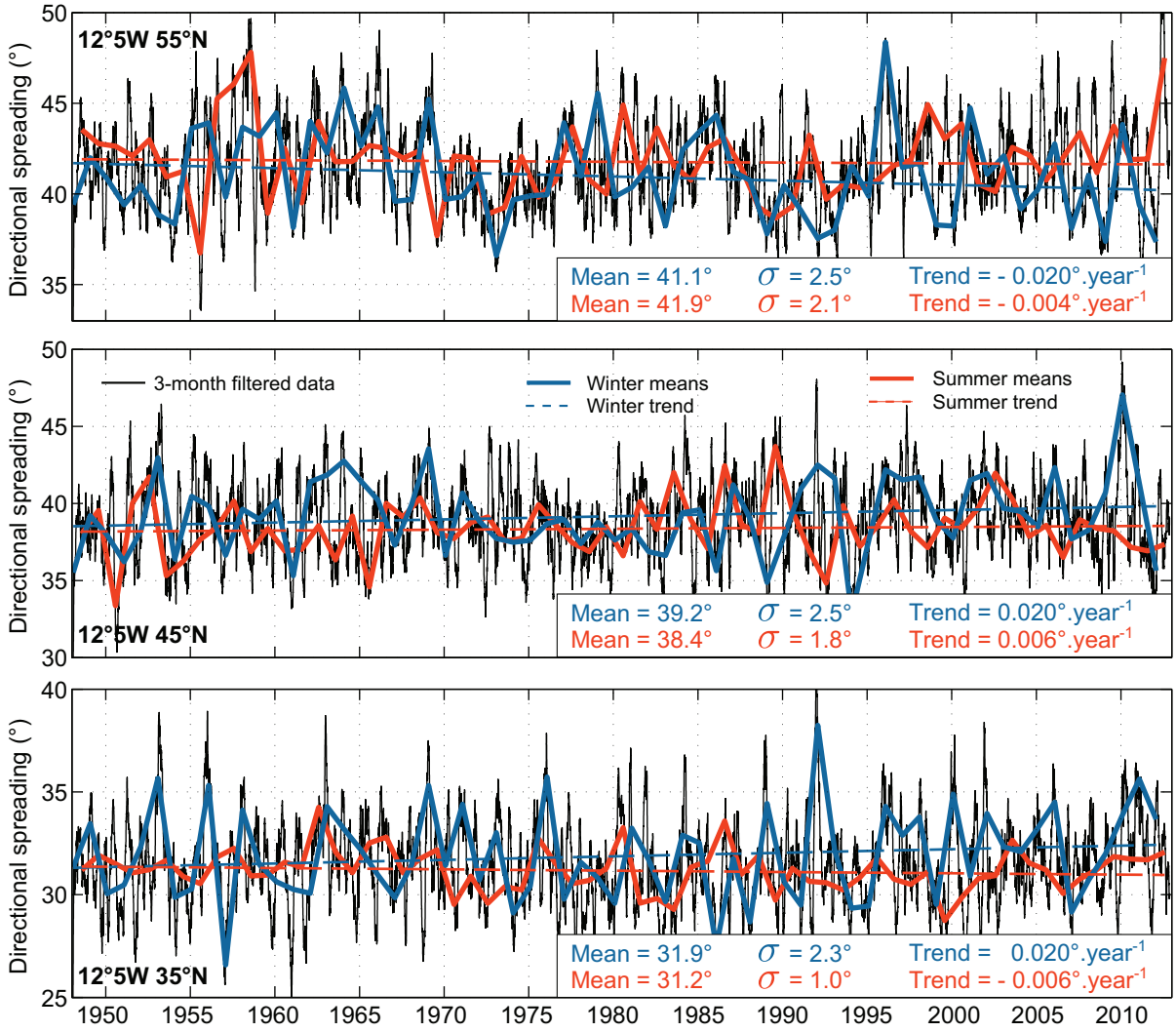

Figure 6.8: Time-series of directional spreading at P1 (top panel), P2(middle panel) and P3 (bottom panel) from 1948 to 2013: 3-month filtered data(black line), winter averages (blue solid line) and summer averages (red solid line). The dashed lines correspond to linear regressions fitted through the winter (blue) and summer averages (red). The mean values, the standard deviations (σ) and the coefficients of the trends are given for each season (none of the trends is significant with 95% confidence).

6.4 Origin of the wave climate inter-annual variability

The previous section revealed the spatial distributions of yearly and seasonal means of Hs, Mwd, Tp and Spr and the seasonal and inter-annual variabilities associated to these parameters. A clear seasonal cycle is observed for Hs and Tp from northern to southern latitudes while the seasonality of Mwd and Spr is partly hidden by the inter-annual fluctuations (except for Mwd at southern latitudes). The large inter-annual fluctuations of Hs and Mwd winter-means are believed to have strong impacts for off-shore and coastal engineering as well as for coastal morphodynamics and a better understanding of the origins of these fluctuations is of great value. The present section analyses the correlation of the wave climate with the North Atlantic Oscillation (NAO) and discusses the causes and significance of the trends obtained for each parameter.

6.4.1 Correlation with the North Atlantic Oscillation

Several authors [*Bacon and Carter*, 1991; *Bauer*, 2001; *Wang and Swail*, 2002; *Woolf*, 2002; *Bertin et al.*, 2013] have proposed that inter-annual fluctuations in Hs were controlled by the North Atlantic Oscillation (NAO). Furthermore, *Bauer* [2001] showed that Hs was better correlated with the winter NAO index than with the monthly NAO index. In order to verify these hypotheses and to extend the analysis to other wave parameters, Pearson correlation coefficients of the winter (December–March) NAO index (resp. summer (June-September) NAO index) with winter-means (resp. summer-means) of Hs, Mwd, Tp and Spr were calculated over the NEA. The NAO index of *Hurrell* [1995], based on the monthly averaged difference of normalized sea level pressure (SLP) between Lisbon, Portugal and Stykkisholmur/Reykjavik, Iceland since 1864 [*Hurrell*, 1995] was used to perform the correlations with the mean wave parameters.

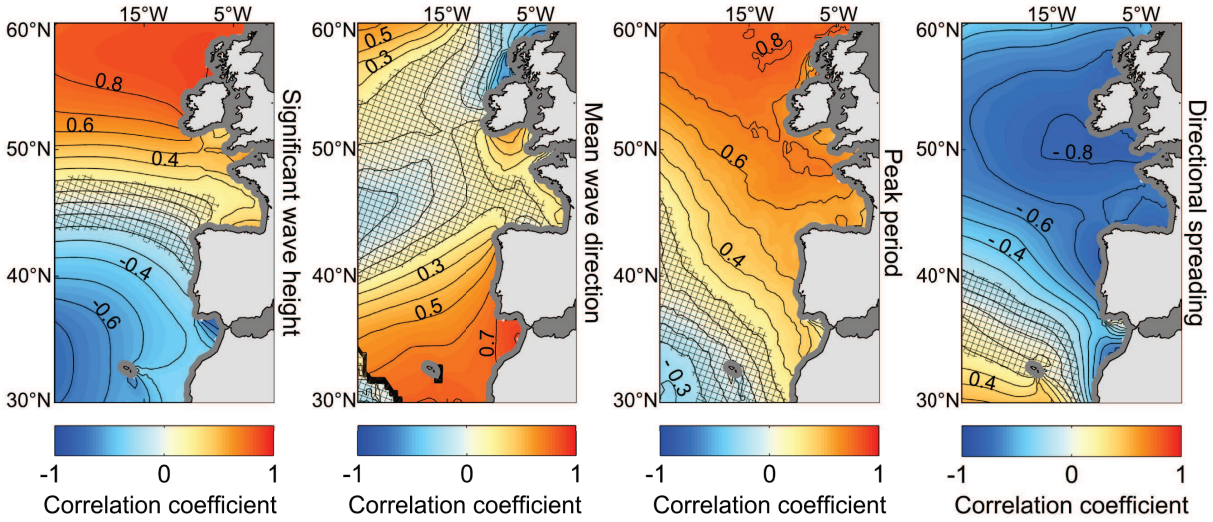

Figure 6.9: Maps of correlation coefficients between the winter NAO index and the significant wave heights (first panel), mean wave directions (second panel), peak periods (third panel) and directional spreading (fourth panel). The dark grey ribbon along the coastline indicates area where the model resolution is insufficient.

Fig.6.9 shows the contour maps of correlation coefficients between the winter NAO index and each wave parameter. For Hs, the correlation coefficients are maximal at latitudes higher than 55°N, with values exceeding 0.8 locally, and then decrease to 0 near latitude 45°N. South of 45°N, only negative correlations occur and the magnitude of the coefficients increase south-

ward up to 0.7. This spatial distribution and the values of the correlation coefficients match very well the correlation maps of *Woolf* [2002] derived from satellite altimeters from 1991 to 2000. For Mwd, strong positive correlations occur mostly at southern latitudes, with the highest coefficients (up to 0.7) located in the Gulfe of Cadiz. For Tp, strong positive correlations up to 0.8 occur at northern latitudes and decrease southward down to 0 near latitude 35°N. A similar spatial distribution of the correlation between the winter NAO index and the mean wave periods was derived from radar altimetry by *Challenor et al.* [2006] over the period 1993–2003. The weaker values obtained by these authors can be explained by the use of monthly-means instead of winter-means. Also, the correlation patterns computed herein between the winter-means of Hs, Mwd and Tp and the winter NAO index for the period 1948-2012 are very similar to the ones obtained by *Dodet et al.* [2010] for the period 1953-2009. The directional spreading, a parameter that was not investigated in the former study, shows strong negative correlations (up to -0.8) at latitudes higher than 45°N, with values decreasing southward and reaching 0 near latitude 35°N. The combination of these four maps highlights the existence of two major zones where an important part of the inter-annual variability of the wave climate is explained by the North Atlantic Oscillation: 1) north of 50°N where Hs, Tp and Spr are strongly correlated with the NAO index while Mwd is weakly correlated ; and 2) south of 40°N where Hs and Mwd are strongly correlated with the NAO index while Tp and Spr are weakly correlated. Finally, a similar analysis applied to the summer-means of the mean wave parameters and the summer NAO index (not shown here) revealed similar distributions of the correlation coefficients but with values around 0.2 lower.

As explained by *Hurrell* [1995], positive values of the NAO index are associated with larger than normal sea level pressure (SLP) gradients, due to the presence of a wide and stable anticyclone centred on the Azores Islands and deep lows crossing Iceland. *Dodet et al.* [2010] computed maps of 4-month averaged SLP field, wind field and wave spectra for two winters: one representative of a strong positive NAO phase (1989) and one representative of a strong negative NAO phase (1969). They showed that the NAO+ configuration resulted in stronger than average westerly winds across the middle latitudes, inducing very large and long-period waves with a mean western direction at northern latitudes. Southern latitudes, kept off storm area, were subjected to smaller-than-average and long-period waves coming from a very narrow north-west directional window. On the contrary, negative values of the NAO index are associated with Icelandic low- and Azores high-pressure centres weaker-than-average and with a more random spatial distribution, resulting in weaker middle latitude westerlies. For the NAO- configuration, Hs and Tp were weaker-than-average and presented a huge directional spreading at northern latitudes, while at southern latitudes Tp were medium, the directional spreading large and Hs larger-than-average. The different energy distribution in the NAO+ and NAO- averaged wave spectra at northern and southern latitudes are well explained by the averaged atmospheric state of the opposite phases of the NAO and coincide well with the correlation maps computed herein.

6.4.2 Causes and significance of the long-term trends

An important question that has been raised by numerous authors investigating the wave climate variability concerns the identification of long-term trends in the wave climate and more particularly the possibility of increasing wave heights in the NEA Ocean [*Bacon and Carter*,

1991; *Kushnir et al.*, 1997; *WASA*, 1998; *Wang and Swail*, 2002; *Dupuis et al.*, 2006; *Young et al.*, 2011; *Bertin et al.*, 2013]. Although most of these studies support the assumption of a significant increase in wave heights during the last decades at latitudes higher than 50°N, the rates of increase generally differ from one study to the other. In addition, the different periods investigated in these studies (from a decade to a century) and the choice of the representative parameters (Hs yearly means, Hs winter-means, Hs 90^{th} percentile or Hs 99^{th} percentile) make the inter-comparison of their conclusion tricky. *Young et al.* [2011] analysed a 23-year (1985-2008) database of calibrated and validated satellite altimeter measurements and found no clear trends in Hs yearly-means in the NEA Ocean but significant positive trends of the order of 0.5 cm.year^{-1} and 1 cm.year^{-1} for the Hs 90^{th} percentile and Hs 99^{th} percentile, respectively. However, the authors of this study conclude that the short-term extent of their data set make it impossible to distinguish between a steadily increasing or accelerating trend, which could be extrapolated into the future, or simply the upward portion of a multidecadal oscillation. *Bertin et al.* [2013] realized a 109-year (1900-2008) wave hindcast with a validated regional wave model covering the North Atlantic Ocean. They detected positive trends in Hs yearly means of the order of 1 cm.year^{-1} north of 50°N and found that this long-term variability was explained by an increase of the wind speed at northern latitude over the studied period.

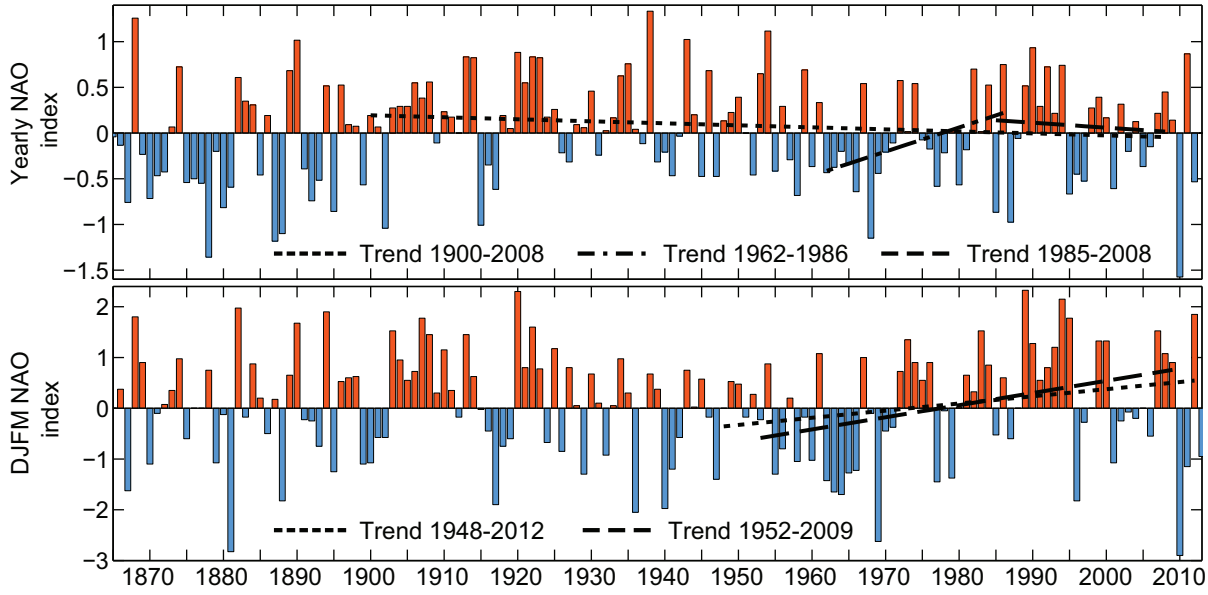

Figure 6.10: Time-series of the yearly (top panel) and winter (bottom panel) NAO indexes of Hurrell [1995] for the period 1864-2013. The linear trends computed with the yearly index for the periods 1900-2008, 1962-1986, 1985-2008, and with the winter index for the periods 1948-2012 and 1952-2009 are superimposed on the corresponding time-series.

In the present study, the strong correlations between the winter mean wave parameters and the winter NAO index promotes the idea that the detected trends during the period 1948-2012 are likely to be explained by a positive trend in the winter NAO index for the same period. In order to verify this assumption and investigate the link between the NAO variability and the trends obtained by *Bacon and Carter* [1991], *Young et al.* [2011] and *Bertin et al.* [2013], a regression analysis was performed through the yearly and winter (DJFM) NAO index of *Hurrell* [1995] for periods considered in these studies. The rates of the trends are given in Table6.2 and appear on Fig.6.10 superimposed on the corresponding NAO index. First of all, these results

highlight the lack of significant trends in the yearly and winter NAO indexes for the period 1885-2013. Then, the highest trend values obtained by *Bacon and Carter* [1991] for the Hs yearly means and by *Dodet et al.* [2010] for the Hs winter means can be explained by the significant positive trends in the corresponding NAO index for the respective studied periods. The slightly lower trends obtained in the Hs winter trends for the period 1948-2012 compared to the period 1953-2009 considered by *Dodet et al.* [2010] is in agreement with the lower trend in the NAO index for the period 1948-2012. This difference in the NAO trend is mainly due to the very low negative NAO value (the lowest of the whole record) observed in winter 2010. The null trend obtained by *Young et al.* [2011] for Hs yearly means is supported by the insignificant trend in the NAO index during the period 1985-2008. For the same period, the winter NAO index presents a larger negative trend, not statistically significant though. Notwithstanding, the corresponding Hs trend was computed for the same period at the location 12.5°W, 55.0°N and a small negative trend in Hs winter means was obtained, not statistically significant either. Finally, the 1% rate of increase in yearly Hs and Hs 99^{th} percentile obtained respectively by *Bertin et al.* [2013] for the period 1900-2008 and by *Young et al.* [2011] for the period 1985-2008, while the corresponding NAO index indicates a (not statistically significant) negative trend, indicate that other modes of variability are likely to control the trends in wave-heights. These mode of variability could explain the potential increase of Hs yearly-means over the last century obtained by *Bertin et al.* [2013], or the observed increase in Hs 90^{th} and 99^{th} percentiles shown by [*Young et al.*, 2011] for the period 1985-2008. It seems particularly relevant to understand why the variability of extreme wave heights in the NEA Ocean - unlike the annual and seasonal wave heights - was not primarily controlled by the NAO during the last decades. Further investigation is thus necessary to elucidate this new questioning.

Table 6.2: Linear trends in Hs and NAO index for several investigated periods.

Period	Study	Max. Hs trend (%)	NAO trend (%)
		Winter Hs	*Winter NAO index*
1948-2012	Present study	∼ 1	**1.4***
1985-2008	Present study	∼ -0.003	- 1.3
1953-2009	*Dodet et al.* [2010]	∼ 1.5	**2.4***
1885-2013			0.02
		Yearly Hs	*Yearly NAO index*
1962-1986	*Bacon and Carter* [1991]	∼ 2	**2.6***
1985-2008	*Young et al.* [2011]	∼ 0	- 0.5
1900-2008	*Bertin et al.* [2013]	∼ 1	- 0.2
1885-2013			0.1

* Trends indicated in bold type are significant with a 90% confidence

Regarding the other mean wave parameters selected for this study, it appears that the trends computed for the period 1948-2012 (presented in Section6.3) are generally not statistically significant with 95% confidence, which indicates that the inter-annual variability is too large and the duration of the study period (65 years) too short to identify any long-term tendency. Nevertheless, the results obtained for the peak period revealed significant positive trends at latitudes higher than 50°N for the winter-means and over most of the NEA for the summer-means. The

maximum values were around 1.5% and 1% for the winter- and summer-means respectively. Although this tendency is likely to be associated to the increase of the NAO index for the period considered herein, a correspondence with another mode of variability is not to exclude, as it is the case for Hs. The quasi-absence of published work on this question and the potential impact, although limited, for coastal engineering studies provide an interesting subject for further research.

6.5 Implications for the Albufeira Lagoon

6.5.1 Wave climatology off the Albufeira Lagoon

Monthly means and standard deviations of Hs, Mwd, Tp and Spr were computed 2 km off the Albufeira Lagoon in 30 m water depth (P4 on Fig.6.1) for the period 1948-2012 (Fig.6.11).

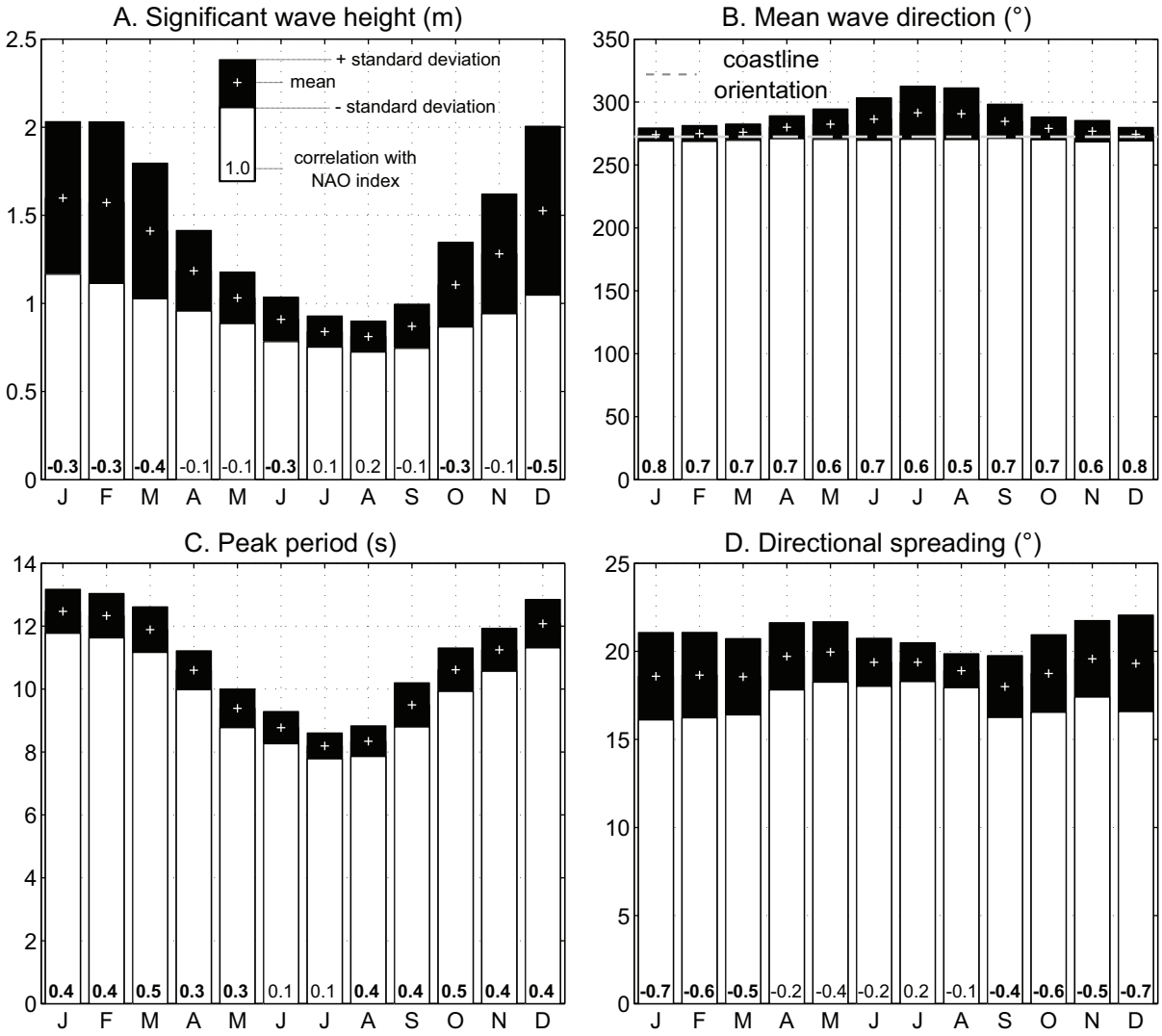

Figure 6.11: Monthly means of significant wave heights (A), mean wave directions (B), peak periods (C) and directional spreading (D) computed from 1948 to 2012. The correlation coefficients between each parameter and the monthly NAO index are given for each month (in bold font type if statistically significant with 95% confidence).

This analysis reveals a huge seasonal variability for Hs with a maximum mean value in January (1.6 m) and a minimum mean value in August (0.8 m). The standard deviation presents a

large seasonal variability with larger values during the winter period (up to 0.4 m) than during the summer period (up to 0.1 m). Such a distribution of the standard deviations is in agreement with the seasonal behaviour of the inter-annual variability obtained in the NEA Ocean. The mean values of Mwd are comprised between 274° and 292° with maximum values during the summer months. The seasonal variability of the standard deviations presents an opposite behaviour compared to the one observed in the NEA with the largest values during the summer months (up to 20°) and the lowest values during the winter months (up to 5°). This contrasting effect can be explained by the local wind seas that generally develop during the months of July and August when persistent North winds blow along the Portuguese coastlines and occasionally prevails over the gentle summer swells that arrive from the NW quadrant. This significant inter-annual variability in the Mwd monthly-means leads to incident waves that sometimes reach the shore with a negative angle of incidence, as indicated by the shoreline orientation on Fig.6.11B. This result indicates that the wave-induced longshore drift is likely to be oriented northwards occasionally. The seasonality of Tp monthly means is well pronounced, with values ranging from 8 s during the summer months to 12.5 s during winter months. The standards deviations present a limited seasonal shift from 0.4 s in summer to 0.7 s in winter.Finally the Spr monthly-means do not show any clear seasonal behaviour as observed in the NEA, corroborating the assumption that the inter-annual variability dominates over the seasonal cycle. The mean values range from 18° to 20° and the standard deviations range from 1° to 3°.

The large variability of the wave climate is believed to have severe implications for the morphodynamics of the Albufeira Lagoon. Indeed, based on 48-year time-series of hindcasted wave spectral information, *Bruneau et al.* [2011b] elaborated a statistical method to construct a set of annual wave climates that include the seasonal variability plus a random signal, corresponding to the inter-annual variability. These authors implemented a morphodynamic modelling system to the Óbidos Lagoon Inlet, a dynamic tidal inlet located hundred kilometres north of the Albufeira Lagoon, and tested the impact of the different forcings. Their results showed that the inter-annual variability of the wave climate was a dominant factor in the morphological behaviour of the inlet that evolved preferably towards different morphological configurations, depending on the wave forcing.

6.5.2 Impact of the North Atlantic Oscillation on the incident wave forcing

The 65-year model hindcast of mean wave parameters in the NEA presented in this chapter revealed significant correlations between the inter-annual variability of Hs, Mwd, Tp and Spr and the NAO. In particular, the maps of correlation coefficients (Fig.6.9) show that the central part of the Portuguese margin, where the Albufeira Lagoon is located, presents statistically significant correlations between the winter NAO index and the winter-means of every selected parameters: Hs is negatively correlated ($r = -0.3$), Mwd is positively correlated ($r = 0.6$), Tp is positively correlated ($r = 0.45$) and Spr is negatively correlated ($r = -0.5$). Since the inter-annual variability of these parameters is large and may have a significant impact on the morphodynamics of the Albufeira Lagoon, the correlations coefficients between the yearly (resp. monthly means) and the yearly (resp. monthly) NAO index were computed in front of the Albufeira Lagoon to investigate the potential impact of each phase of the NAO on the incident

wave forcing. The correlation coefficients obtained for the yearly values, namely -0.3 for Hs, 0.5 for Mwd, 0.4 for Tp and -0.5 for Spr, are in close agreement with the values obtained with the regional model. The analysis on the monthly-means (the values are indicated on Fig.6.11) reveals an interesting monthly variability with higher correlations occurring generally in the winter season, with coefficients reaching -0.5, 0.8, 0.5 and -0.7 for Hs, Mwd, Tp and Spr, respectively.

In order to investigate the impact of positive and negative NAO phases on the wave climate at the Albufeira Lagoon, maps of mean wave parameters were realized for two representative years, based on the results of the local SWAN model. The month of December appeared to be a good candidate to illustrate the largest changes in the mean wave parameters induced by one or the other NAO phase. Indeed, this month presents the largest overall standard deviations and correlation coefficients. According to the monthly NAO index of *Hurrell* [1995] for the period 1948-2012, December 2010 corresponds to the lowest values, while December 2011 corresponds to the highest value of the record. The monthly averages of Hs, Mwd, Tp and Spr are represented on Fig.6.12.

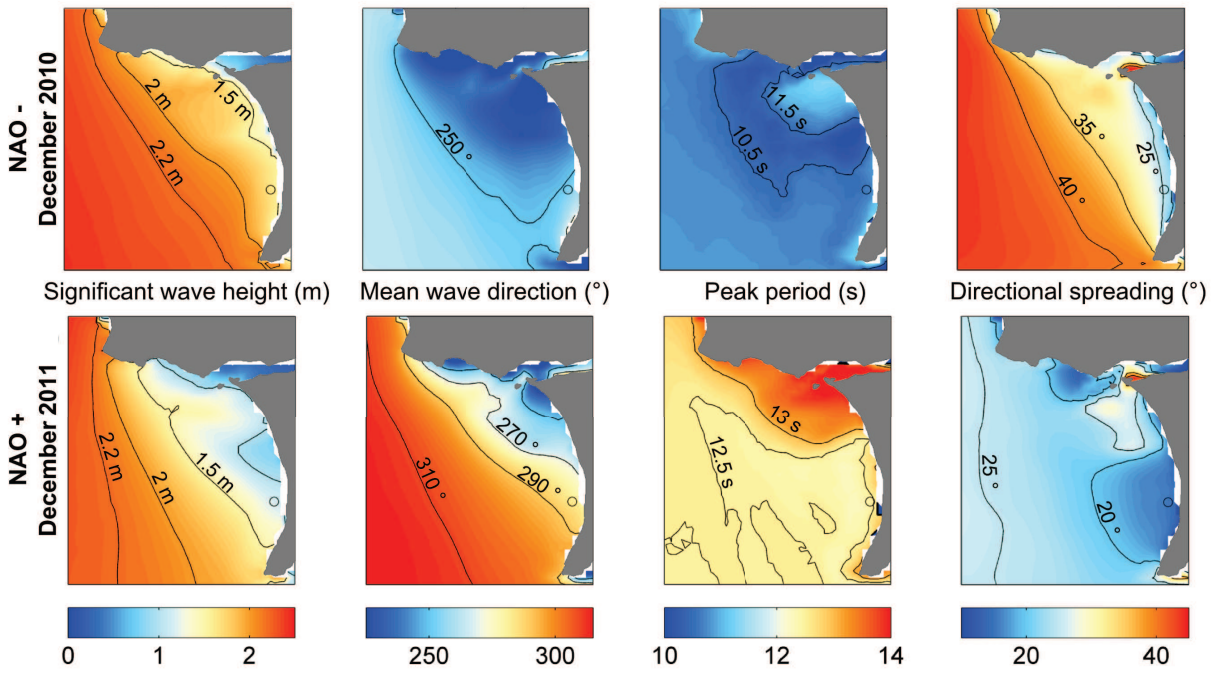

Figure 6.12: Maps of averaged significant wave height (first column), mean wave directions (second column), peak periods (third column) and directional spreading (fourth row) computed for the month of December 2010, representative of a NAO- configuration (upper panel) and for the month of December 2011, representative of a NAO+ configuration (lower panel) for the local model domain. The circle indicates the position of the node in the model domain used to analysis the wave climate at the Albufeira Lagoon.

For the NAO+ representative month (lower panel), the waves reach the Albufeira Lagoon with a mean Hs comprised between 1 m and 1.5 m, a mean direction comprised between 270° and 290°, a mean peak period of around 12.5 s and a mean directional spreading lower than 20°. Compared to the NAO+ representative month, the incident waves during the NAO- representative month (upper panel) are characterized by a higher mean Hs (between 1.5 m and 2 m), a much lower mean direction (around 250°), a lower peak period (around 10.5 s) and a wider directional spreading (around 25°). These results are in close agreement with the correlation coefficients

computed for the period 1948-2012 between the monthly mean wave parameters and the monthly NAO index, and they indicate that the NAO significantly affects the local wave climate at the Albufeira Lagoon. During months of large negative NAO index values, the waves are particularly energetic, with a farther-south-than-average direction, wider-than-average directional spreading, and lower-than-average peak periods. Among the four selected mean wave parameters, Hs and Mwd are known to have the strongest impact on the morphodynamics of the coastline. In particular, large waves with a high incidence angle will induce strong longshore currents that will carry along large quantities of sediments. On the contrary, small waves with a direction normal to the coastline will have a weak impact on the longshore currents and the associated sediment transport. At the specific location of the Albufeira Lagoon, it is observed that not only can the amplitude of the longshore transport be affected by the NAO phase (positive or negative) but also the direction of the transport. Indeed, a well defined NAO- configuration seems to promote a strong northward transport, while other NAO configurations (positive or near-zero index value) will promote a weak-to-large southward transport. Eventually, these results emphasize the key role of the inter-annual variability of the wave climate - highly controlled by the NAO - for the morpho-sedimentary dynamics of the Albufeira Lagoon inlet and provide a first means of explanation for the high variability of the life-span of the open state of the inlet observed by the local authorities.

Summary

The morphodynamics of wave-dominated tidal inlets is greatly affected by the wave climate, whose large seasonal and inter-annual variabilities are believed to alter the geomorphic mechanisms controlling these environments. Understanding the wave climate variability has kept many scientists busy during the last four decades. In particular, the question of a potential increase in wave heights in the North Atlantic Ocean, suggested by the data measured between 1962 and 1986 by shipborne wave recorders, has launched several collaborative projects whose goal was to elucidate this crucial issue. The first section of this chapter, summarized the major results of former studies on the wave climate variability in the North Atlantic Ocean.

A wave modelling system was setup to produce 62-year (1948-2012) times-series of mean wave parameters at a regional scale, corresponding to the North-East Atlantic Ocean, and at a local scale, corresponding to the central region of the Portuguese coast where the Albufeira Lagoon is located. Annual and seasonal averages of significant wave heights, mean wave directions, peak periods and directional spreading were computed over the regional and local domains in order to investigate the spatial and temporal variability of the wave climate at these two scales. The second section of this chapter described the modelling strategy and the validation of the model results against buoy observations.

In a third section, contour maps of the selected mean wave parameters computed with the regional model revealed the meridional distribution of the wave heights and directions and the zonal distribution of the peak period and directional spreading. Time-series of the summer and winter-means highlighted the clear seasonality of the significant wave heights and peak periods and the more noisy signals for the mean wave direction and directional spreading. A large inter-annual variability was observed for each parameter and significant positive trends were found at latitudes higher than 50° for the wave heights and the peak periods.

The fourth section presented maps of correlation coefficients between each parameter and the North Atlantic Oscillation index. Medium-to-strong correlations (positive or negative) were obtained for every parameters, indicating a large control of the inter-annual variability of the wave climate by the North Atlantic Oscillation. The long-term increase in wave heights presented herein and in former studies were principally explained by the trends in the North Atlantic Oscillation index.

Finally, a climatology of the waves near the Albufeira Lagoon was realized from the results of the local model. Monthly values and standard deviations of the wave parameters provided information on their respective seasonal and inter-annual variabilities, and medium-to-large correlation coefficients with the North Atlantic Oscillation index confirmed the results obtained with the regional model. More particularly, negative phases of this index are associated to waves larger than during positive phases, with farther south directions, lower peak periods and a wider directional spreading. These significant changes in the overall wave forcing are believed to have a determinant impact on the morphological behaviour of the tidal inlet. Indeed, not only the intensity of the littoral drift is affected but also the directions is likely to reverse during specific events.

Chapter 7

Wave-current interactions

Wave-current interactions play a central role in the dynamics of wave-dominated tidal inlets. Indeed, when the waves reach the mouth of the inlet and the adjacent beaches they generate longshore and crosshore currents that directly impact the tidal currents and the associated sediment dynamics. Conversely, the tidal currents affect the propagation of the incident waves through several mechanisms such as steepness-induced breaking, Doppler shifting or blocking. These complex interactions between the waves and the currents are highly non-linear and their investigation presents a real challenge for the scientific community. In particular, the development and application of numerical modelling systems able to reproduce accurately the complex interactions between waves and currents constitute an important avenue for scientific research in the field of coastal engineering. After a brief presentation of previous studies on wave-current interactions, this chapter investigates the hydrodynamics of the Albufeira Lagoon tidal inlet through *in-situ* data analysis and applications of the wave-current modelling system. First, the accuracy of the boundary forcing is assessed by comparing the model results against tide gauge and buoy observations. Then, the impacts of the waves on the currents and the impact of the currents on the waves are investigated through analysis of *in-situ* observations and model results and cross-comparisons between them. Finally, the limitations of the modelling systems are discussed and the main findings are summarized. Most of the results presented in this chapter were published in March 2013 [*Dodet et al.*, 2013].

7.1 Previous studies on the wave-current interactions

The hydrodynamics of wave-dominated tidal inlets, when freshwater inflow is negligible, is controlled mainly by the combined effect of tides and waves. The ebb and flood currents interact with the incident wave field to give rise to complex patterns of currents and waves in the vicinity of the inlet mouth and adjacent beaches. The mechanism of such interactions in a two-dimensional framework was formulated by *Longuet-Higgins and Stewart* [1964] who introduced the radiation stress concept and proved the existence of the momentum transfer between waves and currents. The impact of the waves on the hydrodynamic of tidal inlets has been investigated by several authors [*e.g. Bertin et al.*, 2009a; *Olabarrieta et al.*, 2011]. Based on model results, *Olabarrieta et al.* [2011] identified the effects of waves on the circulation of Willapa Bay, Washington State. They showed that the most relevant effect on hydrodynamics of the tidal inlet was a wave-induced setup in the inner part of the estuary. *Bretherton and Garrett* [1967] formulated the wave action equation for directional wave spectra in slowly varying media, and *Huang et al.*

[1972] described the effects of currents on the wave energy spectral shape. Several experimental studies were conducted in wave flumes [*e.g. Thomas*, 1981; *Lai et al.*, 1989; *Chawla*, 2002] or offshore basins [*e.g. Guedes Soares and de Pablo*, 2006] to investigate the evolution of wave characteristics under the influence of currents. Observations of the effects of currents on waves in natural environments are also mentioned in several studies [*Wolf and Prandle*, 1999; *Rusu et al.*, 2011; *van der Westhuysen*, 2012], yet they are still too sparse to give a significant overview of this mechanism in complex coastal systems such as tidal inlets. The process of wave blocking when a wave front encounters a strong facing current has been the subject of several studies [*Lai et al.*, 1989; *Chawla*, 2002; *Suastika*, 2012] but remains difficult to reproduce with numerical models. *Ardhuin et al.* [2012] realized an inter-comparison of the performance of numerical models in conditions with strong currents. They found that for current variations on small scales, the rapid steepening of the waves enhanced wave breaking. The different parameterizations for steepness-induced dissipation produced very different results, none being fully satisfactory, which pointed to the need for more measurements and further refinements of parameterizations.

7.2 Description of the hydrodynamic conditions

7.2.1 Modelling setup

The implementation of the modelling system in the Albufeira Lagoon involved three nested grids (two coarse regular grids and one fine rectilinear grid) for the wave model and one unstructured grid for the circulation model. The spatial resolutions of the different domains are given in Table 7.1 and their extents are shown in Fig.7.1. This domains' setting was defined so that optimal computation time meets the high resolution ($\sim$ 1 m) required to accurately reproduce the flow and the wave propagation in the narrow channels and the wave-breaking dissipation over the steep slope of the beach. The waves were updated every 5 min in order to avoid abrupt variations in the water level and currents read by SWAN, from one simulation to another.

Table 7.1: Computational grids of the modelling system.

Grid name	Type	Nodes	Min. resolution (m)	Max. resolution (m)
SWAN1	Regular	1360	1000	1000
SWAN2	Regular	756	200	200
SWAN3	Rectilinear	5720	90	2.5
SELFE	Triangular	28832	1000*	3.5

* The resolution corresponds to the mean length of the sides of the triangle.

The first grid of the wave model was forced at its external boundaries by 10 km spaced wave spectra generated by the WW3 regional model implemented for the North-East Atlantic Ocean by *Dodet et al.* [2010]. Each nested grid reads the forcing wave spectra computed by its parent grid and ran sequentially to provide spectral forcing for the finer nested grid. The six-hourly ERA-Interim wind fields [*Dee et al.*, 2011] were used to force the wave models. The spectral grids for the regional (WW3) and local wave models (SWAN) used 30 regularly spaced directions and 40 frequencies exponentially spanning the 0.03–0.5 Hz range. The water level provided to the

SWAN model was uniform for the two coarse grids and corresponded to the water level computed by SELFE at the previous iteration at an offshore location ($\sim$ 20 m deep), while the finest grid used the space-variable elevation field computed by SELFE. The physical processes taken into account in the wave model were whitecapping dissipation [*van der Westhuysen et al.*, 2007], including an enhanced dissipation term for breaking dissipation on negative current gradients [*van der Westhuysen*, 2012] whose calibration coefficient was set at 5, bottom friction (default Madsen coefficient, 0.05), depth-induced breaking (constant breaker height to water depth ratio $\gamma = 0.73$), and quadruplet and triad wave-wave interactions. Spectral outputs, computed in the fixed frame, were retrieved after each run (every 5 min) and were used to compute both H_s and T_p. The time series of H_s and T_p were then interpolated on the same time index as the data.

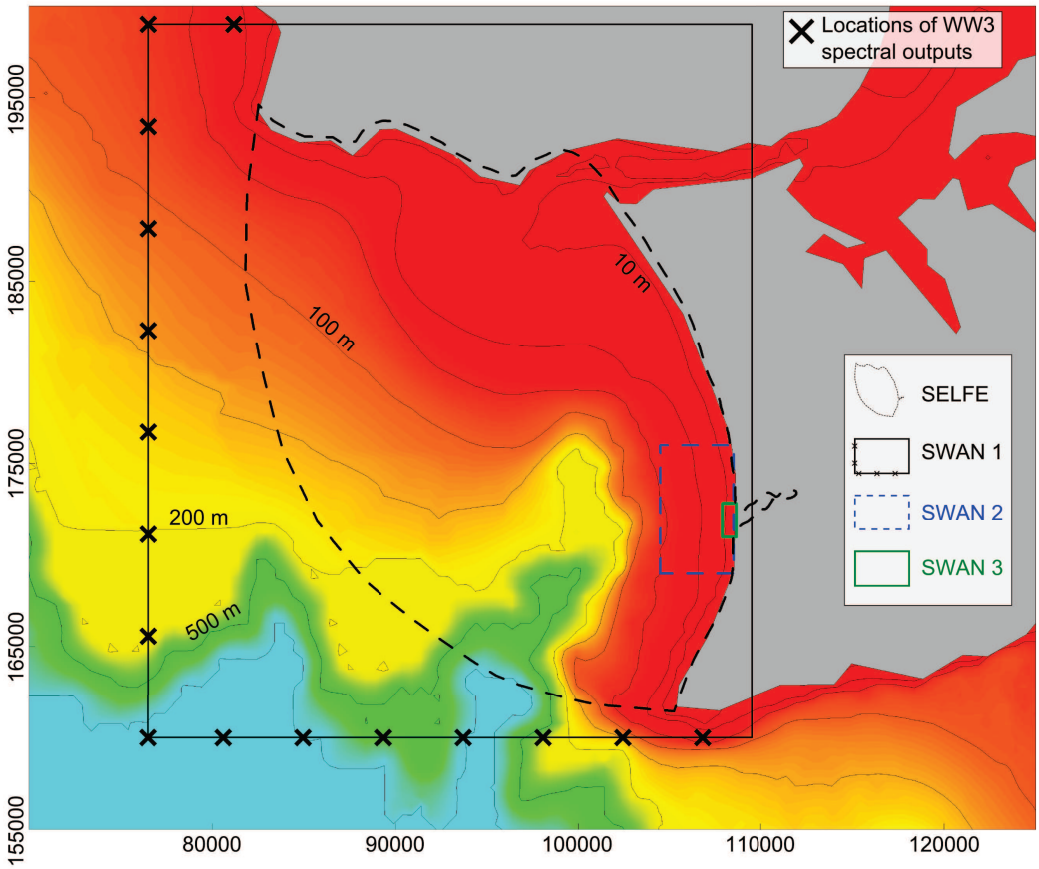

Figure 7.1: Limits of the computational grids of the hydrodynamic model (SELFE) and the wave models (SWAN 1, SWAN 2, and SWAN 3), locations of the WW3 spectra and bathymetry [Dodet et al., 2013].

The SELFE model ran in 2-D barotropic mode on an unstructured triangular grid. The resolution of the grid is maximal (3.5 m) in the channel and along the beaches adjacent to the inlet, where the currents are strong and the depth and current gradients are the largest. The grid extension (dashed black line in Fig.7.1) covers in particular the whole surface area of the inlet-lagoon system, including dry zones like barrier dunes and surrounding lands. The wetting/drying algorithm for shallow areas in SELFE allows the intertidal zone to be alternatively wet or dry whether the total depth at the nodes is above or below a specified minimum threshold (1 cm here). The model was forced at its ocean boundary by 16 tidal constituents whose amplitude and phase were computed with the regional model described in *Bertin et al.* [2012a]. The upstream boundary in the lagoon was defined as a closed boundary since freshwater inflow is negligible.

Five day simulations, including a 1 day ramp-up, with a hydrodynamic time step of 20 s produced outputs of sea surface elevation, velocities, and variance density spectra, saved every 5 min over the domain. The coefficient of *Battjes* [1975] for wave-induced eddy viscosity was set to 0.5. Three configurations of the modelling system were defined for this study: config.1 refers to a simulation without wave; config.2 refers to a simulation with waves, when the wave model reads the elevation field computed by the circulation model but does not read the current field; and config.3 refers to a simulation with waves, when the wave model reads both the elevation and the current field computed by the circulation model. The effect of the wave radiation stresses on the circulation was included in both config.2 and config.3.

7.2.2 Inlet hydrodynamics

This section describes the external forcing that controls the dynamics of the Albufeira Lagoon as well as the hydrodynamic conditions at the inlet during the field campaign. Both numerical results and data time series were analysed and compared in order to highlight the main characteristics of the inlet hydrodynamics.

Incident forcing

The model results were compared to a data set of sea surface elevations and wave parameters representative of the off-shore conditions in order to validate the forcing used to feed the model. The data used to validate the incident modelled tide is a 1 year (2010) time-series of tide gauge measurements at the Cascais marina. After harmonic analysis was applied to the data, a 1 month synthetic tide was reconstructed from the 16 main computed amplitudes and phases and compared to the modelled elevation at the corresponding period and location (Fig.7.2, first panel). The comparison between model and data showed an excellent agreement, with a root mean square error (RMSE) of 0.02 m. The modelled elevation was also compared directly to the measured elevation in order to estimate the contribution of the atmospheric forcing. For the entire month, the RMSE was 0.06 m, and for the 2 days of the campaign, the RMSE was 0.04 m.

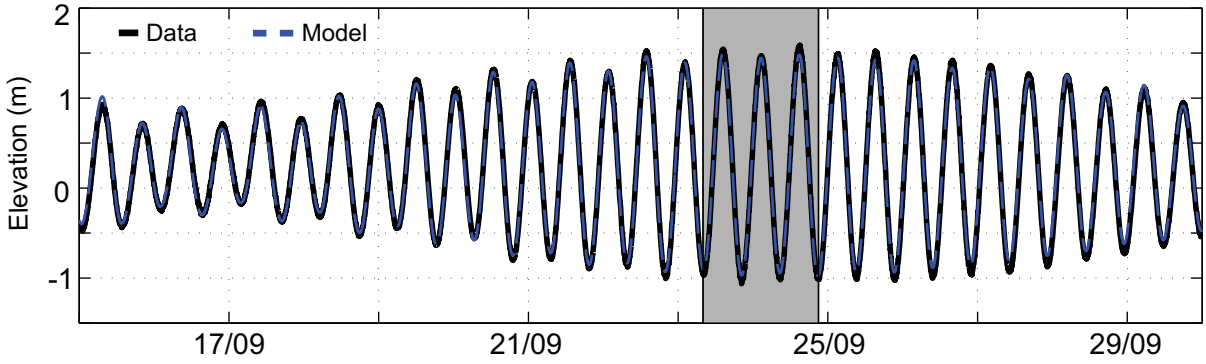

Figure 7.2: Comparison between observed (black line) and modelled (blue dashed line) sea surface elevation at Cascais between 15 and 30 September 2010 [adapted from Dodet et al., 2013]

The modelled H_s, Mwd, and T_p were compared to a 4 month time series of wave data measured by a Triaxys buoy located at the entrance of the Tagus estuary. The respective RMSE were 0.29 m, 20.0°, and 1.83 s, and the scatter indexes (SI) were 17.6% and 15.9%, for H_s and

T_p respectively. Since no data were available at this wave buoy during the field work period, model outputs were also compared to wave data measured 100 km south and 250 km north of the study location and showed similar results for this period.

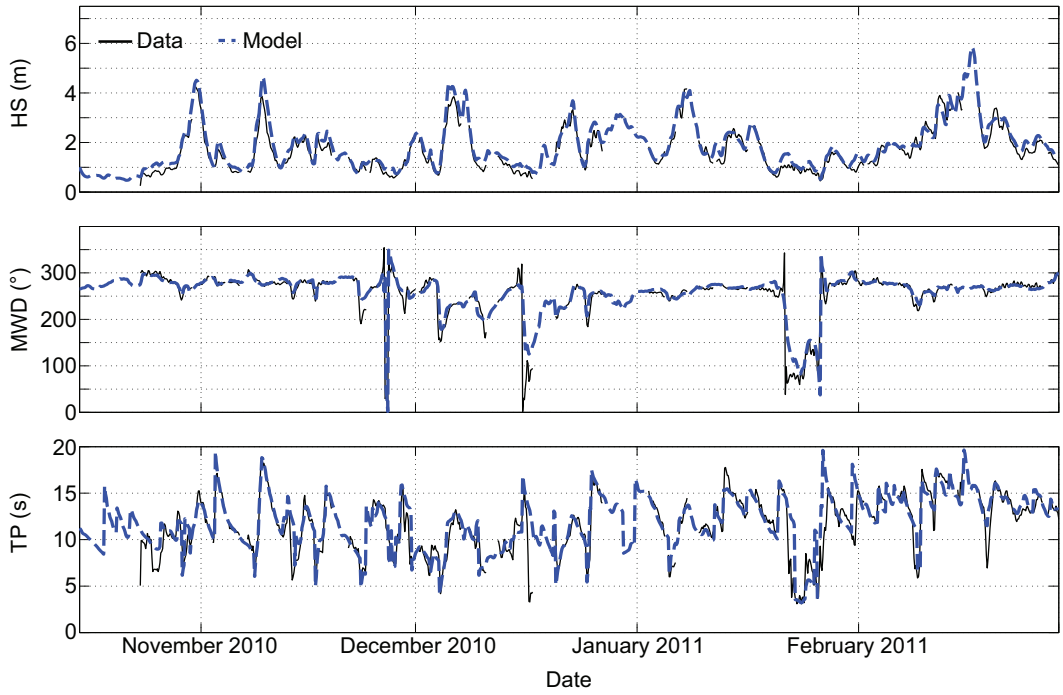

Figure 7.3: Mean wave parameters computed in front of the inlet 5 km off the coast at 150 m water depth between 15 and 30 September 2010: significant wave height (top panel), peak period (middle panel), and mean wave direction (bottom panel) [adapted from Dodet et al., 2013].

Waves at the inlet

The time series of elevation measured by the three pressure transducers were used to compute variance density spectra and the mean wave parameters H_s and T_p during the field work period in order to compare them with the model results (Fig.7.4, 7.5 and 7.6). At each location and during each tidal cycle, the measured H_s signal varied strongly in time, with the lower values (respectively higher) occurring at minimum (respectively maximum) water depth (Fig.7.4). This tide-modulated shape of H_s is characteristic of the depth-induced breaking process and indicates that the instruments recorded waves which had already broken over the shallow bottom. For PT2 and PT3, H_s dropped faster during the ebb phase of each tidal cycle than it rose during flood, whereas it evolved symmetrically at PT1. At PT1, PT2, and PT3, maximum H_s were respectively 1.30, 0.16, and 0.39 m and occurred on 24 September when the oceanic tide and the offshore wave height were the highest.

The peak period did not display such a large spatial variability as for H_s, with mean values very similar for the three sensors (Fig.7.5). The time variation of T_p was characterized by a strong shift between the first and the second tidal cycle, with values increasing from 10–15 s to 20–25 s. When H_s was very low, values of T_p were systematically exceeding (30 s) the frequency range of gravity waves. For this reason, both measured and modelled T_p were discarded if H_s was lower than 0.02 m.

The modelled H_s with config.2 and config.3 exhibited some significant differences (Fig.7.4). The parabolic shape of H_s in config.2 was rather symmetric for the three locations while it was

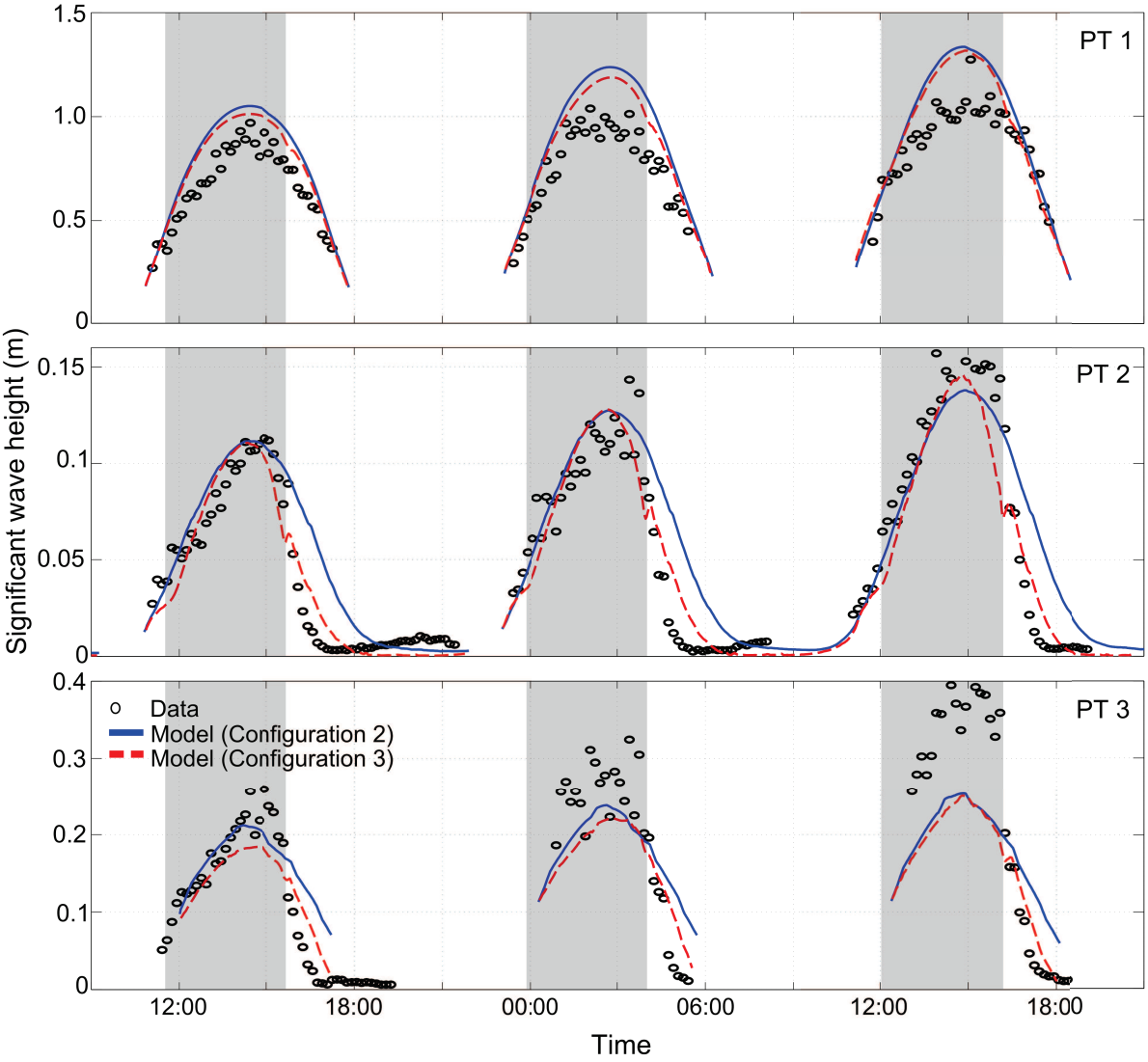

Figure 7.4: Comparisons between modelled and measured significant wave heights at (top) PT1, (middle) PT2, and (bottom) PT3 at the Albufeira Lagoon on 23–24 September 2010. The grey areas indicate flood tide when modelled currents flow toward the lagoon [Dodet et al., 2013].

asymmetric (negative skew) for the two locations in the inlet (PT2 and PT3) when the currents were included in the simulation (config.3). The amplitude of H_s was almost always higher when the currents were not taken into account. The comparisons with the data clearly showed a better match for config.3, especially during the ebb stage at PT2 and PT3 when H_s dropped quickly. The large bias observed between the data and the model during the last tidal cycle at PT3 was attributed to bathymetric changes that occurred during the campaign, particularly near the sand spit where PT3 was located, that were not taken into account in the model. The statistical errors between measurements and model results for H_s are given in Table 7.2.

Regarding the comparisons of T_p, both model configurations matched the data well and captured the transition from the 12 s swell to the 20 s swell (Fig.7.5). The difference between config.2 and config.3 indicates that the currents had an impact on the modelled wave propagation. The statistical errors between measurements and model results for T_p are given in Table 7.3.

To get a better insight on wave energy variation in the inlet and model capabilities, time series of variance density (referred hereafter as energy) spectra at PT1 and PT2, computed from data and model outputs, were plotted and compared with each other (Fig.7.6). The main spectral characteristic deduced from the data was the presence of large amounts of energy not only at the offshore peak frequency f_p, but also at lower frequencies than f_p, corresponding to infra-gravity waves, and at harmonic frequencies, near $2f_p$ and $4f_p$. During the ebb stage, an abrupt decrease of energy was noticed at PT2 starting from the higher frequencies and generalizing to all frequencies in a short time, while the energy distribution at PT1 appeared to be less influenced by the tidal stages.

The modelled spectral energy showed important differences depending on whether the current

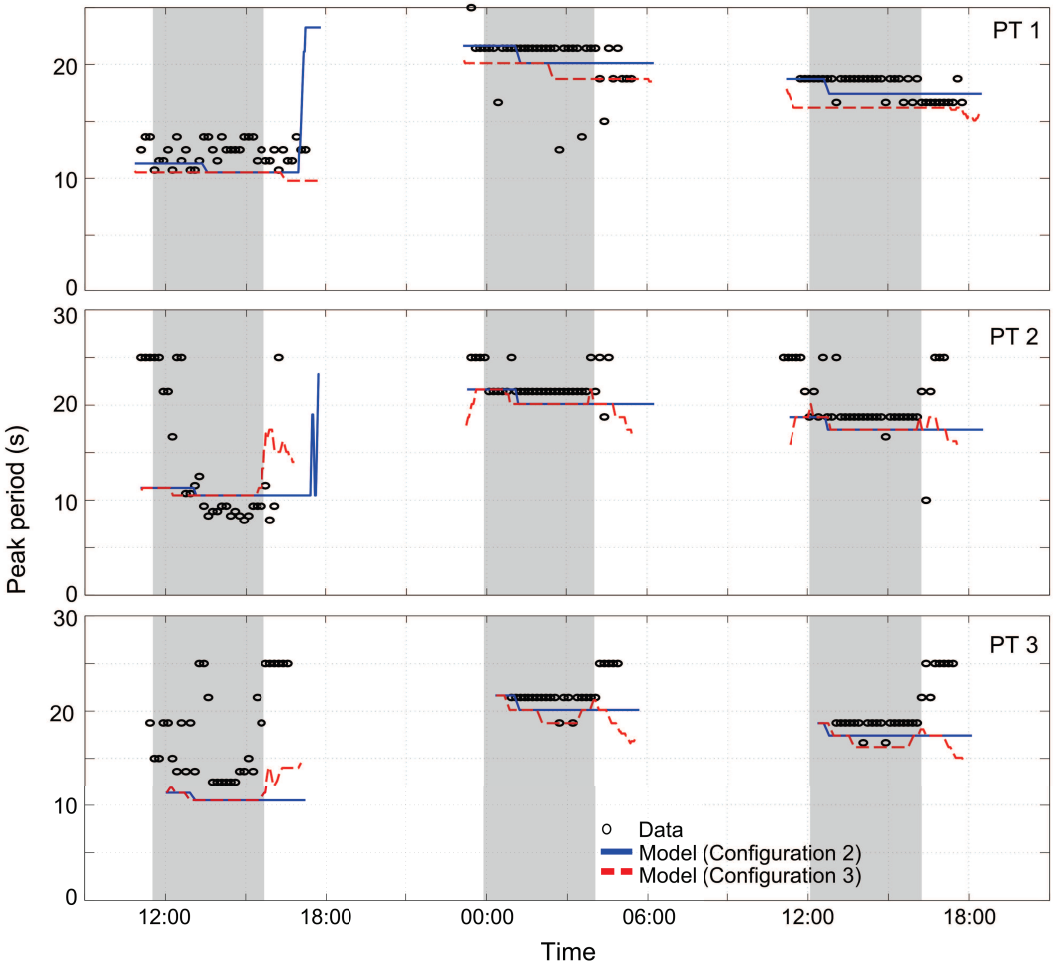

Figure 7.5: Comparisons between modelled and measured peak period at (top) PT1, (middle) PT2, and (bottom) PT3 at the Albufeira Lagoon on 23–24 September 2010. The grey areas indicate flood tide when modelled currents flow toward the lagoon [Dodet et al., 2013].

was taken into account in the wave propagation model (config.3) or not (config.2). For both locations, it appeared that the spectral energy was more diffused over the frequencies when current feedback was activated. In particular the energy patches at f_p, $2f_p$, and $4f_p$ were always less pronounced for config.3; and, in general, the spectral energy modelled with config.3 had more similarities with the measured spectral energy. Also, at PT2, the energy decrease during the ebb tide occurred much sooner compared to config.2, which resembled much better the patterns in the data.

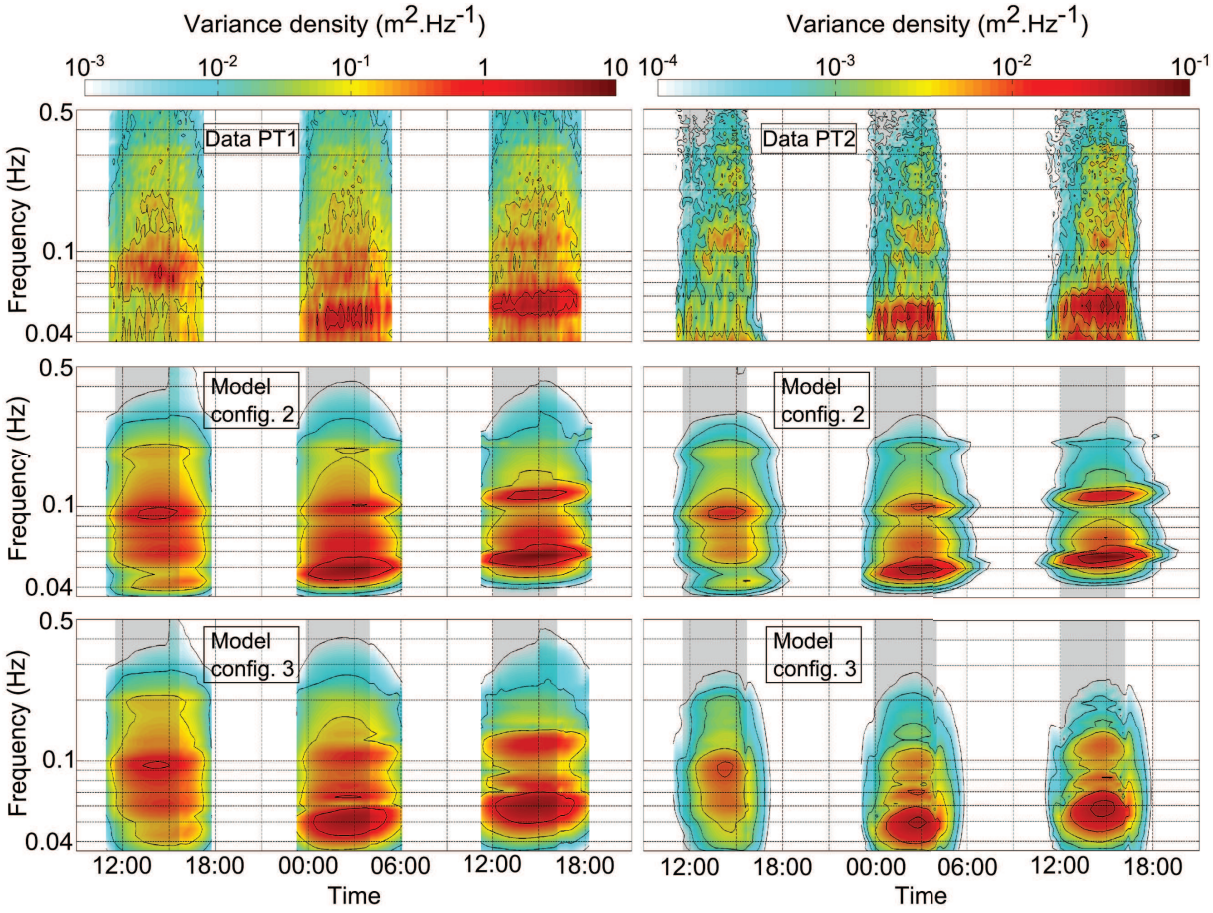

Figure 7.6: Time series of variance density spectra at (left column) PT1 and (right column) PT2 computed from the (top row) data and from the model with (middle row) config.2 and (bottom row) config.3 at the Albufeira Lagoon on 23–24 September 2010. The grey areas indicate flood tide when modelled currents flow toward the lagoon [Dodet et al., 2013].

Table 7.2: Statistical errors between data and model results for H_s.*

	Configuration 2			*Configuration 3*		
	Bias (cm)	RMSE (cm)	SI (%)	Bias (cm)	RMSE (cm)	SI (%)
PT1	15.9	18.5	24.1	12.4	15.3	20.0
PT2	0.9	2.3	40.9	- 0.3	1.6	27.8
PT3	- 1.7	7.9	40.1	- 3.9	7.7	38.6

* RSME: Root Mean Square Error; SI: Scatter Index.

Table 7.3: Statistical errors between data and model results for T_p.*

	Configuration 2			*Configuration 3*		
	Bias (s)	RMSE (s)	SI (%)	Bias (s)	RMSE (s)	SI (%)
PT1	- 0.4	2.1	12.4	- 1.6	2.2	13.2
PT2	- 2.4	4.9	25.7	- 2.2	5.0	26.3
PT3	- 4.0	5.9	29.7	- 4.3	5.7	28.4

Water level at the inlet

The water level measured by the pressure transducers was compared to the model results to assess the model performance in terms of prediction of the sea surface elevation (Fig.7.7). For the three tidal cycles, the maximum measured elevations at PT1 — where the oceanic tide was not subjected to significant changes — were respectively 1.48, 1.41, and 1.61 m. Through the inlet (PT2 and PT3), the maximum elevations decreased on average by 10%. Moreover, the tidal signal was strongly distorted as it passed through the inlet and the flood duration became much shorter (5 h) than the ebb duration (7.5 h).

The model results of config.2 and config.3 exhibited very minor differences (the mean bias and

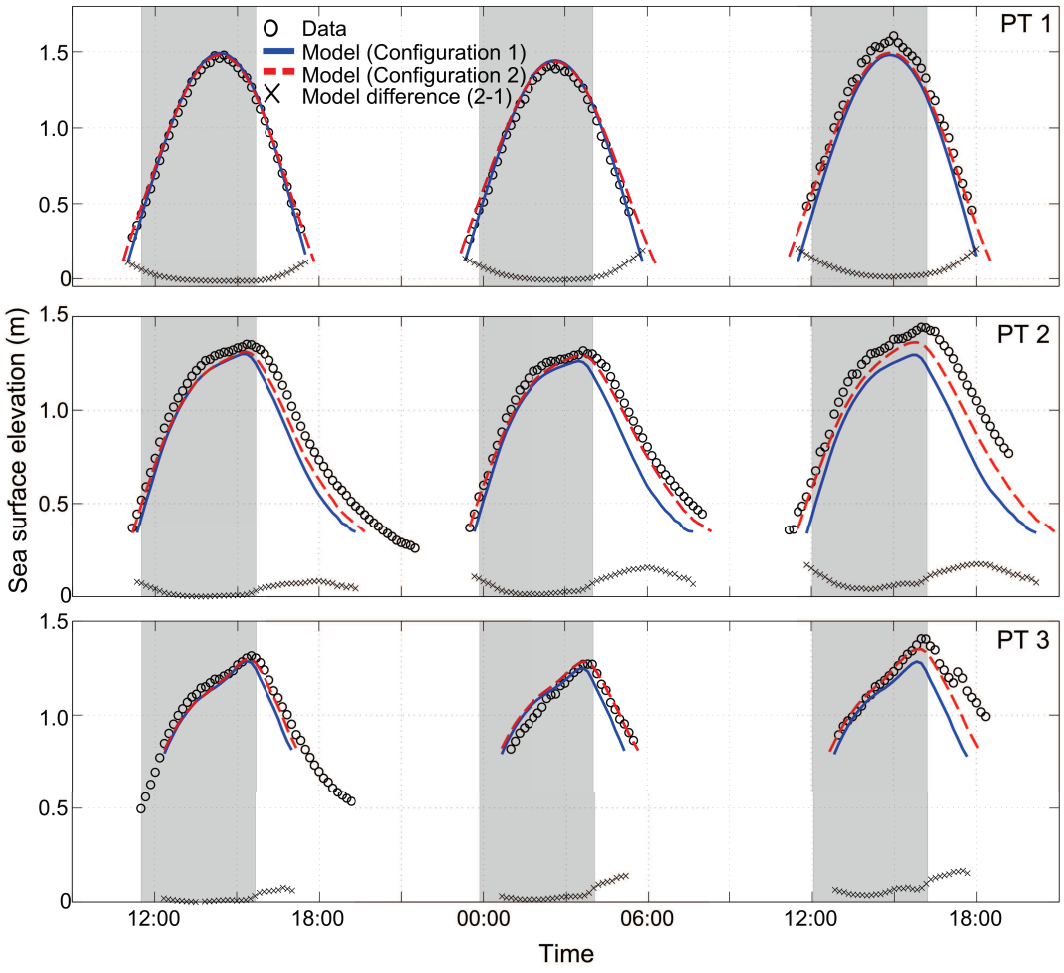

Figure 7.7: Comparisons between modelled and measured sea surface elevation at (top) PT1, (middle) PT2, and (bottom) PT3 at Albufeira lagoon on 23–24 September 2010. The grey areas indicate flood tide when modelled currents flow toward the lagoon [Dodet et al., 2013].

Table 7.4: Statistical errors between data and model results for the elevation.*

	Configuration 2		*Configuration 3*	
	Bias (cm)	RMSE (cm)	Bias (cm)	RMSE (cm)
PT1	- 2.5	7.2	1.3	5.1
PT2	- 14.4	16.7	- 7.6	8.9
PT3	- 6.2	10.9	- 1.9	7.2

RMSE were smaller than 1 cm for the three locations), so only config.2 was used for comparison

with config.1 in Fig.7.7. The comparisons between the model results displayed some significant differences: the elevation in config.2 was always higher than in config.1 (mean difference = 0.04 m), and the largest differences always occurred when the oceanic tide was near the mean sea level (maximum difference = 0.23 m). The comparison with the data showed that the model results of config.2 reproduced the elevation more accurately, decreasing the mean RMSE by 40% (Table 7.4).

Velocity at the inlet

In order to validate the modelled velocity, the currents measured by ECM2 were compared to the model results (Fig.7.8). This data set was the only one which could be exploited. Indeed the measurements of the current profiles by the ADCP, located in the surf zone most of the time, were skewed because of the turbulence induced by the wave breaking process. Moreover ECM3 got buried during the first tidal cycle and its subsequent displacement resulted in a very heterogeneous set of data that was not usable. For a tidal cycle, on average, measured flood velocities lasted 4.3 h and exceeded 0.5 m.s^{-1} during 60% of this duration, with a maximum of 1.4 m s^{-1}, while ebb velocities lasted 8.0 h and were almost always lower than 0.5 m.s^{-1}. However, part of the ebb current was not measured when the sensor was dry and maximum ebb velocities remained unknown. In addition, ECM2 was located on the ramp of the flood-tidal delta, which receives flood currents but is sheltered from the ebb currents that are channelized around the flood-tidal delta [*Hayes*, 1979b].

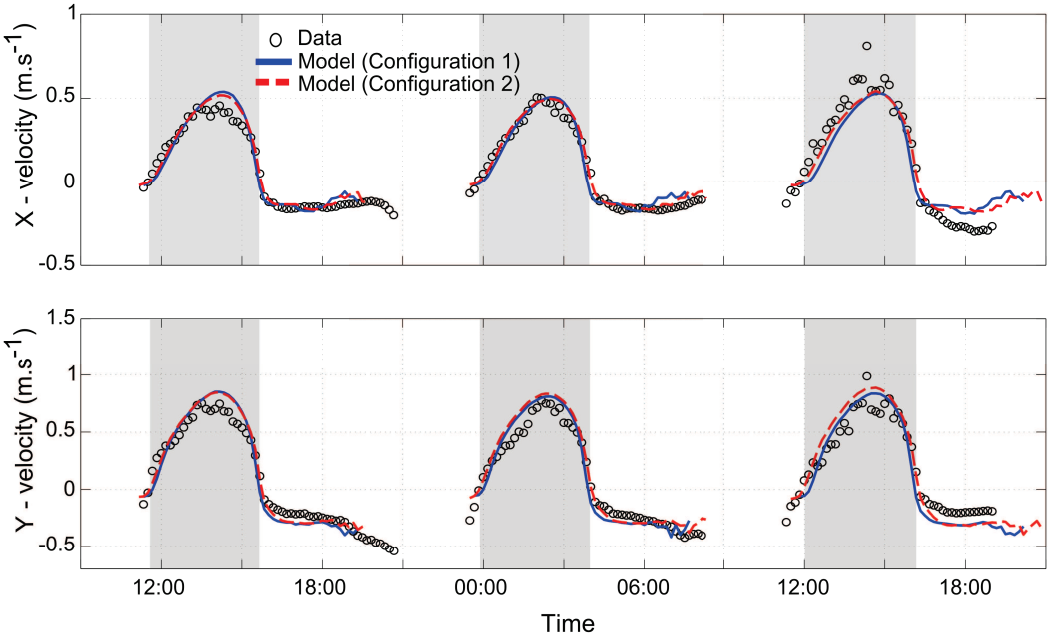

Figure 7.8: Comparisons between modelled and measured current velocities at (top) PT1, (middle) PT2, and (bottom) PT3 at Albufeira lagoon on 23–24 September 2010. The grey areas indicate flood tide when modelled currents flow toward the lagoon [Dodet et al., 2013].

The velocities simulated with the 2-DH modelling system were assumed to be reasonably comparable with the currents measured locally by ECM2 at 0.4 m above the bed. Indeed the large bed forms observed at low tide, the strong measured velocities, and the shallow depth provided a well-mixed environment where currents measured at this height were probably rep-

resentative of velocities integrated over the water column. Comparisons between the data and the model outputs for config.1 and config.2 showed an RMSE of 0.10 m.s^{-1} (SI = 21%) and 0.09 m.s^{-1} (SI = 20%), respectively (Table 7.5).

Significant low frequency fluctuations were observed in the velocity and elevation signals and a spectral analysis revealed that the associated energy was located in the infra-gravity band (0.004–0.04 Hz). The 1–5 min fluctuations of the velocity signal reached up to 50% of the filtered signal and were expected to have a significant impact on the sediment dynamics of the inlet. These low-frequency fluctuations need to be investigated in further detail and will be the subject of future study.

Table 7.5: Statistical errors between data and model results for the current velocity.*

	Configuration 2		*Configuration 3*	
	Bias (cm.s^{-1})	RMSE (cm.s^{-1})	Bias (cm.s^{-1})	RMSE (cm.s^{-1})
PT2	2.8	9.6	3.6	9.2

* RSME: Root Mean Square Error; SI: Scatter Index.

7.3 Wave-current interactions

Based on *in-situ* data and local model outputs, the interactions between waves and currents appeared to be significant for the hydrodynamics of the inlet. The coupled wave-current modelling system was shown to perform well at Albufeira Lagoon in the presence of a complex tidal and wave forcing. The modelling system was used to investigate with more details the interactions between waves and currents as well as their impact on sediment dynamics. In order to verify if the physical processes observed in the data set do not depend on a particular wave climate and to avoid the interference between the variation in the incident forcing and the locally induced variability, an additional set of simulations was performed. These simulations were forced by a synthetic tide represented by the constituent M2 with an amplitude of 1 m (mean tidal amplitude) and yearly means of H_s (1.9 m), T_p (10.5 s), and Mwd (312°). Model outputs were stored over the computational grids during one tidal cycle and were used to compute spatial representations of several forcing terms at two different time steps, representative of flood and ebb situations. These representative time steps were chosen so that flood and ebb flows were of similar intensity and strong enough to have an impact on the wave field. These maps are used along the discussion to support the analysis based on the local data presented in this section.

7.3.1 Impact of the waves on the circulation

When waves break in the surf zone, they release a large fraction of their energy and they transfer their momentum to the water column. This process induces a gradient of the water surface to balance the onshore component of the momentum flux, resulting in a higher water level along the shoreline (wave-induced setup) and at the inlet. *Hench and Luettich Jr* [2003] analysed the momentum balance in both an idealized and a natural inlet without waves and showed that near maximum flood and maximum ebb, the along-stream momentum balance was

dominated by advection, pressure gradient, and bottom friction. *Olabarrieta et al.* [2011] corroborated these results at Willapa Bay, where they applied a fully coupled modelling system. They also showed that when the wave forces were present, the pressure gradient and the bottom friction terms were greatly affected, inducing a significant setup of the water level inside the estuary.

The effect of the waves on the water level at each instrument location was computed as the difference between the elevations simulated with config.1 and config.2 (Fig.37.7). For each location, this difference (hereafter referred to as "setup") was characterized by a strong tidal modulation (Table 7.6). At PT1, the minimum setups were obtained during high tides, as the sensor was near the wave breaking point, while the maximum values occurred at the lowest measured water depths, when the instrument position coincided with the shoreline position. At PT2 and PT3, the setup signal was out-of-phase with the local elevation signal and maximum values occurred when the oceanic tide was near mean sea level.

Table 7.6: Offshore significant wave height and setup.*

		Setup					
		PT1		PT2		PT3	
Tidal cycle	H_s (m)	Abs. (m)	Rel. (%)	Abs. (m)	Rel. (%)	Abs. (m)	Rel. (%)
Tide1	1.17	0.15	12.8	0.22	15.0	0.23	13.4
Tide2	1.47	0.09	7.7	0.16	10.9	0.18	10.5
Tide3	1.72	0.10	8.5	0.16	10.9	0.18	11.0

* Relative setup is normalized by offshore significant wave height.

In order to understand the effect of the waves on the water level inside the lagoon, the magnitude and directions of the dominant terms (barotropic pressure, bottom friction, wave radiation stress gradients, and advection) in the momentum equations were computed for the representative flood and ebb situations (Fig.7.9). The balance between barotropic pressure, bottom friction, and advection mentioned by *Hench and Luettich Jr* [2003] was significantly affected by the contribution of the wave radiation stress term, corroborating the results of *Olabarrieta et al.* [2011]. Indeed, for both situations, the wave radiation stress term oriented toward the lagoon was of the same order of magnitude as the other terms and thus had an important impact on the overall hydrodynamics, the main impact being a wave-induced setup along the shoreline and inside the lagoon. During ebb, when the ocean water level is near mean sea level, the waves break directly over the ebb shoal leading to stronger values of the wave radiation stress term than during flood when the water level is higher and waves are subjected to less intense breaking. This difference in intensity of the wave radiation stress term explains why the higher modelled setup values at PT2 and PT3 were found when oceanic water level was near mean sea level. The friction term in the inlet was generally higher during ebb than during flood and reached very large values at the end of the ebb (not shown here) attesting that sediment transport in such inlet is clearly ebb dominated during low-to-moderate wave energy conditions, as shown by *Bertin et al.* [2009a] at a similar wave-dominated inlet. It is worth noting that values of the different terms of the momentum equations reached almost 0.1 $m.s^{-2}$, which is several orders of magnitude higher than in the case of Willapa Bay [*Olabarrieta et al.*, 2011] and other large systems [*Hench and Luettich Jr*,

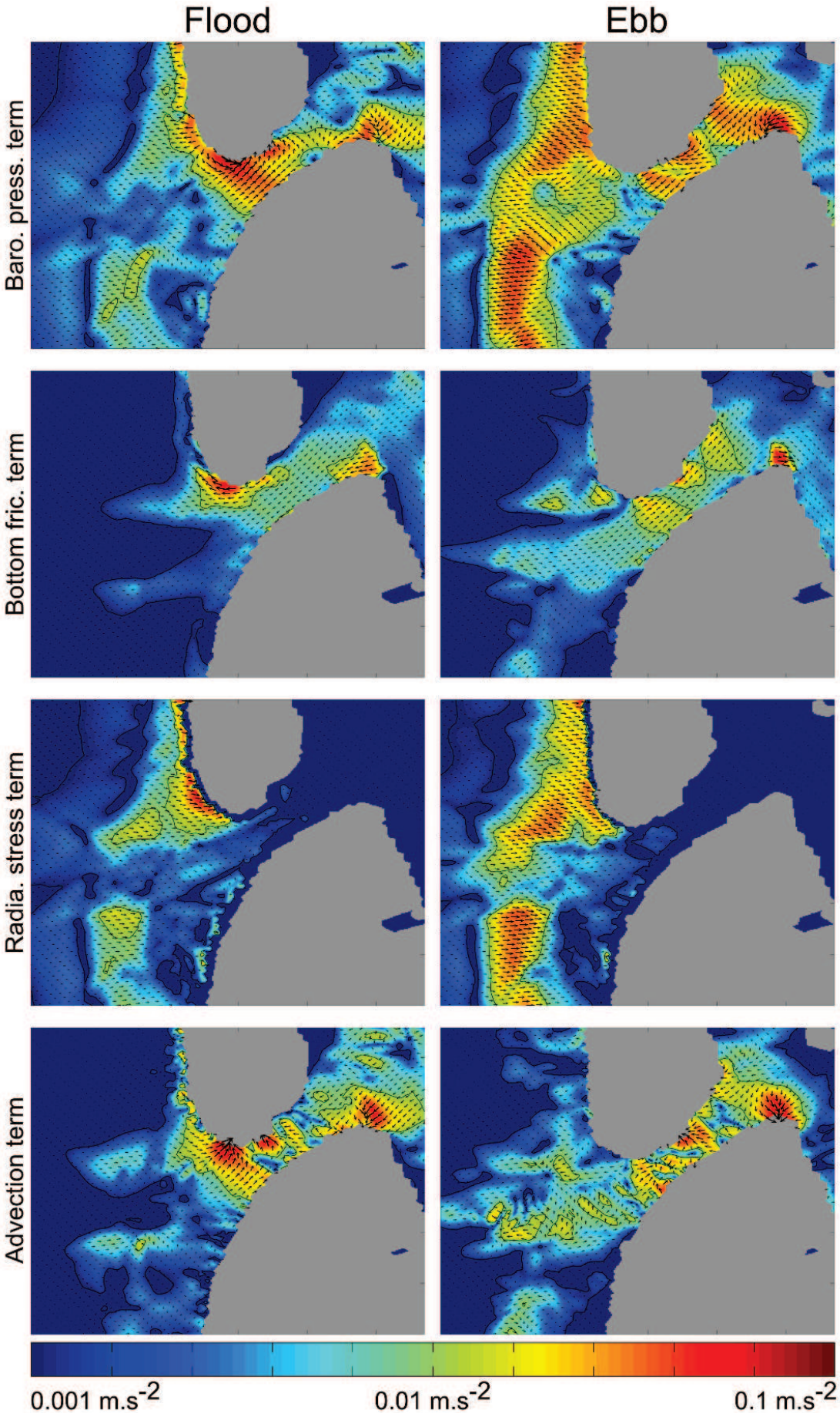

Figure 7.9: Dominant terms of the momentum equations: (first row) barotropic pressure term, (second row) bottom friction term, (third row) wave radiation stress term, and (fourth row) advection term for (left column) flood and (right column) ebb. The colors represent the magnitude of each term. The vectors represent the direction of each term [Dodet et al., 2013].

2003]. This difference supports the fact that very shallow wave-dominated inlets (1 m deep) are extremely dynamic and thus represent a great challenge for measurements collections and model applications.

For PT1, PT2, and PT3, the maximum setup occurred during the third tidal cycle, when offshore wave height was maximal (1.72 m), reaching the respective values of 0.23, 0.18, and 0.19 m. On average, the maximum setup represented 11% of the offshore wave height (Table 7.6), corroborating the 10–14% range estimated by *Nguyen et al.* [2007] for storm-induced setup at narrow and shallow inlet mouth. Finally, other simulations carried out with a shore-normal and deeper inlet morphology (not shown here) produced lower maximum setups (7% of the offshore wave height on average), which corroborated the findings of *Malhadas et al.* [2009] who used model simulations to show that the wave-induced setup in an inlet was lower for the deeper morphology of their synthetic tidal inlet.

The impact of the waves on the currents was almost negligible at ECM2 as shown by the difference between the currents modelled with config. 1 and config. 2 (Fig.7.8). However, spatial plots of the current magnitude difference for these two configurations at key phases of the tide (not shown) revealed that the wave-induced currents could reach up to 1 m.s^{-1} near the ebb shoal during ebb and 0.5 m s^{-1} along the beach as longshore drift. These results also confirmed that the wave-induced currents were very weak in the channel for the considered offshore wave climate.

7.3.2 Impact of currents on wave propagation

Among the effects of currents on the incident wave field, summarized for instance by *Wolf and Prandle* [1999], the current-induced refraction, the Doppler shift of wave frequency, and the wave blocking (in the case of counter currents) are all represented in the formulation of wave action conservation in phase-averaged wave models, with some limitations though (see Section 7.4). Several authors tested the skills of coupled wave-current modelling systems by comparing model results either with laboratory measurements [*Ris and Holthuijsen*, 1996; *Rusu et al.*, 2011] or with field data [*van der Westhuysen*, 2012]. In general, the models were able to reproduce the main effects of the ambient current on the wave field, although some inaccuracies remained, particularly in the presence of strong opposing currents [*Ris and Holthuijsen*, 1996; *Van Dongeren et al.*, 2011]. In order to analyse the ability of our modelling system to reproduce the effects of the currents on the incident wave field, model results obtained with config.2 and config.3 were compared with field data (Fig.7.4). The H_s signal was better reproduced with config.3 particularly during the ebb tide. The larger differences between the two configurations were observed in the inlet (PT2 and PT3) where the waves were subjected to opposing currents as they passed through the inlet: for each tidal cycle, the modelled H_s was much more asymmetric if the currents were taken into account in the wave model, particularly during the ebb tide when the H_s experienced a fast drop.

Several authors reported that wave propagation could be blocked in the presence of strong counter-currents, based on physical and numerical modelling results [*Lai et al.*, 1989; *Chawla*, 2002]. Perhaps due to the difficulty of installing instruments in such dynamic environments, *in-situ* measurements of wave-blocking conditions have very rarely been published to this day. *Ris*

and Holthuijsen [1996] proposed that wave heights propagating over strong opposing, partially blocking currents were often overestimated due to insufficient steepness dissipation. *van der Westhuysen* [2012] implemented an enhanced dissipation term for waves on negative current gradients to counteract this overestimation. The model results presented in this study benefit from this recent development, which improved the comparison of H_s in the inlet during ebb. In order to investigate the effect of following and counter-currents on the wave field and determine if the strong attenuation of H_s during the ebb tide was the result of steepness dissipation on negative current gradients and wave blocking mechanism, numerical simulations were carried out using the synthetic forcing. For the flood and ebb situations, the current velocity U, the intrinsic group velocity C_g , the velocity gradient $\partial U_s/\partial s$, where U_s is the current velocity component in the direction of wave propagation and s is the coordinate in the wave direction, H_s, and the relative H_s difference $((Hs_{current} - Hs_{nocurrent})/Hs_{current})$ were computed (Fig.7.10). During flood, the incident waves were refracted by the currents at the entrance of the inlet and the wave action focused on the edge of the main current as shown by the increase in H_s (up to 10%) on the margins of the main channel and the decrease in H_s (up to 10%) along the channel. The current gradients encountered by the incident waves were mainly positive and thus did not impact on the whitecapping dissipation process. Large H_s differences (up to 30%) appeared after the wave passed the inlet and can be explained by current-induced refraction. However, these differences concern only very small waves and their impact on the overall inlet dynamics was very limited since most of the waves' energy had already been dissipated after propagation through the channel. During ebb, currents were strong enough (up to 1.5 m.s^{-1}) to cancel the intrinsic group velocity in the inlet. In addition, the negative current gradients at the entrance of the inlet reached large values (up to 0.03 s^{-1}), strongly increasing wave steepness responsible for enhanced whitecapping dissipation, as proposed by *van der Westhuysen* [2012]. The relative difference of H_s showed that the waves were refracted by the ebb-jet current at the entrance of the inlet where H_s of config.3 was locally 20% larger when currents were included in the wave model. As the waves travelled along the inlet, their H_s quickly decreased and became much lower (up to 50%) than in the situation without currents. It is assumed that the strong H_s attenuation during the ebb, as observed in the data, resulted from current-induced breaking dissipation at the entrance of the inlet and from the blocking of the wave energy when the current approached the absolute wave group velocity.

The difference in current magnitudes for config.2 and config.3 (not shown here) indicated that the current-induced modification of the wave field near the inlet had a minor impact on the currents in the channel (less than 0.05 m.s^{-1}) but could reach up to 0.5 m.s^{-1} at the entrance of the inlet where the ebb jet induced an increase of H_s and thus a more energetic breaking.

7.3.3 Importance of low-frequency fluctuations

A significant part of the spectral energy was found in the infragravity band (0.004 Hz - 0.04 Hz) of the energy density spectra derived from the elevation data measured along the inlet. Fig.7.11 shows the energy density spectra over the frequency range 0.007 Hz - 1 Hz computed at PT2 during the three tidal cycles, which exhibits very high values of energy densities in the infragravity band.This low-frequency incident energy resulted in low-frequency fluctuations of the elevation, wave heights and current velocities. These fluctuations were particularly visible in

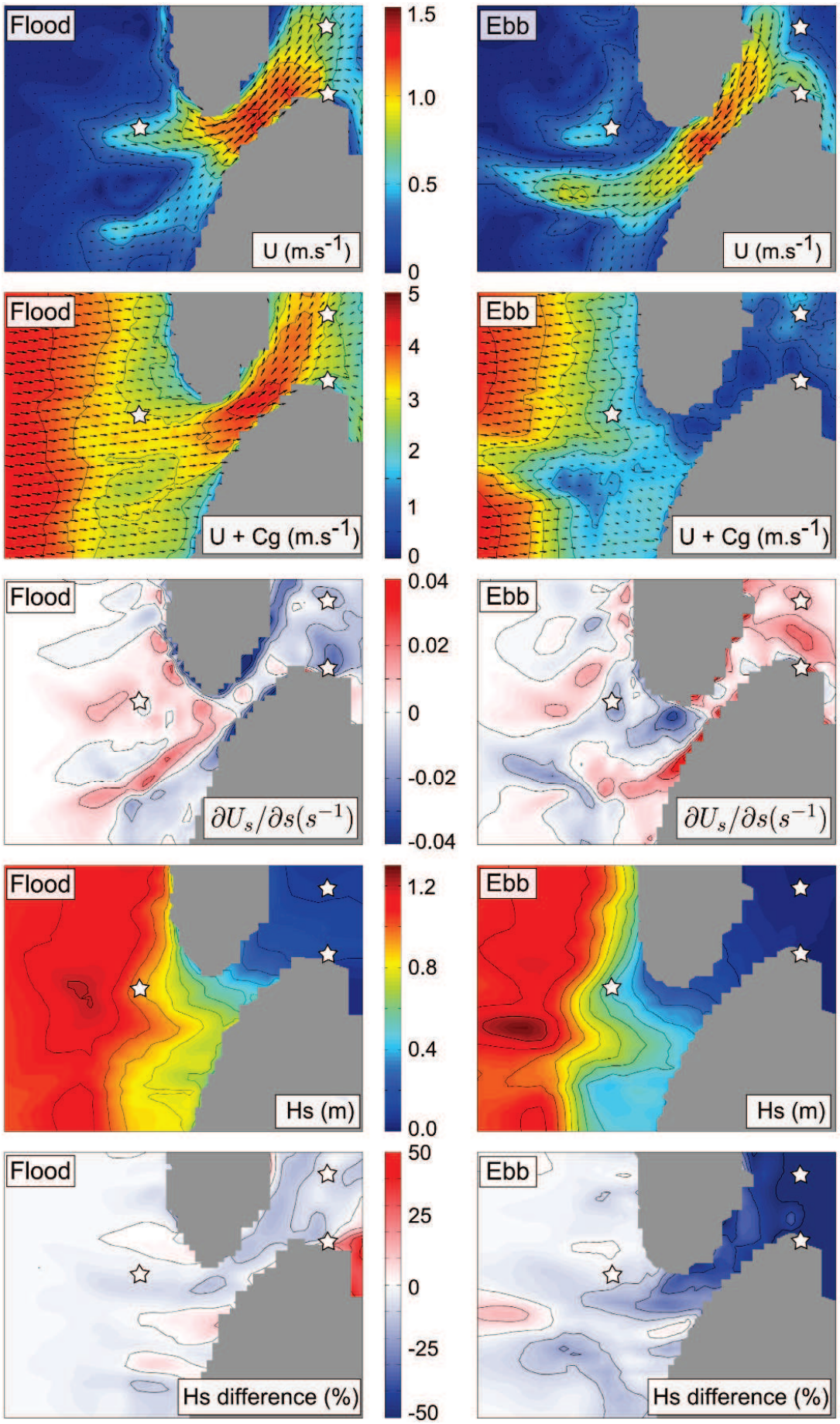

Figure 7.10: (first row) Currents, (second row) intrinsic wave group velocity, (third row) gradient along the wave propagation direction of the velocity component in the direction of the wave direction, (fourth row) significant wave height, and (fifth row) relative difference between significant wave height computed with config.3 and config.2 normalized by the wave height computed with config.3, during (left column) flood and (right column) ebb [Dodet et al., 2013].

the measured elevations, wave heights and current velocities at PT2, when comparing the 1-min running averaged with the 60-min running averaged time-series (Fig.7.12). These fluctuations reached up to 10%, 20% and 50% of the 60-min filtered signal, respectively. Moreover, the amplitudes of these low-frequency fluctuations were maximal during the last tidal cycle, when the offshore H_s and T_p increased significantly. Infragravity motions of the sea surface elevation, related to the wave groupiness [*Munk*, 1949] were shown to be an increasing function of the offshore wave height and period [*Stockdon et al.*, 2006], which explains the larger low-frequency fluctuations observed at the end of the campaign.

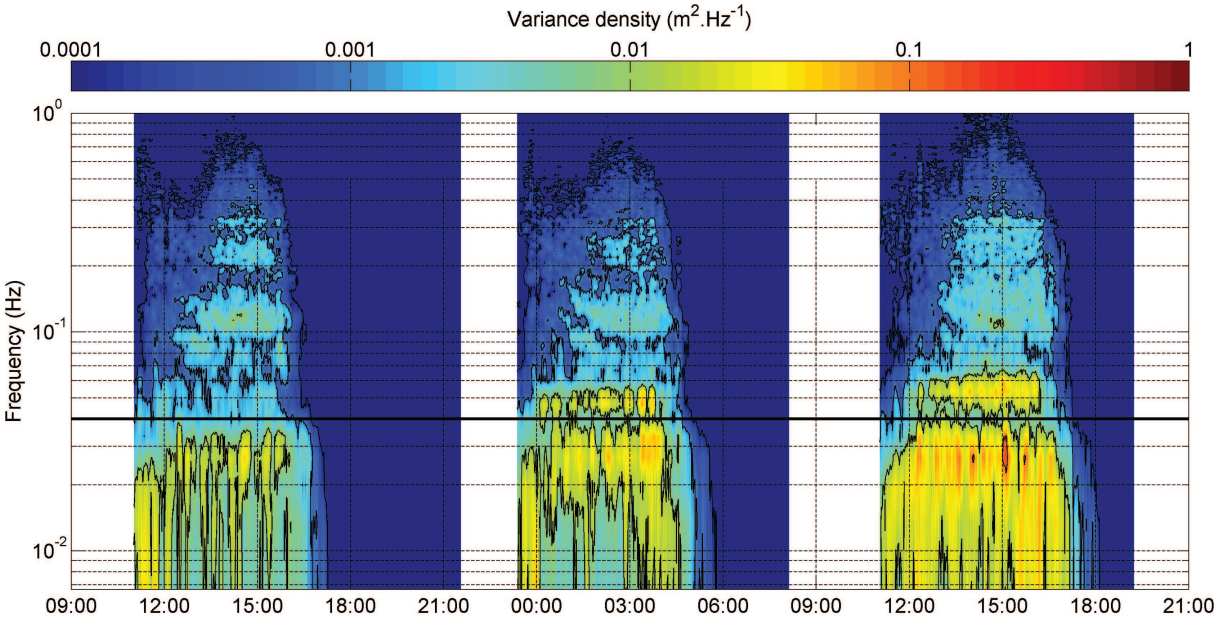

Figure 7.11: 1-min and 60-min running averaged time-series of depth, velocity (U), significant wave height (H_s) and total transport (Q_t) at ECM2.

While determining the physical processes that could explain these infragravity waves is beyond the scope of this dissertation, estimating their contribution to the sediment dynamics of the inlet appeared to be relevant. In this context, the total transport induced by waves and currents was computed at ECM2 with the formula of Soulsby-Van Rijn [*Soulsby*, 1997], using on the one hand the 60-min filtered time-series of elevation, H_s and velocity (the wave orbital velocity was computed using the linear theory) and on the other hand the 1-min filtered time-series that include the low-frequency oscillations. The total transport computed with the 1-min filtered data was up to 8 times as high as the one computed with the 60-min filtered data, and the net total transport integrated over the three (resp. last) tidal cycles was 1.3 times (resp. 1.6 times) as high as when the low-frequency were taken into account: 3.24 $m^3.m^{-1}$ (resp. 1.49 $m^3.m^{-1}$) with the 60-min filtered data against 4.18 $m^3.m^{-1}$ (resp. 2.33 $m^3.m^{-1}$). Although, considerable efforts were already done to simulate infra-gravity waves dynamics [*Roelvink et al.*, 2009], these last results highlight the need to further investigating the behaviour of infragravity waves in tidal inlets in order to take into account their effect on sediment dynamics in future 2DH and 3D morphodynamic models.

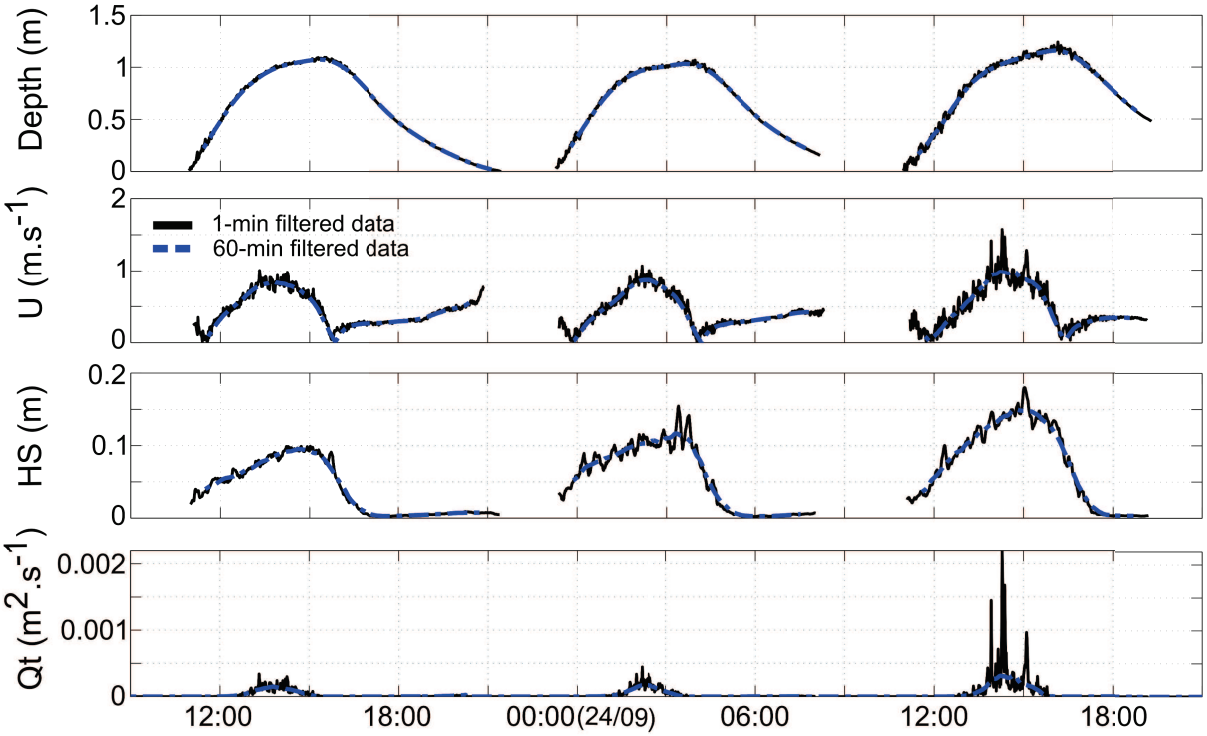

Figure 7.12: 1-min and 60-min running averaged time-series of depth, velocity (U), significant wave height (H_s) and total transport (Q_t) at ECM2.

7.4 Limitations of the modelling system

Besides the lack of infragravity waves-related processes, the wave-current modelling system presented in this study presented other limitations that are discussed in the following paragraphs.

7.4.1 Non-linear effects

As waves encounter strong opposing currents, they become increasingly non-linear, making the linear wave balance equation (2) and the linear kinematic expressions (3)–(5) inadequate. *Chawla* [2002] showed that non-linear amplitude dispersion affected significantly their results near the blocking point. They used a third-order Stokes dispersion relation and compared their results with the same model using a linear dispersion relation. The former performed much better and was more accurate to predict the position of the blocking point along the flume. The modelling system presented in this study used the SWAN wave model which does not provide the possibility to use different formulations for the dispersion relation. Hence, the different physical processes investigated herein were described in a qualitative manner as much as possible. Therefore, potential improvements for this modelling system could be the implementation of a higher order dispersion relation in the wave model to take into account the effect of amplitude dispersion near the blocking point. Another alternative to accurately predict the wave propagation in a strongly inhomogeneous media is given by *Toledo et al.* [2011] who derived a new form of the wave action equations based on the extended mild-slope equation. Their sophisticated formulation resolves higher-order bottom and current effects and is therefore adapted to shallow inlet applications.

7.4.2 Current-induced wave reflection

Smith [1975] showed that away from the blocking region, the wave field consists of an incident wave and a much shorter reflected wave. *Suastika et al.* [2001] observed reflected waves by blocking currents in laboratory experiments. In SWAN, wave components are not propagated into the opposing current once the blocking point is reached for that component. So, at that point, the variance density becomes zero at that component's spectral bin. In order to model accurately the wave field in an inlet during ebb when tidal currents are likely to block the incident waves, the wave model should simulate wave propagation in all directions. Taking into account this effect would enable to reproduce more accurately the wave spectra in the inlet.

7.4.3 Wave energy dissipation induced by counter-currents

Several studies based on SWAN results showed that the modelled wave height was overestimated when waves encountered strong opposing currents [*Ris and Holthuijsen*, 1996; *van der Westhuysen*, 2012]. The present study benefited from the recent improvements of *van der Westhuysen* [2012] to simulate enhanced wave energy dissipation on negative counter currents. It is worth noting that setting a large calibration coefficient was necessary (5 here against the 0–3 range of *van der Westhuysen* [2012]) to observe significant differences in the model results, and yet the results of our study suggested that the wave model still overestimates wave heights during ebb. Given the limitation of our data set and the complexity of the study site, the calibration of the enhanced dissipation term was mostly qualitative. The objectives of the present study were to highlight physical processes induced by wave-current interactions much more than calibrating and validating a new empirical formulation. The results of this study confirmed the fact that the wave model overestimated wave height during ebb. This raises the need to pursue experimental research on enhanced wave energy dissipation in opposing currents.

Summary

This chapter investigated the interactions between tidal currents and incident waves at the Albufeira Lagoon inlet. The main objective of this work was to gain a better understanding of the physical processes driving the hydrodynamics in wave-dominated tidal inlets.

The wave-current modelling system was implemented to the Albufeira Lagoon and the wave and tide boundary forcings were validated by comparing the simulated waves and sea surface elevations against wave buoy and tide gauge observations, respectively. These comparisons presented an excellent match and confirmed the validity of the modelling strategy.

The comparisons of the model results with *in-situ* hydrodynamic data in the inlet were very satisfactory and improved when waves and wave-current interactions were taken into account. In order to highlight the effects of the interactions between waves and currents on the overall hydrodynamics, a set of simulations was performed with a synthetic forcing representative of yearly mean conditions. The analysis of the results revealed that:

1. the wave-induced setup in the lagoon was comprised between 7% and 12% of the offshore significant wave height, depending on the inlet morphology: the shallower the inlet, the higher the setup;

2. during ebb, the wave height increased at the entrance of the inlet (up to 20%) and was attenuated through the inlet (up to 40%). The main responsible mechanisms were wave blocking and current-induced wave breaking dissipation;

3. during flood, the currents had less impact on the waves: current-induced refraction decreased the wave heights along the inlet gorge (up to 10%) and increased the wave heights on the exterior part of the ebb shoals;

Finally, low-frequency fluctuations of the sea surface elevation, wave heights and current velocities were measured by the sensors installed along the main channel. The impact of these low-frequency fluctuations on the sediment transport was estimated by computing the total sediment transport in the channel with the observations filtered with a 1-min running average and filtered with a 60-min running average (smoothing the low-frequency fluctuations). The total transport computed with the 1-min filtered data was up to 8 times as high as the one computed with the 60-min filtered data, indicating that infragravity waves-related processes may severely impact the sediment dynamics of wave-dominated inlets.

Chapter 8

Sediment transport and morphodynamics of the Albufeira Lagoon inlet

The Albufeira Lagoon inlet is a *mixed-energy wave-dominated tidal inlet* according to the classification of *Hayes* [1975]. The morphodynamics of these tidal inlets are strongly controlled by the wave climate and its variability, which make their evolution relatively fast and difficult to predict in comparison to the more stable tide-dominated inlets. The land-use management of coastal areas near dynamic inlets raises a certain number of problems that can hardly be addressed without systematic environmental studies and adequate methods. Numerical morphodynamic modelling systems are becoming essential tools in the integrated coastal management of complex coastal environments, and despite their limited predictive skills, they provide powerful means for investigating the physical processes that control the morphodynamics ot these environments for a wide range of spatial and temporal scales. In this chapter, the morphological changes of the Albufeira Lagoon inlet surveyed from April 2010 to December 2010 are first described. The skills of the newly developed morphodynamic modelling system are then assessed through comparisons between model results and observations. The sediment dynamics of the Albufeira Lagoon inlet and its adjacent beaches is investigated through the application of different configurations of the model. Finally, the inter-annual variability of the littoral drift is discussed based on the analysis of a 65-year hindcast of longshore sediment transport.

8.1 Observed morphological changes at the Albufeira Lagoon in 2010

8.1.1 Topographic surveys from April 2010 to December 2010

The tidal inlet of the Albufeira Lagoon was artificially open on April 15, 2010 and the lagoon remained connected to the ocean until the end of December 2010. During this 8-month period, nine topographic surveys were realized with a Real Time Kinematic Differential Global Positioning System (RTK-DGPS) during spring low tides at approximately one-month intervals. The topographic measurement were then processed into nine digital elevation models (Fig.8.1). The processing method and a detailed analysis of the observed morphological evolution of the

inlet are given in *Nahon et al.* [2012b].

The 8-month surveyed period can be divided into two distinct periods:

1 From the end of April to the end of September, the main and secondary channels of the inlet developed and their cross-sectional area enlarged. During the first month, the main channel migrated around 25 m northward and, from the end of May, it started migrating southward until the end of August at an average rate of 2.25 m.day^{-1}. During this period, the progradation of the north beach and the erosion of the south bank created an offset in the beach alignment. During the month of September, the north beach spit eroded and the south bank accreted allowing the main channel and the north channel to align. This 5-month period is very similar to the stages of maximum hydraulic efficiency following the opening of the inlet and the subsequent offset development, described by *Freitas and Andrade* [1994] from field observations.

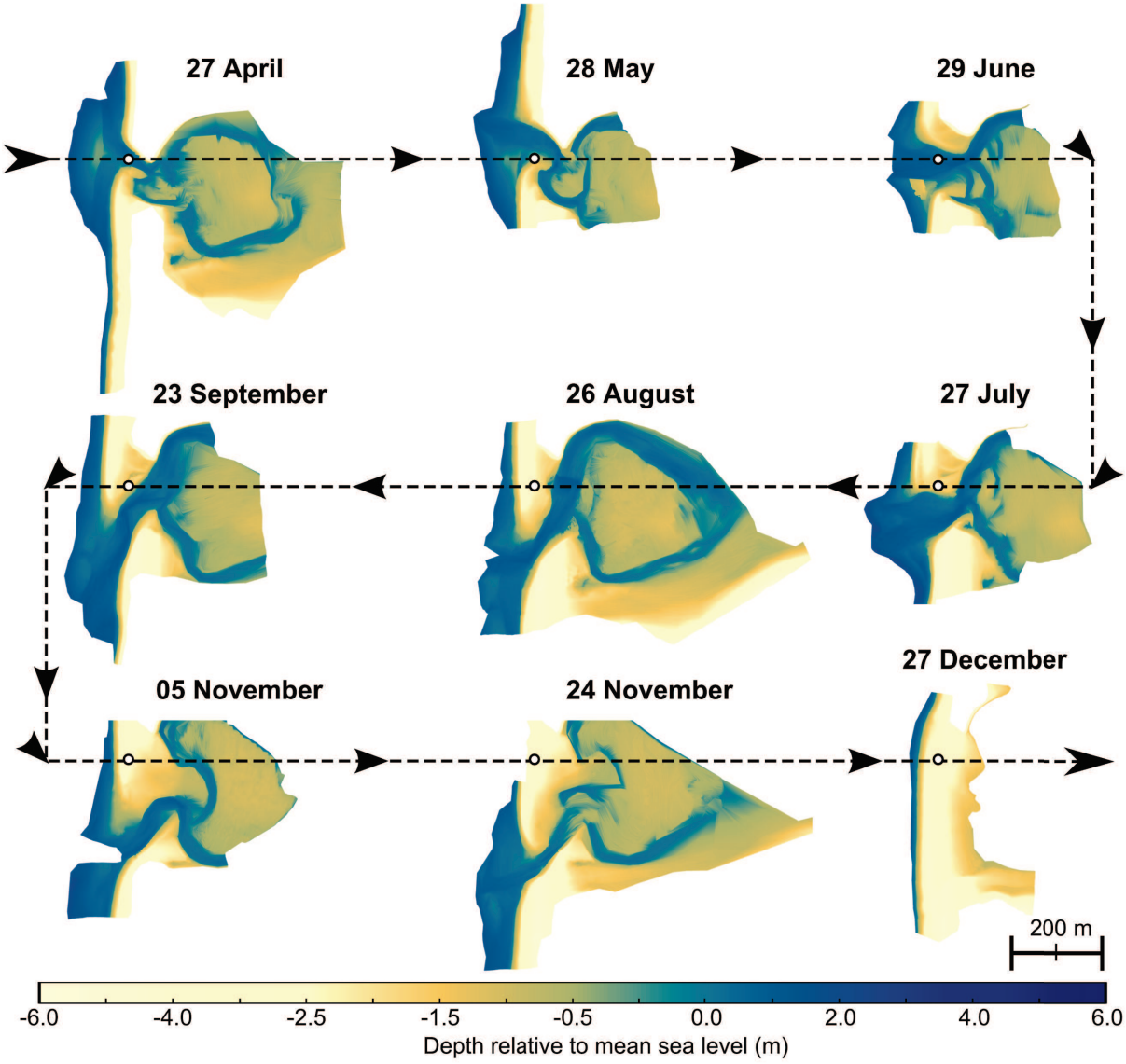

Figure 8.1: Observed morphological evolution of the Albufeira Lagoon inlet from April 27 to December 27, 2010 based on nine topographic surveys. The white dot indicates the position of the inlet gorge on April 27.

2 Between the end of September and the end of December, the morphology of the inlet was subjected to major modifications. The topography of November 5 suggests that a large overwash partly obstructed the north channel and activated the south channel. This hypothesis is also supported by the erosion of the dune in the northern barrier (fig 1.2), where the beach appeared to have been flooded. At the end of November, all the channels had significantly accreted. Finally, the topography of December 27 shows the lagoon disconnected from the ocean after closure of the inlet. An aerial photograph of the inlet taken on December 15 shows the morphology of the inlet in a very different configuration to the one of November, 24 (Fig.8.2). Indeed, a long sand spit extending northward from the former south bank of the main channel guides a shallow stream of water flowing alongshore into the ocean. In addition, a massive sand bank has welded to the former north bank and the south channel follows a straight path, contrasting with the meandered path observed on November 24. Finally, the flood delta presents a crescent-shaped morphology gently sloping on the seaward face and falling abruptly on the side of the lagoon. This photograph attests that the inlet remained active several weeks after the topographic survey of November 24 but it suffered strong morphological changes, probably occurring during episodes of large waves and high water level.

Figure 8.2: Aerial photograph of the Albufeira Lagoon on December 15, 2010, a few days before the closure of the inlet (credits: João Herdeiro / SIARL (IGP/EPRLFinisterra)).

The morphological changes of the Albufeira Lagoon inlet observed between April 27 and December 27, 2010 present a seasonal behaviour similar to the one described by *Bertin et al.* [2009a] for the Óbidos Lagoon, another wave-dominated lagoon located a hundred kilometres north of the Albufeira Lagoon. These authors observed the development of the inlet during fair weather conditions characteristics of the summer period and the infilling of the inlet during the winter period. From the observations presented here above, the infilling of the inlet in winter appears to be associated to energetic events whose impacts may perturb radically the hydrodynamic circulation that controls the stability of the inlet.

8.1.2 Hydrodynamic conditions in 2010

The seasonal behaviour of the observed morphological changes at the Albufeira Lagoon inlet is believed to be intimately related to the variability of the mean sea level and the wave climate along the year. The time-series of significant wave heights, peak periods and mean wave directions simulated with the wave model in front of the Albufeira Lagoon in 2010 shows the seasonal changes of the wave climate described in Chapter6: significant wave heights and peak periods are larger in winter than in summer and the mean wave direction is lower during the summer period than during the winter period (Fig.8.3, bottom and lower panel). An other sig-

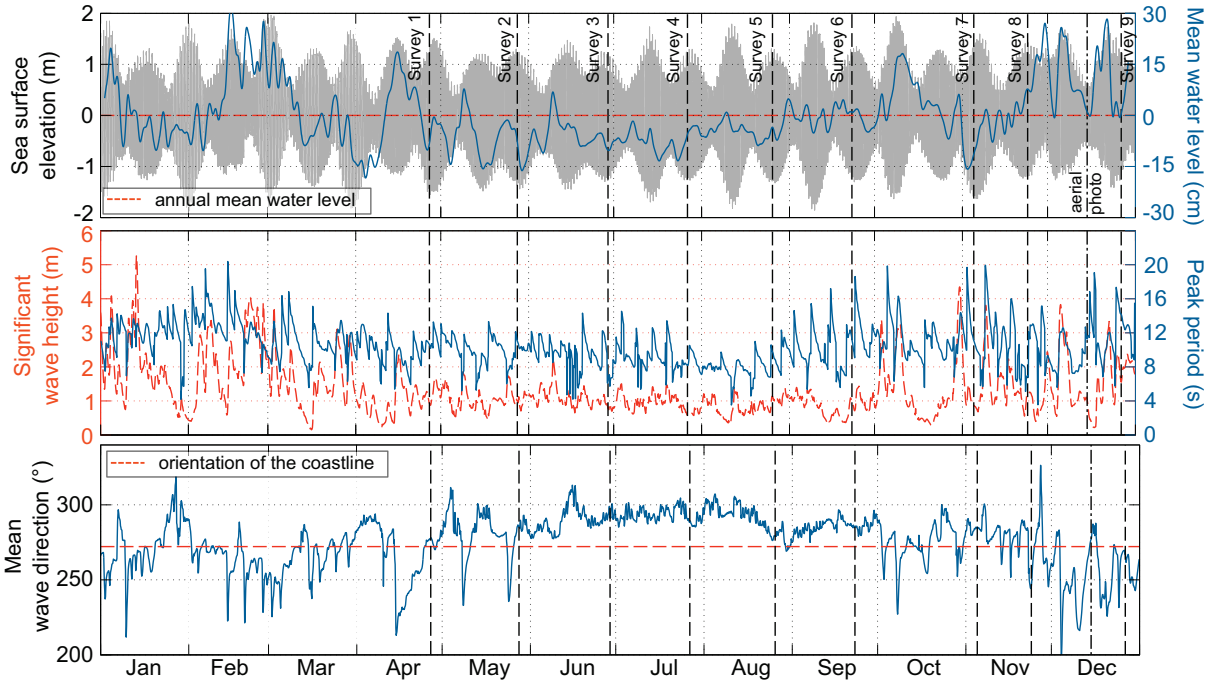

Figure 8.3: Hydrodynamic forcing in front of the Albufeira Lagoon in 2010: sea surface elevation and mean water level (top panel), significant wave height and peak period (middle panel) and mean wave direction (bottom panel).

nature of the seasonal behaviour is the weak variability of the mean wave parameters during the summer months, contrasting with the large amplitude of these changes during the rest of the year.

The variability of the mean water level in 2010 was investigated through the time-series of sea surface elevation measured at the Cascais tide gauge. A Demerliac filter was applied to this time-series in order to highlight the infra-annual fluctuations of the mean sea level (Fig.8.3), top panel). The mean water level displays a seasonal evolution, with values generally higher-than-average (up to 30 cm) during the winter period, and lower-than-average during the summer period (up to 15 cm). The fluctuations of the mean water level were also more pronounced during the winter months and could even be lower-than-average during several weeks.

Finally, the evolution of the amplitudes of the semi-diurnal tidal constituents M_2 and M_4 in the Albfueira lagoon were deduced from a 1-month sliding window harmonic analysis of the 7-month time series of sea surface elevation measured in the Lagoa Grande (Fig.8.4). The amplitude of M_2 and M_4 was comprised between 0.1 - 0.3 m, and 0.04 - 0.1 m, respectively, and constantly increased from June to September. At the end of October, the amplitude of M_2 was

10 cm lower than in September and decreased until mid-November. This seasonal behaviour was described by *Bertin et al.* [2009a] for the Óbidos Lagoon and was related to the morphological evolution of the inlet that enlarged during the summer and filled in during the winter.

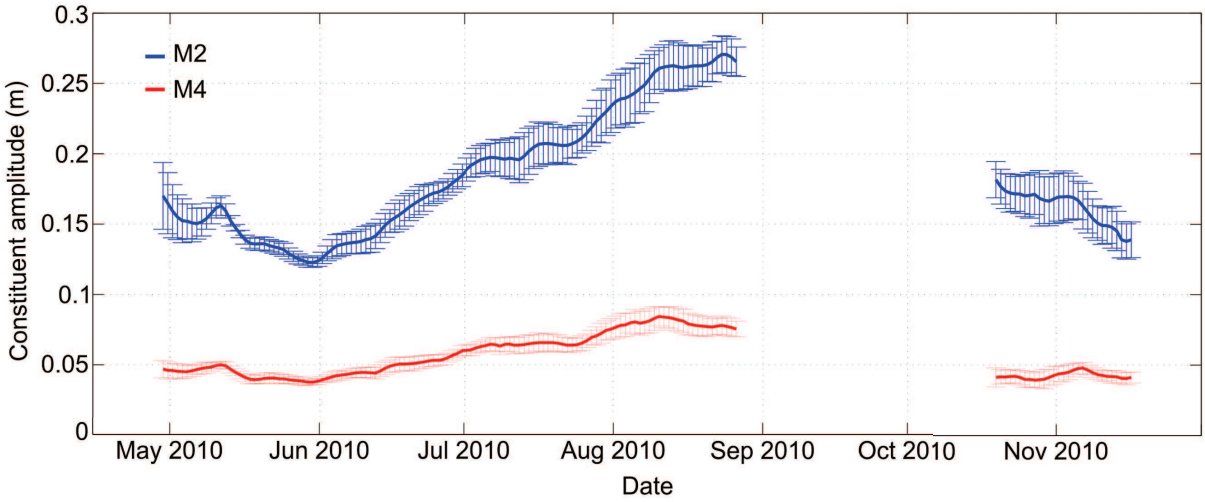

Figure 8.4: Amplitudes and 95% confidence intervals for the tidal constituents M2 (blue) and M4 (red) in the lagoon between April and December 2010 [Dodet et al., 2013].

The analysis of the time-series of wave conditions and mean water level at shorter time-scales (daily-to-monthly) revealed specific characteristics of the hydrodynamic regime during the year 2010 that partly explain the observed morphological changes at the Albufeira Lagoon inlet. In May, two episodes are associated to 2-m waves coming from WSW directions that may have induced northward longshore transport and caused the northward migration of the inlet during this period. From June to October, the wave regime is characterized by persistent waves from the W-NW sector, which matches well the continuous southward migration of the inlet during this period. In October, an episode of large waves with long periods is associated to a higher-than-average mean water level and spring tides. The overwash footprint observed in the topographic survey of November 5 and suggested by the aerial photograph of December 15 (Fig.8.2) is likely to have occurred during this episode of very high water level. Finally several energetic wave events from the W-SW sector occurred during the beginning of December and may have caused the development of the long spit pointing northward that is depicted in the aerial photograph of December 15.

The analysis of the hydrodynamic conditions in 2010 provides a first basis to explain some of the morphological changes observed at the Albufeira Lagoon inlet during this year. However, the physical processes responsible of these morphological changes are not well understood yet. In particular, the rapid infilling and closure of the inlet at the end of December occurred during a period of higher-than-normal mean water level and rapidly changing wave conditions. The interactions between the waves, the currents and the morphological changes are so tightly coupled that they can hardly be investigated without a process-based modelling system. The following sections will be dedicated to the verification of the predictive skills of the modelling system, prior its application to analyse the physical processes responsible for these morphological changes.

8.2 Predictive skills of the morphodynamic modelling system

The validation of the morphodynamic modelling system was carried out both qualitatively and quantitatively. The qualitative validation consisted in assessing whether the simulated morphological changes agreed with the observations while the quantitative one consisted in comparing time-series of observed and simulated water levels in the lagoon. Among the nine digital elevation models available for the year 2010, the one of November 5 was selected and the validation focused on the period November 5 - December 27. This choice was motivated by the challenging goal of reproducing the migration and closure of the inlet during a period of energetic waves. In addition, several limitations of the modelling system, such as the absence of swash and infragravitary waves, prevented the morphological changes associated to the overwash that possibly occurred on October from being accurately simulated. Hence, the validation of the model for the period September - December was discarded after several inconclusive tests.

8.2.1 Setup of the modelling system

The fully coupled wave-current-sediment-transport modelling system was set up to simulate the morphological changes at the Albufeira Lagoon inlet between November 5 and December 27, 2010. The modelling system used a single computational grids composed of approximately 60000 triangular elements (30000 nodes) with a resolution ranging from 1000 m to 3.5 m, and covering the whole bay comprised between Cape Roca and Cape Espichel (a detailed description of the grid is given in Chapter5 and the grid is shown on Fig.5.2).

The Wind Wave model (WWM-II) used a spectral grid of 18 regularly-spaced directions and 18 frequencies exponentially spanning the 0.03 - 0.5 Hz range. The physics of the wave model included quadruplet (DIA) and triad (LTA) wave-wave interactions, whitecapping [*Bidlot*, 2007], depth-induced wave breaking (with a McCowan-type criterion $\gamma = 0.73$) and bottom friction, following the formulation of *Hasselman et al.* [1973] with a friction coefficient $C_b = 0.067 m^2.s^{-1}$. Wave spectra computed with the North Atlantic regional wave model (described in Chapter6) were used to force WWM-II at its ocean boundaries.

The circulation model SELFE ran in depth-averaged (2DH) barotropic mode. The hydrodynamic time step was set to 10 seconds. The model was forced at its ocean boundary with time-series of sea surface elevation measured at the Cascais tide gauge. The series was filtered to remove seiches, and a few small gaps were filled with harmonic predictions. The upstream boundary in the lagoon was defined as a closed boundary based on the assumption that the freshwater inflow was negligible. The friction was parametrized with a space-variable manning coefficient ranging from 0.02 to 0.04 $s^2.m^{-1/3}$.

The sediment transport model used a single grain size of 0.0008 m over the entire domain that corresponds to the average value observed near the tidal inlet. The bed load and suspended load transport were computed with the unified transport formulae of *van Rijn* [2007a,b]. The effect of the bed slope on the transport was taken into account following the method of *Lesser et al.* [2004] that considers the effects of the slope along the current direction and perpendicular to it. In order to dampen the numerical oscillations inherent to the modelling system, a diffusive

factor ϵ of 4 was used and the non-linear filter for local extrema was activated.

8.2.2 Qualitative validation

A 56-day simulation was performed with the morphodynamic modelling system and daily outputs of the simulated depths (relative to mean sea level) were retrieved. 8 snapshots of the model results are presented on Fig.8.5. From November 5 to November 24, the model simulates

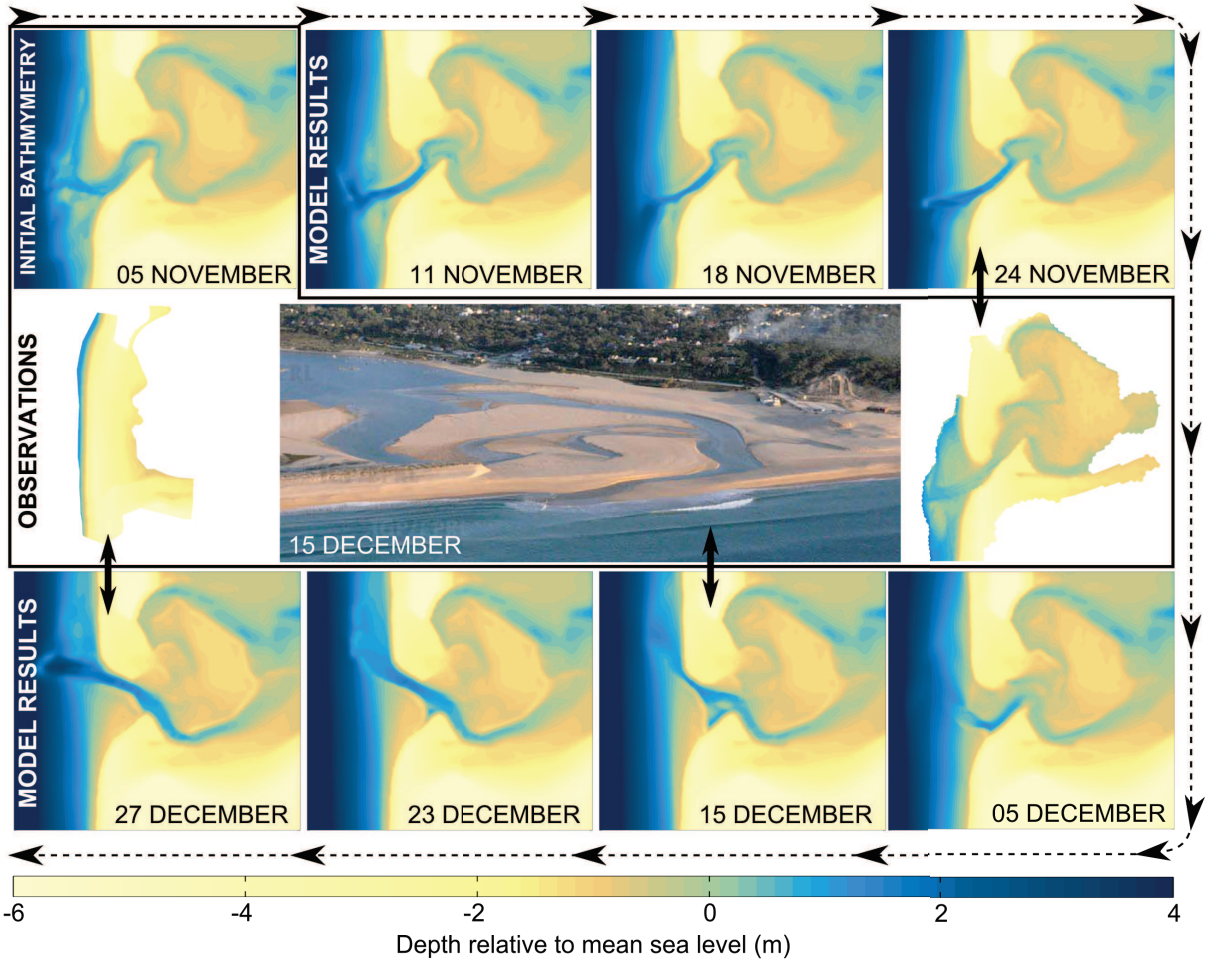

Figure 8.5: Simulated morphological changes of the Albufeira Lagoon inlet between November 5 and December 27, 2010. Two measured topography (on November 24 and December 27) and one aerial photograph of the inlet (taken on December 15) are given for comparisons (middle panel).

the deepening and southward migration of the main channel, and the welding of sand banks to the south beach. The comparison between the modelled and the observed morphology on November 24 shows that the simulated southward migration of the main channel is in agreement with the measurement, although the channel does not deepen in the reality. From the end of November until the end of December, the model simulates the northward migration of the inlet associated to the development of a sand spit growing northward from the south margin of the channel. The cross-sectional area shrinks during the first two weeks, displaying a very narrow section around December 15, and enlarges again afterwards. The simulated inlet morphology of December 15 shows striking similarities with the aerial photograph taken on the same day. Indeed, a long spit oriented northward is clearly visible on the aerial photograph of December 15 and the model results for the same day. This sand spit forms a barrier between the lagoon and the ocean and only a narrow water stream makes its path from the bay to the open sea.

Finally, the topographic survey of December 27 reveals that the lagoon is totally closed at this time while the model predicts the breaching of the spit and the enlargement of the inlet after December 15.

The comparisons of the morphological evolutions computed with the morphodynamic modelling system and the topographic measurements show that the model is able to reproduce the dominant morphological changes induced by the combined action of the tides and the waves. The closure of the inlet is almost reproduced by the model. However, the high water levels occurring at the end of December 2010, as a consequence of a higher-than-average mean water level combined with spring tides (Fig.8.3), provoked the breaching of the barrier in the model results while the barrier developed both vertically and horizontally in the reality.

8.2.3 Quantitative validation

The water level signal in the lagoon can be used as a proxy for estimating the bulk morphology of the tidal inlet. Indeed, when the tidal inlet is well-developed, such as during the summer period, the tidal wave propagates into the lagoon with less damping than when the main channel is shallow, narrow or strongly meandered and close to be fully obstructed. In the latter case, the amplitudes of the semi-diurnal constituents are attenuated and the resulting tide presents a small tidal range in comparison to the tidal range in the ocean. The disappearance of the periodic signal also indicates the exact date of the definitive closure of the inlet.

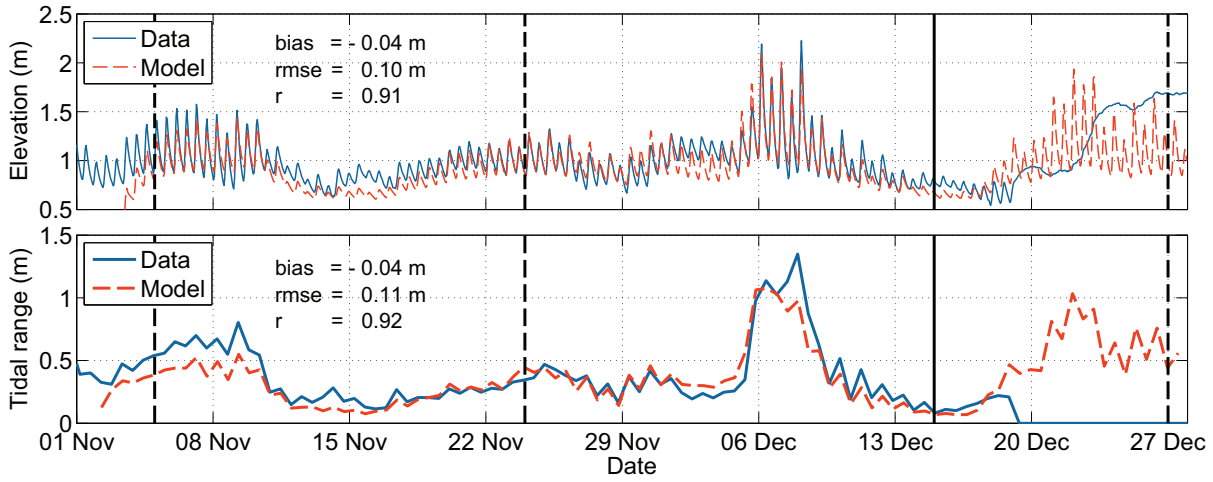

Figure 8.6: Time-series of measured and simulated water elevations in the lagoon (top panel) and corresponding tidal range for each tidal cycle. The dashed and solid black vertical lines indicate the dates of the topographic surveys and of the aerial photograph, respectively.

The sea surface elevations in the lagoon simulated with the morphodynamic modelling system during 56 days were extracted and compared to the observations in order to verify that the simulated morphological changes produced a realistic impact on the propagation of the tide into the lagoon (Fig.8.6). In addition, the tidal ranges of the observed and simulated tidal signals were computed to highlight the tidal attenuation induced by the morphology of the inlet. The amplitude of the constituent M_2 could have been chosen instead of the tidal range, but the 28-day time window necessary to separate M_2 from the other constituents, according to the Rayleigh

criterion, would have deteriorated the temporal resolution of the analysis. The comparison of the simulated and observed tidal ranges in the lagoon are shown on Fig.8.6. These comparisons provide a good validation of the morphodynamic model for the selected period. Indeed, the fluctuations of the tidal signal are well captured by the model. In particular, the rapid decrease of the tidal range around November 10, the abrupt increase around December 5 and the rapid fall of the tidal range after December 8 occur simultaneously in the model and in the observations, and with a similar amplitude. From December 19, the observed tidal range vanishes while it increases in the simulation. This diverging behaviour is attributed to the enlargement of the main channel predicted by the model instead of the observed definitive closure, which indicates that important processes are still missing in the model in order to reproduce accurately the inlet closure.

8.3 Sediment dynamics during fair-weather conditions

The Albufeira Lagoon inlet, like other wave-dominated tidal inlets, has been observed to enlarge significantly during the summer months when the wave climate is more gentle than during the winter months. A detailed description of the inlet hydrodynamics and sediment dynamics during fair-weather conditions appears to be necessary to understand the physical processes that control the development of the inlet during the summer period. The morphodynamic modelling system was used to simulate the currents and the associated sediment transport in the inlet for several configurations of tides and mean water levels. Three synthetic tides representative of neap, mean and spring tides, and three mean water levels representative of lower-than-average, mean and higher-than-average oceanic water levels were defined (Table 8.1). The bathymetry of September 23 was selected for these synthetic tests because the skills of the wave-current model were validated against observations during this period (see Chpater 7). The computational grid was forced at its open boundaries with different combinations of these synthetic tides and water levels. 3-day simulations were carried out in order to give enough time for the lagoon to reach an equilibrium level. In these simulations, the bed update module was switched off to allow consistent comparisons of the results of the different model configurations. The simulated elevations, velocities and total transport were integrated over the last tidal cycle in order to investigate the distribution of the net transport in the inlet. In addition, the net transport was

Table 8.1: Parameters used for the model simulations.

Simulation	Tidal range (m)	MSL (m)	H_s (m)	Mwd (°)	T_p (s)	Current feedback
1	2.0	0.00	0.0			
2	1.0	0.00	0.0			
3	3.0	0.00	0.0			
4	2.0	- 0.15	0.0			
5	2.0	0.15	0.0			
6	0.0	0.00	4.0	310	10	yes
7	3.0	0.00	1.0	310	10	yes
8	3.0	0.00	2.5	310	10	yes
9	2.0	0.00	2.5	310	10	no
10	2.0	0.00	2.5	310	10	yes

integrated across the main channel to estimate the volume of sediment entering or leaving the

inlet during a tidal cycle. Time-series of elevations in the ocean, in the main channel and in the lagoon and time-series of current velocity in the main channel provided informations on the inlet hydrodynamics.

8.3.1 Ebb-dominance of tidal currents and sediment transport

When tides propagate into the lagoon, the semi-diurnal tidal constituents are damped, whereas higher harmonic constituents develop [*Friedrichs and Aubrey*, 1988]. As a consequence, the durations of the flood- and ebb-tides in the lagoon become asymmetric and dominance of the flood or ebb currents occurs, affecting the stability of the tidal inlet. The circulation in the Albufeira Lagoon inlet was simulated with the modelling system in the absence of waves and with an average tidal amplitude of 1 m, corresponding to the mean annual tidal range (Simulation 1, Table 8.1). The superposition of 24-hour time-series of water elevations in the ocean, in the inlet and in the lagoon illustrates the strong distortion of the tidal signal along its path from the ocean to the lagoon (Fig8.7, top panel). Indeed, the tidal range is strongly attenuated in the inlet and in the lagoon (down to 43% of the oceanic tidal range for this particular bathymetry) and the water level oscillates around a mean water level higher than the oceanic mean water level (+20 cm in the inlet and +45 cm in the lagoon). The tidal signal becomes strongly asymmetric and the duration of the flood is reduced to 4.5 hours in the inlet and less than 4 hours in the lagoon, with time lags between low tide slack-waters much larger than between high tide slack-waters (around 4 hours against 2 hours). This strong attenuation of the tidal amplitude and flood durations in the Albufeira Lagoon was measured by *Freitas and Andrade* [1994] for different morphological stages of the inlet and modelled by *Fortunato et al.* [2014]. They obtained amplitude attenuation comprised between 8 and 43% and flood durations between 3.75 and 5 hours, with time lags between low tide slack-waters always longer than between high tide slack-waters. *Lincoln and Fitzgerald* [1988] proposed that, for very shallow inlets with a channel depth relative to mean sea level lower than the average tidal amplitude, an elongated ebb duration in the lagoon was necessary to prevent the truncation of the lower portion of the oceanic tide. This situation occurs in the Albufeira Lagoon inlet, where the depths of the main channel relative to mean sea level were smaller than the mean tidal amplitude (1 m).

The distortion of the elevation signal through the inlet necessarily impacts the water flow between the ocean and the lagoon, and a strong asymmetry of the current velocity occurs (Fig.8.7, bottom panel). The currents in the inlet result from the gradient between the water levels in the ocean and in the lagoon. Since the mean water level is higher in the lagoon than in the ocean, ebb-currents prevail in the inlet during most of the tidal cycle, even during the flood tide (a counter-intuitive mechanism at first glance). Moreover, the maximum amplitudes of the tidal currents differ between the flood-tide and the ebb-tide. According to the principle of mass conservation, it is common to assume that the flood velocities are larger than the ebb velocities when the ebb tide lasts longer than the flood tide and *vice versa*. However, for very shallow inlets, the total depth in the channel is smaller during ebb than during flood [*Fortunato and Oliveira*, 2007a] and the magnitude of currents can be larger during ebb than during flood even though the duration of the ebb currents is longer than the flood currents [*Bertin et al.*, 2009a]. The circulation model, validated against observations in Chapter 7, simulates ebb currents up to 1.3 $m.s^{-1}$ while the maximum flood currents reach 1.1 $m.s^{-1}$. These results contrast with the

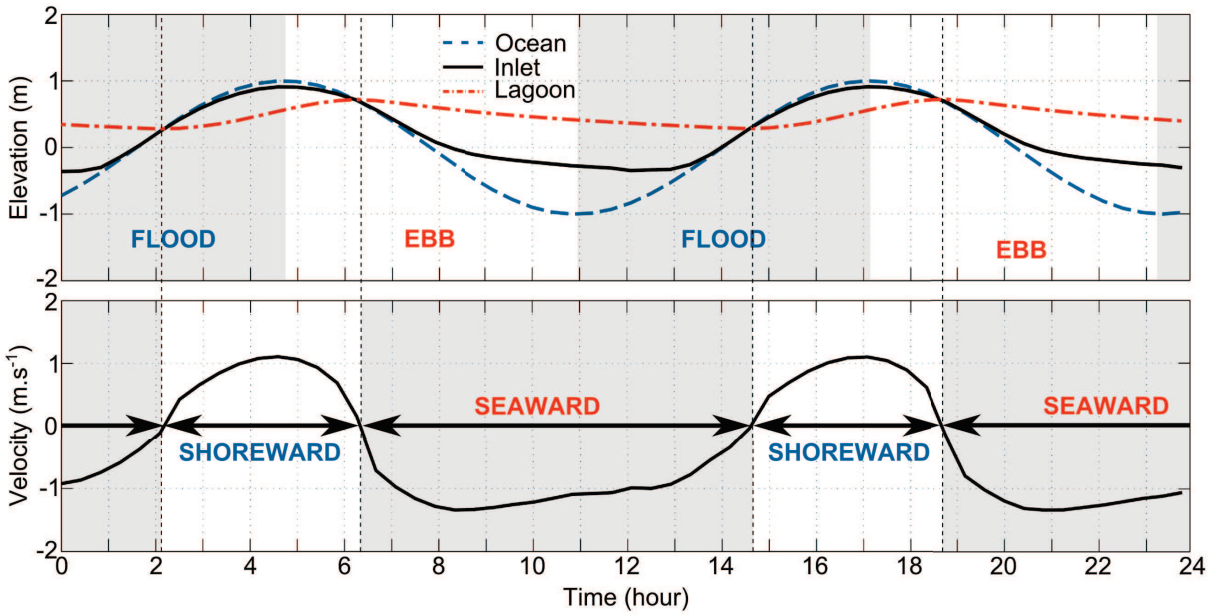

Figure 8.7: 24-hour time-series of simulated elevations in the ocean, in the inlet and in the lagoon (top panel), and current velocities in the inlet (bottom panel).

current velocities estimated by *Freitas and Andrade* [1994] based on the tidal duration only and assuming a constant mean water level in the inlet. The average currents of 1.2 m.s^{-1} for the flood and 0.64 m.s^{-1} for the ebb that they computed might have been biased by this simplification.

The simulated circulation in the Albufeira Lagoon inlet revealed that the geometry of the inlet-lagoon system combined with the local oceanic tide produced ebb currents of longer duration and slightly larger intensities than the flood currents. The bottom shear stress is inversely proportional to the total depths. Therefore, the ebb transport capacity is enhanced because the channel depths are lower during ebb than during flood. Moreover, the magnitude of the sediment fluxes is a function of the current velocities raised to a power comprised between two [*Meyer-Peter and Mueller*, 1948] and five [*Engelund and Hansen*, 1967]. Therefore, the ebb-dominance of the currents in terms of duration and magnitude is expected to promote the ebb-dominance of the sediment transport. The net total transport computed with the model was integrated over a tidal cycle (12.42 hours) in order to investigate the spatial distribution of the net sediment transport in the inlet (Fig.8.8). The net transport in the inlet was mostly oriented seawards with maximum values exceeding 10 tons.m^{-1} in the inlet gorge. The north and south banks of the inlet were mostly inundated during the upper stage of the tide, when the currents flew towards the lagoon. These regions were therefore dominated by shoreward net sediment transport. The integration of the net sediment transport along a section normal to the inlet gorge provided the sediment budget seaward and shoreward.

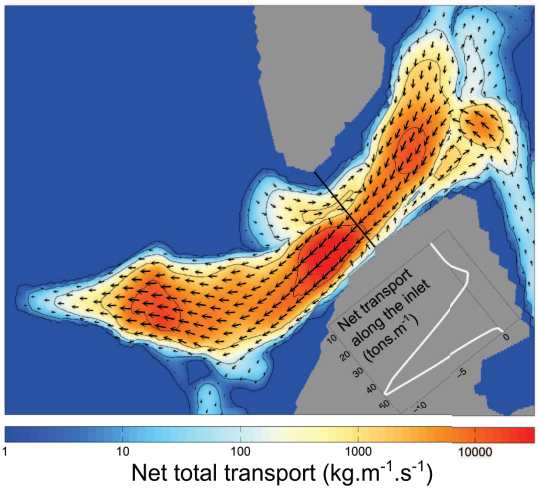

Figure 8.8: Maps of net total transport in the inlet based on model results.

Over a tidal cycle, more than 220 tons of sediments were flushed out of the lagoon while less than 80 tons entered the lagoon, representing only 25% of the gross sediment balance.

8.3.2 Impact of the tidal range

The impact of the tidal range on the net sediment transport in the inlet was investigated with the modelling system. In addition to the simulation presented here above and forced with a 2-m tidal range corresponding to the annual mean tidal range, two other simulations were carried out: one forced with a tidal range of 1 m representing neap tide conditions (Simulation 2, Table 8.1) and one forced with a tidal range of 3 m representing spring tide conditions (Simulation 3). Time-series of elevations (converted into total depth) and current velocities in the inlet provided informations on the hydrodynamics along the inlet, and maps of net total transport and integrated net transport along the inlet section provided information on the sediment balance over a tidal cycle. The comparisons of the total depth in the inlet for each model configuration shows that an increase of the tidal range results in a significant increase of the water depths in the inlet along the whole tidal cycle and a decrease of the flood duration (Fig.8.9). These differences result in large differences of the tidal currents: the larger the tidal range, the higher the ebb and flood velocities and the shorter the duration of flood velocities.

In terms of sediment dynamics, the impact of the tidal range appears clearly on the maps of net transport. In neap tide conditions, the net transport in the inlet over a tidal cycle is ebb-dominated and hardly exceeds 1000 kg.m^{-1}. In mean tide conditions, the net transport is ebb-dominated in the inlet gorge and reaches 10000 kg.m^{-1} while the transport over the inlet banks is flood-dominated but remains lower than 1000 kg.m^{-1}. For the spring tide conditions, the net transport in the inlet gorge is flood-dominated and exceeds 10000 kg.m^{-1} while the transport over the inlet banks is flood-dominated and is comprised between 1000 and 10000 kg.m^{-1}. The values of net transport integrated along the inlet section show that the transport is ebb-dominated for each tidal range considered. However, the values computed for the mean and spring tide conditions are two orders of magnitudes larger than for the neap tide conditions. The percentages of sediments flushed out or pushed into the lagoon show that the ebb-dominance is exacerbated during neap tide conditions.

8.3.3 Seasonal variability of the mean sea level

The time-series of sea surface elevations measured by the Cascais tide gauge in 2010 revealed a strong variability of the mean sea level. During the winter months, the mean water level was observed to fluctuate between values 30 cm higher and 15 cm lower than the mean annual water level. During the rest of the year, the mean water level was mostly lower than the annual mean. The seasonal and pluri-annual variability of the mean sea level was investigated based on pluri-annual tide gauge measurement and satellite observations. The former correspond to the sea surface elevations measured at Cascais between 2000 and 2011. The latter corresponds to the AVISO products "Ssalto/Duacs" [*Ducet et al.*, 2000] provided by the CNES/LEGOS, which covers the period 1992-2013 without time gaps. Although the time-series of monthly mean sea level measured by the tide gauge and the satellite show some difference, the overall variability is reproduced with a good agreement between the two signals (Fig.8.10). These time-series

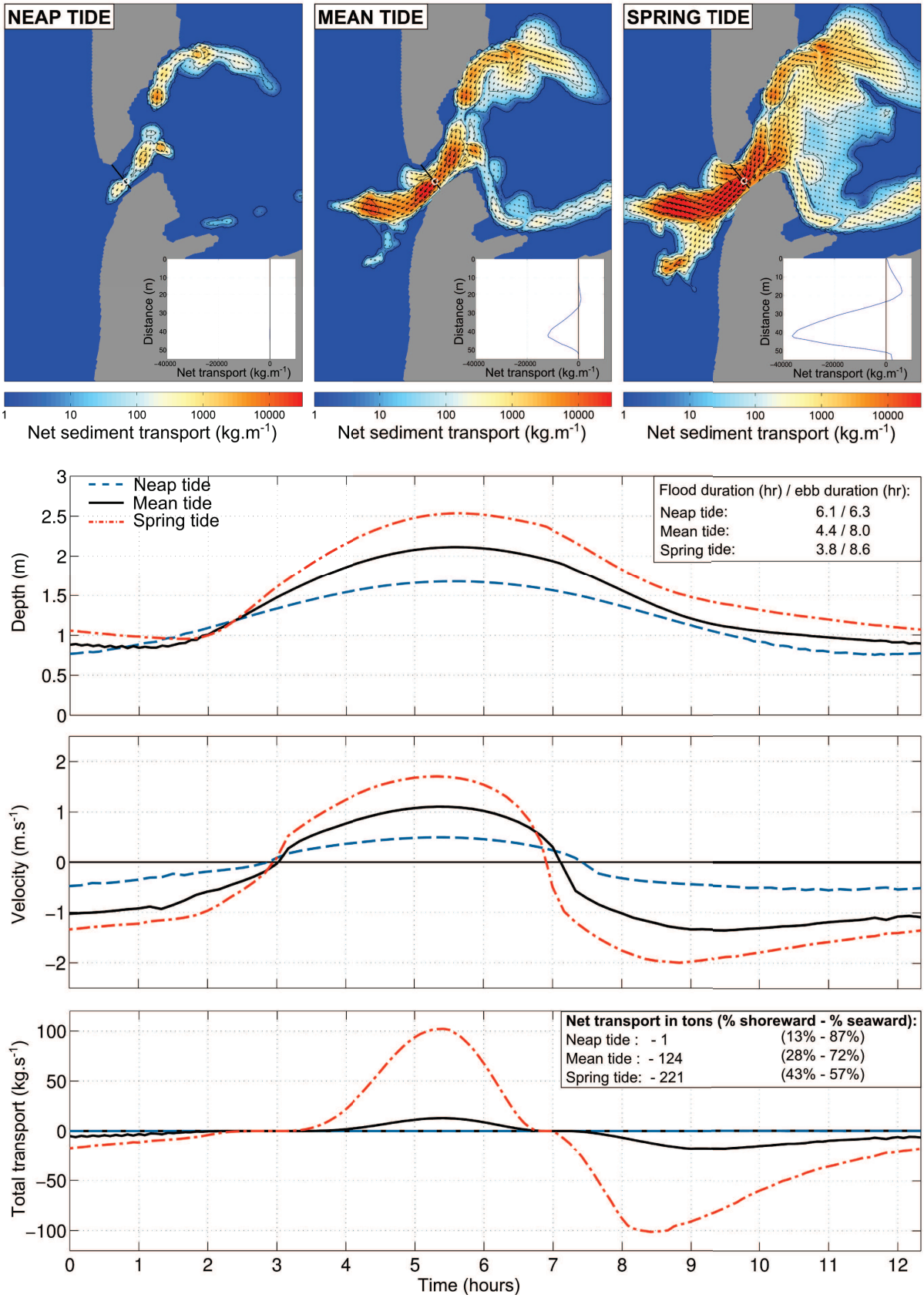

Figure 8.9: Maps of net sediment transport over a tidal cycle for neap, mean and spring tide conditions (top panel), time-series of water depth and velocities in the inlet and net transport integrated over the inlet section for the three tidal conditions.

highlight the large infra- and inter-annual variability of the mean sea level, with values ranging between +25 cm and -15 cm for the period 1992-2013. The seasonal fluctuations of the mean sea level is characterized by high values in winter and low values in summer, although the opposite behaviour occur episodically (*e.g.,* winter 1994). The 22-year time-series of yearly mean sea level computed from the satellite observations (the gaps in the tide gauge time-series prevented the computation of yearly means) presents a positive trend, estimated to 2.85 mm.year^{-1} from linear regression analysis. This value is given for information only since further analysis and literature review would be necessary to discuss this result with confidence, which is beyond the scope of this dissertation. Nevertheless, the yearly time-series presents a significant inter-annual variability ($\sigma = 0.02m$), superimposed to the long-term trend, that is worth considering when investigating the morphodynamics of coastal inlets. Indeed, based on model results *Bertin et al.* [2009a] showed that a higher mean water level enhances the tidal propagation through the tidal inlet of the Óbidos Lagoon and attenuates the tidal asymmetry, and thus affected the sediment dynamics in the inlet.

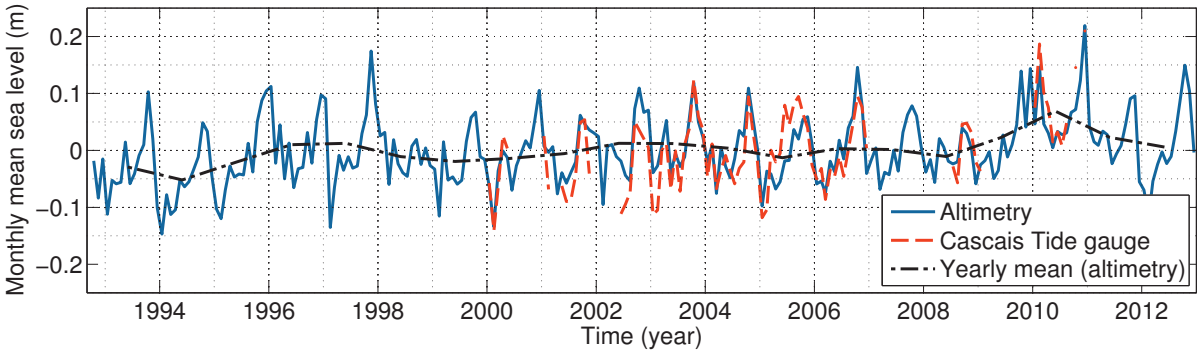

Figure 8.10: Time-series of monthly mean sea level derived from tide gauge measurements at Cascais and satellite observations (AVISO) off the bay of Cascais (CNES/LEGOS).

The impact of the mean sea level on the net sediment transport in the inlet was investigated with the modelling system. Three model simulations were performed in which the mean sea level was set to 0 m (Simulation 1, Table 8.1), -0.15 (Simulation 4) m and +0.15 m (Simulation 5). The time-series of water depth in the inlet for each model configuration show that the difference in water levels remains more or less constant over the tidal cycle, with only a small attenuation during low tide. The differences in current velocity are more pronounced, with an increase of the flood and ebb velocities when the mean sea level increases. Moreover, a higher mean sea level results in longer flood durations and attenuates the asymmetry of the tide. In terms of net sediment transport, the simulation with the highest mean sea levels present values of net sediment transport around twice as large as for the simulation with the mean sea level 0.15 m lower-than-average. Once integrated over the inlet section it appears that the ebb-dominance is slightly exacerbated when the mean sea level is lower-than-average, while it is attenuated when the mean water level is higher-than-average.

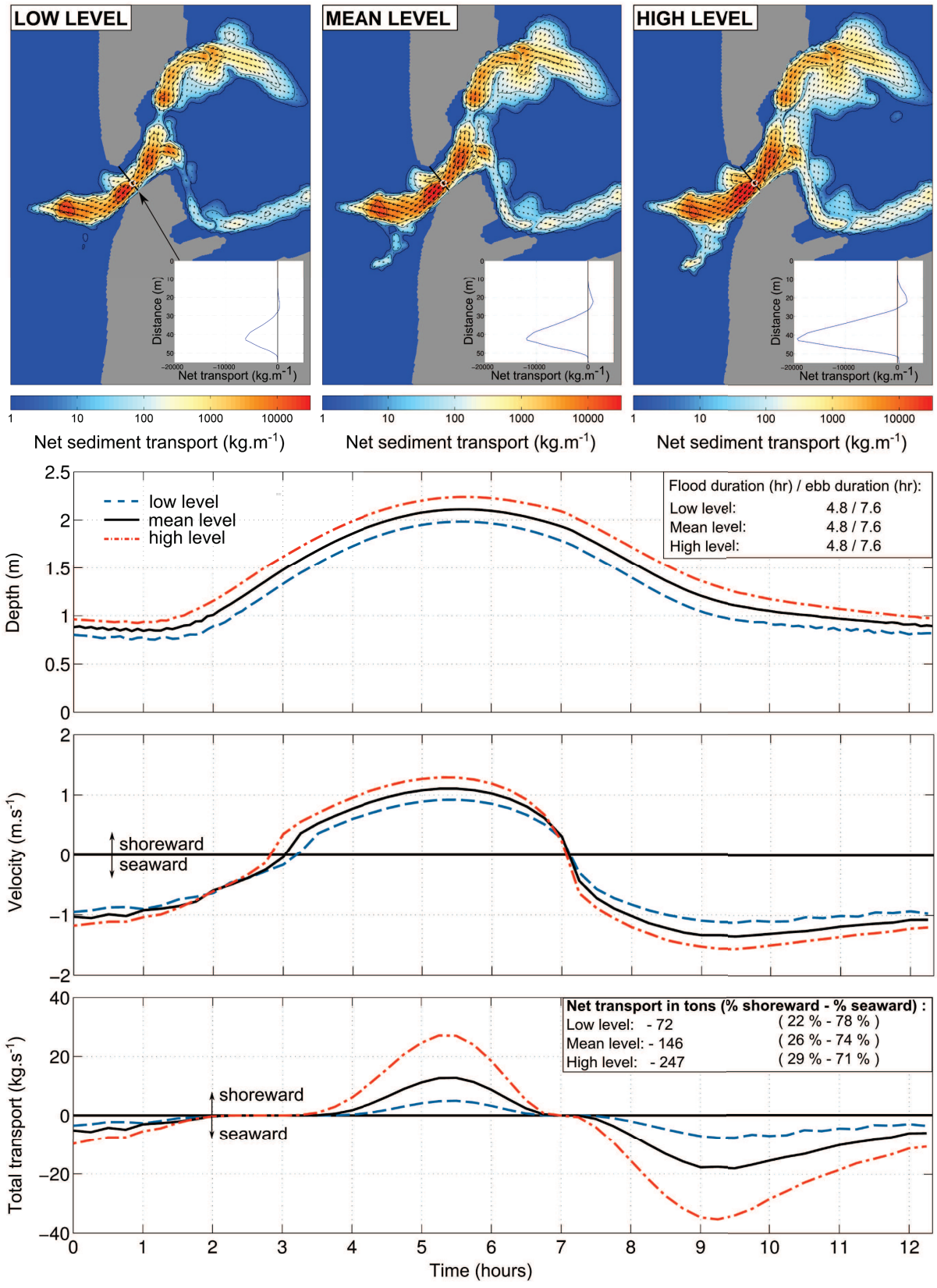

Figure 8.11: Maps of net sediment transport over a tidal cycle for neap, mean and spring tide conditions (top panel), time-series of water depth and velocities in the inlet and net transport integrated over the inlet section for the three tidal conditions.

8.4 Impact of the waves on the dynamics of the inlet

8.4.1 Impact of the waves on the circulation

The Albufeira Lagoon inlet was observed to enlarge during summer and to infill from November to December until its definitive closure at the end of December 2010. The wave climate, much rougher in winter than in summer, is thus expected to alter the overall sediment dynamics of the inlet and reverse the ebb-dominance of the transport in the main channel that prevails during fair weather conditions. Hydrodynamic simulations (without bottom update) in the presence of waves were carried out in order to assess the impact of the waves on the circulation. In a first stage, the tidal forcing was ignored and a wave forcing representative of energetic winter conditions was defined (Simulation 6, Table 8.1). This forcing was maintained constant along the open boundary and the duration of the simulation was sufficiently long (5 days) to allow the model to converge to an equilibrium state. The significant wave heights, sea surface elevations, current velocities, wave forces, barotropic pressure forces and the net forces resulting from the sum of the wave and barotropic forces are shown on Fig.8.12.

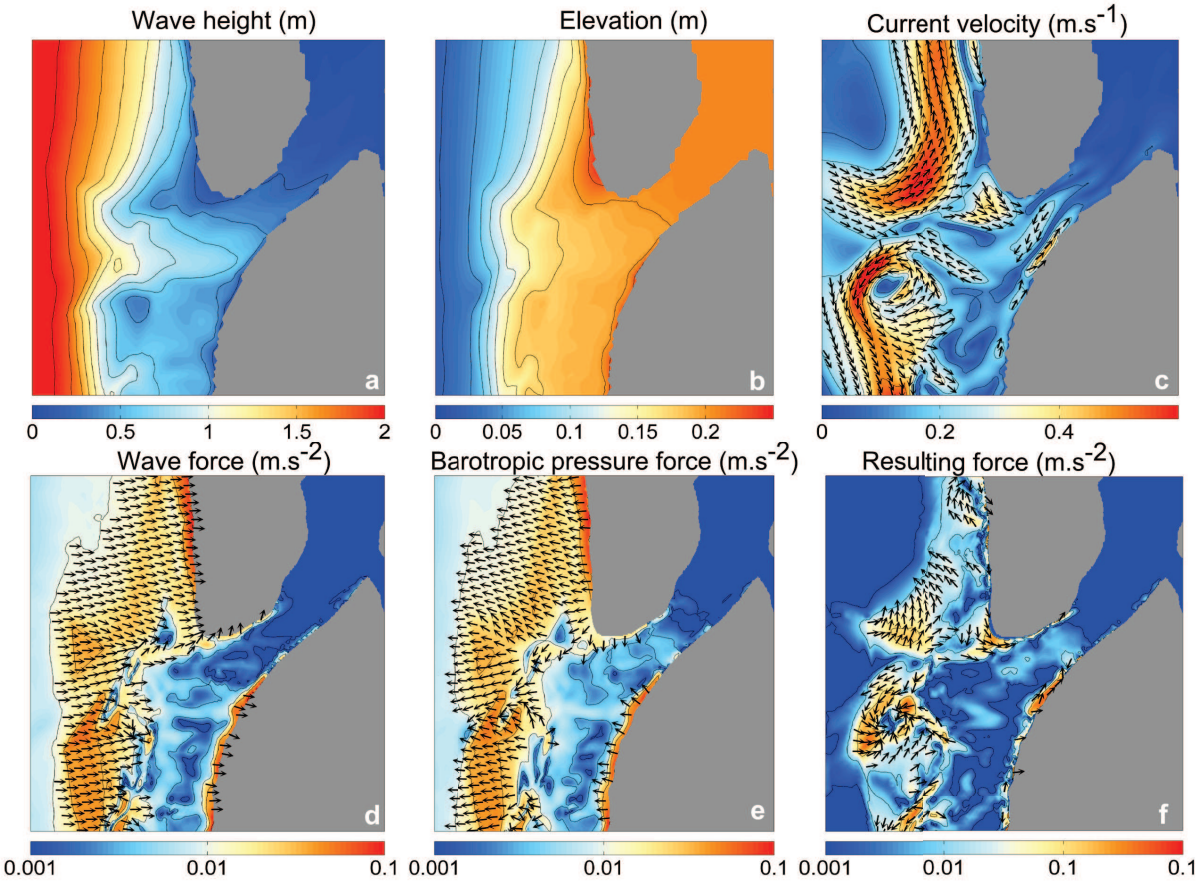

Figure 8.12: Maps of significant wave heights (a), sea surface elevations (b), current velocities(c), wave forces (d), barotropic pressure forces (e), and resultant forces (sum of the barotropic pressure forces and wave forces) computed with the model. For clarity, the vectors are all scaled to unity and they are not represented where the forces and currents are negligible.

When the waves break over the shoaling depths of the ebb-tidal delta and adjacent beaches, they release an excess of momentum flux to the water column, which induces a gradient of the water surface to balance the onshore component of the wave forces. As a consequence, the water

level rises along the shoreline (and decreases near the breaking point) and the wave-induced setup propagates into the lagoon. In Simulation 6, the wave height at the breaking point is around 2.0 m (Fig.8.12a) and the wave setup reaches up to 0.20 m in the lagoon and exceeds 0.25 m on the beach (Fig.8.12b). This spatial distribution of the wave setup occurs because the setup propagating through the inlet is spread over the lagoon while, along the shoreline, it is contained by the beach. Since the water level is higher on the beaches than in the inlet, the barotropic pressure gradient force induces strong lateral forces along the margins of the main channel (Fig.8.12e), that are not balanced by the wave forces (Fig.8.12d). The resulting forces along the channel margins converge towards the lagoon and induce shoreward velocities (Fig.8.12, f and c). This lateral gradient of wave-induced setup around the inlet was already shown by *Bertin et al.* [2009a], through numerical modelling experiments at the Óbidos Lagoon inlet. Moreover, these authors obtained net forces with a strong shoreward component in front of the inlet. This so-called "bulldozer effect" was attributed to the shoreward component of the forces induced by the waves breaking over the ebb-delta that was not compensated by the seaward component of the barotropic forces, due to the lower setup in the lagoon. This relevant mechanism was not reproduced at the Albufeira Lagoon inlet probably because the ebb shield was not well represented in the bathymetry. *Bertin et al.* [2009a] encountered a similar problem and counteracted it by adding empirically an elliptic ebb-delta to their bathymetry. Since the "bulldozer effect" is believed to participate to the infilling of the inlet during energetic wave conditions, it appears necessary to further investigate it at he Albufeira Lagoon in the future.

Finally, the refraction of the waves over the ebb shoals result in eddies and longshore currents that are likely to impact the tidal currents and interact with them.

8.4.2 Impact of the waves on the sediment dynamics

The waves significantly affect the circulation and the sediment dynamics in the vicinity of tidal inlets. When they reach the shores with a non-zero angle of incidence, they induce longshore currents that carry sediments along the beaches toward the inlet. The convergence of the currents along the margins of the inlet towards the lagoon, caused by the horizontal gradient in the wave-induced setup, promotes the flood-dominance in the inlet. The higher water level in the lagoon resulting from the wave-induced setup attenuates the tidal asymmetry, increasing the duration of the flood currents. Finally, the wave orbital velocities and the injection of turbulent kinetic energy through the water column by wave breaking enhance the stirring of sediments. All these effects are likely to significantly impact the sediment dynamics in the inlet.

To investigate the impact of the waves on the sediment dynamics, three model configurations were considered: a configuration with spring tides and without waves (Simulation 3, Table 8.1), a configuration with spring tide and waves representative of summer conditions (Simulation 7), and a configuration with spring tide and waves representative of the winter conditions (Simulation 8). The time-series of water depths in the channel revealed a maximum 10 cm wave-induced setup for the winter conditions (Fig.8.13). The current velocities in the channel were only slightly affected by the waves. Despite the limited impact of the waves on the elevation and the currents, the sediment transport integrated across the main channel showed significant differences for the three configurations considered herein. During flood, the transport was strongly enhanced by

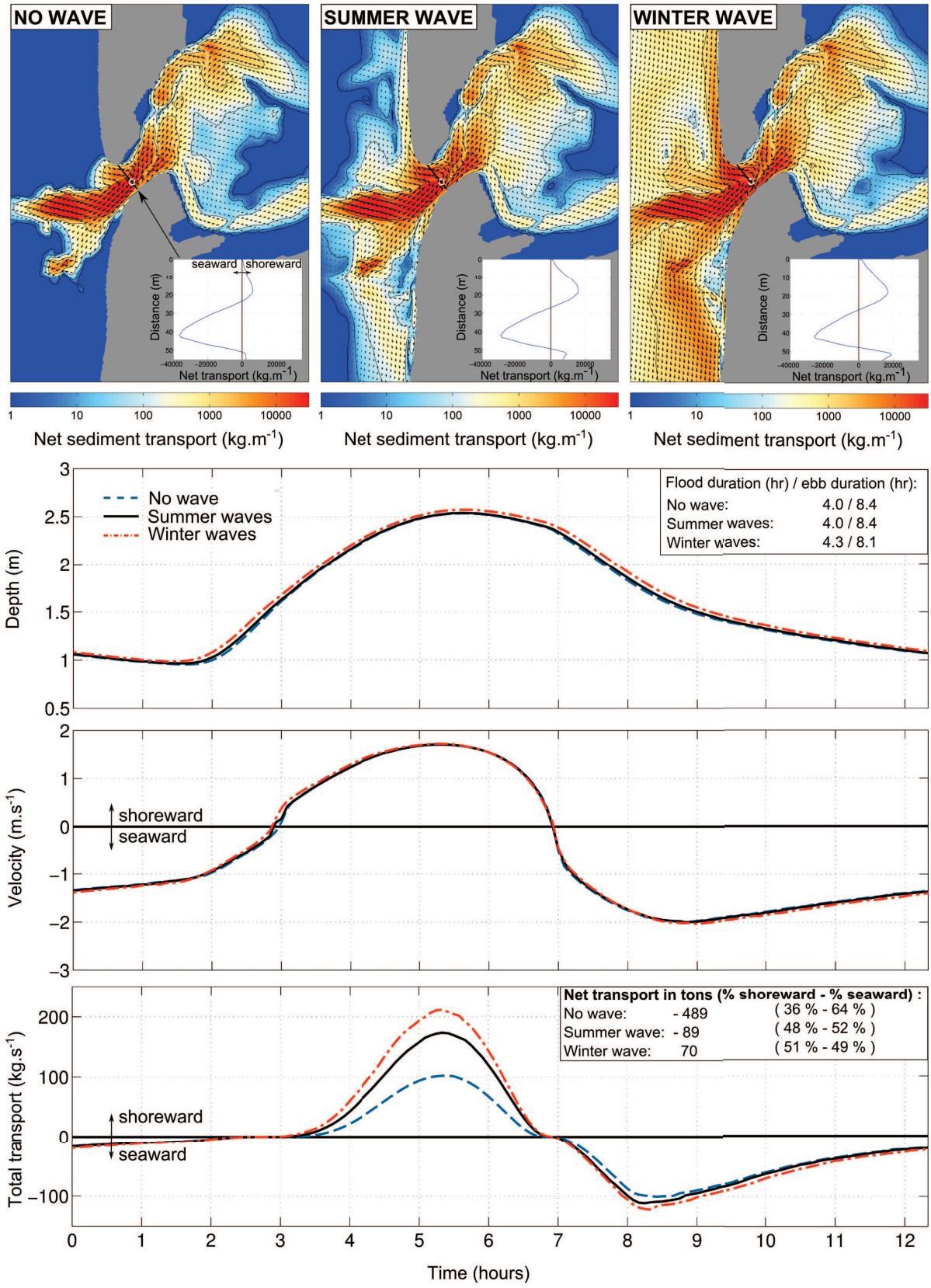

Figure 8.13: Maps of net sediment transport over a tidal cycle for neap, mean and spring tide conditions (top panel), time-series of water depth and velocities in the inlet and net transport integrated over the inlet section for the three tidal conditions.

the presence of waves, while during ebb the amplitude of seaward transport computed for the configurations with waves was only slightly larger than for the configuration with the tide only. The larger depths in the channel during flood allow the waves to propagate into the lagoon and their stirring effects increase the shoreward transport. The convergence of the longshore currents towards the inlet above-mentioned may also explain the larger values of net shoreward transport on the shallow banks of the channel when the waves are considered. During the ebb, the channel depths are shallower and the waves generally break over the ebb shoals. When they penetrate the inlet, they have lost most of their energy and their stirring effect weakly enhance the seaward transport. As a result, the strong ebb-dominance in terms of sediment transport in the absence of waves is significantly attenuated for the configuration with summer waves, and even reversed into flood-dominance when the winter waves are considered.

8.4.3 Effect of the current feedback on the wave field

In Chapter 7, the tidal currents were shown to significantly alter the wave field; the ebb currents increased the wave height at the entrance of the inlet and attenuated it in the main channel due to wave blocking and current-induced wave breaking dissipation, and the flood currents decreased the wave height along the inlet throat and increased it on the exterior part of the ebb shoals due to current-induced refraction. These current-induced changes in the wave field are expected to impact the sediment dynamics in the inlet. To investigate this process, two simulations were carried out: in the first one, the waves were not affected by the current (Simulation 9, Table 8.1) and in the second one the currents affected the waves (Simulation 10).

The time-series of elevations and current velocities in the inlet for the two model configurations only show minor differences. However, the maps of net sediment transport showed noteworthy differences along the main channel (Fig.8.14). The net transport obtained with Simulation 9 (no current feedback) was higher in the deeper region of the channel (where the transport is oriented seaward) in comparison to the transport obtained with Simulation 10 (with current feedback). Along the margins of the channel the opposite behaviour occurred: the net transport, oriented shoreward was higher when the current affected the waves than when it did not. The integration of the transport rates along a section perpendicular to the inlet gorge revealed that during flood the shoreward transport was enhanced in the simulation with the current feedback, and during ebb, the seaward transport was also enhanced in the simulation with the current feedback (Fig.8.14, bottom panel). Hence the ebb-dominance in terms of sediment transport was attenuated when the impact of the currents on the wave field was taken into account.

These differences were directly correlated to the impact of the currents on the wave field. Indeed, ebb currents induced enhanced dissipation and partial blocking of the incident waves, decreasing their orbital velocity and thus their sediment stirring effect. During flood, wave energy focused on either sides of the currents, increasing the wave height and orbital velocity on the exterior part of the ebb shoals and decreasing the wave height and orbital velocity on the interior part of the shoals and in the channel. Based on these findings, the impact of the currents on the incident wave field hinders the seaward sediment transport and may even tip the scale in favour to flood dominance, in some part of the inlet. This process is believed to contribute to

the accretion of wave-dominated inlets during energetic conditions and justifies the importance of including the current effects on wave propagation in morphodynamic modelling systems for the study of similar environments.

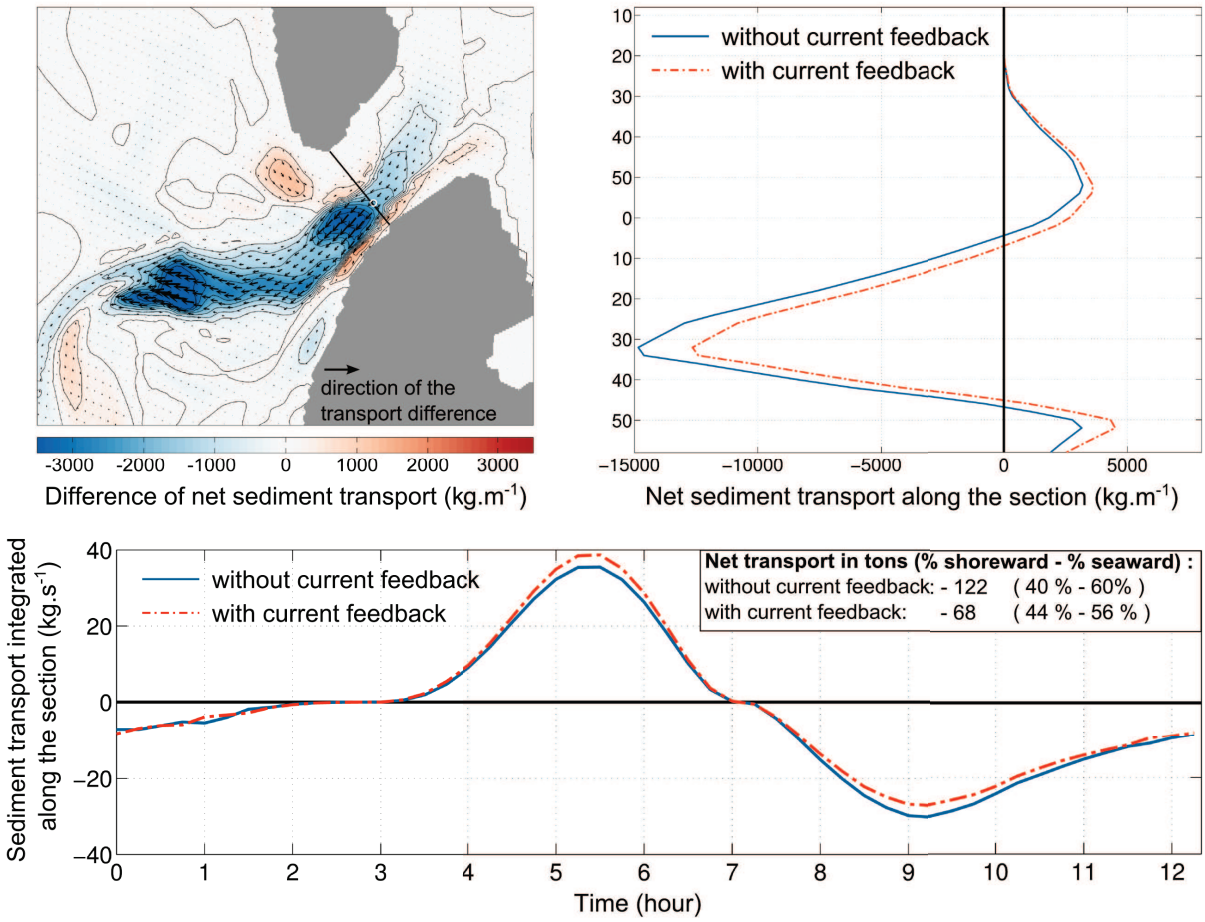

Figure 8.14: Maps of the difference of net sediment transport between the simulation including the current feedback on the waves and the simulation that does not include it (top left); net sediment transport computed across the channel for the two configurations (top right); time-series of sediment transport integrated across the channel for the two configurations (bottom panel).

8.5 Inter-annual variability of the longshore sediment transport

The wave-induced longshore sediment transport plays a key role in the sediment balance of a tidal inlet. The concept of overall stability for tidal inlets introduced by *Bruun* [1978] postulates that low values (lower than 50) of the ratio of the spring tidal prism volume to the gross annual littoral drift indicates a poor stability of the inlet. On the contrary, high values (larger than 150) of this ratio characterize stable tidal inlets. Several authors showed that the annual littoral drift displays a large inter-annual variability [*Bertin et al.*, 2008; *Silva et al.*, 2012]. Near the Albufeira Lagoon, the gross annual littoral drift obtained by *Teixeira* [1990] ranged from 2500 to 3000 m^3 while *Nahon et al.* [2012b] obtained a value of 316400 m^3. Although the difference in the methods used by these authors to compute the littoral drift may explain the divergence of their results, it is also highly likely that these divergences highlight a strong variability of the longshore transport in the region near the Albufeira Lagoon. In order to gain a better insight on this issue, the results of the wave hindcast presented in Chapter 6 were used to realize a 65-year

hindcast of the littoral drift near the study site.

8.5.1 Modelling strategy

The most widely used model for estimating total longshore sediment transport rate is the "CERC" formula given in the *Shore Protection Manual* [*USACE*, 1984]. The model, based on the assumption that the total longshore sediment transport rate is proportional to longshore energy flux, is given as:

$$Q = \frac{K}{16(\rho_s - \rho_0)(1-\lambda)\sqrt{\gamma_b}} \rho_0 \sqrt{g} H_{sb}^{\frac{5}{2}} \sin 2\theta_b \tag{8.1}$$

where Q is the submerged total longshore transport rate (in $\mathrm{m}^3.\mathrm{s}^{-1}$), K is an empirical coefficient, ρ_s and ρ_0 are the sediment and water densities, respectively, λ is the sediment porosity, γ_b is the breaker index, g is the acceleration due to gravity, H_{sb} is the significant wave height at the breaking point, and θ_b is the wave angle at the breaking point. The *Shore Protection Manual* recommends a value of K of 0.39, which was derived from tracer experiments. Later, *Kamphuis* [1991] developed a relationship for estimating longshore sediment transport rates based primarily on physical model experiments. The equation is expressed as:

$$Q = \frac{2.27}{(\rho_s - rho_0)(1-\lambda)} H_{sb}^2 T_p^{1.5} m_b^{0.75} d_{50}^{-0.25} \sin^{0.6}(2\theta_b) \tag{8.2}$$

in which T_p is the peak wave period, m_b is the beach slope from the breaker line to the shoreline, and d_{50} is the median grain size. The CERC formula was shown to provide good estimates of longshore transport when the coefficient K was calibrated against measurement. In addition, the accuracy of this formula deteriorates when the breaking conditions change [*Smith et al.*, 2003]. The formula of *Kamphuis* [1991], that includes the peak period and the beach slope, is less dependant on the breaker type and was thus selected for this study that covers a full range of conditions and did not benefit from *in-situ* observations for calibration.

65-year time-series of wave spectra were extracted from the results of the regional run described in Chapter 6. This time-series was used to simulate the wave propagation from deep water until the coastline with the SWAN model. A nesting method was implemented including three nested grids that are described in Chapter 7.The mean wave parameters computed by the finest grid were retrieved at the breaking point, defined as the location along a cross-shore profile where the breaking index Q_b exceeds 5%. Finally the longshore transport rate was computed every three hours and integrated over time to produce monthly and yearly time-series. This methodology was already used by several authors and provided reasonable comparisons with field data [*Bertin et al.*, 2008; *Silva et al.*, 2007]. The goal of this study is to investigate the variability of the longshore transport at pluri-decadal scales in terms of magnitude and direction. The estimation of the order of magnitude of net monthly and annual longshore sediment transport rate, presented here above, provide the preliminary basis to address this question.

8.5.2 65-year hindcast of longshore sediment transport

The analysis of the 3-hour time-series of longshore transport rate (not shown here) revealed that, during the 65-year time period, the sediment transport was oriented southward more than

80% of the time. This first result corroborates the conclusions of [*Teixeira*, 1990] who estimated a minimum angle of wave refraction a dozen of kilometres north of the lagoon, inducing southward transport in the lower region of the Caparica-Espichel coastal stretch and northward transport in its upper region. However, *Nahon et al.* [2012b] who used a similar methodology as the one presented herein obtained a northward net littoral drift for the period May 2010 - December 2010. The maximum rates of northward and southward transport computed from the present results are 1.6 $m^3.s^{-1}$ and -0.5 $m^3.s^{-1}$, which indicates that the northward transport is likely to be more intense than the southward transport. *Teixeira* [1990] obtained much larger refraction angles near the Albufeira Lagoon for SW waves than for W and NW waves, providing a first explanation for the higher rates of northward transport rates obtained herein.

The time-series of net monthly longshore sediment transport revealed the strong asymmetry between northward and southward transport (Fig.8.15, top panel). Indeed the average value for net northward transport was 95000 m^3 (with a maximum of 500000 m^3) while it was 45000 m^3 for southward transport (with a maximum value of 200000 m^3). The episodes of northward transport are thus much more intense, nevertheless they are also less frequent, with less than 20% of occurrence during the 65-year period. These intense episodes of northward transport occur principally (80%) during the months of November, December, January, February and March, which indicates a potential relation with the winter atmospheric circulation.

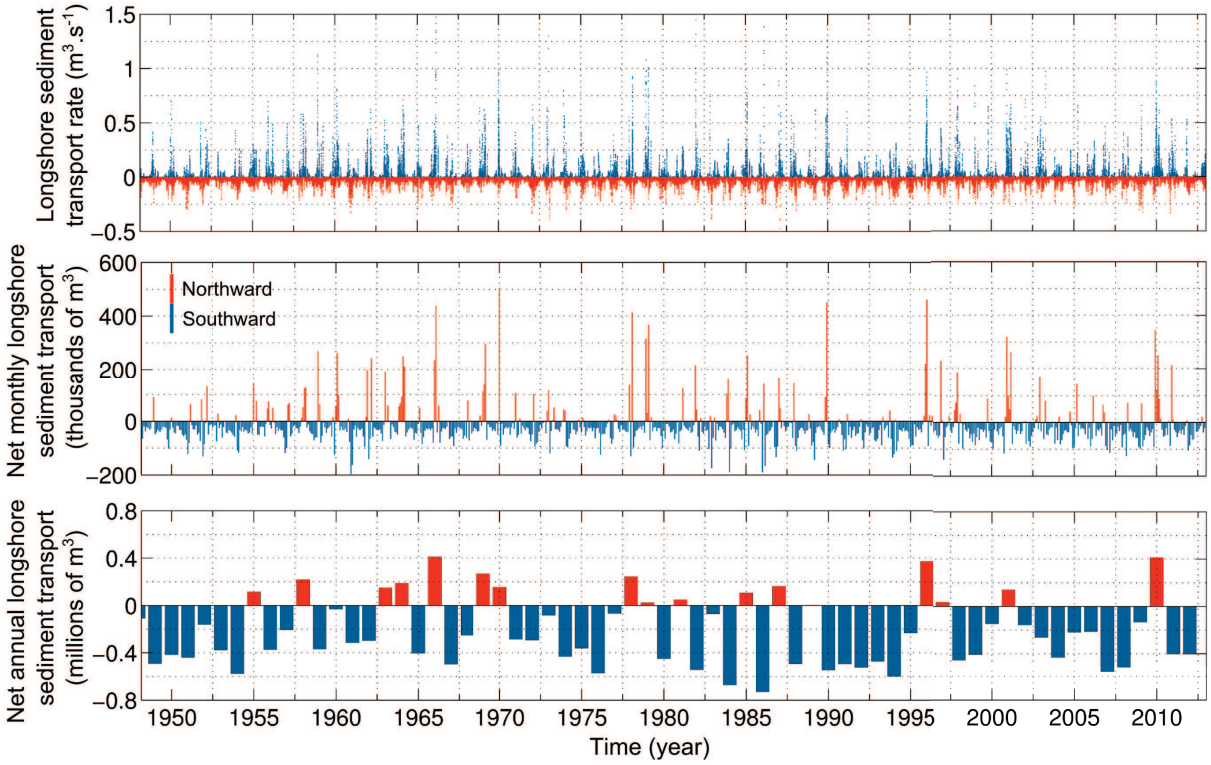

Figure 8.15: Time-series of net monthly (top panel) and annual (bottom panel) longshore sediment transport rates in front of the Albufeira Lagoon.

The time-series of net annual longshore sediment transport show a majority of negative values, indicating the dominance of southward transport (Fig.8.15, bottom panel). The mean value computed over the 65-year is around 220000 m^3, which is rather low compared to the

mean annual rate of 1 million m^3 computed by *Silva et al.* [2012] for a region in the north of Portugal. This difference in net transport can be explained by the different coastal settings. Indeed, these authors computed the longshore sediment transport for an open coast that receives the most of the north swell, while the Albufeira Lagoon is much more sheltered. The inter-annual variability of the net annual longshore transport is clearly evidenced on Fig.8.15, with values of net transport oriented northward ranging from 3000 m^3 to 410000 m^3 and values of net transport oriented southward ranging from 30000 m^3 to 730000 m^3. The net northward transport obtained by *Nahon et al.* [2012b] for the period April 2010 - December 2010 is in agreement with the positive value for the year 2010 (413000 m^3) obtained herein.

8.5.3 Discussion

The net monthly longshore transport in front of the Albufeira Lagoon inlet presents a large variability, with episodic events of strong northward transport, occurring principally during the winter period. It is very likely that this winter peaks of northward transport are related to the seasonal and inter-annual variability of the wave climate. The time-series of mean wave parameters at the breaking point show a clear seasonal cycle, with winter periods characterized with large wave heights, long periods and directions farther-south than average (Fig.8.16). Moreover, the mean direction associated to the waves exceeding the 95^{th} percentile of significant

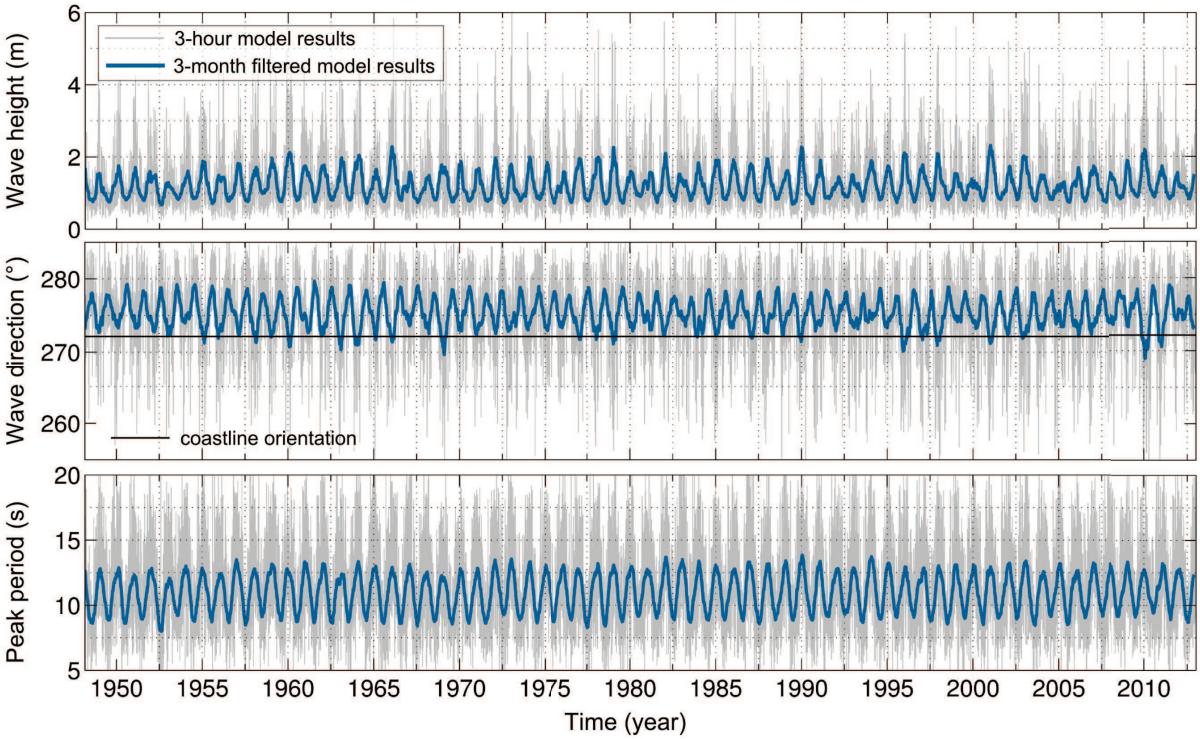

Figure 8.16: 65-year time-series (1948-2012) of significant wave height (top panel), mean wave direction (middle panel) and peak period (bottom panel) at the breaking point in front of the Albufeira Lagoon

wave height at the breaking point is lower than 270° while the mean directions computed over the entire time-series is 275°. Since the orientation of the coastline near the Albufeira Lagoon is around 272°, the breaking waves will induce southward transport most of the time but the largest waves will generally be associated to northward transport. The most severe storms in Portugal occur almost systematically during the winter period when a low pressure system passes over the Iberian Peninsula. When the trajectories of the mid-latitude cyclones is farther-south

than average, both the swell and the wind sea have directions farther south than average and the resulting wind field reaches the shore with an angle of incidence lower-than-average.

In Chapter 6, a strong correlation between the North Atlantic Oscillation (NAO) and the wave climate in front of the Albufeira Lagoon was evidenced. The longshore sediment transport is mostly controlled by the wave height, direction and period at the breaking point, and its variability is directly related to the variability of these parameters. The coefficients of correlation were computed between the monthly and annual rates of longshore sediment transport and the corresponding NAO indexes of *Hurrell* [1995] (Fig.8.17). The two parameters presented negative correlation coefficients larger than 0.5 indicating a significant dependence of the magnitude and direction of the sediment transport rates with the NAO, corroborating the findings of *Silva et al.* [2012] who also obtained negative correlation coefficients for the net annual rate ($r = 0.74$). Finally the same analysis was carried out for the net winter (December-to-March) transport rate and associated NAO index, and a higher correlation coefficient was obtained ($r = -0.81$) than for the monthly and annual values ($r = -0.55$ and $r = -0.67$, respectively). This last result is in agreement with the strong correlation obtained between the winter wave climate and the NAO in Chapter 6 and provides a great opportunity to further investigate the relationship between the longshore transport and the NAO and its potential support for understanding long-term morphological evolution such as the inter-annual variability of the morphological changes at the Albufeira Lagoon inlet.

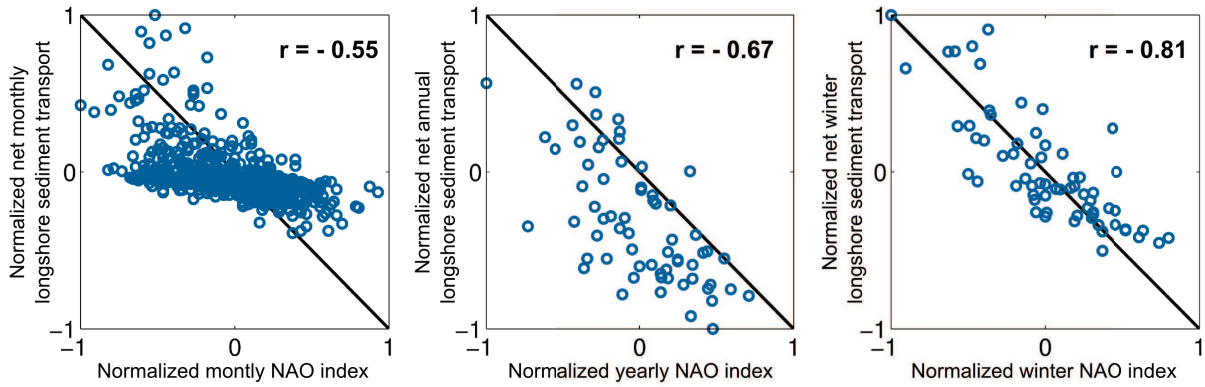

Figure 8.17: Scatter diagrams of net longshore sediment transport rates against NAO indexes and associated coefficient of correlations (significant with 99% of confidence) for monthly values (left panel), annual values (middle panel) and winter values (right panel). The transport rates and NAO indexes were normalized by their maximum values.

Summary

The morphological changes of the Albufeira Lagoon inlet were analysed between April 2010 and December 2010 based on 9 topograhic surveys. The main channel was observed to enlarge and migrate southward from the end of May until the end of September. In October, an overwash is likely to have obstructed the northern channel and favoured the development of the southern channel. Between November and December, the channels accreted and the inlet closed at the end of December after a long spit growing northward from the south bank separated the lagoon from the ocean. These morphological changes were explained by the evolution of the wave conditions and the mean sea level during the studied period.

The morphodynamic modelling system was set up to simulate the morphological changes at the Albufeira Lagoon inlet between November 5 and December 27, 2010. The model was able to reproduce the major changes of the inlet morphology during this period. In particular the southward migration of the main channel in November and the spit growth in December were reproduced by the model. The water levels in the lagoon were also correctly simulated by the model

The physical processes controlling the morphological changes of the inlet during fair weather conditions were investigated by forcing the model with synthetic tidal forcings. In the absence of waves, the sediment transport in the inlet was shown to be strongly ebb-dominated. This ebb-dominance was attenuated when the tidal range was increased or when the mean oceanic water level was higher than average. 22-year time-series of mean sea level satellite observations revealed the seasonal fluctuations of the mean sea level, with high values during winter (up to 30 cm) and low values during summer (up to -15 cm). A weaker inter-annual variability ($\sigma = 0.02m$) was also evidenced from this data set.

Model simulations with different wave forcings revealed the strong impact of the waves on the circulation and the sediment dynamics of the inlet. Wave heights representative of the winter conditions inverted the direction of the net transport through the inlet from ebb-dominated to flood dominated.

The variability of the longshore transport was investigated through a 65-year hindcast of longshore transport rates computed from the modelled wave parameters at the breaking point in front of the Albufeira Lagoon inlet for the period 1948-2012. The longshore transport was oriented southward more than 80% of the time but occurrences of intense northward transport in winter significantly affected the net transport rates. The net annual transport was estimated around 200000 m^3 southward but the values computed from 1948 to 2012 spread over 3 order of magnitudes and even reversed towards the north during certain years. This large variability of the net longshore transport was strongly correlated to the North Atlantic Oscillation, particularly when only the winter periods were considered.

Chapter 9

Conclusions and perspectives

Synthesis of the research work

The main objective of this dissertation was to gain a better understanding of the physical processes that control the morphological changes of wave-dominated tidal inlets. In order to achieve this goal, a comprehensive investigation of the morphodynamics of the Albufeira Lagoon inlet, an ephemeral barrier-inlet-lagoon system located on the west coast of Portugal, was carried out. This comprehensive study was based on both observations and model results, and covered a wide range of spatial and temporal scales.

A detailed description of the geomorphological and hydro-sedimentary settings of the Albufeira Lagoon and its associated tidal inlet revealed the complex dynamics of this coastal system. Several aspects of this tidal inlet, that are common to many other wave-dominated tidal inlets, were identified and provided a guideline to conduct this research work. The Albufeira Lagoon inlet is a shallow and narrow tidal inlet that experiences drastic morphological changes on monthly time-scales and closes systematically. Its natural opening being very rare, the barrier beach that separates the lagoon from the ocean is artificially breached every year to allow the renewal of the lagoon waters. To this day, the duration of the inlet lifespan, ranging from a fortnight to several months, has remained completely uncertain and appeared, somewhat, arbitrary. Hence, the analysis of the mechanisms leading to the closure of the inlet was addressed at infra-annual time scale - what are the physical processes that lead to the closure of wave-dominated tidal inlets? - and pluri-decadal time scale - which forcing controls the inter-annual variability of the morphological changes of these coastal environments?

A two-day field work was conducted at the Albufeira Lagoon in September 2010. Topographic and hydrodynamic measurements were collected during spring tides and energetic incident wave conditions. The analysis of time-series of sea surface elevation, current velocities and mean wave parameters along the inlet revealed the complex nature of the wave-current interactions and their impact on the circulation in the tidal inlet. The analysis of nine digital elevation models based on monthly topographic survey between April 2010 and December 2010 highlighted the seasonal behaviour of the inlet: in summer, the inlet enlarged and migrated southward in a rather smooth fashion, while in winter, rapid and chaotic morphological changes occurred, such as channel obstruction due to overwash episodes, reversing of the direction of migration and inlet closure, all

associated to energetic wave events.

The development of a morphodynamic modelling system to simulate the morphodynamics of complex coastal systems such as wave-dominated tidal inlets was an essential step of this research work, as it provided a comprehensive tool to analyse numerous aspects of the dynamics of tidal inlets. A numerical platform composed of existing wave (WW3, SWAN, WWM-II) and circulation (SELFE) models and a new 2DH sediment transport - bottom update model (SED2D) was developed in a collaborative framework. In its final form, the modelling system enabled the full coupling of the wave, current, and sediment units, each of them sharing a single unstructured grid and the same domain decomposition. The sophisticated numerical methods of the different models and the parallelization of the modelling system based on Message Passing Interface produced an efficient tool able to simulate the morphodynamics of complex coastal systems, subjected to tides, waves and atmospheric forcings, for a broad range of spatial and temporal scales.

In a first stage, the long-term variability of the wave forcing that controls to a large extent the morphological changes at the Albufeira Lagoon inlet was investigated through the application of a wave model. A 65-year hindcast (1948-2012) of the wave climate in the North-East Atlantic Ocean and in the region of the Albufeira Lagoon was realized by forcing the wave model with the NCEP-NCAR Reanalysis wind fields. The regional analysis revealed a large spatial and temporal variability of the wave climate. In particular, the huge inter-annual variability of the significant wave height, mean wave direction, peak period, and directional spreading was shown to be strongly correlated to the North Atlantic Oscillation. The long-term trends obtained by linear regressions through the annual and winter-average significant wave heights were in close agreement with the trends evidenced by previous studies. However, these trends were largely explained by the trends in the North Atlantic Oscillation index, strongly dependent on the selected period, and their low statistical significance did not allow to conclude about the increase in wave heights in the North Atlantic, as proposed by several authors. The local results of the wave hindcast were used to compute the wave climatology near the Albufeira Lagoon. Medium-to-large correlation coefficients between the mean wave parameters and the North Atlantic Oscillation index were obtained. In particular, negative phases of this index were associated to waves larger-than-average, with farther south directions, lower peak periods and a wider directional spreading. Finally, the impact of the wave climate variability on the longshore sediment transport was investigated. An empirical formula for estimating the longshore transport with the mean wave parameters at the breaking point was used in combination with the 65-year wave hindcast. The mean annual net longshore transport was estimated as 200000 m^3 oriented southwards. Nevertheless, a strong inter-annual variability was evidenced and the annual rates computed over the 65-year period spread over three order of magnitudes (from 3000 $m^3.year^{-1}$ to 730000 $m^3.year^{-1}$) and were oriented northward 25% of the time. The magnitudes and the direction of the net longshore sediment transport was strongly correlated to the North Atlantic Oscillation. The inter-annual variability observed in the morphological behaviour of the Albufeira Lagoon inlet is proposed to be significantly explained by the strong inter-annual variability in the wave climate in general and in the longshore sediment transport in particular.

In a second stage, the sediment dynamics of the tidal inlet at infra-annual time-scales (from a tidal cycle to several weeks) was investigated through the application of the morphodynamic modelling system. In the absence of waves, the inlet was shown to be clearly ebb-dominated in terms of tidal current and sediment dynamics. The ebb-tidal currents in the inlet systematically lasted longer than the flood tidal currents and their magnitude was slightly larger. This counter-intuitive process was explained by the much shallower depths in which the ebb currents occurred compared to the flood currents. The enlargement of the inlet during the summer period is proposed to be associated to the ebb-dominance of the inlet during fair-weather conditions. A higher-than-average oceanic mean water level and larger tidal ranges were shown to attenuate the ebb-dominance in the inlet, through the alteration of the duration and magnitude of the tidal currents and the increase of the total depth in the inlet. Higher than average mean sea level is usually observed in Autumn, which period corresponds to the shoaling/closure of the inlet. The impact of the waves on the sediment dynamics in the inlet was investigated by forcing the model with synthetic wave conditions. The waves significantly affected the circulation in the inlet, mainly through the propagation of the wave-induced setup into the lagoon. This wave-induced setup was higher on the beaches than in the lagoon and lateral barotropic pressure gradient forces, together with shoreward wave forces, promoted the convergence of the currents towards the channel. Moreover, the sediment stirring effect of the waves had a considerable impact on the net sediment transport through the inlet. During flood, the higher depths in the inlet and the flood currents allowed larger waves to propagate through the inlet and the shoreward sediment transport was strongly enhanced. During ebb, the shallower depths in the inlet and the counter-currents dampened the wave propagation through the inlet, and the seaward sediment transport was weakly enhanced. As a consequence, the ebb-dominance in the inlet was strongly attenuated in the presence of waves and wave heights representative of winter conditions were able to reverse the net sediment transport towards flood-dominance. The combination of large waves and higher-than-average mean water level that occurred the week prior to the inlet closure in 2010 is likely to have caused the rapid infilling of the inlet and the development of the barrier. In addition, the occurrences of several energetic SW wave events promoted the growth of a sand spit northward that eventually obstructed the main channel.

Perspectives

The large panel of scientific issues tackled in this dissertation - from the questioning of the long-term increase of wave heights in the North Atlantic to the complex modelling of non-linear wave-current interactions in shallow tidal inlets - has brought out a number of exciting challenges for future research. Moreover, the development of a new modelling platform dedicated to the morphodynamic modelling of complex coastal environments, and the preliminary explanations for the morphological behaviour of an ephemeral tidal inlet, have paved the way for further investigations of the morphodynamics of coastal system controlled by tidal and wave forces. Before ending this dissertation, several recommendations are worth mentioning in this last chapter.

First of all, scientific investigation on the dynamics of wave-dominated tidal inlets, such as the Albufeira Lagoon inlet, could greatly benefit from the implementation of systematic long-term monitoring methods of the inlet morphology. A basic and costless warning system allowing

the regular "users" of the lagoon (fishermen, boat drivers, windsurfer, kite-surfers, beach goers) to alert the local authorities in case of major changes in the morphology of the inlet (e.g., closure of the inlet, natural breaching) would produce highly valuable archives of morphological informations. For instance, the correlation between the North Atlantic Oscillation index and the wave-induced longshore sediment transport in front of the Albufeira Lagoon, presented in Chapter 8, provides a stimulating opportunity to investigate the impact of extreme values of the North Atlantic Oscillation index on the morphological behaviour of the inlet, only feasible with a sufficiently long time-series of morphological informations. Moreover, the implementation of Argus-type video monitoring systems overlooking wave-dominated tidal inlets would provide amazing material for morphodynamic studies and model validation, and is worth considering in future research project on tidal inlet dynamics.

The morphodynamic modelling system recently developed has shown satisfying predictive skills and reasonable performance in terms of computation time for the complex case considered herein. Although a number of morphodynamic model results at pluri-decadal or even centennial time scales have already been published [*e.g., Cayocca*, 2001; *Hibma et al.*, 2003; *Dastgheib et al.*, 2008], simulating the seasonal morphological changes of a small coastal system subjected to an energetic wave climate is still extremely challenging. Indeed, the high spatial (O(1 m)) and temporal resolutions (O(1 s)) required by the models to resolve the physical processes controlling the dynamic of small tidal inlets - in particular those related to waves - make their simulations particularly time-consuming. Moreover, the strongly non-linear mechanisms of wave-current interactions in shallow depths, such as wave blocking and steepness-induced dissipation by counter currents, require further research in order to be accurately reproduced by wave-current models [*Ardhuin et al.*, 2012]. In this context, the applications of morphodynamic modelling systems to small scale wave-dominated coastal environments for medium-term predictions are strongly encouraged as they often highlight unexpected numerical limitations to overcome and complex physical processes to be explored.

In the light of the field observations, data analysis and model results gathered during this research work, a number of physical processes have shown to play an important role in the overall sediment dynamics of the inlet and need to be implemented in the morphodynamic modelling system to reproduce the morphological evolutions of wave-dominated tidal inlets with more accuracy. The oscillating uprush and backwash movements of the waves in the swash zone have been observed to be particularly active in the vicinity of the Albufeira Lagoon inlet. The steep slope of the adjacent beaches and the near-vertical sand walls that make up the banks of the main channel after its opening or after a severe erosive event are constantly shaped by swash-induced sediment transport processes. The absence of swash dynamics in the sediment transport module could explain, for instance, the difficulty of the model to build up the barrier and reproduce the definitive closure of the inlet. In addition, significant low-frequency signals were observed during the field campaign in all the hydrodynamic measurements. The release of infra-gravity wave energy in the surf zone induced large oscillations in the sea surface elevation and current velocities that were estimated to increase significantly the sediment transport. Also, when the mean water level is higher than usual and the tidal range is large, the wave-induced low-frequency fluctuations of the water surface can produce overwashes transporting an important quantity of

sediments beyond the barrier and changing radically the morphology of the inlet. Finally, due to the 2DH simplification, the modelling system does not take into account the vertical structure of the current velocities and the three-dimensional contributions of the waves in the simulated currents. Although the development of a 3D fully coupled wave-current-sediment modelling system was carried out simultaneously during the research project 3D-MOWADI, the prohibitive computational time required by this model fostered the development of a more efficient 2DH platform. Hence, further research should be devoted to the development and application of 3D morphodynamic modelling system and to extensive comparisons with their 2DH counterparts.

Bibliography

Abgrall, R. (2006), Residual distribution schemes: Current status and future trends, *Computers & Fluids*, *35*(7), 641–669, doi:10.1016/j.compfluid.2005.01.007.

Ackers, P., and W. R. White (1973), Sediment transport: New approach and analysis, *Journal of the Hydraulics Division*, *99*(11), 2041–2060.

Almeida, L. P., . Ferreira, M. I. Vousdoukas, and G. Dodet (2011), Historical variation and trends in storminess along the Portuguese South Coast, *Nat. Hazards Earth Syst. Sci.*, *11*(9), 2407–2417, doi:10.5194/nhess-11-2407-2011.

Alves, J. H. G. M., and M. L. Banner (2003), Performance of a saturation-based dissipation-rate source term in modeling the fetch-limited evolution of wind waves, *Journal of Physical Oceanography*, *33*(6), 1274–1298, doi:10.1175/1520-0485(2003)033<1274:POASDS>2.0.CO;2.

Ambar, I., N. Serra, M. J. Brogueira, G. Cabeçadas, F. Abrantes, P. Freitas, C. Gonçalves, and N. Gonzalez (2002), Physical, chemical and sedimentological aspects of the Mediterranean outflow off Iberia, *Deep Sea Research Part II: Topical Studies in Oceanography*, *49*(19), 4163–4177.

Andrade, C., C. Teixeira, R. Reis, and M. d. C. Freitas (1996), The record of storminess of the Portuguese NW coast in newspaper sources, in *Partnership in coastal zone management*, edited by J. Taussik and J. Mitchell, pp. 159–166, Samara, Cardigan, UK.

Andrade, C., H. O. Pires, R. Taborda, and M. C. Freitas (2007), Projecting future changes in wave climate and coastal response in Portugal by the end of the 21st century, *Journal of Coastal Research*, *50*, 263–257.

Andrews, D. G., and M. E. McIntyre (1978), An exact theory of nonlinear waves on a lagrangian-mean flow, *Journal of Fluid Mechanics*, *89*(04), 609–646.

Antunes, C., and R. Taborda (2009), Sea level at Cascais tide gauge: Data, analysis and results, *Journal of Coastal Research*, (SI 56), 218–222.

Ardhuin, F., B. Chapron, and F. Collard (2009), Observation of swell dissipation across oceans, *Geophysical Research Letters*, *36*(6), doi:10.1029/2008GL037030.

Ardhuin, F., et al. (2010), Semiempirical dissipation source functions for ocean waves. part i: Definition, calibration, and validation, *Journal of Physical Oceanography*, *40*(9), 1917–1941, doi:10.1175/2010JPO4324.1.

Ardhuin, F., et al. (2012), Numerical wave modeling in conditions with strong currents: Dissipation, refraction, and relative wind, *Journal of Physical Oceanography*, *42*(12), 2101–2120, doi:10.1175/JPO-D-11-0220.1.

Ashton, A., A. B. Murray, and O. Arnoult (2001), Formation of coastline features by large-scale instabilities induced by high-angle waves, *Nature*, *414*(6861), 296–300, doi:10.1038/35104541.

Ashton, A. D., and A. B. Murray (2006), High-angle wave instability and emergent shoreline shapes: 1. modeling of sand waves, flying spits, and capes, *Journal of Geophysical Research: Earth Surface*, *111*(F04011), doi:10.1029/2005JF000422.

Bacon, S., and D. J. T. Carter (1991), Wave climate changes in the North Atlantic and North Sea, *International Journal of Climatology*, *11*(5), 545–558, doi:10.1002/joc.3370110507.

Bacon, S., and D. J. T. Carter (1993), A connection between mean wave height and atmospheric pressure gradient in the North Atlantic, *International Journal of Climatology*, *13*(4), 423–436, doi:10.1002/joc.3370130406.

Bagnold, R. (1966), An approach to the sediment transport problem from general physics, *USGS Professional Paper*, *422-I*(I), 37.

Balouin, Y. (2001), Les embouchures mésotidales (tidal inlets) et leur relation avec les littoraux adjacents - exemple de la Barra Nova, sud Portugal, Ph.D. thesis.

Barnes, R. (1994), The coastal lagoons of Europe, *Coastline*, *3*(2), 1–8.

Bascom, W. N. (1951), The relationship between sand size and beach-face slope, *Transactions, American Geophysical Union*, *32*(6), 866, doi:10.1029/TR032i006p00866.

Battjes, J., and J. Janssen (1978), Energy loss and set-up due to breaking of random waves, pp. 569–587.

Battjes, J. A. (1974), *Computation of Set-up, Longshore Currents, Run-up and Overtopping Due to Wind Generated Waves*, Technische Hogeschool Delft.

Battjes, J. A. (1975), Modelling of turbulence in the surf zone, pp. 1050–1062, ASCE, San Francisco.

Bauer, E. (2001), Interannual changes of the ocean wave variability in the North Atlantic and in the North Sea, *Climate Research*, *18*(1/2), 63–69.

Bennis, A.-C., F. Ardhuin, and F. Dumas (2011), On the coupling of wave and three-dimensional circulation models: Choice of theoretical framework, practical implementation and adiabatic tests, *Ocean Modelling*, *40*(3–4), 260–272, doi:10.1016/j.ocemod.2011.09.003.

Bertin, X., and G. Dodet (2010), Variabilité du climat de houle dans le Golfe de Gascogne au cours des six dernières décennies, pp. 35–44, Editions Paralia, doi:10.5150/jngcgc.2010.005-B.

Bertin, X., B. Castelle, E. Chaumillon, R. Butel, and R. Quique (2008), Longshore transport estimation and inter-annual variability at a high-energy dissipative beach: St. Trojan beach, SW Oléron island, France, *Continental Shelf Research*, *28*(10-11), 1316–1332, doi:10.1016/j.csr.2008.03.005.

Bertin, X., A. B. Fortunato, and A. Oliveira (2009a), A modeling-based analysis of processes driving wave-dominated inlets, *Continental Shelf Research*, *29*(5–6), 819–834, doi:10.1016/j.csr.2008.12.019.

Bertin, X., A. B. Fortunato, and A. Oliveira (2009b), Morphodynamic modeling of the Ancão inlet, South Portugal, *Journal of Coastal Research*, (SI 56), 10–14.

Bertin, X., N. Bruneau, J.-F. Breilh, A. B. Fortunato, and M. Karpytchev (2012a), Importance of wave age and resonance in storm surges: The case Xynthia, Bay of Biscay, *Ocean Modelling*, *42*(0), 16–30, doi:10.1016/j.ocemod.2011.11.001.

Bertin, X., K. Li, A. Roland, J.-F. Breilh, and E. Chaumillon (2012b), Contributions des vagues dans la surcote associée à la tempête Xynthia, février 2010, pp. 909–916, Editions Paralia, doi:10.5150/jngcgc.2012.099-B.

Bertin, X., E. Prouteau, and C. Letetrel (2013), A significant increase in wave height in the North Atlantic Ocean over the 20th century, *Global and Planetary Change*, doi:10.1016/j.gloplacha.2013.03.009.

Bidlot, J. (2007), *A revised formulation of ocean wave dissipation and its model impact*, no. 509 in ECMWF technical memorandum, European Centre for Medium-Range Weather Forecasts, Reading, Berks.

Bischof, B., A. Mariano, and E. Ryan (2003), The Portugal current system (http://oceancurrents.rsmas.miami.edu/atlantic/portugal.html, accessed on august 15, 2013).

Blender, R., K. Fraedrich, and F. Lunkeit (1997), Identification of cyclone-track regimes in the North Atlantic, *Quarterly Journal of the Royal Meteorological Society*, *123*(539), 727–741, doi:10.1002/qj.49712353910.

Bond, J. K., A. N. Green, A. Cooper, and M. S. Humphries (2013), Seasonal and episodic variability in the morphodynamics of an ephemeral inlet, Zinkwazi estuary, South Africa., *Journal of Coastal Research*, *SI 65*, 446–451.

Booij, N., R. C. Ris, and L. H. Holthuijsen (1999), A third-generation wave model for coastal regions: 1. model description and validation, *Journal of Geophysical Research: Oceans*, *104*(C4), 7649–7666, doi:10.1029/98JC02622.

Bouws, E., and G. J. Komen (1983), On the balance between growth and dissipation in an extreme depth-limited wind-sea in the southern North Sea, *Journal of Physical Oceanography*, *13*(9), 1653–1658, doi:10.1175/1520-0485(1983)013<1653:OTBBGA>2.0.CO;2.

Boyd, R., R. Dalrymple, and B. Zaitlin (1992), Classification of clastic coastal depositional environments, *Sedimentary Geology*, *80*(3–4), 139–150, doi:10.1016/0037-0738(92)90037-R.

Bretherton, P., F., and G. R. Garrett, C. (1967), Wave trains in inhomogeneous moving media, *Proceedings of the Royal Society of London A*, *302*(1471), 529–554, doi:10.1098/rspa.1968.0034.

Brown, E. L. (1928), Inlets on sandy coasts, *American Society of Civil Engineers - Proceedings*, *54*(2), 505–553.

Bruneau, N., G. Dodet, X. Bertin, and A. B. Fortunato (2011a), Development of a three-dimensional coupled wave-current model for coastal environments, *Journal of Coastal Research*, (SI 64), 986–990.

Bruneau, N., A. B. Fortunato, G. Dodet, P. Freire, A. Oliveira, and X. Bertin (2011b), Future evolution of a tidal inlet due to changes in wave climate, sea level and lagoon morphology (Óbidos lagoon, Portugal), *Continental Shelf Research*, *31*(18), 1915–1930, doi:10.1016/j.csr.2011.09.001.

Bruun, P. (1966), *Tidal inlets and littoral drift*, Universitetsforlaget, Oslo.

Bruun, P. (1978), *Stability of Tidal Inlets: Theory and Engineering*, Elsevier.

Bruun, P., and F. Gerritsen (1959), Natural bypassing of sand at coastal inlets, *Journal of the Waterways and Harbors Division*, *85*, 401–412.

Bruun, P., and F. Gerritsen (1960), *Stability of coastal inlets*, North-Holland Pub. Co.

Callaghan, D. P., F. Saint-Cast, P. Nielsen, and T. E. Baldock (2006), Numerical solutions of the sediment conservation law; a review and improved formulation for coastal morphological modelling, *Coastal Engineering*, *53*(7), 557–571, doi:10.1016/j.coastaleng.2006.03.001.

Camenen, B., and M. Larson (2005), A general formula for non-cohesive bed load sediment transport, *Estuarine, Coastal and Shelf Science*, *63*(1–2), 249–260, doi:10.1016/j.ecss.2004.10.019.

Camenen, B., and M. Larson (2008), A general formula for noncohesive suspended sediment transport, *Journal of Coastal Research*, *243*, 615–627, doi:10.2112/06-0694.1.

Cameron, W., and D. Pritchard (1963), Estuaries, in *The Sea*, vol. 2, edited by M. Hill, pp. 306–324, John Wileey and Sons, New-York.

Carmo, J. S. A. d. (1995), Contribuição para o estudo dos processos morfodinâmicos em regiões costeiras e estuarinas, Ph.D. thesis, Faculdade de Ciências e Tecnologia da Universidade de Coimbra.

Cavaleri, L., and P. M. Rizzoli (1981), Wind wave prediction in shallow water: Theory and applications, *Journal of Geophysical Research: Oceans*, *86*(C11), 10,961–10,973, doi:10.1029/JC086iC11p10961.

Cayocca, F. (2001), Long-term morphological modeling of a tidal inlet: the Arcachon basin, France, *Coastal Engineering*, *42*(2), 115–142, doi:10.1016/S0378-3839(00)00053-3.

Challenor, P., D. Woolf, C. Gommenginger, M. Srokosz, D. Cotton, D. Carter, and N. Sykes (2006), Satellite altimetry: A revolution in understanding the wave climate, in *Proceedings of the Symposium on 15 Years of Progress in Radar Altimetry*, p. 13–18.

Chawla, A. (2002), Monochromatic and random wave breaking at blocking points, *Journal of Geophysical Research*, *107*(C7), doi:10.1029/2001JC001042.

Chawla, A., and H. L. Tolman (2008), Obstruction grids for spectral wave models, *Ocean Modelling*, *22*(1-2), 12–25, doi:10.1016/j.ocemod.2008.01.003.

Compo, G. P., et al. (2011), The twentieth century reanalysis project, *Quarterly Journal of the Royal Meteorological Society*, *137*(654), 1–28, doi:10.1002/qj.776.

Costa, M., R. Silva, and J. Vitorino (2001), Contribuição para o estudo do clima de agitação marítima na costa portuguesa, *Proceedings das 2as Jornadas Portuguesas de Engenharia Costeira e Portuária*.

Cromwell, J. (1971), Barrier coast distribution: a world-wide survey, in *Second Coastal and Shallow Water Research Conference*, Los Angeles.

Crosby, A., N. White, G. Edwards, and D. J. Shillington (2008), Evolution of the Newfoundland–Iberia conjugate rifted margins, *Earth and Planetary Science Letters*, *273*(1-2), 214–226, doi:10.1016/j.epsl.2008.06.039.

Dastgheib, A., J. Roelvink, and Z. Wang (2008), Long-term process-based morphological modeling of the Marsdiep tidal basin, *Marine Geology*, *256*(1-4), 90–100, doi:10.1016/j.margeo.2008.10.003.

Davis, R. A., and J. C. Gibeaut (1990), *Historical Morphodynamics of Inlets in Florida: Models for Coastal Zone Planning*, Florida Sea Grant College.

De Swart, H. E., and J. T. F. Zimmerman (2009), Morphodynamics of tidal inlet systems, *Annual review of fluid mechanics*, *41*, 203–229.

de Vriend, H., M. Capobianco, T. Chesher, H. de Swart, B. Latteux, and M. Stive (1993), Approaches to long-term modelling of coastal morphology: A review, *Coastal Engineering*, *21*(1-3), 225–269, doi:10.1016/0378-3839(93)90051-9.

Dee, D. P., et al. (2011), The ERA-Interim reanalysis: configuration and performance of the data assimilation system, *Quarterly Journal of the Royal Meteorological Society*, *137*(656), 553–597, doi:10.1002/qj.828.

Dissanayake, D., J. Roelvink, and M. van der Wegen (2009), Modelled channel patterns in a schematized tidal inlet, *Coastal Engineering*, *56*(11-12), 1069–1083, doi:10.1016/j.coastaleng.2009.08.008.

Dodet, G., X. Bertin, and R. Taborda (2010), Wave climate variability in the North-East Atlantic Ocean over the last six decades, *Ocean Modelling*, *31*(3–4), 120–131, doi:10.1016/j.ocemod.2009.10.010.

Dodet, G., X. Bertin, N. Bruneau, A. B. Fortunato, A. Nahon, and A. Roland (2013), Wave-current interactions in a wave-dominated tidal inlet, *Journal of Geophysical Research: Oceans*, p. n/a–n/a, doi:10.1002/jgrc.20146.

Ducet, N., P. Y. Le Traon, and G. Reverdin (2000), Global high-resolution mapping of ocean circulation from TOPEX/Poseidon and ERS-1 and -2, *Journal of Geophysical Research: Oceans*, *105*(C8), 19,477–19,498, doi:10.1029/2000JC900063.

Dupuis, H., D. Michel, and A. Sottolichio (2006), Wave climate evolution in the Bay of Biscay over two decades, *Journal of Marine Systems*, *63*(3-4), 105–114, doi:10.1016/j.jmarsys.2006.05.009.

Eldeberky, Y., and J. A. Battjes (1996), Spectral modeling of wave breaking: Application to Boussinesq equations, *Journal of Geophysical Research: Oceans*, *101*(C1), 1253–1264, doi:10.1029/95JC03219.

Eldeberky, Y., Technische Hogeschool Delft, and Afdeling der Civiele Techniek (1996), *Nonlinear transformation of wave spectra in the nearshore zone*, Faculty of Civil Engineering, Delft University of Technology, [Delft, Netherlands].

Engelund, F., and E. Hansen (1967), *A monograph on sediment transport in alluvial streams*, Technical Report, Technical University of Denmark.

Escoffier, F. F. (1940), The stability of tidal inlets, in *Shore and Beach*, pp. 111–114.

Escoffier, F. F. (1977), *Hydraulics and stability of tidal inlets*, Dept. of Defense, Dept. of the Army, Corps of Engineers, Coastal Engineering Research Center.

Eurosion (2004), *Living with coastal erosion in Europe: sediment and space for sustainability : results from the eurosion study*, Office for Official Publications of the European Communities, Luxembourg.

Ferrarin, C., G. Umgiesser, A. Cucco, T. W. Hsu, A. Roland, and C. L. Amos (2008), Development and validation of a finite element morphological model for shallow water basins, *Coastal Engineering*, *55*(9), 716–731.

Fischer, E. M., and C. Schär (2010), Consistent geographical patterns of changes in high-impact European heatwaves, *Nature Geoscience*, *3*(6), 398–403, doi:10.1038/ngeo866.

FitzGerald, D. M. (1982), Sediment bypassing at mixed energy tidal inlets, *Coastal Engineering Proceedings*, *1*(18).

FitzGerald, D. M. (1988), Shoreline erosional-depositional processes associated with tidal inlets, in *Lecture Notes on Coastal and Estuarine Studies*, vol. 29, edited by D. G. Aubrey and L. Weishar, pp. 186–225, American Geophysical Union, Washington, D. C.

FitzGerald, D. M. (1996), Geomorphic variability and morphologic and sedimentologic controls on tidal inlets, *Journal of Coastal Research*, (SI23).

FitzGerald, D. M., N. C. Kraus, and E. B. Hands (2000), *Natural mechanisms of sediment bypassing at tidal inlets*, US Army Corps of Engineers Vicksburg, MS.

Fiúza, A. F., M. Hamann, I. Ambar, G. Díaz del Río, N. González, and J. M. Cabanas (1998), Water masses and their circulation off western Iberia during may 1993, *Deep Sea Research Part I: Oceanographic Research Papers*, *45*(7), 1127–1160.

Fiúza, A. F. D., M. E. DeMacedo, and M. R. Guerreiro (1982), Climatological space and time-variation of the Portuguese coastal upwelling, *Oceanologica Acta*, *5*(1), 31–40.

Fortunato, A., and A. Oliveira (2000), On the representation of bathymetry by unstructured grids, in *Computational methods in water resources*, L.R. bentley ed., pp. 889–896.

Fortunato, A. B., and A. Oliveira (2004), A modeling system for tidally driven long-term morphodynamics, *Journal of Hydraulic Research*, *42*(4), 426–434.

Fortunato, A. B., and A. Oliveira (2007a), Case study: Promoting the stability of the Óbidos lagoon inlet, *Journal of Hydraulic Engineering*, *133*(7), 816–824.

Fortunato, A. B., and A. Oliveira (2007b), Improving the stability of a morphodynamic modeling system, *Journal of Coastal Research*, *50*, 486–490.

Fortunato, A. B., L. Pinto, A. Oliveira, and J. S. Ferreira (2002), Tidally generated shelf waves off the western Iberian coast, *Continental Shelf Research*, *22*(14), 1935–1950.

Fortunato, A. B., et al. (2014), Morphological evolution of an ephemeral tidal inlet from opening to closure: The Albufeira inlet, Portugal, *Continental Shelf Research*, *73*, 49–63, doi:10.1016/j.csr.2013.11.005.

Freitas, M. C., C. Andrade, and A. Cruces (2002), The geological record of environmental changes in southwestern Portuguese coastal lagoons since the lateglacial, *Quaternary International*, *93*, 161–170.

Freitas, M. d. C. (1995), A laguna de albufeira (peninsula de setubal): Sedimentologia, morfologia e morfodinamica, Ph.D. thesis, Universidade de Lisboa, Faculdade de Ciências.

Freitas, M. d. C., and C. Andrade (1994), Tidal inlet evolution and hydraulic characteristics at albufeira lagoon, in *Proceedings of LITTORAL 1994 conference*, Lisbon, Portugal.

Freitas, M. d. C., and T. Ferreira (2004), Lagoa de Albufeira. geologia., in *Lagoa de Albufeira. Geologia. Comunidade de Aves. Avaliação ecológica e socioeconómica e factores que influenciam a gestão*, pp. 11–52, Instituto da Conservação da Natureza, Centro de Zonas Húmidas, Lisboa, Portugal.

Friedrichs, C. T., and D. G. Aubrey (1988), Non-linear tidal distortion in shallow well-mixed estuaries: a synthesis, *Estuarine, Coastal and Shelf Science*, *27*(5), 521–545, doi:10.1016/0272-7714(88)90082-0.

Frouin, R., A. F. G. Fiúza, I. Ambar, and T. J. Boyd (1990), Observations of a poleward surface current off the coasts of Portugal and Spain during winter, *Journal of Geophysical Research: Oceans*, *95*(C1), 679–691, doi:10.1029/JC095iC01p00679.

Gao, S., and M. Collins (1994), Tidal inlet stability in response to hydrodynamic and sediment dynamic conditions, *Coastal Engineering*, *23*(1–2), 61–80, doi:10.1016/0378-3839(94)90015-9.

Günther, H., S. Hasselmann, and P. A. E. M. Janssen (1992), The WAM model cycle 4 (revised version), *Tech. Rep. 4*, Deutsch. Klim. Rechenzentrum, Hamburg, Germany.

Grant, W. D., and O. S. Madsen (1979), Combined wave and current interaction with a rough bottom, *Journal of Geophysical Research: Oceans*, *84*(C4), 1797–1808, doi:10.1029/JC084iC04p01797.

Guedes Soares, C., and H. de Pablo (2006), Experimental study of the transformation of wave spectra by a uniform current, *Ocean Engineering*, *33*(3–4), 293–310, doi:10.1016/j.oceaneng.2005.05.005.

Hasselman, K., T. Barnett, E. Bouws, D. Carlson, and P. Hasselmann (1973), Measurements of wind-wave growth and swell decay during the joint north sea wave project (JONSWAP), *Deutsche Hydrographische Zeitschrift*, *8*(12).

Hasselmann, K. (1962), On the non-linear energy transfer in a gravity-wave spectrum part 1. general theory, *Journal of Fluid Mechanics*, *12*(04), 481–500, doi:10.1017/S0022112062000373.

Hasselmann, S., K. Hasselmann, J. H. Allender, and T. P. Barnett (1985), Computations and parameterizations of the nonlinear energy transfer in a gravity-wave specturm. part II: parameterizations of the nonlinear energy transfer for application in wave models, *Journal of Physical Oceanography*, *15*(11), 1378–1391, doi:10.1175/1520-0485(1985)015<1378:CAPOTN>2.0.CO;2.

Hayes, M. O. (1975), Morphology of sand accumulations in estuaries, in *Estuarine Research*, vol. 2, L.E. cronin ed., pp. 3–22, Academic press, New-York.

Hayes, M. O. (1979a), Barrier island morphology as a function of tidal and wave regime, in *Barrier islands from the Gulf of St. Lawrence to the Gulf of Mexico*, S.P. leatherman ed., pp. 1–27, Academic Press, New-York.

Hayes, M. O. (1979b), Barrier island morphology as a function of tidal and wave regime, in *Barrier Islands: From the Gulf of St. Lawrence to the Gulf of Mexico*, edited by S. P. Leatherman, pp. 1–29, Academic Press, New-York.

Hayes, M. O., V. Goldsmith, and C. H. Hobbs (1972), *Offset Coastal Inlets. Forms of Sediment Accumulation in the Beach Zone*, Defense Technical Information Center.

Haynes, R., and E. D. Barton (1990), A poleward flow along the Atlantic coast of the Iberian peninsula, *Journal of Geophysical Research: Oceans*, *95*(C7), 11,425–11,441, doi:10.1029/JC095iC07p11425.

Hench, J. L., and R. A. Luettich Jr (2003), Transient tidal circulation and momentum balances at a shallow inlet, *Journal of Physical Oceanography*, *33*(4), 913–932.

Hibma, A., H. de Vriend, and M. Stive (2003), Numerical modelling of shoal pattern formation in well-mixed elongated estuaries, *Estuarine, Coastal and Shelf Science*, *57*(5–6), 981–991, doi:10.1016/S0272-7714(03)00004-0.

Horikawa, K. (1988), *Nearshore dynamics and coastal processes: theory, measurement, and predictive models*, University of Tokyo Press, Tokyo, Japan.

Huang, N. E., D. T. Chen, C.-C. Tung, and J. R. Smith (1972), Interactions between steady won-uniform currents and gravity waves with applications for current measurements, *Journal of Physical Oceanography*, *2*(4), 420–431, doi:10.1175/1520-0485(1972)002<0420:IBSWUC>2.0.CO;2.

Hubbard, D. K., G. Oertel, and D. Nummedal (1979), The role of waves and tidal currents in the development of tidal-inlet sedimentary structures and sand body geometry; examples from North Carolina, South Carolina, and Georgia, *Journal of Sedimentary Research*, *49*(4), 1073–1091, doi:10.1306/212F78B5-2B24-11D7-8648000102C1865D.

Hume, T. M., and C. E. Herdendorf (1992), Factors controlling tidal inlet characteristics on low drift coasts, *Journal of coastal research*, *8*(2), 355–375.

Hurrell, J. W. (1995), Decadal trends in the North Atlantic Oscillation: Regional temperatures and precipitation, *Science*, *269*(5224), 676–679, doi:10.1126/science.269.5224.676, PMID: 17758812.

Idier, D., B. Castelle, E. Charles, and C. Mallet (2013), Longshore sediment flux hindcast: spatio-temporal variability along the sw atlantic coast of france, *Journal of Coastal Research*, (SI 65), 1785–1790.

Ikeda, S. (1982), Lateral bed load transport on side slopes, *Journal of the Hydraulics Division*, *108*(11), 1369–1373.

Janssen, P. A. E. M. (1982), Quasilinear approximation for the spectrum of wind-generated water waves, *Journal of Fluid Mechanics*, *117*, 493–506, doi:10.1017/S0022112082001736.

Janssen, P. A. E. M. (1991), Quasi-linear theory of wind-wave generation applied to wave forecasting, *Journal of Physical Oceanography*, *21*(11), 1631–1642, doi:10.1175/1520-0485(1991)021<1631:QLTOWW>2.0.CO;2.

Jarrett, J. (1976), Tidal prism - inlet area relationships, *GITI report 3*, Coastal Engineering Research Center, US Army Corps of Engineers, Fort Belvoir, Virginia.

Johnson, D. W. (1919), *Shore Processes and Shoreline Development*, Hafner Publishing Co, New-York.

Johnson, H. K., and J. A. Zyserman (2002), Controlling spatial oscillations in bed level update schemes, *Coastal Engineering*, *46*(2), 109–126.

Kalnay, E., et al. (1996), The NCEP/NCAR 40-year reanalysis project, *Bulletin of the American Meteorological Society*, *77*(3), 437–471, doi:10.1175/1520-0477(1996)077<0437:TNYRP>2.0.CO;2.

Kamphuis, J. (1991), Alongshore sediment transport rate, *Journal of Waterway, Port, Coastal, and Ocean Engineering*, *117*(6), 624–640, doi:10.1061/(ASCE)0733-950X(1991)117:6(624).

Keller, J. B. (1958), Surface waves on water of non-uniform depth, *Journal of Fluid Mechanics*, *4*(06), 607–614, doi:10.1017/S0022112058000690.

Keulegan, G. H. (1967), Tidal flow in entrances; water-level fluctuations of basins in communication with seas, *Tech. rep.*, DTIC Document.

Kjerfve, B. (1986), Comparative oceanography of coastal lagoons, in *Estuarine Variability*, edited by D. A. Wolfe, pp. 63–81, Academic Press; Academic Press.

Kjerfve, B. (1994), Coastal lagoons, in *Coastal Lagoon Processes*, *Elsevier Oceanography Series*, vol. 60, Elsevier.

Komar, P. (2011), Coastal erosion processes and impacts: The consequences of earth's changing climate and human modifications of the environment, in *Treatise on Estuarine and Coastal Science*, edited by Eric Wolanski and Donald McLusky, pp. 285–308, Academic Press, Waltham.

Komar, P. D., and M. C. Miller (1975), On the comparison between the threshold of sediment motion under waves and unidirectional currents with a discussion of the practical evaluation of the threshold; reply, *Journal of Sedimentary Research*, *45*(1), 362–367, doi:10.1306/212F6D66-2B24-11D7-8648000102C1865D.

Komen, G. J., L. Cavaleri, M. Donelan, K. Hasselmann, S. Hasselmann, and P. A. E. M. Janssen (1994), *Dynamics and Modelling of Ocean Waves*, Cambridge University Press, Cambridge.

Kraus, N. (2000), Reservoir model of ebb-tidal shoal evolution and sand bypassing, *Journal of Waterway, Port, Coastal, and Ocean Engineering*, *126*(6), 305–313, doi:10.1061/(ASCE)0733-950X(2000)126:6(305).

Krueger, O., F. Schenk, F. Feser, and R. Weisse (2013), Inconsistencies between long-term trends in storminess derived from the 20CR reanalysis and observations, *Journal of Climate*, *26*(3), 868–874, doi:10.1175/JCLI-D-12-00309.1.

Kubatko, E. J., J. J. Westerink, and C. Dawson (2006), An unstructured grid morphodynamic model with a discontinuous Galerkin method for bed evolution, *Ocean Modelling*, *15*(1-2), 71–89, doi:10.1016/j.ocemod.2005.05.005.

Kushnir, Y., V. J. Cardone, J. G. Greenwood, and M. A. Cane (1997), The recent increase in North Atlantic wave heights, *Journal of Climate*, *10*(8), 2107–2113.

Lai, R. J., S. R. Long, and N. E. Huang (1989), Laboratory studies of wave-current interaction: Kinematics of the strong interaction, *Journal of Geophysical Research: Oceans*, *94*(C11), 16,201–16,214, doi:10.1029/JC094iC11p16201.

Lankford, R. (1977), Coastal lagoons of Mexico. their origin and classification., in *Estuarine processes*, vol. Vol. II, edited by M. L. Wiley, pp. 182–215, Academic Press, New-York.

Larson, M., B. Camenen, and P. T. Nam (2011), A unified sediment transport model for inlet application, *Journal of Coastal Research*, *59*, 27–38, doi:10.2112/SI59-004.1.

Latteux, B. (1995), Techniques for long-term morphological simulation under tidal action, *Marine Geology*, *126*(1–4), 129–141, doi:10.1016/0025-3227(95)00069-B.

Leconte, L. (1905), Discussion of "Notes on the improvement of river and harbor outlets in the united states", *Transactions of the American Society of Civil Engineers*, *LV*(2), 306–317.

Leonard, B. (1991), The ULTIMATE conservative difference scheme applied to unsteady one-dimensional advection, *Computer Methods in Applied Mechanics and Engineering*, *88*(1), 17–74, doi:10.1016/0045-7825(91)90232-U.

Lesser, G., J. Roelvink, J. van Kester, and G. Stelling (2004), Development and validation of a three-dimensional morphological model, *Coastal Engineering*, *51*(8–9), 883–915, doi:10.1016/j.coastaleng.2004.07.014.

Lincoln, J. M., and D. M. Fitzgerald (1988), Tidal distortions and flood dominance at five small tidal inlets in southern Maine, *Marine Geology*, *82*(3–4), 133–148, doi:10.1016/0025-3227(88)90137-5.

Longuet-Higgins, M., and R. Stewart (1964), Radiation stresses in water waves; a physical discussion, with applications, *Deep Sea Research and Oceanographic Abstracts*, *11*(4), 529–562, doi:10.1016/0011-7471(64)90001-4.

Madsen, O. S., Y.-K. Poon, and H. C. Graber (2011), Spectral wave attenuation by bottom friction: theory, *Coastal Engineering Proceedings*, *1*(21), doi:10.9753/icce.v21.

Malhadas, M. S., P. C. Leitão, A. Silva, and R. Neves (2009), Effect of coastal waves on sea level in Óbidos lagoon, Portugal, *Continental Shelf Research*, *29*(9), 1240–1250, doi:10.1016/j.csr.2009.02.007.

Martins, C. S. (2002), Surface circulation in the eastern North Atlantic, from drifters and altimetry, *Journal of Geophysical Research*, *107*(C12), doi:10.1029/2000JC000345.

Martins, R., M. Azevedo, R. Mamede, B. Sousa, R. Freitas, F. Rocha, V. Quintino, and A. Rodrigues (2012), Sedimentary and geochemical characterization and provenance of the Portuguese continental shelf soft-bottom sediments, *Journal of Marine Systems*, *91*(1), 41–52, doi:10.1016/j.jmarsys.2011.09.011.

Mellor, G. (2013), Waves, circulation and vertical dependence, *Ocean Dynamics*, *63*(4), 447–457, doi:10.1007/s10236-013-0601-9.

Merrifield, M., et al. (2010), The global sea level observing system (GLOSS), in *Proceedings of the OceanObs'09: Sustained Ocean Observations and Information for Society Conference*, vol. 2, pp. 695–701, European Space Agency, Venice, Italy, doi:10.5270/OceanObs09.cwp.63.

Metha, A. (1996), A perspective on process related research needs for sandy inlets, *Journal of Coastal Research*, (SI23), 3–21.

Meyer-Peter, E., and R. Mueller (1948), Formulae for bed-load transport, in *IAHR*, Stockholm.

Meyssignac, B., and A. Cazenave (2012), Sea level: A review of present-day and recent-past changes and variability, *Journal of Geodynamics*, *58*, 96–109, doi:10.1016/j.jog.2012.03.005.

Miche, A. (1944), Mouvements ondulatoires de la mer en profondeur croissante ou décroissante. forme limite de la houle lors de son déferlement. application aux digues maritimes. troisième partie. forme et propriétés des houles limites lors du déferlement. croissance des vitesses vers la rive, *Annales des Ponts et Chaussées*, *Tome 114*, 369–406.

Mil-Homens, M., R. Stevens, I. Cato, and F. Abrantes (2007), Regional geochemical baselines for Portuguese shelf sediments, *Environmental Pollution*, *148*(2), 418–427, doi:10.1016/j.envpol.2006.12.007.

Miles, J. W. (1957), On the generation of surface waves by shear flows, *Journal of Fluid Mechanics*, *3*(02), 185–204, doi:10.1017/S0022112057000567.

Mota Oliveira, I. B. (1970), Natural flushing ability in tidal inlets, pp. 1827–1845, ASCE.

Munk, W. (1949), Surf beats, *Eos, Transactions American Geophysical Union*, (30), 849–854.

Nahon, A., X. Bertin, A. B. Fortunato, and A. Oliveira (2012a), Process-based 2DH morphodynamic modeling of tidal inlets: A comparison with empirical classifications and theories, *Marine Geology*, *291-294*, 1–11, doi:10.1016/j.margeo.2011.10.001.

Nahon, A., P. Freire, A. R. Pires, G. Dodet, X. Bertin, M. d. C. Freitas, A. B. Fortunato, and C. Andrade (2012b), Morphodynamique d'une embouchure tidale artificielle éphémère : la lagune d'Albufeira, Portugal, pp. 355–362, Editions Paralia, doi:10.5150/jngcgc.2012.038-N.

Nelson, J. (1999), Erosion and sedimentation, *Eos, Transactions American Geophysical Union*, *80*(15), 176–177, doi:10.1029/99EO00128.

Nguyen, X. T., H. Tanaka, and H. Nagabayashi (2007), Wave setup at river and inlet entrances due to an extreme event, in *Proceedings of International Conference on Violent Flows, Organized by RIAM, Kyushu University, Fukuoka, Japan.*

Nichols, M., and G. Allen (1981), Sedimentary processes in coastal lagoons, in *Proceedings of Coastal Lagoon Research, Present and Future*, *UNESCO Technical Papers in Marine Science (33)*, vol. 33, pp. 27–80.

Nicholson, J., I. Broker, J. A. Roelvink, D. Price, J. M. Tanguy, and L. Moreno (1997), Intercomparison of coastal area morphodynamic models, *Coastal Engineering*, *31*(1), 97–123.

O'Brien, M. P. (1931), Estuary tidal prisms related to entrance area, *Civil Engineering, ASCE*, *1*(8), 738–739.

O'Brien, M. P. (1969), Equilibrium flow areas of tidal inlets on sandy coasts, in *Coastal Engineering Proceedings*, vol. 10, Tokyo, Japan.

Olabarrieta, M., J. C. Warner, and N. Kumar (2011), Wave-current interaction in Willapa Bay, *Journal of Geophysical Research*, *116*(C12), doi:10.1029/2011JC007387.

Oliveira, A., and A. B. Fortunato (2002), Toward an oscillation-free, mass conservative, Eulerian–Lagrangian transport model, *Journal of Computational Physics*, *183*(1), 142–164, doi:10.1006/jcph.2002.7180.

Oliveira, A., A. Santos, A. Rodrigues, and J. Vitorino (2007), Sedimentary particle distribution and dynamics on the Nazaré canyon system and adjacent shelf (Portugal), *Marine Geology*, *246*(2-4), 105–122, doi:10.1016/j.margeo.2007.04.017.

Pasch, R., and T. Kimberlain (2011), Hurricane igor, *Tropical cyclone report*, US National Oceanic and Atmospheric Administration. National Hurricane Center.

Peltier, W. (2004), GLOBAL GLACIAL ISOSTASY AND THE SURFACE OF THE ICE-AGE EARTH: the ICE-5G (VM2) model and GRACE, *Annual Review of Earth and Planetary Sciences*, *32*(1), 111–149, doi:10.1146/annurev.earth.32.082503.144359.

Phillips, O. M. (1960), On the dynamics of unsteady gravity waves of finite amplitude part 1. the elementary interactions, *Journal of Fluid Mechanics*, *9*(02), 193–217, doi:10.1017/S0022112060001043.

Phleger, F. (1981), A review of some general features of coastal lagoons, in *Proceedings of Coastal Lagoon Research, Present and Future*, *UNESCO Technical Papers in Marine Science (33)*, vol. 33, pp. 7–14.

Pinheiro, L. M., R. C. L. Wilson, R. Pena dos Reis, R. B. Whitmarsh, and A. Ribeiro (1996), The western Iberia margin: a geophysical and geological overview, in *Proceedings of the Ocean Drilling Program, scientific results*, p. 3–26.

Pinto, L., A. Fortunato, Y. Zhang, A. Oliveira, and F. Sancho (2012), Development and validation of a three-dimensional morphodynamic modelling system for non-cohesive sediments, *Ocean Modelling*, *57-58*, 1–14, doi:10.1016/j.ocemod.2012.08.005.

Pires, H. N. O., and L. E. V. Pessanha (1986), Wave power climate of portugal, in *Hydrodynamics of Ocean Wave-Energy Utilization*, edited by D. V. Evans and A. F. O. Falcão, pp. 157–167, Springer Berlin Heidelberg, Berlin, Heidelberg.

Pond, S., and G. L. Pickard (1983), *Introductory Dynamical Oceanography*, Gulf Professional Publishing.

Pérez, F. F., C. G. Castro, X. Álvarez–Salgado, and A. F. Ríos (2001), Coupling between the Iberian basin — scale circulation and the Portugal boundary current system: a chemical study, *Deep Sea Research Part I: Oceanographic Research Papers*, *48*(6), 1519–1533, doi:10.1016/S0967-0637(00)00101-1.

Pritchard, D. W. (1952), Estuarine hydrography, *Advances in Geophysics*, *1*, 243.

Quadrio, A., and R. Taborda (2010), Portugual western coast, in *Review of climate Change Impact on Storm Occurrence Occurrence—Micore Project Deliverable 202798*, edited by . Ferreira, M. I. Vousdoukas, and P. Ciavola, pp. 71–78.

Ranasinghe, R., and C. Pattiaratchi (1999), The seasonal closure of tidal inlets: Wilson inlet—a case study, *Coastal Engineering*, *37*(1), 37–56.

Ranasinghe, R., C. Pattiaratchi, and G. Masselink (1999), A morphodynamic model to simulate the seasonal closure of tidal inlets, *Coastal Engineering*, *37*(1), 1–36.

Reineck, P. D. H.-E., and D. I. B. Singh (1973), *Introduction*, Springer Study Edition, Springer Berlin Heidelberg.

Reis, A. H., and C. Gama (2010), Sand size versus beachface slope — an explanation based on the constructal law, *Geomorphology*, *114*(3), 276–283, doi:10.1016/j.geomorph.2009.07.008.

Relvas, P., E. Barton, J. Dubert, P. B. Oliveira, l. Peliz, J. da Silva, and A. M. P. Santos (2007), Physical oceanography of the western iberia ecosystem: Latest views and challenges, *Progress in Oceanography*, *74*(2-3), 149–173, doi:10.1016/j.pocean.2007.04.021.

Ris, R. C., and L. H. Holthuijsen (1996), Spectral modelling of current-induced wave-blocking, *Coastal Engineering Proceedings*, *1*(25), doi:10.9753/icce.v25.

Roelvink, D., A. Reniers, A. van Dongeren, J. van Thiel de Vries, R. McCall, and J. Lescinski (2009), Modelling storm impacts on beaches, dunes and barrier islands, *Coastal Engineering*, *56*(11-12), 1133–1152, doi:10.1016/j.coastaleng.2009.08.006.

Roelvink, J. (2006), Coastal morphodynamic evolution techniques, *Coastal Engineering*, *53*(2-3), 277–287, doi:10.1016/j.coastaleng.2005.10.015.

Rogers, W. E., J. M. Kaihatu, H. A. H. Petit, N. Booij, and L. H. Holthuijsen (2002), Diffusion reduction in an arbitrary scale third generation wind wave model, *Ocean Engineering*, *29*(11), 1357–1390.

Roland, A. (2009), Spectral wave modelling on unstructured meshes, Ph.D. thesis.

Roland, A., Y. J. Zhang, H. V. Wang, Y. Meng, Y.-C. Teng, V. Maderich, I. Brovchenko, M. Dutour-Sikiric, and U. Zanke (2012), A fully coupled 3D wave-current interaction model on unstructured grids, *Journal of Geophysical Research*, *117*, doi:10.1029/2012JC007952.

Rusu, L., M. Bernardino, and C. Guedes Soares (2011), Modelling the influence of currents on wave propagation at the entrance of the Tagus estuary, *Ocean Engineering*, *38*(10), 1174–1183, doi:10.1016/j.oceaneng.2011.05.016.

Santamaría-Gómez, A., M. Gravelle, X. Collilieux, M. Guichard, B. M. Míguez, P. Tiphaneau, and G. Wöppelmann (2012), Mitigating the effects of vertical land motion in tide gauge records using a state-of-the-art GPS velocity field, *Global and Planetary Change*, *98–99*, 6–17, doi:10.1016/j.gloplacha.2012.07.007.

Santos, F., K. Forbes, and R. Moita (2001), *Climate change in Portugal. Scenario, impacts and adaptation measures*, gradiva ed., Lisbon, Portugal.

Sauvaget, P., E. David, and C. Guedes Soares (2000), Modelling tidal currents on the coast of Portugal, *Coastal engineering*, *40*(4), 393–409.

Shyy, W., M.-H. Chen, R. Mittal, and H. Udaykumar (1992), On the suppression of numerical oscillations using a non-linear filter, *Journal of Computational Physics*, *102*(1), 49–62, doi:10.1016/S0021-9991(05)80004-X.

Silva, A., R. Taborda, A. Rodrigues, J. Duarte, and J. Cascalho (2007), Longshore drift estimation using fluorescent tracers: New insights from an experiment at Comporta Beach, Portugal, *Marine Geology*, *240*(1-4), 137–150, doi:10.1016/j.margeo.2007.02.009.

Silva, A., R. Taborda, X. Bertin, and G. Dodet (2012), Seasonal to decadal variability of longshore sand transport at the northwest coast of Portugal, *Journal of Waterway, Port, Coastal, and Ocean Engineering*, *138*(6), 464–472, doi:10.1061/(ASCE)WW.1943-5460.0000152.

Smith, D. (1987), The hydrology and geomorphology of tidal basins, in *The closure of tidal basins*, Delft University Press, Delft.

Smith, E. R., P. Wang, and J. Zhang (2003), Evaluation of the CERC formula using large-scale model data, in *Proceedings of Coastal Sediments*, vol. 3.

Smith, R. (1975), The reflection of short gravity waves on a non-uniform current, *Mathematical Proceedings of the Cambridge Philosophical Society*, *78*(03), 517–525, doi:10.1017/S0305004100052002.

Smith, W. H. F., and D. T. Sandwell (1997), Global sea floor topography from satellite altimetry and ship depth soundings, *Science*, *277*(5334), 1956–1962, doi:10.1126/science.277.5334.1956.

Soulsby, R. (1997), *Dynamics of Marine Sands: A Manual for Practical Applications*, Thomas Telford.

Srivastava, S. P., J.-C. Sibuet, S. Cande, W. R. Roest, and I. D. Reid (2000), Magnetic evidence for slow seafloor spreading during the formation of the newfoundland and iberian margins, *Earth and Planetary Science Letters*, *182*(1), 61–76.

Stockdon, H. F., R. A. Holman, P. A. Howd, and A. H. Sallenger (2006), Empirical parameterization of setup, swash, and runup, *Coastal Engineering*, *53*(7), 573–588, doi:10.1016/j.coastaleng.2005.12.005.

Stutz, M. L., and O. H. Pilkey (2011), Open-ocean barrier islands: Global influence of climatic, oceanographic, and depositional settings, *Journal of Coastal Research*, *272*, 207–222, doi:10.2112/09-1190.1.

Suastika, I., M. Jong, and J. Battjes (2001), Experimental study of wave blocking, in *Coastal Engineering 2000*, pp. 227–240, American Society of Civil Engineers.

Suastika, I. K. (2012), A spectral model for blocking of random waves, *Coastal Engineering Journal*, *54*(02), 1250,013, doi:10.1142/S0578563412500131.

Taveira-Pinto, F., J. Pais-Barbosa, and F. Veloso-Gomes (2009), Coastline evolution at Esmoriz-Furadouro stretch (Portugal), *Journal of Coastal Research*, (SI 56 Proceedings of the 10th International Coastal Symposium), 673–677.

Teixeira, M. A. C., and S. E. Belcher (2002), On the distortion of turbulence by a progressive surface wave, *Journal of Fluid Mechanics*, *458*, doi:10.1017/S0022112002007838.

Teixeira, S. (1990), MSc thesis: Dinâmica das praias da península de Setúbal (Portugal)., *Tech. rep.*

Teixeira, S. (1994), Dinâmica morfosedimentar da Ria de Aveiro Portugal, Ph.D. thesis, University of Lisbon.

Thanh Tung, T. (2011), Morphodynamics of seasonally closed coastal inlets at the central coast of Vietnam, Ph.D. thesis, Delft University of Technology.

Thomas, G. P. (1981), Wave-current interactions: an experimental and numerical study. part 1. linear waves, *Journal of Fluid Mechanics*, *110*, 457–474, doi:10.1017/S0022112081000839.

Toledo, Y., T.-W. Hsu, and A. Roland (2011), Extended time-dependent mild-slope and wave-action equations for wave–bottom and wave–current interactions, *Proceedings of the Royal Society A: Mathematical, Physical and Engineering Science*, doi:10.1098/rspa.2011.0377.

Tolman, H. L. (1992), Effects of numerics on the physics in a third-generation wind-wave model, *Journal of Physical Oceanography*, *22*(10), 1095–1111, doi:10.1175/1520-0485(1992)022<1095:EONOTP>2.0.CO;2.

Tolman, H. L. (2003), Treatment of unresolved islands and ice in wind wave models, *Ocean Modelling*, *5*(3), 219–231, doi:10.1016/S1463-5003(02)00040-9.

Tolman, H. L. (2008), A mosaic approach to wind wave modeling, *Ocean Modelling*, *25*(1-2), 35–47, doi:10.1016/j.ocemod.2008.06.005.

Tolman, H. L. (2009), User manual and system documentation of WAVEWATCH III TM version 3.14, *Technical note, MMAB Contribution*, (276).

Tomczak, M., and J. S. Godfrey (1994), *Regional oceanography: an introduction*, Pergamon.

Townend, I. (2005), An examination of empirical stability relationships for UK estuaries, *Journal of Coastal Research*, pp. 1042–1053, doi:10.2112/03-0066R.1.

Tracy, B. A., and D. T. Resio (1982), Theory and calculation of the nonlinear energy transfer between sea waves in deep water., *Tech. rep.*

Tucker, M. J., and E. G. Pitt (2001), *Waves in ocean engineering*, Elsevier.

Tung, T. T., D. Walstra, J. van de Graaf, and M. J. Stive (2009), Morphological modeling of tidal inlet migration and closure, pp. 1080–1084.

Umlauf, L., and H. Burchard (2003), A generic length-scale equation for geophysical turbulence models, *Journal of Marine Research*, *61*(2), 235–265, doi:10.1357/002224003322005087.

United Nations (2013a), UN atlas of the oceans.

United Nations (2013b), World population prospects: The 2012 revision, key findings and advance tables, *Tech. rep.*, United Nations, Department of Economic and Social Affairs, Population Division, New-York.

United States Census Bureau (2011), International data base.

USACE (1984), *Shore protection manual. United States Army Corps of Engineers*, Vicksburg, Miss. : Dept. of the Army, Waterways Experiment Station, Corps of Engineers, Coastal Engineering Research Center ; Washington, DC : For sale by the Supt. of Docs., U.S. G.P.O.

van der Linden, P., and J. Mitchell (Eds.) (2009), *ENSEMBLES: Climate Change and its Impacts: Summary of research and results from the ENSEMBLES project*, Met Office Hadley Centre, Exeter, UK.

van der Wegen, M., and J. A. Roelvink (2008), Long-term morphodynamic evolution of a tidal embayment using a two-dimensional, process-based model, *Journal of Geophysical Research*, *113*(C3), doi:10.1029/2006JC003983.

van der Westhuysen, A. J. (2012), Spectral modeling of wave dissipation on negative current gradients, *Coastal Engineering*, *68*, 17–30.

van der Westhuysen, A. J., M. Zijlema, and J. A. Battjes (2007), Nonlinear saturation-based whitecapping dissipation in SWAN for deep and shallow water, *Coastal Engineering*, *54*(2), 151–170, doi:10.1016/j.coastaleng.2006.08.006.

Van Dongeren, A., et al. (2011), Spectral wave modelling in tidal inlet seas: results from the SBW Wadden Sea project, *Coastal Engineering Proceedings*, *1*(32), waves.44, doi:10.9753/icce.v32.waves.44.

van Rijn, L. (2007a), Unified view of sediment transport by currents and waves. i: Initiation of motion, bed roughness, and bed-load transport, *Journal of Hydraulic Engineering*, *133*(6), 649–667, doi:10.1061/(ASCE)0733-9429(2007)133:6(649).

van Rijn, L. C. (1987), Mathematical modelling of morphological processes in the case of suspended sediment transport, Ph.D. thesis, Delft University of Technology.

van Rijn, L. C. (2007b), Unified view of sediment transport by currents and waves. II: suspended transport, *Journal of Hydraulic Engineering*, *133*(6), 668–689, doi:10.1061/(ASCE)0733-9429(2007)133:6(668).

van Vledder, G., and D. Hurdle (2002), Performance of formulations for whitecapping in wave prediction models.

Vanney, J.-R., and D. Mougenot (1981), *La plate-forme continentale du Portugal et les provinces adjacentes analyse géomorphologique*, Direccao geral de geologia e minas, serviços geologicos de Portugal, Lisbonne.

Veloso-Gomes, F., and F. Taveira-Pinto (2004), Eurosion case study: Cova do Vapor - Costa da Caparica (Portugal), *Tech. rep.*

Veloso-Gomes, F., J. Costa, A. Rodrigues, F. Taveira-Pinto, J. Pais-Barbosa, and L. das Neves (2009), Costa da Caparica artificial sand nourishment and coastal dynamics, *Journal of Coastal Research*, (SI56), 678–682.

Villaret, C., J.-M. Hervouet, R. Kopmann, U. Merkel, and A. G. Davies (2013), Morphodynamic modeling using the Telemac finite-element system, *Computers & Geosciences*, *53*, 105–113, doi:10.1016/j.cageo.2011.10.004.

Walden, H., N. Hogben, M. Burkhart, R. Dorrestein, W. Warnsink, and Y. Yamanouchi (1970), Long term variability, in *4th International Ship Structures Congress*, pp. 49–59, Tokyo, Japan.

WAMDI (1988), The WAM Model—A third generation ocean wave prediction model, *Journal of Physical Oceanography*, *18*(12), 1775–1810, doi:10.1175/1520-0485(1988)018<1775:TWMTGO>2.0.CO;2.

Wang, X. L., and V. R. Swail (2002), Trends of Atlantic wave extremes as simulated in a 40-yr wave hindcast using kinematically reanalyzed wind fields, *Journal of Climate*, *15*(9), 1020–1035, doi:10.1175/1520-0442(2002)015<1020:TOAWEA>2.0.CO;2.

Warner, J. C., C. R. Sherwood, R. P. Signell, C. K. Harris, and H. G. Arango (2008), Development of a three-dimensional, regional, coupled wave, current, and sediment-transport model, *Computers & Geosciences*, *34*(10), 1284–1306, doi:10.1016/j.cageo.2008.02.012.

Warren, I., and H. Bach (1992), MIKE 21: a modelling system for estuaries, coastal waters and seas, *Environmental Software*, *7*(4), 229–240, doi:10.1016/0266-9838(92)90006-P.

WASA (1998), Changing waves and storms in the Northeast Atlantic?, *Bulletin of the American Meteorological Society*, *79*(5), 741–760, doi:10.1175/1520-0477(1998)079<0741:CWASIT>2.0.CO;2.

Webb, D. (1978), Non-linear transfers between sea waves, *Deep Sea Research*, *25*(3), 279–298, doi:10.1016/0146-6291(78)90593-3.

Wolf, J., and D. Prandle (1999), Some observations of wave–current interaction, *Coastal Engineering*, *37*(3), 471–485.

Woolf, D. K. (2002), Variability and predictability of the North Atlantic wave climate, *Journal of Geophysical Research*, *107*(C10), doi:10.1029/2001JC001124.

Wright, L. D., and A. D. Short (1984), Morphodynamic variability of surf zones and beaches: a synthesis, *Marine geology*, *56*(1), 93–118.

Wu, W. (2004), Depth-averaged two-dimensional numerical modeling of unsteady flow and nonuniform sediment transport in open channels, *Journal of Hydraulic Engineering*, *130*(10), 1013–1024, doi:10.1061/(ASCE)0733-9429(2004)130:10(1013).

Yanenko, N., N. (1971), *The Method of Fractional Steps - The Solution of Problems of Mathematical Physics in Several Variables*, Springer, Berlin.

Young, I. R., S. Zieger, and A. V. Babanin (2011), Global trends in wind speed and wave height, *Science*, *332*(6028), 451–455, doi:10.1126/science.1197219.

Zenkovitch, V. P. (1959), On the genesis of cuspate spits along lagoon shores, *The Journal of Geology*, *67*(3), 269–277, doi:10.1086/626583.

Zhang, H., O. S. Madsen, S. A. Sannasiraj, and E. Soon Chan (2004), Hydrodynamic model with wave–current interaction in coastal regions, *Estuarine, Coastal and Shelf Science*, *61*(2), 317–324.

Zhang, Y., and A. M. Baptista (2008a), SELFE: a semi-implicit Eulerian–Lagrangian finite-element model for cross-scale ocean circulation, *Ocean Modelling*, *21*(3–4), 71–96, doi:10.1016/j.ocemod.2007.11.005.

Zhang, Y. J., and A. M. Baptista (2008b), An efficient and robust tsunami model on unstructured grids. part i: Inundation benchmarks, *Pure and Applied Geophysics*, *165*(11-12), 2229–2248, doi:10.1007/s00024-008-0424-7.

Zhang, Y. J., R. C. Witter, and G. R. Priest (2011), Tsunami–tide interaction in 1964 Prince William sound tsunami, *Ocean Modelling*, *40*(3–4), 246–259, doi:10.1016/j.ocemod.2011.09.005.

Appendix A

Applications of the model to academic test cases

In the preliminary stage of development of the morphodynamic modelling system, two applications were realized against academic test cases, in order to assess qualitatively the skills of the model.

A.1 Trench migration

This test reproduced the laboratory experiment of [*van Rijn*, 1987] and provides a means of validation for the transport and bottom update modules, in the absence of wave. The experiment described by *van Rijn* [1987] consisted of measuring velocity profiles, sediment concentration profiles and bed level changes in a straight and long channel (length = 30 m, width = 0.5 m) with a vertical depression (trench) in the mobile sand bed. The gradient of velocities on either part of the trench lead to the migration of the trench. The channel profile was measured after 15 hours. The characteristic diameter of the sediment was d50 = 0.16 mm. The water depth and the mean flow velocity upstream of the trench was held constant (h0 = 0.39 m, u0 = 0.51 m/s).

Numerical simulations were performed with the morphodynamic modelling system in a 30 m long channel with a characteristic diameter of 0.14 mm. The total load transport was simulated with the Soulsby-Van Rijn formula [*Soulsby*, 1997]). Simulations were run for 15 hours and the final bathymetry was compared to the observations. Fig.A.1 shows the model results for three

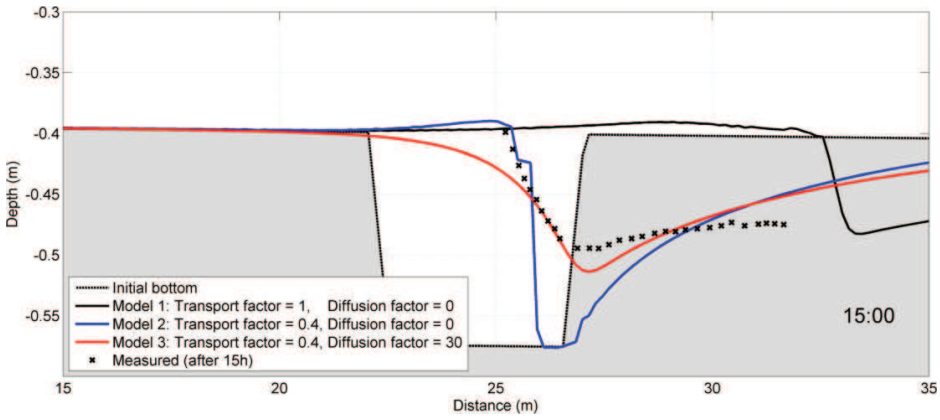

Figure A.1: Model/data comparison for the trench migration test case of van Rijn [1987].

configurations: 1) a baseline configuration (black line) were the trench migration was strongly overestimated; 2) a second configuration where the total transport was multiplied by a factor 0.4 in order to counteract the transport overestimation obtained with the baseline configuration; and 3) a configuration were the transport was scaled by 0.4 and the diffusive factor ϵ of equation 5.73 was set to 30. These preliminary results showed that the model reproduce the trench migration. However the transport formula of Soulsby-Van Rijn tended to overestimate the transport. With a scaling factor of 0.4 applied to the sediment flux, the migration rate of the trench in the simulations was comparable to the one of the experiment. Finally the huge diffusive factor was applied to observe its effect on the behaviour of the model. This last configuration provided the best comparisons although such calibration is obviously not realistic for real case application. Further simulations will be performed with this test case in order to assess the multi-class version of the sediment transport model, that is currently under development. Comparisons with the results obtained by [*Pinto et al.*, 2012] with a 3D morphodynamic modelling system will also be performed.

A.2 Breakwater test case

The breakwater test case was defined by *Nicholson et al.* [1997] in order to perform an inter-comparison of several morphodynamic modelling systems. This case represents a single, shore-parallel, offshore breakwater founded on a plane sloping beach and subjected to the action of normally-incident, storm waves. The wave energy gradient caused by the breakwater induce lateral wave forces and subsequent current circulation, which promotes the accretion in front of the breakwater. After 72 hours, a tombolo-like feature is observed in most of the model results. Fig.A.2 shows the significant wave height, the current velocities and the initial and final

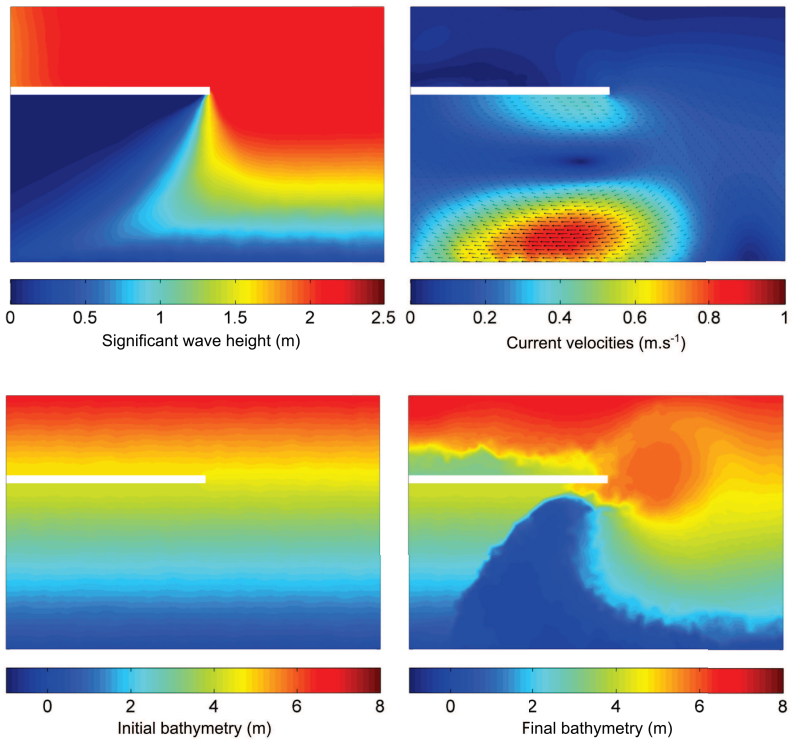

Figure A.2: Model results for the breakwater case of Nicholson et al. [1997]: significant wave height, current velocities, initial bathymetry and final bathymetry.

bathymetry (after 72 hours) computed by the morphodynamic modelling system. Although severe erosion occurred behind the breakwater, probably due to inadequate boundary conditions that induced undesired radiation stress gradients, the model reproduced the expected current field and accretion pattern in front of the breakwater.

The application of the modelling system to this academic test case was only undertaken to verify that the behaviour of the model in the presence of waves was correct. However, a more detailed analysis and inter-comparison with other morphodynamic modelling system would provide relevant information for the validation of the modelling system.